



THE HONG KONG  
POLYTECHNIC UNIVERSITY

香港理工大學

Pao Yue-kong Library

包玉剛圖書館

---

## Copyright Undertaking

This thesis is protected by copyright, with all rights reserved.

**By reading and using the thesis, the reader understands and agrees to the following terms:**

1. The reader will abide by the rules and legal ordinances governing copyright regarding the use of the thesis.
2. The reader will use the thesis for the purpose of research or private study only and not for distribution or further reproduction or any other purpose.
3. The reader agrees to indemnify and hold the University harmless from and against any loss, damage, cost, liability or expenses arising from copyright infringement or unauthorized usage.

### IMPORTANT

If you have reasons to believe that any materials in this thesis are deemed not suitable to be distributed in this form, or a copyright owner having difficulty with the material being included in our database, please contact [lbsys@polyu.edu.hk](mailto:lbsys@polyu.edu.hk) providing details. The Library will look into your claim and consider taking remedial action upon receipt of the written requests.

**STRUCTURAL BEHAVIOR OF  
FRP-REINFORCED CONCRETE ARCHES**

**XIA ZHIYU**

**PhD**

The Hong Kong Polytechnic University

This programme is jointly offered by The Hong Kong Polytechnic  
University and Zhejiang University

**2025**

The Hong Kong Polytechnic University  
Department of Civil and Environmental Engineering

Zhejiang University  
College of Civil Engineering and Architecture

**STRUCTURAL BEHAVIOR OF  
FRP-REINFORCED CONCRETE ARCHES**

**XIA Zhiyu**

A thesis submitted in partial fulfilment of the requirements for the degree of  
Doctor of Philosophy

February 2025

## CERTIFICATE OF ORIGINALITY

I hereby declare that this thesis is my own work and that, to the best of my knowledge and belief, it reproduces no material previously published or written, nor material that has been accepted for the award of any other degree or diploma, except where due acknowledgement has been made in the text.

\_\_\_\_\_ (Signed)

XIA Zhiyu (Name of student)

*To My Parents*

## **ABSTRACT**

Arches are a common type of structures that have been extensively used in the field of civil engineering, known for their excellent spanning and load-bearing capabilities. Traditionally employed in tunnel linings and bridges, arch structures are typically designed for a long service life (e.g., more than 100 years). However, steel-reinforced concrete (RC) arch structures often suffer from degradation due to steel corrosion, resulting in massive maintenance and repair costs. To address the durability problem, the use of fiber-reinforced polymer (FRP) bars in substitution of traditional steel rebars has gained increasing applications, particularly for structures exposed to a corrosive environment.

This PhD study is concerned with the structural behavior of FRP-RC arches. The study started with preliminary investigations on an FRP-RC arch, which validate the feasibility of such arch structures while elucidating two key challenges that they may face: (1) the use of existing FRP stirrup products, whose horizontal legs take up a significant portion of space in shallow arches, may negatively affect the flexural stiffness/strength and lead to locally weak sections in such arches; (2) the relatively low elastic modulus of glass FRP (GFRP) compared to steel may result in significant load drops accompanied with the opening of major cracks in under-reinforced arches. Furthermore, it was found in the preliminary investigations that the existing simplified theoretical models fail to account for geometric nonlinearity and may thus overestimate the load-bearing capacity of FRP-RC arches.

This study was then focused on addressing these challenges so as to facilitate the wide practical applications of FRP-RC arches. Firstly, a novel form of narrow closed FRP stirrups, fabricated via a filament winding process, was developed. The horizontal legs are purposely removed in the novel stirrups to minimize the reduction of concrete area and the resulting local weakening of section capacity, while the use of filament winding method leads to enhanced strength at the bent region of the stirrups compared to the pultruded FRP stirrup products in the market. The effectiveness of the novel stirrups as shear reinforcement of concrete structures were demonstrated in this study by systematic laboratory tests.

To mitigate the effects of relatively low elastic modulus of GFRP rebars, it is recommended that GFRP-reinforced concrete arches shall be designed as over-reinforced members to meet the serviceability requirements and to reduce/eliminate the load drops associated with opening of cracks. A systematic experimental study was then conducted on over-reinforced FRP-RC arches with the novel stirrups proposed in this PhD project. The structural behavior of these arches was thoroughly examined, and it was demonstrated that they can sustain a monotonically increasing load without significant load drops upon cracking, and that their load-bearing capacities are comparable to the steel-reinforced concrete arch with a similar reinforcement ratio.

Furthermore, to gain a comprehensive understanding of the structural behavior of FRP-RC arches, two advanced predictive methods were developed: one based on one-dimensional (1D) theoretical modeling and the other based on three-dimensional (3D) finite element (FE) simulations. The 1D theoretical model was developed based on an enhanced deflection method, offering a unified approach for handling both small- and large-curvature problems in 1D members, with an emphasis on its applicability to FRP-RC arches and other FRP-enabled arches. The enhanced deflection method considers the interaction between axial forces and

bending moments while ignoring shear contributions, and it is thus suitable for efficiently analyzing simple uniaxial or biaxial load cases at relatively small computational costs.

The sophisticated 3D FE model was developed to provide more in-depth insights into the behavior of FRP-RC arches. This model effectively captures complex load interactions (e.g., combined effects of axial load, shear load, and bending moment) and the bond-slip relationship between FRP rebars and the surrounding concrete. The model was validated using the test results and was subsequently employed in a parametric study on FRP-RC arches, considering a wide range of parameters that may affect their structural behavior. The results of the parametric study have laid a solid foundation for the design of FRP-RC arches to suit various structural demands.

## LIST OF PUBLICATIONS

### Refereed Journal Papers

Xia, Z.Y., Jiang, T., and Yu, T. (2023) Innovating arch structures with fiber-reinforced polymer composites: A review. *Advances in Structural Engineering* 26(13): 2341-2358.

Xia, Z.Y., Jiang, T., and Yu, T. (2024) Enhanced deflection method for large-curvature problems: Formulation, verification and application to FRP-enabled arches. *Advances in Structural Engineering* 13694332241263871.

Xia, Z.Y., Yu, T., and Jiang, T. (2024) Novel narrow closed FRP stirrups fabricated via a filament winding process: Concept and behavior. *Construction and Building Materials*. (Under review).

Xia, Z.Y., Jiang, T., and Yu, T. (2024) Behavior of over-reinforced FRP-reinforced concrete arches with tailored stirrups. Nearly ready for submission.

Xia, Z.Y., Yu, T., and Jiang, T. (2024) Finite element modelling of FRP bar reinforced concrete arches: Analysis and parametric study. Nearly ready for submission.

### Conference Paper

**Xia, Z.Y.**, Yu, T., and Jiang, T. (2023) Behaviour of FRP-reinforced concrete arches. *Proceedings of 11th International Conference on Fibre-Reinforced Polymer (FRP) Composites in Civil Engineering* 23-26 July, Rio de Janeiro, Brazil.

**Other Referred Journal Papers During Ph.D. Study:**

Wu, D.Y., Wu, W.T., Zhao, J.L. and **Xia, Z.Y.\*** (2024) Flexural behaviour of BFRP grid/bar reinforced UHPC beams and slabs. *Journal of Building Engineering* 111121.

Xie, E.L., Jiang, T., **Xia, Z.Y.**, and Xu, W.S. (2023) Postbuckling behaviour of FRP bending-active arches subjected to a central point load. *Journal of Composites for Construction* 27(5): 04023039.

Bao, H.X., **Xia, Z.Y.**, and Jiang, T. (2024). One-dimensional deflection method using Euler spiral as deflection function. *Spatial Structures*.

## ACKNOWLEDGMENTS

First and foremost, I would like to express my heartfelt gratitude to my chief supervisor, Professor Yu Tao of The Hong Kong Polytechnic University, and my co-supervisor, Associate Professor Jiang Tao of Zhejiang University, for providing me with the opportunity to pursue my doctoral studies under their tutelage. Their rigorous training, enlightening guidance, and unwavering support have been instrumental throughout my academic journey.

I am also profoundly grateful to both former and current members of Prof. Yu's research group, whose shared knowledge and assistance were invaluable during my Ph.D. pursuit. Special thanks go to Associate Professor Lin Guan of the Southern University of Science and Technology, as well as Dr. Michael Chan, Dr. Xiang Yu, Dr. Xia Bing, Dr. Huang Le, Dr. Huang Zheng, Dr. Zhang Pan, Dr. Liu Kai-Cheng, Mr. Li Rui-Long, Mr. Zhu Jia-Ming, Mr. Han Dong, Mr. Liu Po-Chang, Mr. Cai Jia-Jie, Mr. Zhang Jun-Jie, Miss Li Xin-Yun and Miss Cui Chu-Yin of The Hong Kong Polytechnic University, for their significant contributions to my experimental and theoretical work. I also deeply appreciate the support and encouragement from Prof. Jiang's research group, including Dr. Wang Xiao-Meng, Dr. Xie En-Li, Mr. Song Yi-Xiong, Mr. Chen Yao-Lun, Mr. Ji Ping, Mr. Chen Peng, Mr. Chen Yong, Mr. Bai Yong-Ze, and Mr. Bao Heng-Xing.

I wish to extend my sincere thanks to the technical staff at Zhejiang University and The Hong Kong Polytechnic University, as well as Mr. Lu Ming-Ru and Mr. Tang Yong-Xin from

Hangzhou Construction Component Co. and Mr. Mei Wei-Jun from Hangzhou Lian Fiberglass Co., for their valuable advice and assistance with my experimental work.

I gratefully acknowledge the financial support provided by the Hong Kong Research Grants Council (Project No.: T22-502/18-R) and the National Natural Science Foundation of China (Project No.: 51778569). I am also deeply thankful to The Hong Kong Polytechnic University and Zhejiang University for their excellent research environments and facilities, as well as the PolyU-ZJU Joint PhD Program for facilitating my PhD journey under the joint supervision of the two supervisors.

Last but not least, I extend my deepest gratitude to my family. I owe an immeasurable debt to my family, whose unwavering support and sacrifice allowed me to remain dedicated to my Ph.D. research.

## CONTENTS

CERTIFICATE OF ORIGINALITY .....	I
ABSTRACT .....	III
ACKNOWLEDGMENTS.....	VIII
CONTENTS .....	X
LIST OF FIGURES.....	XVII
LIST OF TABLES .....	XXIII
LIST OF ACRONYMS.....	XXV
NOTATION .....	XXVII
CHAPTER 1 INTRODUCTION .....	1
1.1 BACKGROUND .....	1
1.2 FRP-REINFORCED CONCRETE ARCHES .....	3
1.3 OBJECTIVES AND SCOPE.....	6
1.4 THESIS OUTLINE.....	7
1.5 REFERENCES .....	10
CHAPTER 2 LITERATURE REVIEW .....	15
2.1 INTRODUCTION .....	15

2.2 MANUFACTURING METHODS FOR CURVED FRP MEMBERS .....	16
2.2.1 Vacuum infusion .....	16
2.2.2 Filament winding .....	17
2.2.3 Pultrusion .....	18
2.2.4 Active bending .....	19
2.3 ALL-FRP ARCHES.....	20
2.3.1 Vacuum infusion-manufactured arches .....	20
2.3.2 Pultruded arches.....	21
2.3.3 Bending-active arches .....	23
2.4 FRP-INCORPORATING HYBRID ARCHES .....	24
2.4.1 FRP bar-reinforced concrete arch segments .....	24
2.4.2 FRP-concrete arch panels .....	25
2.4.3 Concrete-filled FRP tubular arches.....	26
2.4.4 FRP-concrete-steel double-skin tubular arches .....	28
2.5 SUMMARY AND RESEARCH NEEDS .....	29
2.5.1 Brief summary .....	29
2.5.2 Research needs for all-FRP arches .....	30
2.5.3 Research needs for FRP-incorporating hybrid arches .....	33
2.6 CONCLUDING REMARKS.....	36
2.7 REFERENCES .....	38

## CHAPTER 3 PRELIMINARY INVESTIGATION ON FRP

REINFORCED CONCRETE ARCHES.....	60
3.1 INTRODUCTION .....	60
3.2 EXPERIMENTAL PROGRAM .....	60
3.2.1 Specimen details .....	60
3.2.2 Material properties .....	61
3.2.3 Test setup .....	63
3.3 TEST RESULTS AND DISCUSSION .....	64
3.4 ANALYSIS OF LOAD CAPACITY .....	66
3.5 KEY ISSUES AND POTENTIAL IMPROVEMENTS.....	68
3.5.1 FRP stirrups .....	68
3.5.2 Failure modes of under-reinforced and over-reinforced concrete arches .....	71
3.5.3 Predictive model .....	73
3.6 CONCLUSIONS.....	75
3.7 REFERENCES .....	77

## CHAPTER 4 NOVEL NARROW CLOSED FRP STIRRUPS

FABRICATED VIA A FILAMENT WINDING PROCESS.....	86
4.1 INTRODUCTION .....	86
4.2 NOVEL NARROW CLOSED FRP STIRRUPS.....	88
4.3 LABORATORY DEMONSTRATION OF FABRICATION.....	90
4.4 TENSILE TESTS.....	91

4.5 BENDING TESTS .....	93
4.5.1 Specimen details .....	93
4.5.2 Test setup and instrumentation .....	93
4.5.3 Test results and discussions .....	94
4.5.4 Comparison with design equations .....	96
4.6 CONCLUSIONS.....	98
4.7 REFERENCES .....	99

## CHAPTER 5 EXPERIMENTAL STUDY OF FRP REINFORCED

CONCRETE ARCHES .....	113
5.1 INTRODUCTION .....	113
5.2 EXPERIMENTAL PROGRAM .....	116
5.2.1 Test samples.....	116
5.2.2 Preparation of the arch specimens .....	117
5.2.3 Material properties .....	120
5.2.4 Bond-slip properties of GFRP bars and concrete .....	123
5.2.5 Test setup and loading scheme .....	124
5.3 RESULTS AND DISCUSSION .....	127
5.3.1 Failure modes and crack patterns.....	127
5.3.2 Load-deflection curves.....	130
5.3.3 Strain development of longitudinal reinforcement .....	131
5.3.4 Efficiency of longitudinal reinforcement.....	133

5.3.5 Serviceability .....	135
5.3.6 Strain development of transverse reinforcement .....	139
5.4 CONCLUSIONS.....	141
5.5 REFERENCES .....	143

## CHAPTER 6 THEORETICAL MODEL FOR FRP REINFORCED

### CONCRETE ARCHES AND OTHER FRP-ENABLED ARCHES

.....	169
6.1 INTRODUCTION .....	169
6.1.1 Numerical simulation.....	169
6.1.2 Deflection method.....	171
6.2 MODEL FORMULATION .....	174
6.2.1 Discretization process .....	174
6.2.2 Deflection function .....	175
6.2.3. Solution procedure .....	179
6.2.4. Handling of intermediate hinge joints.....	181
6.2.5. Handling of semi-rigid connections.....	182
6.3 VERIFICATION.....	183
6.3.1 Comparisons with analytical results of linear elastic arches .....	183
6.3.2 Comparisons with numerical result of slender FRP-confined RC columns .	186
6.4 APPLICATION TO FRP-REINFORCED ARCHES AND OTHER FRP-ENABLED ARCHES.....	187

6.4.1 FRP-reinforced concrete arches .....	187
6.4.2 FRP bending-active arches .....	192
6.4.3 Concrete-filled FRP tubular (CFFT) arches .....	194
6.5 LIMITATIONS.....	196
6.6 CONCLUSIONS.....	198
6.7 REFERENCES .....	201

## CHAPTER 7 FINITE ELEMENT MODELING OF FRP REINFORCED

CONCRETE ARCHES .....	227
7.1 INTRODUCTION .....	227
7.2 FINITE ELEMENT MODELING.....	230
7.2.1 General.....	230
7.2.2 Boundary conditions and loading schemes.....	231
7.2.3 Material modeling of concrete .....	232
7.2.4 Material modeling of steel and FRP reinforcement.....	233
7.2.5 Interface modeling of reinforcement and concrete .....	235
7.2.6 Material modeling of steel supports and beam foundation.....	238
7.3 VALIDATION OF FE MODEL.....	238
7.3.1 Load-deflection responses .....	238
7.3.2 Crack patterns and development.....	240
7.3.3 Strain distribution and development .....	241
7.4 PARAMETRIC STUDY .....	243

7.4.1 Description of the parametric study .....	243
7.4.2 Effect of concrete cover thickness .....	244
7.4.3 Effect of longitudinal reinforcement ratio .....	246
7.4.4 Effect of concrete compressive strength .....	249
7.4.5 Effect of longitudinal reinforcement in compression .....	250
7.5 CONCLUSIONS.....	252
7.6 REFERENCES .....	255
<b>CHAPTER 8 CONCLUSIONS.....</b>	<b>278</b>
8.1 INTRODUCTION .....	278
8.2 CHALLENGES IN FRP-REINFORCED CONCRETE ARCHES.....	279
8.3 NOVEL FRP STIRRUPS .....	280
8.4 EXPERIMENTAL STUDY.....	280
8.5 THEORETICAL MODEL.....	282
8.6 FINITE ELEMENT ANALYSIS .....	283
8.7 RECOMMENDATIONS.....	284
8.8 FUTURE RESEARCH .....	285
8.8.1 Experimental research on FRP anchorage systems .....	285
8.8.2 Further experimental research on FRP-reinforced concrete arches .....	285
8.8.3 Development of simplified design formulas for load-bearing capacity.....	286

## LIST OF FIGURES

Figure 2.1 Sketch diagram of vacuum infusion .....	53
Figure 2.2 Sketch diagram of filament winding .....	53
Figure 2.3 Sketch diagram of pultrusion.....	54
Figure 2.4 Sketch diagram of active bending technique.....	54
Figure 2.5 Footbridge made of GFRP pultruded profiles in Lleida, Spain (Hollaway, 2013).....	55
Figure 2.6 Curved-pultruded GFRP footbridge in Beijing, China (Liu et al., 2021).....	55
Figure 2.7 Footbridge manufactured by vacuum infusion in Moscow, Russia (Hollaway, 2013).....	56
Figure 2.8 Scaled model of FRP self-stressed bowstring footbridge (Caron et al., 2009).....	56
Figure 2.9 Prototype of bending-active tied footbridge (Bessini et al., 2019).....	57

Figure 2.10 GFRP bar-reinforced tunnelling lining segment (Caratelli et al., 2016).....	57
Figure 2.11 SFCBs/BFRP bar-reinforced semi-circular arch and such-based tunnel (Zhao et al., 2022) .....	57
Figure 2.12 FRP-concrete arch panel (Jung et al., 2012) .....	58
Figure 2.13 Buried CFFT arch bridge in Maine, USA (Dagher et al., 2012) .....	58
Figure 2.14 Typical sections of DSTMs (Yu et al., 2006).....	59
Figure 2.15 DSTA bridge constructed at University of Queensland, Australia (Burnton et al., 2019) .....	59
Figure 3.1 Sketch of arch specimen .....	80
Figure 3.2 Details of arch specimen (Unit: mm) .....	80
Figure 3.3 Test setup of arch test .....	81
Figure 3.4 Load-deflection curve .....	82
Figure 3.5 Fracture of concrete near the arch crown at the failure point...	82
Figure 3.6 Specimen after test.....	83
Figure 3.7 Diagram of analysis .....	84
Figure 3.8 The effect of stirrup' s horizontal length on axial load-bending moment curve .....	84

Figure 3.9 The effect of stirrup’ s horizontal length on bending moment- curvature curve .....	85
Figure 3.10 The effect of longitudinal reinforcement ratio on bending moment-curvature curve .....	85
Figure 4.1 Novel filament-wound stirrups .....	107
Figure 4.2 Tensile test on novel stirrups .....	107
Figure 4.3 Configuration of beams reinforced with novel filament wound GFRP stirrup .....	108
Figure 4.4 Strengthened specimens for bending tests.....	108
Figure 4.5 Test setup for bending tests .....	109
Figure 4.6 Cracking pattern and development path in bending test .....	110
Figure 4.7 Load-deflection curves in bending test.....	111
Figure 4.8 Strain development on inner surface of stirrups in bending test .....	112
Figure 5.1 Stirrup evolution for novel configuration.....	153
Figure 5.2 GFRP-RC arch specimens .....	153
Figure 5.3 Details of arch specimens .....	155
Figure 5.4 Concreting casting .....	155
Figure 5.5 Production process of curved FRP bars.....	156
Figure 5.6 Tensile tests on steel bars .....	156

Figure 5.7 Tensile tests on GFRP bars.....	157
Figure 5.8 Production of novel FRP stirrups .....	157
Figure 5.9 Tensile tests on novel FRP stirrups .....	158
Figure 5.10 Compressive tests on concrete.....	158
Figure 5.11 Slump tests on concrete .....	159
Figure 5.12 Test setup of pullout tests .....	159
Figure 5.13 Bond stress-slip curves for GFRP bars.....	160
Figure 5.14 Test setup of arch tests.....	161
Figure 5.15 Arrangement at loading head.....	162
Figure 5.16 Layout of deflection measurement .....	162
Figure 5.17 Cracking patterns and development paths.....	163
Figure 5.18 Load-deflection curves .....	164
Figure 5.19 Load-strain relationship of longitudinal reinforcement .....	165
Figure 5.20 Sectional strain distribution at the arch apex.....	166
Figure 5.21 Serviceability analysis of FRP-RC arches.....	167
Figure 5.22 Strain development of FRP stirrups in NCG13L .....	167
Figure 5.23 Failure at the arch crown of NCG13L (View from the back side) .....	168
Figure 6.1 Schematic of the theoretical model .....	213
Figure 6.2 Illustration of the deflection function .....	214

Figure 6.3 Illustration of a circular arch subjected to a uniform radial pressure.....	215
Figure 6.4 Results of analytical verification .....	216
Figure 6.5 Results of numerical verification.....	217
Figure 6.6 Representation of arch specimen with support system in theoretical model (dimensions in mm) .....	218
Figure 6.7 Comparisons of load-strain curves of longitudinal reinforcement in tension.....	219
Figure 6.8 Comparisons of load-deflection curves at arch crown .....	220
Figure 6.9 Comparisons of load-deflection curves at L/4 .....	221
Figure 6.10 Loading tests on active-bending arches (Xie et al., 2023) ...	222
Figure 6.11 Comparisons with load-deflection curves of FRP bending-active arches .....	223
Figure 6.12 Comparisons with deflected shapes of specimen L16SR60	223
Figure 6.13 Hinge-supported CFFT arches (Dagher et al., 2012) .....	224
Figure 6.14 Comparisons with load-deflection curves of CFFT arches..	225
Figure 6.15 A fixed CFFT arch (Majeed et al., 2021) .....	226
Figure 7.1 Configurations of RC arches .....	268
Figure 7.2 FE model of arch specimen with supports and beam foundation .....	269

Figure 7.3 Comparisons of load-deflection curves .....	270
Figure 7.4 The comparisons and distributions of tensile damage of concrete .....	271
Figure 7.5 Crack development of NCG13H .....	272
Figure 7.6 Load-strain development near arch apex.....	273
Figure 7.7 FE model of full-scale arch rib .....	274
Figure 7.8 Effect of concrete cover to the structural responses.....	274
Figure 7.9 Effect of longitudinal reinforcement ratio to the structural responses .....	275
Figure 7.10 Effect of concrete strength to the structural responses.....	276
Figure 7.11 Effect of compressed FRP bar to the structural responses ...	277

## LIST OF TABLES

Table 2.1 Manufacturing/forming methods for curved FRP members.....	51
Table 2.2 Previous FRP-incorporating arch projects and relevant concepts .....	52
Table 3.1 Material properties .....	79
Table 3.2 Mix proportions.....	79
Table 4.1 Test results of tensile tests .....	104
Table 4.2 Test results of bending tests.....	105
Table 4.3 Comparison between test results and predictions.....	106
Table 5.1 Experimental program.....	151
Table 5.2 Mechanical properties of reinforcement and concrete.....	151
Table 5.3 Results of pullout tests on GFRP bars .....	152
Table 5.4 Experimental results.....	152
Table 6.1 Internal forces caused by distributed loads.....	210
Table 6.2 Unknown initial values and boundary conditions of typical types of supports .....	210

Table 6.3 Comparison between predictions and test results of steel/FRP-reinforced concrete arches.....	211
Table 6.4 Geometrical and material properties of CFFT arches.....	212
Table 7.1 Comparisons of key results from experiment and FE analysis	264
Table 7.2 Details of investigated arch ribs and key results from parametric study .....	264

## LIST OF ACRONYMS

BFRP	Basalt Fiber-Reinforced Polymer
CDP	Concrete Damage Plasticity
CEM	Portland-Composite Cement
CFFTA	Concrete-Filled FRP Tubular Arch
CFFTC	Concrete-Filled FRP Tubular Column
CFFTM	Concrete-Filled FRP Tubular Member
CFRP	Carbon Fiber-Reinforced Polymer
COV	Coefficient of Variation
DSTA	Double-Skin Tubular Arch
DSTB	Double-Skin Tubular Beam
DSTC	Double-Skin Tubular Column
DSTM	Double-Skin Tubular Member
FEA	Finite Element Analysis
FRP	Fiber-Reinforced Polymer
FRP-RC	FRP Reinforced Concrete
GFRP	Glass Fiber-Reinforced Polymer
LVDT	Linear Variable Differential Transducer
MCFT	Modified Compression-Field Theory

PFA	Pulverized Fuel Ash
RC	Reinforced Concrete
SFCB	Steel-Fiber Composite Bar
SLS	Serviceability Limit State
SSC	Seawater Sea-Sand Concrete
steel-RC	Steel Reinforced Concrete
TBM	Tunnel Boring Machine
ULS	Ultimate Limit state
1D	One-Dimensional
3D	Three-Dimensional

## NOTATION

$\alpha$	dimensionless flexibility of spring
$\alpha_c$	parameter in stress-strain model for concrete in compression
$\alpha_s, s_{s,1}, s_{s,2},$ $s_{s,3}$	parameters in a bond stress-slip model for steel bar and concrete
$\alpha_t$	parameter in stress-strain model for concrete in tensile
$\beta$	central angle at the point of interest
	ratio of the distance from the elastic cracked section neutral axis to the
$\beta_{cr}$	extreme tension fiber to the distance from the elastic cracked section neutral axis
$\beta_{s_i}$	central angle of segment $i$
$\gamma$	rotation at boundary
$\epsilon$	flow potential eccentricity in CDP model
$\epsilon_c$	axial strain of concrete
$\epsilon_{co}$	strain corresponding to the compressive strength
$\epsilon_{cu}$	ultimate strain of concrete
$\epsilon_{frp}$	axial strain of FRP bar
$\epsilon_{frp,t}$	rupture strain of FRP bar
$\epsilon_{i+\frac{1}{2}}$	axial strain of centroidal axis at the midpoint of segment $i$

$\varepsilon_s$	strain of steel bar
$\varepsilon_{t0}$	strain corresponding to the tensile strength
$\varepsilon_{0.5}$	the maximum recorded stirrup strain corresponding to 0.5 mm crack width
$\varepsilon_{0.7}$	the maximum recorded stirrup strain corresponding to 0.7 mm crack width
$\zeta$	fibers orientation of FRP stirrups with respect to longitudinal axis
$\eta$	utilization efficiency factor
$\theta_{i,l}$	inclination angle relative to $x$ -axis of the left point in segment $i$
$\theta_{i,r}$	inclination angle relative to $x$ -axis of the right point in segment $i$
$\theta_{i+\frac{1}{2}}$	inclination angle relative to $x$ -axis of the midpoint in segment $i$
$\theta_{S_i}^0$	initial orientation relative to $x$ -axis of segment $i$
$\lambda$	geometrical parameter reflecting both the slenderness and shallowness of arch
$\mu$	vertical displacement at boundary
$\nu$	horizontal displacement at boundary
$\rho_l$	longitudinal reinforcement ratio
$\rho_{S_i}$	radius of curvature of neutral axis for segment $i$
$\sigma_{b0}$	initial biaxial compressive yield stress in CDP model
$\sigma_c$	compressive stress of concrete
$\sigma_{c0}$	uniaxial compressive yield stress in CDP model
$\sigma_{frp}$	axial stress of FRP bar
$\sigma_s$	axial stress of steel bar
$\sigma_t$	tensile stress of concrete
$\tau_{frp}$	bond stress between FRP bar and concrete

$\tau_{frp,f}$	residual bond stress between FRP bar and concrete
$\tau_{frp,max}$	peak bond stress between FRP bar and concrete
$\tau_s$	bond stress between steel bar and concrete
$\tau_{s,f}$	residual bond stress between steel bar and concrete
$\tau_{s,max}$	peak bond stress between steel bar and concrete
$v_0$	vertical displacement of arch crown
$\phi$	dilation angle in CDP model
$\phi_{i+\frac{1}{2}}$	curvature of neutral axis at the midpoint for segment $i$
$\varphi$	central angle at a given point
$\psi$	angle of critical diagonal crack relative to longitudinal axis
$\omega_i$	additional rotation induced by bending moment acting on spring at grid point $i$
$A_{frp}$	cross-sectional area of FRP bar
$A_{fs}$	total cross-sectional area of FRP bars
$d_c$	concrete cover thickness
$d_{cn}$	distance between centroidal axis and neutral axis
$d_{fe}$	equivalent nominal diameter
$d_v$	effective depth of beam
$E_c$	elastic modulus of concrete
$E_{frp,t}$	elastic modulus of FRP bar in tension
$E_s$	elastic modulus of steel bar
$f$	rise of arch
$f_{cu}$	concrete compressive strength from cylinders

$f_{frp,b}$	tensile strength of novel FRP stirrup in curved portion
$f_{frp,sa}$	allowable stress of FRP stirrup in standard
$f_{frp,t}$	tensile strength of FRP bar
$f_{fs}$	allowable stress of FRP bar
$f_s$	yield strength of steel bar
$f_t$	tensile strength of concrete
$f(x)$	shape function of centroidal axis in rectangular coordinate system
$H$	horizontal force at boundary
$H_{ext,i}$	applied concentrated load on grid point $i$ in horizontal direction
$H_i$	internal force of grid point $i$ in horizontal direction
$H_{i+\frac{1}{2}}$	internal force of the midpoint in segment $i$ in horizontal direction
$H_R$	reaction at support in horizontal direction
$K_c$	ratio of the second stress invariant on the tensile meridian to that on the compressive meridian in CDP model
$k_b$	bond factor in the calculation for $f_{fs}$
$k_i$	stiffness of spring at grid point $i$
$L$	total arc length of arch axis
$L_{S_i}$	length of segment $i$
$L_{S_i}^0$	initial length of segment $i$
$M$	section moment; bending moment at boundary
$M_{ext,i}$	applied bending moment at grid point $i$
$M_i$	bending moment at grid point $i$
$M_{i+\frac{1}{2}}$	bending moment at the midpoint of segment $i$

$M_R$	bending moment at support
$N$	section load
$N_{E2}$	the second mode flexural buckling load of a pin-ended column with equal rotational end restraints
$N_i$	axial force at grid point $i$
$N_{i+\frac{1}{2}}$	axial force at the midpoint of segment $i$
$n$	number of grid points; shape parameter for concrete constitutive model
$q_{R,S_i}$	distributed load on segment $i$ in radial direction
$q_{S,S_i}$	distributed load on segment $i$ along arc length
$q_{x,S_i}$	distributed load on segment $i$ in horizontal direction
$q_{y,S_i}$	distributed load on segment $i$ in vertical direction
$R$	radius of arch
$R_s$	inner bend radius of novel FRP stirrup at bent portion
$R_{S_i}$	radius of curvature of neutral axis for segment $i$
$S_i$	segment $i$
$s$	spacing of stirrups
$s_{frp}$	slip between FRP bar and concrete
$s_{frp,1}$	slip corresponding to peak bond stress between FRP bar and concrete
$s_{frp,2}, \alpha_{frp},$	parameters in a bond stress-slip model for FRP bar and concrete
$p$	
$s_s$	slip between steel bar and concrete
$t_f$	thickness of the FRP strip for rectangular sections
$u$	viscosity parameter in CDP model

$V$	vertical force at boundary
$V_c$	shear resistance of concrete
$V_{Exp}$	shear strength from experiment
$V_{ext}$	applied concentrated load in vertical direction
$V_{ext,i}$	applied concentrated load on grid point $i$ in vertical direction
$V_{fs}$	shear resistance of FRP stirrup
$V_i$	internal force of grid point $i$ in vertical direction
$V_{i+\frac{1}{2}}$	internal force of the midpoint in segment $i$ in vertical direction
$V_{Peak}$	peak shear load
$V_R$	reaction at support in vertical direction
$V_{Sta}$	predicted shear resistance from standards
$V_{0.5}$	shear load corresponding to 0.5 mm crack width
$V_{0.7}$	shear load corresponding to 0.7 mm crack width
$w_f$	width of the FRP strip for rectangular sections
$x$	abscissa
$x_i$	abscissa of grid point $i$
$x_{i+\frac{1}{2}}$	abscissa of the midpoint of segment $i$
$y$	ordinate
$y_i$	ordinate of grid point $i$
$y_{i+\frac{1}{2}}$	ordinate of the midpoint of segment $i$
$\Delta\theta_i$	difference between inclination angles at the left and right of grid point $i$
$\Delta f$	initial step size

$\Delta H_{i+\frac{1}{2},q_R}$	contribution from the distributed load $q_R$ of the left half in segment $i$ to the internal force in horizontal direction
$\Delta H_{i+\frac{1}{2},q_S}$	contribution from the distributed load $q_S$ of the left half in segment $i$ to the internal force in horizontal direction
$\Delta H_{i+\frac{1}{2},q_x}$	contribution from the distributed load $q_x$ of the left half in segment $i$ to the internal force in horizontal direction
$\Delta M_{i+\frac{1}{2},q_R}$	contribution from the distributed load $q_R$ of the left half in segment $i$ to the bending moment
$\Delta M_{i+\frac{1}{2},q_S}$	contribution from the distributed load $q_S$ of the left half in segment $i$ to the bending moment
$\Delta M_{i+\frac{1}{2},q_x}$	contribution from the distributed load $q_x$ of the left half in segment $i$ to the bending moment
$\Delta M_{i+\frac{1}{2},q_y}$	contribution from the distributed load $q_y$ of the left half in segment $i$ to the bending moment
$\Delta_{Peak}$	vertical deflection at loading point corresponding the peak shear load
$\Delta V_{i+\frac{1}{2},q_R}$	contribution from the distributed load $q_R$ of the left half in segment $i$ to the internal force in vertical direction
$\Delta V_{i+\frac{1}{2},q_S}$	contribution from the distributed load $q_S$ of the left half in segment $i$ to the internal force in vertical direction
$\Delta V_{i+\frac{1}{2},q_y}$	contribution from the distributed load $q_y$ of the left half in segment $i$ to the internal force in vertical direction
$\Delta x_i$	difference between abscissas at the left point and right point in segment $i$
$\Delta x_{i+\frac{1}{2}}$	difference between abscissas at the left point and midpoint in segment $i$
$\Delta y_i$	difference between ordinates at the left point and right point in segment $i$

$\Delta y_{i+\frac{1}{2}}$  difference between ordinates at the left point and midpoint in segment  $i$

# **CHAPTER 1**

## **INTRODUCTION**

### **1.1 BACKGROUND**

Arches are curvilinear structures resting on supports at the two ends. An arch primarily bears axial compression due to the development of horizontal reaction forces at the supports, which effectively reduce the shearing force and bending moment at any section of the arch. This distinguishing feature enables arch structures to span a large distance.

Early examples of human-built arches, found in Mesopotamian brick architecture, date back to the second millennium BC (Rahman, 2015). This technique then spread to a number of civilizations in the ancient Near East in succession. However, the early applications were limited to underground structures, such as drains, in which case the horizontal reaction forces were resisted by the surrounding soil (Rasch, 1985). It was the Romans who first began systematic use of the arch structure in their engineering feats, which included applications in bridges, aqueducts and gates (Robertson, 1969). Withstanding the test of time, today, arches still remain a mainstream structural form. Due to their outstanding capabilities of spanning and load bearing, arches are favored by engineers in the design of long-span structures such as bridges and roofs, as well as heavy structures such as tunnel linings and dams. Arches have

also found applications in smaller-scale structures, such as buildings and tents, thanks to their aesthetically pleasing appearance and ability to enclose space.

Development of building materials is a major driving force behind the evolution of structures. Arches are no exception. Mainstream materials used for arches have shifted from masonry and timber in early times to concrete and steel nowadays. The use of modern building materials, in tandem with advances in construction technology, has substantially lifted the span limit and enriched the forms of arch structures. The world's longest-span arch bridge, Ping-Nan Third Bridge (located in Ping-Nan, a county in China's Guangxi Province), whose arch ribs are in the form of concrete-filled steel tubular truss, stands at a span of 575 m.

Along the development trajectory of building materials, FRP composites have gained increasing popularity over the past few decades (Teng et al., 2002; Wang and Lau, 2021; Lu et al., 2022). FRP is a non-metallic, high-strength and lightweight composite material that has exceptional resistance to corrosion. When FRP composites first made their entrance to the field of civil engineering in the 1980s, they were mainly used in strengthening applications of reinforced concrete (RC) structures. The success in this area encouraged researchers to investigate their potential for use in new construction. Their efforts have resulted in an expanding variety of FRP members, including reinforcing bars, profiles, confining tubes, cables and bridge decks, among others (Hollaway, 2010). To date, the applications of FRP in new construction have been mostly centered in the domain of linear members (e.g., slabs, beams and columns) and such-based structures (e.g., frames). By contrast, FRP's potential for use in arch structures has received inadequate research attention due to the complexities arising from their curvilinear nature.

In fact, the unique properties of FRP composites, alongside the various methods available for making curved FRP members, offer diverse possibilities for the promotion of this new building material in arch structures. An obvious one that has paramount significance is to use FRP to address the issue of degradation caused by steel corrosion, which is a major challenge facing RC and steel structures (Koch et al., 2016; Roberge, 2019; Cui et al., 2021), including arch structures, especially those exposed to a corrosive environment (e.g., underground environments, marine and coastal areas, and cold regions where de-icing salts are frequently used) (Caratelli et al., 2016; Tang et al., 2020; Lee and Shin, 2010; Dagher et al., 2012; Jiang, 2020).

## **1.2 FRP-REINFORCED CONCRETE ARCHES**

The research on FRP bar-reinforced concrete arches has been mainly intended for underground tunnelling applications. Underground construction today has a life expectancy of over 100 years, with some projects reaching 200 years. The durability of tunnel linings, with particular reference to corrosion of steel reinforcement, is therefore critical. An attractive solution is to use pultruded curved GFRP bars as a substitution for conventional steel reinforcement in concrete tunnel segments, especially for construction in harsh environmental conditions (e.g., sewer tunnels or aggressive soils). The use of GFRP bars brings an extra benefit related to the non-conductivity of GFRP. When tunnel rings assembled from GFRP bar-reinforced segments are installed at regular intervals of a conventional RC tunnel lining, they function as dielectric joints that interrupt the stray currents, thus providing a remedy to electro-corrosion of steel components. This method is particularly suitable for railway tunnels in urban areas where traditional electrical insulation measures are hard or costly to implement.

Due to the above advantages, GFRP bar-reinforced precast tunnel segments have received pioneer research efforts recently and have demonstrated promising potential. Caratelli et al.

(2016) and Tengilimoğlu (2019) conducted a series of full-scale tests on such segments to evaluate their structural performance under flexure and a condition that simulated the thrust action of tunnel boring machine (TBM). Caratelli et al. (2017) further compared three different GFRP reinforcement cage typologies (closed-ring, lattice, and wirenet) and concluded that the closed-ring typology appeared to be advantageous over the other two in terms of cost effectiveness and concrete crack control. Meda et al. (2020; 2019) and Rivat (2019) conducted similar tests on precast concrete tunnel segments reinforced with short steel fibers and GFRP bars and found that the presence of GFRP reinforcement enhanced the flexural strength and reduced the crack width of the precast segments. These efforts paved the way for practical applications. Recently, GFRP bar-reinforced precast tunnel segments were used in the construction of Milan Metro Line 4 in Italy (Manuele et al., 2020).

FRP reinforcement has also been envisaged for use in waterfront protective structures, where steel corrosion is of critical concern. In this respect, Tang et al. (2020) proposed the use of basalt FRP (BFRP) bars or hybrid steel-BFRP composite bars (SFCBs) to replace steel reinforcement in concrete arches/tunnels. The SFCB, initially proposed by Luo et al. (2009), takes the form of a steel bar with a BFRP coating, and is thus expected to provide ductility, in addition to corrosion resistance, to the protective structure that it reinforces. In protective engineering, ductility is also a favored property needed to resist blast loads, such as an explosion. The proposed protective structures with BFRP or SFCB reinforcement are still in the development phase. A series of tests have been conducted on semi-circular arch specimens and such-based tunnels to evaluate the static performance and blast resistance (Tang et al., 2020; Tang et al., 2021; Zhao et al., 2022; Wu et al., 2022).

Despite the few pioneer applications, several issues need to be addressed before the widespread application of FRP bar-reinforced concrete arches can be realized. First, the diverse

manufacturing techniques for creating curved FRP components, as detailed in Section 2.2, offer innovative potential for optimizing the configuration of FRP stirrups in arch structures. Specifically, the use of filament winding techniques in producing FRP products has proven effective in mitigating these defects (Yuan et al., 2022; Dong et al., 2018). Indeed, it is viable to optimize the layout and shape of stirrups and therefore reduce material usage thanks to the creativeness of the winding process (Oval et al., 2020; Yang et al., 2018; Yang, 2018; Spadea et al., 2017).

Second, further experimental studies are essential for better understanding this novel structural form. While there have been some experiments on FRP-RC arches, most existing research has been limited in two key aspects, making additional testing necessary to complement the current body of knowledge: (1) the boundary conditions in existing experiments have been restricted to simple supports at both ends, akin to curved beams (Caratelli et al., 2016; Caratelli et al., 2017; De Rivat et al., 2019; Hosseini et al., 2022) or pin-ended conditions in two-hinge arches (Tang et al., 2020; Tang et al., 2021; Zhao et al., 2022; Wu et al., 2022). To the best of the author's knowledge, no experiments have been conducted with fixed-end boundary conditions (fixed arches) for FRP-RC arches, which would better represent the service conditions commonly encountered in arch structures. (2) the arch configurations in existing studies have been largely limited to full-scale tunnel lining segments (Caratelli et al., 2016; Caratelli et al., 2017; De Rivat et al., 2019; Hosseini et al., 2022) and semi-circular arches (Tang et al., 2020; Tang et al., 2021; Zhao et al., 2022; Wu et al., 2022), with limited testing on other types of arches (e.g., arch ribs used in arch bridges). As a result, the structural behavior of FRP-RC arches remains inadequately understood. To address this gap, additional experimental investigations are therefore needed to expand the structural forms and applications of FRP-RC arches.

Third, comprehensive theoretical research is needed to supplement the experimental work. To the best knowledge of author, no existing theoretical study has focused specifically on the structural performance of FRP-RC arches. Most numerical studies on FRP-RC members have been limited to straight elements (Rasheed et al., 2004; Abushanab and Alnahhal, 2021; Sarhan and Al-Zwainy, 2022; Hussein et al., 2022; Liao et al., 2023; Zinkaah et al., 2022). Although the underlying theories for FRP-RC arches are similar to those for steel-RC arches, the unique characteristics of FRP reinforcement (e.g., lower elastic modulus, linear elastic behavior) warrant particular attention.

Theoretical approaches for analyzing structures generally fall into two categories. The first is the deflection method, which relies on section analysis and geometrical compatibility but neglects shear effects. This approach simplifies structural members into one-dimensional beam/column elements, leading to efficient computations. Its effectiveness has been well-validated for linear members (Shen and Lu, 1983; Jiang and Teng, 2012; Gao et al., 2021). The second is finite element analysis (FEA), which is capable of constructing three-dimensional models to accurately analyze complex configurations and load interactions, as well as to capture local nonlinear behavior and stress concentrations. While the deflection method is efficient for analyzing simple uniaxial or biaxial load cases, FEA is more suitable for intricate three-dimensional structural analyses involving more complex load interactions and boundary conditions.

### **1.3 OBJECTIVES AND SCOPE**

Based on the aforementioned research background, the following issues need to be addressed, which form the main objectives of the present Ph.D. study:

1. To assess the structural behavior of FRP-reinforced concrete arches and identify the associated challenges and suitable solutions;
2. To enhance the performance of FRP stirrups in FRP-reinforced concrete arches;
3. To evaluate the performance of modified FRP-reinforced concrete arches and elaborate on the underlying structural mechanisms governing their behavior;
4. To develop a theoretical model to predict the behavior of FRP-reinforced slender arches;
5. To establish FE models to provide in-depth insights into the behavior of FRP-reinforced concrete arches under the combined effects of axial load, shear load, and bending moment.

## **1.4 THESIS OUTLINE**

This thesis presents a combined experimental and theoretical research program on the “Structural Behavior of FRP-Reinforced Concrete Arches”. The layout of the thesis is outlined below:

**Chapter 3** presents a preliminary investigation of FRP-reinforced concrete arches. Structural performance and failure mechanisms were analyzed through a quasi-static loading test. Theoretically, a fundamental analytical method was developed to evaluate the load-bearing capacity. The issues identified during experimentation, as elaborated below, were highlighted, and corresponding solutions and design recommendations were provided, laying a foundation for further research in subsequent chapters.

*Issue 1:* The transversely oriented FRP stirrups, particularly their horizontal legs, may negatively affect the flexural stiffness and strength of reinforced members, especially for those with a shallow cross-section.

*Issue 2:* Due to the lower elastic modulus of GFRP compared to steel, significant load drops may occur when a major crack develops in under-reinforced GFRP-reinforced concrete arches with a low reinforcement ratio. This is because GFRP bars cannot immediately take up the load released by the reduction in tensile stress of concrete.

*Issue 3:* Although the fundamental analysis method can be used to understand the general behavior of the arch and estimate its load capacity, the lack of comprehensive consideration for geometric nonlinearity may lead to overestimation of structural capacity.

To address *Issue 1*, **Chapter 4** introduces a novel narrow closed FRP stirrup fabricated via filament winding process. Each new stirrup has a narrow cross-section consisting of two vertical legs connected by rounded end portions, devoid of conventional horizontal legs. The horizontal legs are purposely removed to minimize the reduction of concrete area and the resulting local weakening of section capacity, noting that the vertical legs are the main components contributing to the shear capacity of a reinforced member. The effectiveness of the new FRP stirrups was validated through a series of tensile tests on the stirrups, as well as bending tests on stirrup-reinforced concrete members.

In response to *Issue 2*, over-reinforced configuration is recommended to ensure satisfactory performance in terms of deflection and crack control while reducing the tendency of catastrophic failure. **Chapter 5** presents a comprehensive experimental investigation of over-reinforced configurations combined with the novel FRP stirrups, evaluating the effects of longitudinal reinforcement ratio, concrete strength, and transverse reinforcement ratio under concentrated loading at the arch crown. The results were analyzed in terms of serviceability limit state, ultimate limit state, and material effectiveness.

To tackle *Issue 3*, **Chapter 6** proposes a one-dimensional theoretical model based on an enhanced deflection method, offering a unified approach to address both small and large curvature problems. The accuracy and feasibility of the model were validated through comprehensive comparisons with analytical solutions, numerical predictions and experimental results from representative cases of all-FRP arches and FRP-incorporating hybrid arches.

The deflection method is instrumental in understanding the behavior of FRP-reinforced slender arches, however, it only accounts for uniaxial stress/strain, considering the interaction between axial forces and bending moments while ignoring shear contributions. Although this simplification generally applicable when analyzing slender arches, where cross-sections predominantly experience uniaxial stresses along the arch axis, it may lead to overestimation of stiffness and load capacity in scenarios where shear effects are non-negligible. To overcome these limitations, **Chapter 7** presents a finite element simulation of FRP-reinforced concrete arches, capable of accurately capturing failure mechanisms under combined actions of axial load, shear load, and bending moment (axial-shear-flexural interaction).

**Chapter 8** closes the thesis by summarizing the main conclusions drawn in the previous chapters and identifying areas that need further research.

## 1.5 REFERENCES

- Abushanab A and Alnahhal W. (2021) Numerical parametric investigation on the moment redistribution of basalt FRC continuous beams with basalt FRP bars. *Composite Structures* 277: 114618.
- Caratelli A, Meda A, Rinaldi Z, et al. (2016) Precast tunnel segments with GFRP reinforcement. *Tunnelling and Underground Space Technology* 60: 10-20.
- Caratelli A, Meda A, Rinaldi Z, et al. (2017) Optimization of GFRP reinforcement in precast segments for metro tunnel lining. *Composite Structures* 181: 336-346.
- Cui FK, Li HH, Dong X, et al. (2021) Improved time-dependent seismic fragility estimates for deteriorating RC bridge substructures exposed to chloride attack. *Advances in Structural Engineering* 24(3): 437-452.
- Dagher HJ, Bannon DJ, Davids WG, et al. (2012) Bending behavior of concrete-filled tubular FRP arches for bridge structures. *Construction and Building Materials* 37: 432-439.
- De Rivat B, Giamundo N, Meda A, et al. (2019) Hybrid solution with fiber reinforced concrete and glass fiber reinforced polymer rebars for precast tunnel segments. *Proceedings of Tunnels and Underground Cities: Engineering and Innovation Meet Archaeology, Architecture and Art*. CRC Press, 2018-2025.
- Dong HL, Wang DY, Wang ZY, et al. (2018) Axial compressive behavior of square concrete columns reinforced with innovative closed-type winding GFRP stirrups. *Composite Structures* 192: 115-125.
- Gao K, Xie H, Li Z, et al. (2021) Study on eccentric behavior and serviceability performance

- of slender rectangular concrete columns reinforced with GFRP bars. *Composite Structures* 263: 113680.
- Hollaway LC. (2010) A review of the present and future utilisation of FRP composites in the civil infrastructure with reference to their important in-service properties. *Construction and Building Materials* 24(12): 2419-2445.
- Hussein A, Huang H, Okuno Y, et al. (2022) Experimental and numerical parametric study on flexural behavior of concrete beams reinforced with hybrid combinations of steel and BFRP bars. *Composite Structures* 302: 116230.
- Jiang S. (2020) *Hybrid FRP-concrete-steel Double-skin Tubular Truss Bridge: Design, Construction and Testing*. Queensland, Australia: The University of Queensland.
- Jiang T and Teng JG. (2012) Slenderness limit for short FRP-confined circular RC columns. *Journal of Composites for Construction* 16(6): 650-661.
- Koch G, Varney J, Thompson N, et al. (2016) International measures of prevention, application, and economics of corrosion technologies study. *NACE International* 216: 2-3.
- Lee GP and Shin HS. (2010) A numerical study on feasibility of the circled fiber reinforced polymer (FRP) panel for a tunnel lining structure. *Journal of Korean Tunnelling and Underground Space Association* 12(6): 451-461.
- Liao Q, Yu JT, Su YR, et al. (2023) Shear failure mechanism and parametric study for seawater sea-sand engineered cementitious composites beams reinforced by FRP bars: Finite element analysis. *Construction and Building Materials* 407: 133497.
- Lu CH, Yang YT, Ruan XJ, et al. (2022) A comparative study of the flexural performance of

hybrid-reinforced (glass fiber reinforced polymer and steel bars) concrete beams before and after exposure to chloride environment. *Advances in Structural Engineering* 25(6): 1295-1309.

Luo YB, Wu G, Wu ZS, et al. (2009) Study on fabrication technique of steel fiber composite Bar (SFCB). *Earthquake Resist Engineering Retrofit* 31(1): 28-34.

Manuele G, Bringiotti M, Lagana G, et al. (2020) Fiber glass and “green” special composite materials as structural reinforcement and systems; use and applications from Milan Metro, Brenner Tunnel up to high speed train Milan–Genoa. *Proceedings of Tunnels and Underground Cities: Engineering and Innovation Meet Archaeology, Architecture and Art*. CRC Press, 2625-2634.

Meda A, Rinaldi Z, Spagnuolo S, et al. (2019) Hybrid precast tunnel segments in fiber reinforced concrete with glass fiber reinforced bars. *Tunnelling and Underground Space Technology* 86: 100-112.

Meda A, Rinaldi Z, Spagnuolo S, et al. (2020) Experimental behaviour of precast tunnel segments in steel fiber reinforcement with GFRP rebars. *Fib Bulletin*: 153-162.

Oval R, Costa E, Thomas-McEwen D, et al. (2020) Automated framework for the optimisation of spatial layouts for concrete structures reinforced with robotic filament winding. *Proceedings of ISARC 2020: The 37th International Symposium on Automation and Robotics in Construction*. Kitakyushu, Japan: International Association for Automation and Robotics in Construction, 1541-1548.

Rahman MM. (2015) Islamic architecture and arch. *International Journal of Built Environment and Sustainability* 2(1): 8-16.

- Rasch JJ. (1985) *Die Kuppel in der römischen Architektur: Entwicklung, Formgebung, Konstruktion*: Dt. Kunstverl.
- Rasheed HA, Nayal R and Melhem H. (2004) Response prediction of concrete beams reinforced with FRP bars. *Composite Structures* 65(2): 193-204.
- Roberge PR. (2019) *Handbook of Corrosion Engineering*: McGraw-Hill Education.
- Robertson DS. (1969) *Greek and Roman Architecture*: Cambridge University.
- Sarhan MM and Al-Zwainy FMS. (2022) Analytical investigations of concrete beams reinforced with FRP bars under static loads. *Structures* 44: 152-158.
- Shen ZY and Lu LW. (1983) Analysis of initially crooked, end restrained steel columns. *Journal of Constructional Steel Research* 3(1): 10-18.
- Spadea S, Orr J and Ivanova K. (2017) Bend-strength of novel filament wound shear reinforcement. *Composite Structures* 176: 244-253.
- Tang ZX, Zhou YZ, Feng J, et al. (2021) Concrete protective arches reinforced with BFRP bars: Construction and quasi-static structural performances. *Tunnelling and Underground Space Technology* 108: 103731.
- Tang ZX, Zhou YZ, Feng J, et al. (2020) Blast responses and damage evaluation of concrete protective arches reinforced with BFRP bars. *Composite Structures* 254: 112864.
- Teng JG, Chen JF, Smith ST, et al. (2002) *FRP-strengthened RC Structures*, West Sussex, England: John Wilkey & Sons, Ltd.
- Tengilimoğlu O. (2019) *An Experimental Study to Investigate the Possibility of Using Macro-*

*synthetic Fibers in Precast Tunnel Segments*. Ankara, Turkey: Middle East Technical University.

Wang XQ and Lau D. (2021) Atomistic investigation of GFRP composites under chloride environment. *Advances in Structural Engineering* 24(6): 1138-1149.

Wu J, Zhou J, Xu Y, et al. (2022) Dynamic responses of blast-loaded shallow buried concrete arches strengthened with BFRP bars. *Materials* 15(2): 535.

Yang Y. (2018) *Novel Reinforcement for Flexibly-formed Concrete Structures*. Bath, England: University of Bath.

Yang YZ, Orr J and Spadea S. (2018) Shear behavior of variable-depth concrete beams with wound fiber-reinforced polymer shear reinforcement. *Journal of Composites for Construction* 22(6): 04018058.

Yuan Y, Wang Z and Wang D. (2022) Shear behavior of concrete beams reinforced with closed-type winding glass fiber-reinforced polymer stirrups. *Advances in Structural Engineering* 25(12): 2577-2589.

Zhao CJ, Tang ZX, Wang P, et al. (2022) Blast responses of shallow-buried prefabricated modular concrete tunnels reinforced by BFRP-steel bars. *Underground Space* 7(2): 184-198.

Zinkaah OH, Alridha Z and Alhawat M. (2022) Numerical and theoretical analysis of FRP reinforced geopolymer concrete beams. *Case Studies in Construction Materials* 16: e01052.

## **CHAPTER 2**

### **LITERATURE REVIEW**

#### **2.1 INTRODUCTION**

Fiber-reinforced polymer (FRP) composites are a class of advanced non-metallic materials featuring advantages of high strength, light weight and excellent corrosion resistance. These advantages, in conjunction with the various methods available for making curved FRP members, create a wide range of possibilities for innovating arch structures with FRP composites.

In view of the diverse and exciting opportunities for innovating arch structures with FRP, this subject deserves much wider research attention and participation. To this end, there exists a need to conduct a review of existing work scattered in the literature. Such a review is presented in this chapter. The chapter begins with an overview of four methods that are capable of making curved FRP members, followed by a review of existing arch projects and relevant novel concepts, which are classified into categories of all-FRP arches and FRP-incorporating hybrid arches. Based on this review, directions for future development of each of the two categories are highlighted, with a number of challenges and potential solutions discussed. The scope of this chapter is limited to the use of FRP in arches for new construction; strengthening applications are not covered.

## **2.2 MANUFACTURING METHODS FOR CURVED FRP MEMBERS**

While a vast variety of manufacturing methods are available for composites production (Zoghi, 2013; GangaRao and Prachasaree, 2021), not all of them are suitable for infrastructure applications. The main limiting factors are the large size of structural members and the low profit margin of the construction industry. Therefore, any viable method must be able to make large-scale members at a low cost. The geometry of arches poses a third challenge, that is, the competence to create curved members. Based on these criteria, four different methods are selected and reviewed in this section, with an emphasis on their capability of creating curved FRP members and potential applications in arch structures. The first three are standard processes for composites production, while active bending is a technique used to form arches by bending ready-made and initially straight members (typically pultruded hollow-section profiles). The main features of the four methods reviewed in this section are summarized in Table 2.1.

### **2.2.1 Vacuum infusion**

Vacuum infusion, also known as vacuum-assisted resin transfer molding, is a process that uses vacuum pressure to drive a low-viscosity resin into a fiber bed (Hindersmann, 2019). Initially, the fiber bed is formed by laying out dry fiber materials on top of the surface of a custom mold which is sealed in a vacuum bag. The airtight mold is connected to an inlet valve at one end and a vacuum pump at the other (Figure 2.1). The pump extracts air from the space enclosed by the mold and the vacuum bag to create a vacuum that compacts the fiber bed. The resin is then infused from the inlet and is driven by the vacuum pressure (i.e., pressure difference between the resin supply and

the vacuum) into the fiber bed. Finally, the formed part is de-molded after the resin cures.

Vacuum infusion provides a cost-effective solution to manufacturing large objects with complex geometries. It is traditionally used to make large objects, such as boat hulls and wind turbine blades (Beckwith and Hyland, 1999; Rajak et al., 2019). By adapting the mold into the target shape, vacuum infusion can be used to create arch bridge spans completely made of FRP using a single mold. The span size is generally limited by the transportation logistics, rather than by the vacuum infusion technology itself. Vacuum infusion is a relatively labor-intensive process and is difficult to be automated. Therefore, it is not suitable for high-volume production. Note that in the literature vacuum infusion is often used as a broad term that refers to a large class of variants (Hindersmann, 2019). The description of this process herein is brief and not intended to be exhaustive.

### **2.2.2 Filament winding**

Filament winding is an automated process that involves winding resin-saturated, continuous strands of fiber over a rotating mandrel (Mantell and Springer, 1994). In this process, continuous strand rovings are fed through a resin bath and then delivered onto a rotating mandrel from a carriage that travels the length of the mandrel back and forth in a direction parallel with the mandrel axis [Figure 2.2(a)]. The winding program stops once the target number of layers of fibers is applied. The laminate is then left on the mandrel for curing until the molded part is ready for removal from the mandrel.

Filament winding is a classical method used for manufacturing tubular parts of both open- and closed-end forms, such as tubes, pressure vessels and rocket motor cases

(Shen, 1995; Azeem et al., 2022). The winding angle (i.e., the angle of fiber strand relative to mandrel axis) of the part can be tailored to satisfy specific mechanical needs. The tubular parts resulted from a filament winding process typically have a axisymmetric shape (Frketic et al., 2017; Rajak et al., 2021). Production of non-axisymmetric parts [Figure 2.2(b)], for example, those with a curved axis (e.g., pipe bends), is also possible, with the use of an advanced winder with multiple axes (Mantell and Springer, 1994; Laval, 2006).

In the field of structural engineering, filament-wound tubes have gained acceptance as a confining device (a confining tube has a winding angle close to the hoop direction, e.g.,  $\pm 80^\circ$ ) for concrete columns (Vincent and Ozbakkaloglu, 2013; Xie et al., 2020). This technique can be extended to small-scale arches without much difficulty by filling a curved FRP tube with a concrete core. It is also possible to further extend it to large-scale arches. In such an application, the arch may be built from short segments of concrete-filled FRP tube with some form of internal steel reinforcement that facilitates connection. The tube segment itself can be either linear or curvilinear, but the choice of the former is technically and economically more viable and should suffice in most situations.

### **2.2.3 Pultrusion**

Pultrusion is also an automated process. It is used for the manufacture of profiles having a constant cross-sectional shape (e.g., channels, tubes and I-sections) and a length typically much larger than the dimensions of the cross section (Starr, 2000). Pultrusion is a portmanteau term created by a blend of “pull” and “extrusion” (Rajak et al., 2021). In this process, continuous fiber strands are guided through a resin bath for

impregnation. The saturated fibers are then pulled through a metal die with a predefined shape. The die defines the cross-sectional shape of the profile and is heated for rapid curing of the resin. Finally, the molded profile exiting the die is conveyed to a platform, where it is cut into pre-programmed lengths by a cut-off saw [Figure 2.3(a)].

A conventional pultrusion process (known as linear pultrusion) is limited to fabricating straight profiles. This limitation has been removed in the latest development, termed curved pultrusion (or radius pultrusion) (Tonatto et al., 2020). In a curved pultrusion process, an additional processing step, incorporated between steps of molding and cutting, is employed to shape the partially cured profile to the desired curvature, by taking advantage of the high deformability of the resin matrix when it is not completely hardened [Figure 2.3(b)]. Typically, only circular curvatures are permitted (Liu et al., 2021).

Various possibilities exist for applications of pultruded products in arch structures. Straight profiles (e.g., channels, tubes and I-sections) are suitable for construction of FRP truss arches (Sobrino and Pulido, 2002). Large curved profiles can function as a standalone arch span (Liu et al., 2021) while curved bars can serve as replacement for steel reinforcement in concrete arches (Caratelli et al., 2016; Tang et al., 2021). Of particular interest is the possibility to form arches by bending initially straight pultruded members, which is discussed in the subsequent sub-section.

#### **2.2.4 Active bending**

Unlike the three methods reviewed above, active bending is not a method for manufacturing FRP products from raw materials; rather, it is a technique for generating curved geometries from initially straight or flat members that are ready-made through

active use of elastic bending (Douthe et al., 2010). Despite this difference, it is still included in this section as it is well suited to forming arches made of FRP, whose elastic strain limit, not paralleled by any other commonly used building material, is high enough to resist the large elastic deformation induced in the bending process.

Structures that derive their curved geometries through active bending are known as bending-active structures (Douthe et al., 2007; Lienhard et al., 2013). Bending-active arches are the simplest form of bending-active structures (Figure 2.4). More sophisticated forms include bending-active grid shells (Happold and Liddell, 1975; Nicholas et al., 2013; Pone et al., 2013) and bending-active continuous shells (Sonntag et al., 2017). Owing to the contradiction between the need for flexibility in the forming stage and the need for stiffness in the service stage, bending-active arches are usually limited to a small scale. In particular, the lightweight feature of FRP makes FRP bending-active arches suitable for use as rapidly assembled structures that are intended to provide temporary accommodation or usage (e.g., disaster-relief shelters and military crossing bridges). On the other hand, larger-scale FRP bending-active structures are also possible. In such a case, proper post-forming stiffening measures (e.g., adding stiffening cables) are needed for enhanced performance of the bending-active system in the service stage.

## **2.3 ALL-FRP ARCHES**

### **2.3.1 Vacuum infusion-manufactured arches**

Vacuum infusion offers a solution to manufacturing standalone arch spans using a single mold, where the need for connections between composite parts is eliminated. A frequently quoted example is the footbridge located in Moscow, Russia (Potyrala, 2011;

Pyrzowski and Miśkiewicz, 2017; Hollaway, 2013). Completed in June 2008, it is the first composite bridge in Russia made by vacuum infusion. The footbridge consists of an arched central span and two side beams (Figure 2.5). The arch span is forked at the two ends, covering a distance of 22.6 m. The width of the footbridge is 2.8 m and the total weight is only approximately 5 t. Other documented examples include two FRP overpasses installed in the Netherlands as wildlife crossing passages. The two overpasses, both of which have a shallow arch shape, have a span of 24 m and 36 m, respectively (Bell et al., 2020).

The longest-span arch bridge manufactured by vacuum infusion is probably the Ooypoort GFRP footbridge in Denmark, which officially opened in February 2014. This footbridge was built from three segments, which were joined together to span a distance of 56 m. All composite parts of the bridge were manufactured by vacuum infusion (Pyrzowski and Miśkiewicz, 2017). This bridge was designed to accommodate houseboats even in case of high water levels and withstand frequent flooding since it is located at the entrance of a nature reserve of a marshy area.

### **2.3.2 Pultruded arches**

Pultruded FRP members have been used in bridge structures since early 1990s (Vedernikov et al., 2020). Among these applications, an early example concerning arch bridge is a footbridge completed in October 2001 in Lleida, Spain (Sobrino and Pulido, 2002). Having a span of 38 m, a rise of 6.2 m, and a deck width of 3 m, this footbridge was built to cross a roadway and a railway line between Madrid and Barcelona (Figure 2.6). The components of this double-tied arch bridge, including the two tied arch ribs, the truss connecting the two ribs, hangers and decks, were all made of GFRP pultruded

profiles. The overall curved shape of the arch ribs was achieved by assembling straight segments of GFRP profiles. All joints of the bridge were bolted using stainless steel brackets and bolts. The lightness (total weight of the footbridge was only approximately 19 t) derived from using GFRP allowed for rapid installation, which was completed by a crane within three hours (Sobrino and Pulido, 2002; Pyrzowski and Miśkiewicz, 2017), representing an important advantage as traffic interruptions can be minimized. Another important reason for choosing GFRP was that GFRP had no magnetic interaction with the electrified railway line.

A more recent example worth mentioning is a 20 m-span footbridge built in 2021 in Beijing, China (Liu et al., 2021). The distinguishing feature of this bridge is that curved GFRP components manufactured by a curved-pultrusion process were directly used to form the arch span. Specifically, the proposed arch form is created by transverse mechanical connection of several identical paralleling glass GFRP I-sections that are curved-pultruded. This way, each pair of adjacent I-sections, with the edges of their flange plates further connected by adhesive bonding, forms a box section that has considerably enhanced torsional stiffness and resistance than the original I-sections. Besides, the webs are thickened to achieve a lower slenderness ratio and restrain the flange plates, thereby increasing the in-plane flexural stiffness and load-carrying capacity. Liu et al. (2021) conducted destructive lab tests on full-scale arch spans and assessed their failure mode, load-carrying capacity and deflection responses. Subsequently, the footbridge was designed, assembled and tested under the serviceability limit state before it was installed on site by a crane (Figure 2.7). The test results showed satisfactory performance in strength, deflection and vibration properties,

which demonstrate the significant prospect of the proposed form of curved-pultruded GFRP arch bridge.

### **2.3.3 Bending-active arches**

Although the history of bending-active arches can be traced to ancient times (Ashby and Cebon, 2005) when residents of Ma'dan (present-day southern Iraq) learned to use actively bent reed bundles to support their reed houses, the concept of FRP bending-active arch systems only emerged very recently. Caron et al. (2009) proposed the concept of FRP self-stressed bowstring footbridge. The proposed bowstring system consists of two bows (arch ribs) formed by elastic bending of pultruded straight GFRP pipes, which are stabilized by a carbon FRP (CFRP) string system composed of lower spanning cables and a web of secondary stays. The bridge decks are supported by crossbars fastened to the spanning cables (Figure 2.8). More recently, Bessini et al. (2019) proposed a similar concept of bending-active tied arch module. Each of the proposed modules is composed of a pultruded FRP rod bent into shape by a cable pulling at both ends of the rod. Secondary struts are placed at certain intervals along the rod to deviate the tensioning cable (Figure 2.9). They envisioned applications of such modules as construction units for lightweight footbridges and roofs, and built a 5 m-span prototype footbridge for demonstration. The prototype footbridge was an assembly of two of the proposed bending-active modules, which were connected by transverse links at both the rod and cable levels (Figure 2.9). In the author's view, the proposed modules may also find applications as rapidly assembled military crossing bridges.

## **2.4 FRP-INCORPORATING HYBRID ARCHES**

### **2.4.1 FRP bar-reinforced concrete arch segments**

FRP bar-reinforced concrete arch segments are mainly intended for underground tunnelling applications. Underground construction today has a life expectancy of over 100 years, with some projects reaching 200 years. Durability of tunnel linings, with particular reference to corrosion of steel reinforcement, is therefore critical. An attractive solution is to use pultruded curved GFRP bars as substitution for conventional steel reinforcement in concrete tunnel segments, especially for construction in a harsh environmental condition (e.g., sewer tunnels or aggressive soils). The use of GFRP bars brings an extra benefit related to the non-conductivity of GFRP. When tunnel rings assembled from GFRP bar-reinforced segments are installed at regular intervals of a conventional RC tunnel lining, they function as dielectric joints that interrupt the stray currents, thus providing a remedy to electro-corrosion of steel components. This method is particularly suitable for railway tunnels in urban areas where traditional electrical insulation measures are hard or costly to implement.

Due to the above advantages, GFRP bar-reinforced precast tunnel segments have received pioneer research efforts recently. Caratelli et al. (2016) and Tengilimoğlu (2019) conducted a series of full-scale tests on such segments (Figure 2.10) to evaluate their structural performance under flexure and a condition that simulated the thrust action of TBM. Caratelli et al. (2017) further compared three different GFRP reinforcement cage typologies (closed-ring, lattice, and wirenet) and concluded that the closed-ring typology appeared to be advantageous over the other two in terms of cost effectiveness and concrete crack control. Meda et al. (2020; 2019) and Rivat (2019) conducted similar tests on precast concrete tunnel segments reinforced with short steel

fibers and GFRP bars and found that the presence of GFRP reinforcement enhanced the flexural strength and reduced the crack width of the precast segments. These efforts paved the way for practical applications. Recently, GFRP bar-reinforced precast tunnel segments were used in the construction of Milan Metro Line 4 in Italy (Manuele et al., 2020).

FRP reinforcement has also been envisaged for use in waterfront protective structures, where steel corrosion is of critical concern. In this respect, Tang et al. (2020) proposed the use of BFRP bars or SFCBs to replace steel reinforcement in concrete arches/tunnels. The SFCB, initially proposed by Luo et al. (2009), takes the form of a steel bar with a BFRP coating, and is thus expected to provide ductility, in addition to corrosion resistance, to the protective structure that it reinforces. In protective engineering, ductility is also a favored property needed to resist blast loads, such as an explosion. The proposed protective structures with BFRP or SFCB reinforcement are still in the development phase. A series of tests have been conducted on semi-circular arch specimens and such-based tunnels (Figure 2.11) to evaluate the static performance and blast resistance (Tang et al., 2020; Tang et al., 2021; Zhao et al., 2022; Wu et al., 2022).

#### **2.4.2 FRP-concrete arch panels**

The concept of FRP-concrete arch panels, proposed by Lee et al. (2010; 2011), is similar to that of FRP bar-reinforced concrete arch segments. Both of them are intended for tunnelling applications. The main difference is that in an FRP-concrete arch panel, the FRP reinforcement is a pultruded curved profile rather than curved bars. In the studies of Lee et al. (2010; 2011), the proposed arch panel is composed of a curved GFRP profile (in the form of I-sections with a shared bottom flange) and a concrete

infill between and on top of the I-sections (Figure 2.12). The GFRP profile is manufactured by a curved-pultrusion process and sand-coated to enhance the bond behavior at the FRP-concrete interface. In addition to providing longitudinal reinforcement and shear resistance, the GFRP profile also serves as formwork for concrete casting. Jung et al. (2012) conducted flexure tests as well as numerical analysis on this form of arch panel. Both the experimental and theoretical results indicated a large shear movement at the FRP-concrete interface, especially at the tensile side due to bending-induced tensile stresses. Therefore, proper measures are needed to enhance the composite action between the two constituent materials. Connection between the arch panels, which is another essential practical issue, also needs to be addressed in future research.

#### **2.4.3 Concrete-filled FRP tubular arches**

A concrete-filled FRP tubular member (CFFTM) consists of an FRP tube filled with a plain or reinforced concrete core. The FRP tube, typically filament-wound, not only provides confinement to the concrete core, but also serves as stay-in-place formwork which facilitates construction and protects the concrete core against environmental attacks. Due to the well-known fact that the compressive strength and ductility of concrete can be substantially enhanced through confinement, this technique is well suited to constructing CFFT columns (CFFTCs) and CFFT arches (CFFTAs), both of which primarily bear compression force.

While extensive research has been carried out on CFFTCs (Mirmiran and Shahawy, 1997; Fam and Rizkalla, 2001a; Fam and Rizkalla, 2001b; Zohrevand and Mirmiran, 2013; Xie et al., 2020; Huang et al., 2021; Pei et al., 2021; Xie et al., 2023; Yu and

Teng, 2011), studies on CFFTAs have been mostly limited to a research group of University of Maine. It is worth noting that unlike most of the existing studies on CFFTMs, the FRP tubes used by this group were not filament-wound. Instead, they were manufactured using a vacuum infusion process (Dagher et al., 2012). The concept of CFFTA was initially proposed by this group in Tomblin (2006). Subsequently, a series of studies were conducted, including mechanical tests (Goslin et al., 2011; Dagher et al., 2012), fire tests (Goslin et al., 2014), sectional shape optimization (Goslin and Rofes, 2015), damage repair (Goslin and Arimond, 2015), soil-arch interaction (Walton et al., 2016b; Walton et al., 2016a), and health monitoring (Goslin and Tomlinson, 2016). Their efforts have led to the erection of more than ten buried CFFTA bridges. One of them is shown in Figure 2.13. This bridge, located in Bradley, Maine, USA and completed in 2010, is supported by several parallel CFFTAs with a span of 8.5 m (Dagher et al., 2012). The CFFTAs were topped with an FRP decking that provided lateral support for concrete filling and created a surface for soil backfilling. Headwalls were installed at the outer CFFTAs to hold the soil backfill, with a pavement and guardrail that completed the bridge. Due to transportation limitations, all the built bridges of this form have been limited to a small span. Parry et al. (2014) proposed a segmental solution which requires connection of CFFTA segments to overcome the span limit. The proposed solution employs a combination of internal rebar reinforcing and an external FRP collar to connect adjacent CFFTA segments. However, to the best knowledge of the author, this solution is still under development and has not been used in practical CFFTA bridge projects.

#### **2.4.4 FRP-concrete-steel double-skin tubular arches**

FRP-concrete-steel double-skin tubular members (DSTMs) are an enhanced variant of CFFTM (Jiang et al., 2023; Teng et al., 2007; Zhao et al., 2016; Jiang, 2020; Yao et al., 2015). The difference between the two forms is that a DSTM has an inner steel tube in addition to the outer FRP tube (Figure 2.14). The space between the two tubes is filled with concrete while the steel tube typically remains hollow to reduce self-weight. The FRP tube insulates the steel tube as well as the concrete infill from the external environment; hence, steel corrosion is not a concern. The steel tube not only functions as longitudinal reinforcement, but most importantly, facilitates connection between DSTM segments. Such a segmental solution represents an important advantage as it removes the restriction on the scale of DSTM-based structures.

DSTMs were first developed at The Hong Kong Polytechnic University (Teng et al., 2004; Teng et al., 2007) as columns (DSTCs) and beams (DSTBs) (Yu et al., 2006; Zhao et al., 2016; Xie, 2018). After more than a decade of intensive research, their potential as arches (DSTAs) was recently investigated. De Waal et al. (2018) proposed a novel arch bridge system completely consisting of DSTMs. Burnton et al. (2019) further built a full-scale prototype, in which DSTBs serving as bridge girders were upheld by DSTCs rising from the supporting DSTAs underneath (Figure 2.15). All segments, including those forming the DSTAs, had a linear shape to avoid the complexity involved in manufacturing curved tubes. Connection between the segments was achieved by welding of the steel tubes in combination with joining the FRP tubes using either the pre-preg or the wet lay-up technique. The FRP and steel tubes served as formwork for concrete casting. Shear studs were welded to the outer surface of the steel tube to enhance the composite action between the steel tube and the concrete infill.

This hybrid bridge system represents an promising alternative to conventional arch bridge systems (Jiang, 2020), for its high load-bearing capacity, ductility and durability. It has potential to rival the spanning capacity of concrete-filled steel tubular arch bridges. Table 2.2 summarizes the key information of the arch projects and relevant concepts reviewed in Sections 2.3 and 2.4.

## **2.5 SUMMARY AND RESEARCH NEEDS**

### **2.5.1 Brief summary**

The review provided in the preceding two sections identifies two distinct paths toward applying FRP (with GFRP being the most commonly used due to its relatively low cost) in arch structures. One path is all-FRP arch structures and the other employs FRP in combination with concrete and in some cases steel to form hybrid arch structures. The first path leads to small- or medium-scale arches, which find their applications mostly as footbridges where the benefits of FRP materials are maximized and their weaknesses minimized. On the one hand, the lightweight feature of all-FRP footbridges allows for rapid installation by lifting the bridge into position as a whole using a crane. Typically, the installation process only takes a few hours to complete, which minimizes traffic interruptions. Other important benefits include minimal maintenance costs and zero magnetic interaction. The latter, which is an additional advantage of GFRP due to its non-conductivity, can be a decisive factor in situations where magnetic interaction is of concern (e.g., footbridges crossing electrified railway lines). On the other hand, a footbridge usually has a limited span and is not subjected to heavy loading. The problem of excessive deflection due to the relatively low modulus of elasticity of FRP is therefore not critical. Neither is the concern of fire safety as footbridges are usually

located in an outdoor environment, where fires are less likely to occur and fire detection and evacuation are easier.

The second path, in contrast, chiefly leads to large-scale arch structures which are usually subjected to heavy loading. Targeted areas of application include tunnel linings and long-span arch bridges. In these structures, FRP alone is unable to deliver the strength and/or stiffness required, or is not cost-effective. Instead, it is used in combination with concrete with the primary aim to resolve the issue of steel corrosion, thereby saving maintenance costs and extending service life. Two possible approaches exist. The first is as substitution for steel reinforcement. The second is as external protective and confining tube for the concrete infill. In the latter approach, additional internal steel reinforcement (e.g., an inner steel tube) is preferred in order to provide flexural ductility and facilitate inter-segment connection, which is hard to accomplish with FRP alone owing to its relatively poor connectability. Obviously, due to the distinct objectives of these two paths, the associated research needs are different. The research needs specific to each of the two paths are addressed in the remainder of this section.

### **2.5.2 Research needs for all-FRP arches**

Modular construction is deemed the way forward for future development of all-FRP arch footbridges. The pultrusion process is well suited to modular construction since it is a highly automated process efficient at manufacturing objects of identical shapes. For pultruded FRP members, the lamination structure may be optimized by adding multidirectional fiber fabrics in the pultrusion process (Nunes et al., 2016; Madenci et al., 2020) to avoid the undesired local failure modes caused by the lack of

stiffness/strength in the transverse directions, as reported in existing studies (Nunes et al., 2016; Hai et al., 2010). While there is in principle no limit on the length of a pultruded profile, manufacture difficulty increases with the sectional size of the profile. The width of a typical footbridge generally prevents an all-in-one pultrusion solution, therefrom arises the need to pursue a modular solution that segments a footbridge into identical parallel spans (modules). The number of modular spans needed for assembly depends on the actual width of the footbridge with a consideration of a balance between manufacturing and assembling requirements. Modular construction is also possible with vacuum infusion, although the benefits of vacuum infusion are best exploited in creating standalone free-form arches with varying cross-sectional shapes using a single mold. When used for modular construction, vacuum infusion is less efficient than pultrusion owing to its lower level of automation. For a successful modular design, connection between the modular spans is critical. Metal (e.g., stainless steel) bolting is a potential solution. However, metal bolting disrupts fiber continuity and reduces assembling speed, although the FRP members may be locally strengthened during manufacturing or construction to achieve the desired strength, ductility and efficiency of bolting joints (Liu et al., 2020; Liu, 2021). Furthermore, metal connection should be avoided in some special situations where requirements on corrosion and/or magnetic interference are demanding. In such cases, an all-FRP connection solution, including mechanical connections and adhesive bonding, is favored. Of particular interest is the development of mortise-tenon type joints, which can be realized with sectional shape designs of a convex side and a concave side, where the convex side fits with the concave side of the adjacent module to enable rapid assembly.

Bending-active arches are often used as supporting frames for temporary structures (e.g., tents and shelters). However, the possibility of using them as permanent structures remains inadequately explored. This possibility is discussed in a recent study (Habibi et al., 2022), which showed that as permanent structures, the span limit of FRP bending-active arches, without any post-forming stiffening measures, is between 10 to 30 m depending on the type of FRP used. The span limit may be further increased by adopting certain post-forming measures that enhance the stiffness of the arch. For example, the bending-active arch systems proposed by Caron et al. (2009) and Bessini et al. (2019) employ cables and struts to stiffen the bent arch rib. Future research should focus on the development of permanent bending-active arch structures. Potential application targets include footbridges and roofs. It is worth noting that the few pioneer studies on FRP bending-active arch systems (Caron et al., 2009; Bessini et al., 2019) have thus far been limited to scaled models, which differ from actual bending-active footbridges or roofs in terms of their scale and lifespan. A larger scale is associated with increased complexities in construction and a longer lifespan necessitates the need to consider time-dependent behavior. For scaled models or small-scale bending-active arches, it is practical to manually bend the beam into the arch shape. However, for larger-scale bending-active arches, the forming process requires additional equipment or measures, such as tensioning a cable pulling at both ends of the beam, or using a crane to hoist the beam with necessary mechanical bending at the beam ends. In addition, in the design of actual bending-active arches, the time-dependent behavior of creep and relaxation related to FRP materials is worth particular attention. FRP bending-active arches operate with significant bending prestresses induced in the forming process, making them more susceptible to the detrimental effects of creep and relaxation on time-

dependent structural performance. Therefore, how the long-term behavior of FRP bending-active arches is influenced by the inherent forming-induced prestresses is an important issue to address. For design purposes, a proper limit on the level of prestressing needs to be proposed to restrict the detrimental effects of creep (Sá et al., 2011; Douthe et al., 2010; Abdel-Magid et al., 2003) and relaxation (Shi et al., 2017; Zou, 2003; Zhao et al., 2020).

### **2.5.3 Research needs for FRP-incorporating hybrid arches**

Under this category, FRP bar-reinforced arch segments and DSTAs have shown promise for application in large-scale structures. The two hybrid forms are respectively intended for application as tunnel linings and long-span arch bridges, which represent the two most widely used classes of large-scale and heavily-loaded arch structures. However, a great deal of research is still needed on various aspects of the two types of hybrid arches, thus harnessing their full potential.

Despite the few pioneer applications of FRP bar-reinforced concrete arch structures in tunnel linings, several issues need to be addressed before their widespread application. First, the diverse manufacturing processes for creating curved FRP components, as detailed in Section 2.2, offer innovative potential for the configurations of FRP stirrups in arch structures. Specifically, pultruded bent FRP bars often exhibit reduced strength and elastic modulus compared to their straight counterparts due to the mechanical bending involved in the pultrusion process. This reduced performance is attributed to slacking and kinking of the fibers at the inner or near-inner side of the bars (Ahmed et al., 2010; Morphy, 1999). Nevertheless, the use of filament winding techniques in producing FRP products has proven effective in mitigating these defects (Yuan et al.,

2022; Dong et al., 2018). Indeed, it is viable to optimize the layout and shape of stirrups and therefore reduce material usage thanks to the creativeness of the winding process (Oval et al., 2020; Yang et al., 2018; Yang, 2018; Spadea et al., 2017).

Second, extensive experimental research is essential for this novel structural form. The majority of existing research on FRP bar-reinforced concrete arches has been limited to tunnel lining segments and waterfront protective structures, but even in these areas, available data remains scarce. Even at those aspects, the available test data is still scarce. Consequently, the structural behavior of FRP-reinforced concrete arches remains inadequately understood, particularly in the absence of comprehensive parametric studies. Additional experimental studies are therefore needed to further explore the structural configurations and broaden the potential applications of FRP-reinforced concrete arches.

Third, comprehensive theoretical research is needed to supplement the experimental work. Theoretical studies on arch structures typically fall into two categories. The first is the deflection method, which relies on section analysis and geometrical compatibility but neglects shear effects and complex boundary conditions. This approach simplifies structural members into one-dimensional beam/column elements, leading to efficient computations. Its effectiveness has been well-validated for linear members (Shen and Lu, 1983; Jiang and Teng, 2012; Gao et al., 2021). The second is FEA, which is capable of constructing three-dimensional models to accurately analyze complex configurations, load interactions and boundary conditions, as well as to capture local nonlinear behavior and stress concentrations.

DSTA bridges represent a potent competitor to concrete-filled steel tubular arch bridges, particularly in the context of a corrosive environment (e.g., a marine or coastal environment). Note that the advantage of being corrosion-resistant, brought by the provision of an outer FRP tube that conceals the corrosion-prone steel tube, is realized at a cost of ease in connection. Therefore, innovation in connection techniques lies at the core of future research. The most challenging part resides in realizing the joints where different types of members converge (e.g., DSTA-DSTC joints). A potential solution is to separate such joints from the members that they connect so that they can be prefabricated. Furthermore, the steel tube of the joint as well as that of the member can be flanged to enable member-joint and member-member connection so that welding work at the construction site is minimized. With this joint solution, the members can either be prefabricated or cast on site. The former option is particularly attractive as it minimizes wet work at the construction site, shortens construction time and reduces construction costs.

For DSTA bridges, the bond between the steel tube and the concrete is of great importance to ensure the composite action between the two. The steel tube-to-concrete bond may be improved by shear connectors which can also serve as the stiffeners to the steel tube to enhance its buckling capacity (Peng et al., 2018; Huang et al., 2020). The connectors may also enhance the confinement to the concrete and play a role in the connections between different components/members if designed properly. The selection of form and configuration of shear connectors therefore offers opportunities for structural optimization. Furthermore, the present lack of design standards and/or research for the FRP-incorporating hybrid arches under various loading scenarios also impedes their wide application. There is, for example, a scarcity of research on the

torsional behavior of the hybrid arches, which may be critical in some scenarios. Practical applications should begin with small-scale DSTA bridges and follow an incremental route that gradually leads to safe and confident construction of long-span DSTA bridges.

## **2.6 CONCLUDING REMARKS**

In the past few decades, the use of FRP composites has inspired numerous structural innovations taking advantage of their unique properties. The vast majority of these innovations have been centered in the domain of linear members (e.g., slabs, beams and columns) and such-based structural forms (e.g., frames). In contrast, despite also being a mainstream structural form, arches have received inadequate research attention due to the complexities arising from their curvilinear nature. However, the distinctive properties of FRP materials and the diverse forms of FRP members provide a wide range of opportunities, which cover the full spectrum of span size, for contributing to the advancement of the classical arch structure.

Specifically, FRP-RC arches represent a promising structural form, particularly for large-scale arch structures. The corrosion resistance of FRP provides a solution to the steel corrosion issues commonly encountered in conventional arch structures. Potential applications include tunnel linings and long-span arch bridges. Admittedly, promoting FRP-RC arches as a viable structural solution involves several challenges. First, the configurations of FRP stirrups in arch structures could be optimized for enhanced performance. Second, extensive experimental research is essential to fully understand this novel structural form. Third, comprehensive theoretical research is needed to supplement the experimental work. Potential solutions to these challenges have also

been discussed in this chapter, providing a solid foundation for the innovation and works in the subsequent chapters.

## 2.7 REFERENCES

- Abdel-Magid B, Lopez-Anido R, Smith G, et al. (2003) Flexure creep properties of E-glass reinforced polymers. *Composite Structures* 62(3-4): 247-253.
- Ahmed EA, El-Sayed AK, El-Salakawy E, et al. (2010) Bend strength of FRP stirrups: Comparison and evaluation of testing methods. *Journal of Composites for Construction* 14(1): 3-10.
- Ashby MF and Cebon D. (2005) Materials selection in mechanical design. *MRS Bulletin* 30(12): 995.
- Azeem M, Ya HH, Kumar M, et al. (2022) Application of filament winding technology in composite pressure vessels and challenges: A review. *Journal of Energy Storage* 49: 103468.
- Beckwith SW and Hyland CR. (1999) Resin transfer molding: A decade of technology advances. *Resin Transfer Molding. SAMPE Monograph* 3: 1-14.
- Bell M, Fick D, Ament R, et al. (2020) The use of fiber-reinforced polymers in wildlife crossing infrastructure. *Sustainability* 12(4): 1557.
- Bessini J, Lazaro C, Casanova J, et al. (2019) Efficiency-based design of bending-active tied arches. *Engineering Structures* 200: 109681.
- Burnton P, McDonnell D and Fernando D. (2019) Design and construction of a hybrid double-skin tubular arch bridge. *Proceedings of 9th Australian Small Bridges Conference*. Queensland, Australia, 45-50.

- Caratelli A, Meda A, Rinaldi Z, et al. (2016) Precast tunnel segments with GFRP reinforcement. *Tunnelling and Underground Space Technology* 60: 10-20.
- Caratelli A, Meda A, Rinaldi Z, et al. (2017) Optimization of GFRP reinforcement in precast segments for metro tunnel lining. *Composite Structures* 181: 336-346.
- Caron JF, Julich S and Baverel O. (2009) Selfstressed bowstring footbridge in FRP. *Composite Structures* 89(3): 489-496.
- Dagher HJ, Bannon DJ, Davids WG, et al. (2012) Bending behavior of concrete-filled tubular FRP arches for bridge structures. *Construction and Building Materials* 37: 432-439.
- De Rivat B, Giamundo N, Meda A, et al. (2019) Hybrid solution with fiber reinforced concrete and glass fiber reinforced polymer rebars for precast tunnel segments. *Proceedings of Tunnels and Underground Cities: Engineering and Innovation Meet Archaeology, Architecture and Art*. CRC Press, 2018-2025.
- De Waal L, Jiang S, Torres J, et al. (2018) Design and construction of a hybrid double-skin tubular arch bridge. *Proceedings of 9th International Conference on Fibre-Reinforced Polymer (FRP) Composites in Civil Engineering, CICE 2018*. Paris, France: International Institute for FRP in Construction (IIFC), 878-887.
- Dong HL, Wang DY, Wang ZY, et al. (2018) Axial compressive behavior of square concrete columns reinforced with innovative closed-type winding GFRP stirrups. *Composite Structures* 192: 115-125.
- Douthe C, Baverel O and Caron JF. (2007) Gridshell in composite materials: Towards

- wide span shelters. *Journal of the International Association for Shell and Spatial structures* 48(3): 175-180.
- Douthe C, Caron JF and Baverel O. (2010) Gridshell structures in glass fibre reinforced polymers. *Construction and Building Materials* 24(9): 1580-1589.
- Fam AZ and Rizkalla SH. (2001a) Behavior of axially loaded concrete-filled circular fiber-reinforced polymer tubes. *Structural Journal* 98(3): 280-289.
- Fam AZ and Rizkalla SH. (2001b) Confinement model for axially loaded concrete confined by circular fiber-reinforced polymer tubes. *Structural Journal* 98(4): 451-461.
- Frketic J, Dickens T and Ramakrishnan S. (2017) Automated manufacturing and processing of fiber-reinforced polymer (FRP) composites: An additive review of contemporary and modern techniques for advanced materials manufacturing. *Additive Manufacturing* 14: 69-86.
- GangaRao HV and Prachasaree W. (2021) *FRP Composite Structures: Theory, Fundamentals, and Design*, Boca Raton: CRC.
- Gao K, Xie H, Li Z, et al. (2021) Study on eccentric behavior and serviceability performance of slender rectangular concrete columns reinforced with GFRP bars. *Composite Structures* 263: 113680.
- Goslin K and Arimond J. (2015) *Bridge-in-a-Backpack (TM). Task 7: Investigation of Damage and Repairs for Concrete Filled FRP Tubular Arches*. Maine, America: Maine. Dept. of Transportation.

- Goslin K, Pomeroy B, Dagher H, et al. (2014) *Bridge-in-a-Backpack (TM). Task 8: Investigation of Bridge Performance Under Extreme Temperatures*. Maine, America: Maine. Dept. of Transportation.
- Goslin K and Rofes X. (2015) *Bridge-in-a-Backpack (TM). Task 2.1 and 2.2: Investigate Alternative Shapes with Varying Radii*. Maine, America: Maine. Dept. of Transportation.
- Goslin K and Tomlinson S. (2016) *Bridge-in-a-Backpack (TM). Task 6: Guidelines for Long Term Inspection and Maintenance*. Maine, America: Maine. Dept. of Transportation.
- Goslin K, Walton H, Davids B, et al. (2011) *Bridge-in-a-Backpack (TM). Task 1: Investigation of Span Lengths Up to 70 Feet*. Maine, America: Maine. Dept. of Transportation.
- Habibi T, Rhode Barbarigos L and Keller T. (2022) Fiber-polymer composites for permanent large-scale bending-active elastica beams. *Composite Structures* 294: 115809.
- Hai ND, Mutsuyoshi H, Asamoto S, et al. (2010) Structural behavior of hybrid FRP composite I-beam. *Construction and Building Materials* 24(6): 956-969.
- Happold E and Liddell WI. (1975) Timber lattice roof for the Mannheim Bundesgartenschau. *Structural Engineering* 53(3): 99-135.
- Hindersmann A. (2019) Confusion about infusion: An overview of infusion processes. *Composites Part A: Applied Science Manufacturing* 126: 105583.

- Hollaway LC. (2013) *Applications of Advanced Fibre-reinforced Polymer (FRP) Composites in Bridge Engineering: Rehabilitation of Metallic Bridge Structures, All-FRP Composite Bridges, and Bridges Built with Hybrid Systems*: Elsevier.
- Hosseini SM, Mousa S, Mohamed HM, et al. (2022) Experimental and analytical study on precast high-strength concrete tunnel lining segments reinforced with GFRP bars. *Journal of Composites for Construction* 26(5): 04022062.
- Huang L, Zhang SS, Yu T, et al. (2020) Circular hybrid double-skin tubular columns with a stiffener-reinforced steel inner tube and a large-rupture-strain FRP outer tube: Compressive behavior. *Thin-Walled Structures* 155: 106946.
- Huang YJ, Xiao JZ, Qin L, et al. (2021) Mechanical behaviors of GFRP tube confined recycled aggregate concrete with sea sand. *Advances in Structural Engineering* 24(6): 1196-1207.
- Jiang S. (2020) *Hybrid FRP-concrete-steel Double-skin Tubular Truss Bridge: Design, Construction and Testing*. Queensland, Australia: The University of Queensland.
- Jiang T, Lin G and Xie P. (2023) Behavior of large-scale hybrid FRP-concrete-steel double-skin tubular columns subjected to eccentric compression. *Engineering Structures* 275: 115258.
- Jiang T and Teng JG. (2012) Slenderness limit for short FRP-confined circular RC columns. *Journal of Composites for Construction* 16(6): 650-661.
- Jung WT, Park JS and Kim SH. (2012) A study on the behavior characteristics of curved FRP-concrete composite panel. *Advanced Materials Research* 557: 375-380.

- Laval C. (2006) CADWIND 2006–20 years of filament winding experience. *Reinforced Plastics* 50(2): 34-37.
- Lee GP and Shin HS. (2010) A numerical study on feasibility of the circled fiber reinforced polymer (FRP) panel for a tunnel lining structure. *Journal of Korean Tunnelling and Underground Space Association* 12(6): 451-461.
- Lee GP, Shin HS and Kim SH. (2011) Study on mechanical behavioral characteristics of the curved FRP-concrete composite member for utilization as a tunnel lining structure. *Journal of Korean Tunnelling and Underground Space Association* 13(2): 149-158.
- Lienhard J, Alpermann H, Gengnagel C, et al. (2013) Active bending, a review on structures where bending is used as a self-formation process. *International Journal of Space Structures* 28(3-4): 187-196.
- Liu L, Wang, X., Wu, Z., Keller, T. (2021) Resistance and ductility of FRP composite hybrid joints. *Composite Structures* 255: 113001.
- Liu LL, Wang X, Wu ZS, et al. (2020) Optimization of multi-directional fiber architecture for resistance and ductility of bolted FRP profile joints. *Composite Structures* 248: 112535.
- Liu T, Feng P, Wu Y, et al. (2021) Developing an innovative curved-pultruded large-scale GFRP arch beam. *Composite Structures* 256: 113111.
- Luo YB, Wu G, Wu ZS, et al. (2009) Study on fabrication technique of steel fiber composite Bar (SFCB). *Earthquake Resist Engineering Retrofit* 31(1): 28-34.

- Madenci E, Özkılıç YO and Gemi L. (2020) Buckling and free vibration analyses of pultruded GFRP laminated composites: Experimental, numerical and analytical investigations. *Composite Structures* 254: 112806.
- Mantell SC and Springer GS. (1994) Filament winding process models. *Composite Structures* 27(1-2): 141-147.
- Manuele G, Bringiotti M, Lagana G, et al. (2020) Fiber glass and “green” special composite materials as structural reinforcement and systems; use and applications from Milan Metro, Brenner Tunnel up to high speed train Milan–Genoa. *Proceedings of Tunnels and Underground Cities: Engineering and Innovation Meet Archaeology, Architecture and Art*. CRC Press, 2625-2634.
- Meda A, Rinaldi Z, Spagnuolo S, et al. (2019) Hybrid precast tunnel segments in fiber reinforced concrete with glass fiber reinforced bars. *Tunnelling and Underground Space Technology* 86: 100-112.
- Meda A, Rinaldi Z, Spagnuolo S, et al. (2020) Experimental behaviour of precast tunnel segments in steel fiber reinforcement with GFRP rebars. *Fib Bulletin*: 153-162.
- Mirmiran A and Shahawy M. (1997) Behavior of concrete columns confined by fiber composites. *Journal of Structural Engineering* 123(5): 583-590.
- Morphy RD. (1999) *Behaviour of Fibre-reinforced Polymer (FRP) Stirrups as Shear Reinforcement for Concrete Structures*. Winnipeg, Canada: University of Manitoba.
- Nicholas P, Hernández EL and Gengnagel C. (2013) *The Faraday Pavilion: Activating*

- bending in the design and analysis of an elastic gridshell. *Proceedings of the Symposium on Simulation for Architecture & Urban Design*. San Diego, America, 1-8.
- Nunes F, Correia JR and Silvestre N. (2016) Structural behavior of hybrid FRP pultruded beams: Experimental, numerical and analytical studies. *Thin-Walled Structures* 106: 201-217.
- Oval R, Costa E, Thomas-McEwen D, et al. (2020) Automated framework for the optimisation of spatial layouts for concrete structures reinforced with robotic filament winding. *Proceedings of ISARC 2020: The 37th International Symposium on Automation and Robotics in Construction*. Kitakyushu, Japan: International Association for Automation and Robotics in Construction, 1541-1548.
- Parry H, Rofes X and Lopez Anido R. (2014) *Splicing and Local Reinforcement of Concrete Filled FRP Tubes*. Maine, America: Maine. Dept. of Transportation.
- Pei WC, Wang DY, Wang X, et al. (2021) Axial monotonic and cyclic compressive behavior of square GFRP tube-confined steel-reinforced concrete composite columns. *Advances in Structural Engineering* 24(1): 25-41.
- Peng K, Yu T, Hadi MN, et al. (2018) Compressive behavior of hybrid double-skin tubular columns with a rib-stiffened steel inner tube. *Composite Structures* 204: 634-644.
- Pone S, Colabella S, Parenti B, et al. (2013) Construction and form-finding of a post-formed timber grid-shell. *Proceedings of 2nd International Conference on*

- Structures and Architecture*. Guimaraes, Portugal: Crc Press-Taylor & Francis Group, 245-252.
- Potyrala PB. (2011) *Use of Fibre Reinforced Polymeromposites in Bridge Construction. State of the Art in Hybrid and All-composite Structures*. Catalonia, Spain: Polytechnic University of Catalonia.
- Pyrzowski Ł and Miśkiewicz M. (2017) Modern GFRP composite footbridges. *Proceedings of “Environmental Engineering” 10th International Conference*. Vilnius Gediminas Technical University, Ottawa, Canada, 1-8.
- Rajak DK, Pagar DD, Menezes PL, et al. (2019) Fiber-reinforced polymer composites: manufacturing, properties, and applications. *Polymers* 11(10): 1667.
- Rajak DK, Wagh PH and Linul E. (2021) Manufacturing technologies of carbon/glass fiber-reinforced polymer composites and their properties: A review. *Polymers* 13(21): 3721.
- Sá MF, Gomes AM, Correia JR, et al. (2011) Creep behavior of pultruded GFRP elements–Part 1: Literature review and experimental study. *Composite Structures* 93(10): 2450-2459.
- Shen FC. (1995) A filament-wound structure technology overview. *Materials Chemistry and Physics* 42(2): 96-100.
- Shen ZY and Lu LW. (1983) Analysis of initially crooked, end restrained steel columns. *Journal of Constructional Steel Research* 3(1): 10-18.
- Shi JZ, Wang X, Huang H, et al. (2017) Relaxation behavior of prestressing basalt fiber-

- reinforced polymer tendons considering anchorage slippage. *Journal of Composite Materials* 51(9): 1275-1284.
- Sobrino JA and Pulido MDG. (2002) Towards advanced composite material footbridges. *Structural Engineering International* 12(2): 84-86.
- Sonntag D, Bechert S and Knippers J. (2017) Biomimetic timber shells made of bending-active segments. *International Journal of Space Structures* 32(3-4): 149-159.
- Spadea S, Orr J and Ivanova K. (2017) Bend-strength of novel filament wound shear reinforcement. *Composite Structures* 176: 244-253.
- Starr T. (2000) *Pultrusion for Engineers*, America: CRC.
- Tang ZX, Zhou YZ, Feng J, et al. (2021) Concrete protective arches reinforced with BFRP bars: Construction and quasi-static structural performances. *Tunnelling and Underground Space Technology* 108: 103731.
- Tang ZX, Zhou YZ, Feng J, et al. (2020) Blast responses and damage evaluation of concrete protective arches reinforced with BFRP bars. *Composite Structures* 254: 112864.
- Teng JG, Yu T and Wong YL. (2004) Hybrid FRP-concrete-steel double-skin tubular columns: Stub column tests. *Proceedings of International Conference on Steel and Composite Structures (ICSCS)*. Seoul, Korea.
- Teng JG, Yu T, Wong YL, et al. (2007) Hybrid FRP–concrete–steel tubular columns: Concept and behavior. *Construction and Building Materials* 21(4): 846-854.

- Tengilimoğlu O. (2019) *An Experimental Study to Investigate the Possibility of Using Macro-synthetic Fibers in Precast Tunnel Segments*. Ankara, Turkey: Middle East Technical University.
- Tomblin J. (2006) *Buried FRP-concrete Arches*. Marine, America: The University of Maine.
- Tonatto MLP, Tita V and Amico SC. (2020) Composite spirals and rings under flexural loading: Experimental and numerical analysis. *Journal of Composite Materials* 54(20): 2697-2705.
- Vedernikov A, Safonov A, Tucci F, et al. (2020) Pultruded materials and structures: A review. *Journal of Composite Materials* 54(26): 4081-4117.
- Vincent T and Ozbakkaloglu T. (2013) Influence of fiber orientation and specimen end condition on axial compressive behavior of FRP-confined concrete. *Construction and Building Materials* 47: 814-826.
- Walton HJ, Davids WG, Landon ME, et al. (2016a) Simulation of buried arch bridge response to backfilling and live loading. *Journal of Bridge Engineering* 21(9): 04016052.
- Walton HJ, Davids WG, Landon ME, et al. (2016b) Experimental evaluation of buried arch bridge response to backfilling and live loading. *Journal of Bridge Engineering* 21(9): 04016053.
- Wu J, Zhou J, Xu Y, et al. (2022) Dynamic responses of blast-loaded shallow buried concrete arches strengthened with BFRP bars. *Materials* 15(2): 535.

- Xie P. (2018) *Behavior of Large-scale Hybrid FRP-concrete-steel Double-skin Tubular Columns Subjected to Concentric and Eccentric Compression*. Hong Kong, China: The Hong Kong Polytechnic University.
- Xie P, Lam L and Jiang T. (2023) Compressive behavior of GFRP tubes filled with self-compacting concrete. *Journal of Composites for Construction* 27(1): 04022103.
- Xie P, Lin G, Teng JG, et al. (2020) Modelling of concrete-filled filament-wound FRP confining tubes considering nonlinear biaxial tube behavior. *Engineering Structures* 218: 110762.
- Yang Y. (2018) *Novel Reinforcement for Flexibly-formed Concrete Structures*. Bath, England: University of Bath.
- Yang YZ, Orr J and Spadea S. (2018) Shear behavior of variable-depth concrete beams with wound fiber-reinforced polymer shear reinforcement. *Journal of Composites for Construction* 22(6): 04018058.
- Yao J, Jiang T, Xu P, et al. (2015) Experimental investigation on large-scale slender FRP-concrete-steel double-skin tubular columns subjected to eccentric compression. *Advances in Structural Engineering* 18(10): 1737-1746.
- Yu T and Teng JG. (2011) Design of concrete-filled FRP tubular columns: Provisions in the Chinese technical code for infrastructure application of FRP composites. *Journal of Composites for Construction* 15(3): 451-461.
- Yu T, Wong YL, Teng JG, et al. (2006) Flexural behavior of hybrid FRP-concrete-steel double-skin tubular members. *Journal of Composites for Construction* 10(5):

443-452.

Yuan Y, Wang Z and Wang D. (2022) Shear behavior of concrete beams reinforced with closed-type winding glass fiber-reinforced polymer stirrups. *Advances in Structural Engineering* 25(12): 2577-2589.

Zhao CJ, Tang ZX, Wang P, et al. (2022) Blast responses of shallow-buried prefabricated modular concrete tunnels reinforced by BFRP-steel bars. *Underground Space* 7(2): 184-198.

Zhao JF, Mei KH and Wu J. (2020) Long-term mechanical properties of FRP tendon–anchor systems—A review. *Construction and Building Materials* 230: 117017.

Zhao JL, Teng JG, Yu T, et al. (2016) Behavior of large-scale hybrid FRP-concrete-steel double-skin tubular beams with shear connectors. *Journal of Composites for Construction* 20(5): 04016015-04016011.

Zoghi M. (2013) *The International Handbook of FRP Composites in Civil Engineering*: CRC.

Zohrevand P and Mirmiran A. (2013) Seismic response of ultra-high performance concrete-filled FRP tube columns. *Journal of Earthquake Engineering* 17(1): 155-170.

Zou PXW. (2003) Long-term properties and transfer length of fiber-reinforced polymers. *Journal of Composites for Construction* 7(1): 10-19.

Table 2.1 Manufacturing/forming methods for curved FRP members

Method	Automation level	Product form	Targeted application
Vacuum infusion	Relatively low	Complex-geometry objects	All-FRP arch bridge spans
Filament winding	High	Straight/curved tubes	Confining device for concrete arches
Pultrusion	High	Straight/curved profiles with a constant cross-sectional shape	FRP truss arches; arch bridge spans; reinforcement for concrete arches
Active bending	N/A*	Initially straight profiles (typically pultruded)	Rapidly assembled structures; arch ribs

Note: \*Vacuum infusion, filament winding and pultrusion are standard manufacturing processes for composites production. In contrast, active bending is a technique used to form arches by bending ready-made and initially straight members (typically pultruded hollow-section profiles).

Table 2.2 Existing FRP-incorporating arch projects and relevant concepts

Source	Category	Manufacturing/ forming method	Form of FRP product	Year of completion	Location	Arch span	Form of application
Sobrinho and Pulido, 2002	All-FRP	Pultrusion	Straight profile	2001	Spain	38 m	Footbridge
Liu et al., 2021	All-FRP	Pultrusion	Curved profile	2021	China	20 m	Footbridge
Potyrala, 2011; Pyrzowski and Miśkiewicz, 2017; Hollaway, 2013	All-FRP	Vacuum infusion	Bridge span	2008	Russia	22.6 m	Footbridge
Bell et al., 2020	All-FRP	Vacuum infusion	Bridge span	2020	Netherlands	24/36 m	Wildlife crossing passage
Pyrzowski and Miśkiewicz, 2017	All-FRP	Vacuum infusion	Bridge span segment	2014	Denmark	56 m	Footbridge
Caron et al., 2009	All-FRP	Active bending	Straight profile	2009	France	4 m (1/10 scaled model)	Footbridge
Bessini et al., 2019	All-FRP	Active bending	Straight profile	2019	Spain	5 m (scaled model)	Footbridge
Manuele et al., 2020	Hybrid	Pultrusion	Curved bar	2014	Italy	About 3.5 m	Tunnel segment
Tang et al., 2020; Tang et al., 2021; Zhao et al., 2022; Wu et al., 2022	Hybrid	Pultrusion	Curved bar	2020-2022	China	1.2 m (scaled model)	Waterfront protective structure
Lee et al., 2010; Lee et al., 2011	Hybrid	Pultrusion	Curved profile	2010	Korea	5.062 m	Tunnel segment
Dagher et al., 2012	Hybrid	Vacuum infusion	tube	2010	USA	8.5 m	Arch bridge
De Waal et al., 2018	Hybrid	Filament winding	tube	2014	Australia	12.5 m	Arch bridge

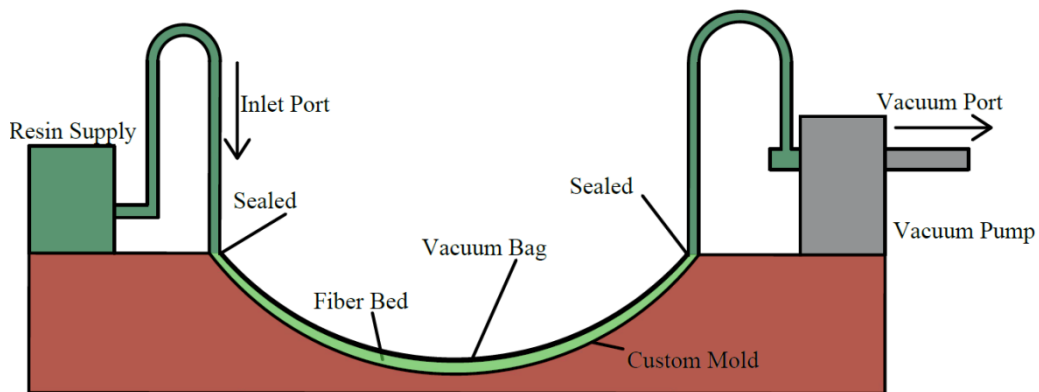
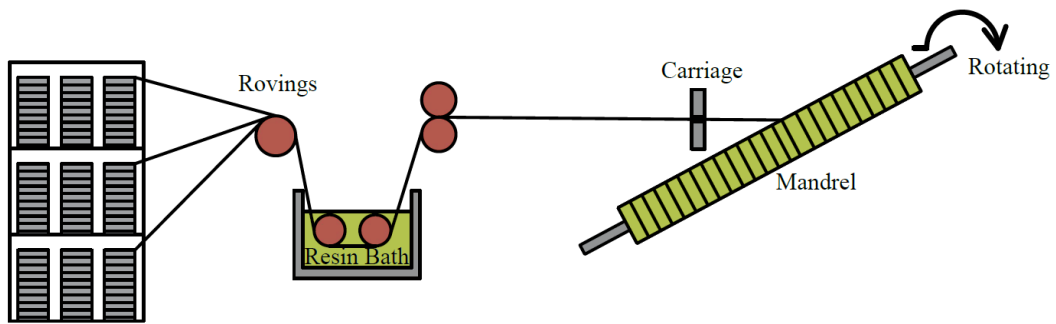
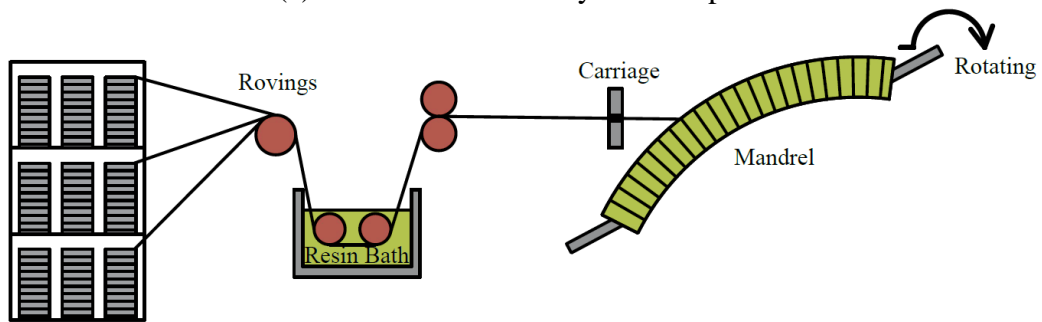


Figure 2.1 Sketch diagram of vacuum infusion

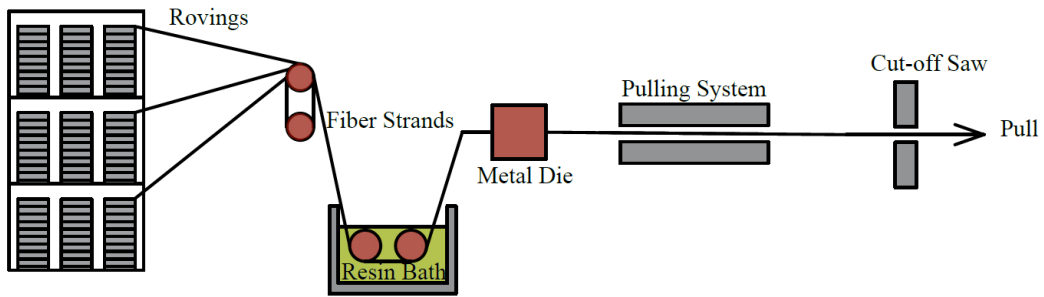


(a) Manufacture of axisymmetric parts

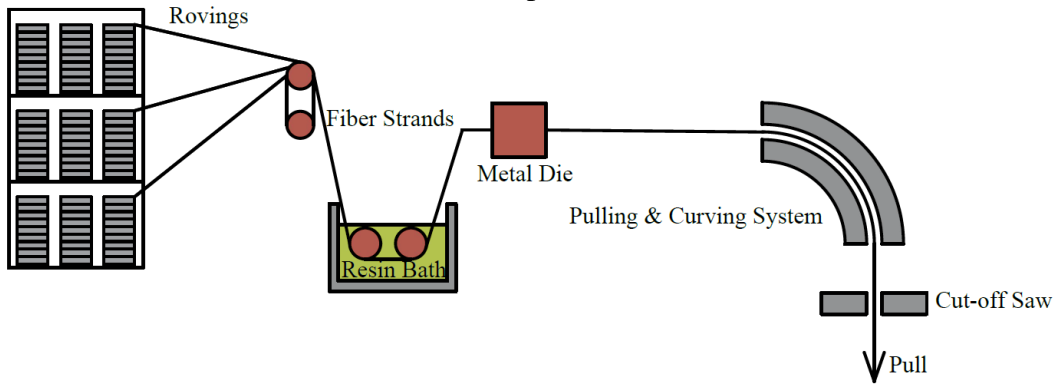


(b) Manufacture of non-axisymmetric parts

Figure 2.2 Sketch diagram of filament winding



(a) Linear pultrusion



(b) Curved pultrusion

Figure 2.3 Sketch diagram of pultrusion

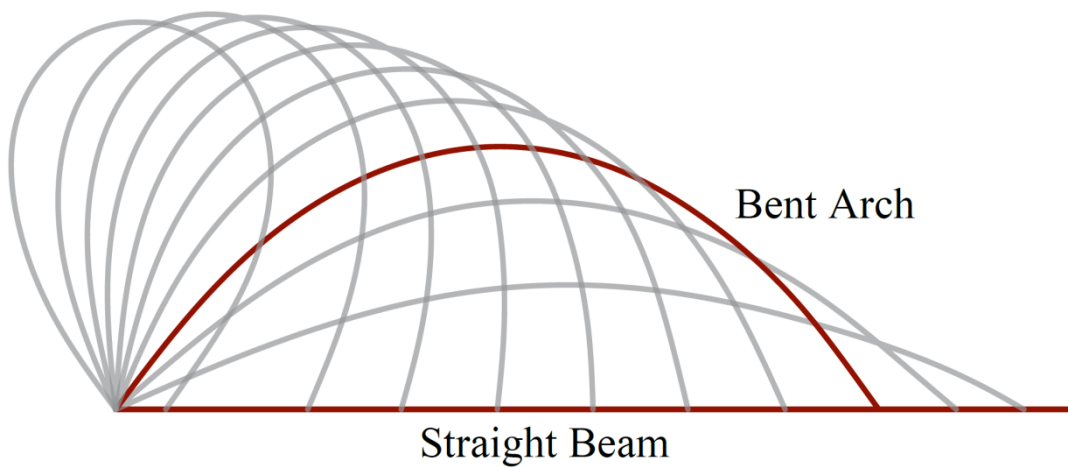


Figure 2.4 Sketch diagram of active bending technique



Figure 2.5 Footbridge made of GFRP pultruded profiles in Lleida, Spain (Hollaway, 2013)



Figure 2.6 Curved-pultruded GFRP footbridge in Beijing, China (Liu et al., 2021)



Figure 2.7 Footbridge manufactured by vacuum infusion in Moscow, Russia (Hollaway, 2013)



Figure 2.8 Scaled model of FRP self-stressed bowstring footbridge (Caron et al., 2009)



Figure 2.9 Prototype of bending-active tied footbridge (Bessini et al., 2019)



(a) GFRP reinforcement cage

(b) Segment geometry

Figure 2.10 GFRP bar-reinforced tunnelling lining segment (Caratelli et al., 2016)



(a) Reinforcement cage

(b) Assembled modular tunnel

Figure 2.11 SFCBs/BFRP bar-reinforced semi-circular arch and such-based tunnel (Zhao et al., 2022)



(a) GFRP profile

(b) Panel geometry

Figure 2.12 FRP-concrete arch panel (Jung et al., 2012)



Figure 2.13 Buried CFFT arch bridge in Maine, USA (Dagher et al., 2012)

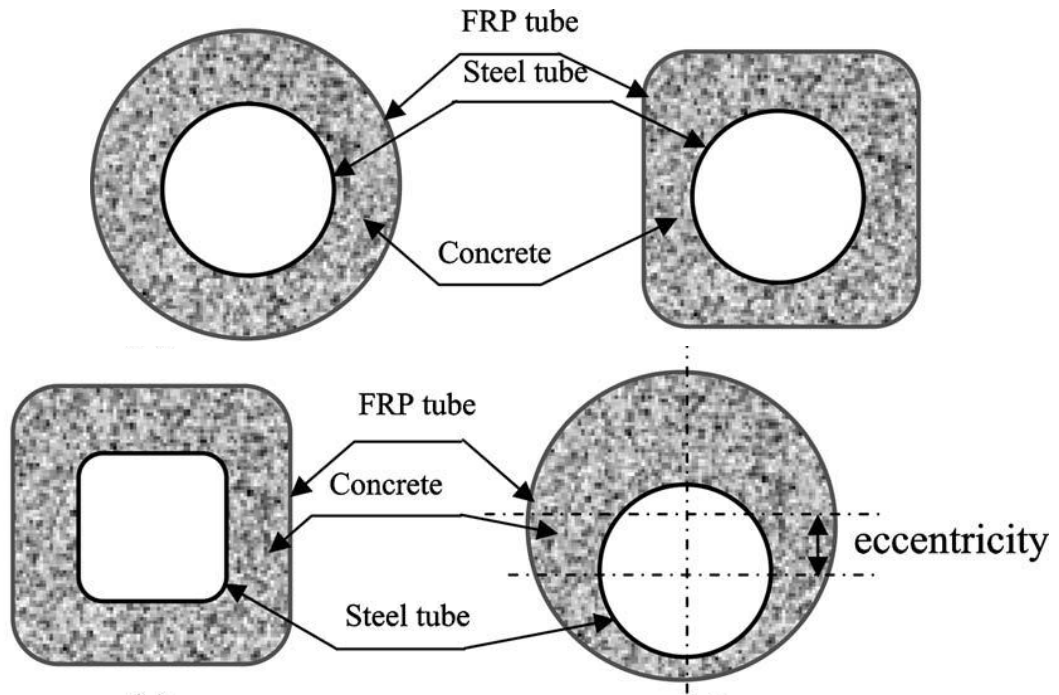


Figure 2.14 Typical sections of DSTMs (Yu et al., 2006)



Figure 2.15 DSTA bridge constructed at University of Queensland, Australia (Burnton et al., 2019)

## **CHAPTER 3**

# **PRELIMINARY INVESTIGATION ON FRP REINFORCED CONCRETE ARCHES**

### **3.1 INTRODUCTION**

This chapter presents preliminary investigation on the structural behavior of FRP-RC arches, involving a combined experimental and theoretical study. The experimental work involved a test on an FRP-RC arch specimen, which provides the first insight into the behavior and failure mode of such arches. Theoretically, a fundamental analytical method to assess its load-bearing capacity was developed. Based on the above work, the chapter identifies and addresses several issues exposed in the experiment on the FRP-RC arch specimen. By analyzing the fundamental mechanisms contributing to these problems, corresponding solutions and design recommendations are addressed. These findings provide a solid foundation for further experimental and theoretical research in subsequent chapters.

### **3.2 EXPERIMENTAL PROGRAM**

#### **3.2.1 Specimen details**

The test specimen (Figures 3.1 and 3.2) had a span length of 3000 mm (measured along the centerline), a sectional width of 300 mm, a sectional depth of 100 mm and a rise-

span ratio of 0.25, representing a scaled model of typical underground half-lining structures with a scale factor of 1:10. The central axis of the arch follows a circular arc with a radius of 1875 mm, forming a central angle of approximately 106.26°.

The arch specimen designed in this chapter is an under-reinforced FRP-reinforced concrete specimen. Two pairs of GFRP bars with a diameter of 6 mm were used as the longitudinal reinforcement close to the top and bottom of the cross-section, respectively, while closed GFRP stirrups with a diameter of 8 mm and spaced at 200 mm intervals along the arch axis were used as the transverse reinforcement and for locating the longitudinal bars (Figure 3.2). The shear design of the specimen adhered to the conservative principle as per ACI 440.1R-15 (2015), with the primary objective of substantially reducing the potential for shear failure. The longitudinal GFRP bars were curved bars manufactured and delivered in a pre-bent state.

In preparing the specimen, the GFRP reinforcement cage was first fabricated and then placed into a steel mold for concrete casting; the cast specimen was then cured following ASTM 192-19 (2019). The arch specimens were demolded 21 days after casting and tested at the curing age of 48 days.

### **3.2.2 Material properties**

The GFRP longitudinal rebars used in the test were supplied by Fenghui Composites Co. in Nanjing, China. Their surfaces were ribbed and sand-coated to enhance the bond performance with concrete. The curved GFRP bars were composed of continuous unidirectional glass-fiber strands (EDR-T910 supplied by Shandong Fiberglass Co.) bonded together using a thermosetting vinyl ester resin (TM-V211), employing

pultrusion and mechanical bending processes, followed by curing in a 150 °C chamber for 1.5 hours.

The mechanical properties of the GFRP bars were determined according to ACI 440.3R-12 (2012). To avoid the challenges associated with measuring the properties of curved GFRP bars, straight bars produced in the same batch using the same raw materials as the curved bars were tested to determine their tensile strength and elastic modulus (Table 3.1), following Spagnuolo et al. (2014). Regarding the performance of FRP bars in compression, current standards do not provide a definitive testing methodology. Existing studies indicate that these standards still underestimate the contribution of FRP bars in compression, and the tested tensile and compressive elastic modulus of the FRP bars were found to be close and both exhibited linear elasticity (Deitz et al., 2003; Maranan et al., 2016).

The GFRP closed stirrups used were also sourced from Fenghui Composites Co., Nanjing, China. The products featured a smooth surface without additional treatment. Their manufacturing process involved a filament winding process, manually wrapping glass fibers around a steel mold in uniform rotation, the dimensions of which were tailored to the internal dimensions of the designed stirrups. The fiber orientation of the stirrups was nearly circumferential. Subsequently, the stirrups, along with the steel mold, were cured in a 250 °C oven for 10 minutes.

Seawater sea-sand concrete (SSC) was used for the specimen. Because of their excellent corrosion resistance in marine environment, the use of FRP bars opens a new avenue for concrete production using seawater and sea-sand as the raw materials, which offers compelling economic and environmental advantages for the construction of coastal and

marine infrastructures (Teng et al., 2011). Nevertheless, it has been shown by existing studies that the short-term mechanical behavior of FRP-reinforced SSC structures is generally similar to FRP-reinforced normal concrete structures (Hao, 2024). The mix proportions of SSC used in this test are given in Table 3.2. The concrete mixture comprised commercial crushed granite with a maximum size of 10 mm as the coarse aggregate and sea-sand as the fine aggregate. Type I 52.5 Portland-Composite Cement (CEM) and pulverized fly ash (PFA) were used, while the seawater was obtained locally in Hong Kong, and the superplasticizer ADVA 109 was used as a water reducer. The compressive properties of concrete were determined through compression tests of three standard cylinders (150 mm × 300 mm), and the results are given in Table 3.1.

Additionally, a slump test was conducted prior to concrete casting to characterize its flowability, indicating a slump value of 220 mm. It is noteworthy that, given that the designed arch specimen was a slender, shallow member in an under-reinforced state, its self-weight could potentially affect the accuracy of subsequent analyses. The density of the concrete was determined to be 2317 kg/m<sup>3</sup>, resulting in an approximate self-weight of 241.71 kg for the arch specimen.

### **3.2.3 Test setup**

A quasi-static test on the arch specimen was conducted in the Structural Laboratory of The Hong Kong Polytechnic University using a compression test system with a load capacity of 500 kN, as shown in Figure 3.3. The arch specimen was connected to the steel plates at both ends using three welded shear studs with a diameter of 19 mm. During the test preparation, these steel plates were bolted to the roller bearings below, as depicted in Figure 3.3. The supports at both ends of the arch were designed as hinged

supports, restricting the displacement of the arch feet while still allowing rotation. However, due to the setup errors, the arch feet could not rotate as intended, thus being treated as fixed supports in subsequent analyses. During the test, the arch specimen was subjected to a monotonically increasing load applied at the apex. A steel rod with a diameter of 25 mm was welded to a steel plate measuring 305 mm in length and 75 mm in width, which was then placed on the extrados of the arch specimen to transmit the applied load. Besides, the loading area beneath the steel plate was leveled with high-strength gypsum to prevent stress concentration and out-of-plane stresses. The displacement-controlled load was applied at a rate of 0.4 mm/min in the initial stage and then gradually increased to 2 mm/min during the test.

### **3.3 TEST RESULTS AND DISCUSSION**

At the initial stage, the load increased linearly with the displacement until a load of 11.05 kN (displacement at crown: 3.26 mm) (Point 1 in Figure 3.4), at which a through-width flexural crack was noticed near the crown of the arch; the crack propagated afterwards from the bottom to the top, ultimately extending to the concrete cover of the top reinforcement within the section (Figure 3.5). Further examination of the cracked section revealed that there was a GFRP stirrup at the section. The second and third major cracks with a substantial width occurred at the arch shoulders on both sides of the mid-span, of which the second one occurred almost at the same time as the first crack, while the third one occurred a bit later. Subsequently, four more major cracks occurred during the loading process, and Figure 3.6 shows the locations of the cracks and their sequence of occurrence. Notably, the occurrence of each major crack was accompanied by a significant load drop (see Figure 3.4); this observation is different from that in normal steel-reinforced concrete arches and may be attributed to two main

factors: (1) the specimen was designed to be an under-reinforced concrete arch with a relatively small reinforcement ratio; (2) the elastic modulus of GFRP bars (i.e., approximately 50 GPa) was considerably lower than that of steel bars (i.e., approximately 200 GPa). Consequently, the GFRP bars were unable to immediately take the load released by the tensile concrete when a major crack occurred. Nevertheless, with the increasing local deformation at the cracked section, the strains in the GFRP bars gradually increased, and the load capacity of the arch could be recovered after the first six major cracks (Figure 3.4).

It is also worth noting that all the cross-sections with major cracks are GFRP stirrup-reinforced sections. It is believed that the presence of the GFRP stirrups, with fibers in the hoop direction and thus having a relatively small stiffness in the longitudinal direction of the arch, somewhat weakened the normal section in terms of their bending capacity, so that cracks tended to occur at these weak sections. This effect might not always be considerable, but it appeared to be pronounced in the test specimen due to its relatively small cross-section.

In structural engineering, ductility is often assessed by the deflection at the arch crown, which is about 80%-90% of its load-bearing capacity. In this test, the deflection at the arch apex was used to reflect the overall deformation of the arch. The bending strength observed was 14.78 kN with a deflection of 21.74 mm. Despite the several major cracks and the associated load drops, the arch could sustain a substantial load until a displacement of 72.25 mm at a load of 12.31 kN (83.28% of its strength) (i.e., Failure point in Figure 3.4), at which the rupture of two bottom GFRP longitudinal bars near the crown occurred when the cross-section reached its bending capacity.

### 3.4 ANALYSIS OF LOAD CAPACITY

The relationship between the applied load and the internal forces/bending moments of the arch can be obtained using the force method for indeterminate structures by applying deformation compatibility and force equilibrium equations (Tang et al., 2021). Due to the symmetry of the load ( $V_{ext}$ ), geometry, boundary conditions of structures, only half of the arch was considered in the analysis, as shown in Figure 3.7. The horizontal and vertical reaction forces  $H_R$  and  $V_R$  as well as the bending moment  $M_R$  at the support can be first calculated using the force method to be:  $H_R = 0.915V_{ext}$ ,  $V_R = 0.5V_{ext}$ ,  $M_R = -0.0651RV_{ext}$ , where  $R = 1875$  mm is the radius of the arch. With these, the internal axial force  $N$  and bending moment  $M$  at any section of the arch can be calculated by:

$$\begin{cases} N = H_R \cos(\varphi) + V_R \sin(\varphi) \\ M = H_R y - V_R x + M_R \end{cases} \quad (3.1)$$

where  $x$  and  $y$  are the coordinates of the section and  $\varphi$  is the central angle at a given point (Figure 3.7). Using Equation (3.1), it can be derived that the maximum sagging bending moment is located at the crown of the arch, while the largest hogging bending moment is located at the arch shoulder with  $\varphi = 29.31^\circ$ . During the test, the first major crack occurred near the apex, while the second and third major flexural cracks occurred approximately symmetrically with respect to the mid-span with an angle of  $\varphi = 28.69^\circ$ , demonstrating the reliability of the analysis. The slight differences between the analytical and test results in the locations are believed to be due to the existence of GFRP stirrups which weakened some of the cross-sections, as discussed in the preceding section.

Using Equation (3.1), the internal axial force and bending moment at the crown section at the applied load 14.76 kN of the failure point (i.e. failure point in Figure 3.4) can be calculated to be:  $N = 13.62$  kN (compression),  $M = 2.28$  kN · m. If the self-weight of the arch is considered, the actual maximum internal forces/moment are slightly different as:  $N = 14.72$  kN (compression),  $M = 2.29$  kN · m.

The section capacity of the arch can be calculated using the section analysis method with the following assumptions: (1) the stress distribution of concrete within the compression zone is assumed to follow a rectangular stress block, as specified in the Australian standard AS 3600-09 (2009); (2) the tensile strength of concrete is ignored; (3) the bond between GFRP bars and concrete is perfect; (4) the GFRP bars exhibit elastic behavior with the same elastic modulus in both tension and compression.

In the test, the final failure of the arch occurred when the bottom GFRP bars ruptured. On the other hand, it was observed that the concrete cover was crushed and detached from the arch during the test (Figure 3.5). Therefore, it is not unreasonable to assume that the maximum strain of the remaining concrete reached its ultimate strain [i.e., 0.3% according to ACI 440.11R-22 (2022)] at the final failure. With the above assumption and considering the contribution of the remaining concrete and the GFRP bars, the section capacity of the arch at the final failure can be calculated to be:  $N = 15.35$  kN (compression),  $M = 2.57$  kN · m. It is evident that the calculated ultimate axial force and bending moment of the mid-section are both close to the test results. The current analysis is performed using the Force Method on the undeformed arch configuration, which neglects geometrical nonlinearity. Consequently, the applied loads were slightly underestimated, leading to lower induced internal forces compared

to those obtained from section analysis. It should however be noted that, although the above analysis is useful for gaining a basic understanding of the test results, it is semi-empirical in nature as it takes some assumptions based on the test observation.

### **3.5 KEY ISSUES AND POTENTIAL IMPROVEMENTS**

#### **3.5.1 FRP stirrups**

FRP composite materials, characterized by a polymer matrix reinforced with fibers, exhibit orthotropic anisotropy due to the fiber orientation. This results in superior mechanical properties, including strength and stiffness, along the fiber direction compared to properties perpendicular to the fibers. Specifically, the mechanical attributes orthogonal to the fibers are largely governed by the polymer matrix between the fibers. FRP stirrups, with fibers oriented transversely, have an elastic modulus ranging from 2 to 4 GPa along the longitudinal axis for stiffness and strength response, which is considerably lower than that of concrete. Consequently, stirrup-reinforced sections often exhibit increased vulnerability in the longitudinal direction of members.

Given the rectangular cross-section of the arch specimen with a width-to-height ratio of 3, the stirrups primarily extend along the width (horizontal length) of the sections (Figure 3.2). However, the shear resistance is predominantly provided by the vertical legs, while the horizontal length of the stirrups makes a minimal contribution. It is believed that reducing the unnecessary horizontal length could effectively mitigate their adverse effect on the stiffness response and load-bearing capacity.

Figure 3.8 presents a parametric analysis of axial load-bending moment diagrams for sections with varying horizontal lengths of an embedded FRP stirrup, evaluating their weakening effect on load-bearing capacity. Apart from the variations in the horizontal

length of the stirrup, other material properties and geometric parameters remained consistent across different groups, as in the test setup. The layer method (also known as fiber model) was employed in the section analysis (Jiang and Teng, 2012). For the calculation of load-bearing capacity, the stress-strain relationship of concrete in compression followed GB 50010 (2015). To accurately simulate stiffness response, the contribution of concrete's tensile strength was considered, assuming linearity in the ascending branch with a slope equal to the compressive elastic modulus. The model proposed by Collins and Mitchell (1986) was used to simulate the descending branch of concrete in tension, which is an improved version of the original Vecchio and Collins's (1986) tension-stiffening model. In the absence of direct concrete tensile property tests, the tensile strength of concrete was estimated from its compressive strength, serving as the peak value for the constitutive model in tension, as suggested by Collins and Mitchell (1997). Additionally, it was assumed that FRP stirrup has equal tensile and compressive stiffness in the normal section (perpendicular to the fiber orientation), valued at 3 GPa. All materials in the cross-section were assumed to be perfectly bonded, allowing collaborative functioning.

Figure 3.8 shows that sections reinforced with FRP stirrup, irrespective of the horizontal length (30 mm, 90 mm, 150 mm, 210 mm, and 270 mm), exhibit a reduction in load-bearing capacity compared to sections without stirrup. As the horizontal length of the stirrup decreases, there is a noticeable improvement in load-bearing capacity. This weakening effect is more pronounced under conditions of high axial compression, whereas it is less apparent in pure bending scenarios. Under pure compression, the strength reduction factors for horizontal lengths of 30 mm, 90 mm, 150 mm, 210 mm, and 270 mm are 0.96, 0.92, 0.89, 0.86, and 0.83, respectively. Notably, the 270 mm

length, corresponding to the dimensions used in the experiment, shows a significant decrease in load-bearing capacity compared to sections without stirrup.

In near-pure bending states, a critical point is observed for all groups at a bending moment of 7 kN·m and an axial force of 41 kN. This point marks the failure threshold, where the ultimate compressive strain of both the concrete and FRP reinforcement simultaneously reaches their limits. As shown in Figure 3.8, below this point, failure is governed by the rupture of FRP reinforcement, with minimal influence from the horizontal length of the stirrup on ultimate load capacity, as evidenced by the near coincidence of the response curves. Above this point, failure is governed by concrete crushing, and the decrease in section eccentricity amplifies the extent to which stirrup reduces load capacity.

Furthermore, Figure 3.9 illustrates the effect of stirrup horizontal length on moment-curvature development, reflecting the stiffness response at the section level. The layer method was utilized for section analysis. During curvature development, the ratio of bending moment to axial force, known as the eccentricity ratio in compression-flexure members, was assumed to be constant, equivalent to the ratio for the critical section at the arch crown in Section 3.4.

Figure 3.9 reveals that cracking of the concrete resulted in a peak point during curvature development in specimens with a relatively small reinforcement ratio. Notably, as the horizontal length of the stirrup was reduced, there was a clear increase in several key parameters: the cracking flexural moment, the valley value after cracking, and the recovery stiffness after the peak value. For stirrups used in the experiment (horizontal length = 270 mm), the cracking peak load was calculated to be 2.74 kN·m,

corresponding to a curvature of  $13.5 \times 10^{-6} \text{ m}^{-1}$ . Compared to sections without stirrup (cracking peak load of  $3.10 \text{ kN}\cdot\text{m}$ , curvature of  $10.0 \times 10^{-6} \text{ m}^{-1}$ ), the peak load decreased by 11.5%, while section deformation increased by 34.9%. When the load-carrying capacity subsequently reclaimed to the pre-cracking level, the curvatures of both conditions were nearly the same at approximately  $13.5 \times 10^{-6} \text{ m}^{-1}$ . When the horizontal length of the stirrup was reduced to 30 mm, the cracking peak load and corresponding curvature differed from those of sections without stirrup by only about 4%, which is negligible.

Based on the above analysis, it can be concluded that the presence of FRP stirrups reduces the stiffness response and load-bearing capacity of the stirrup-reinforced sections. In this experimental setup (Section 3.2), reducing the horizontal length of the stirrups is an effective solution to mitigate the degradation of stiffness and load-bearing capacity. To address this issue, Chapter 4 proposes a novel form of stirrup based on the shape optimization of FRP stirrups, which is expected to effectively reduce the adverse impact of stirrups on the stiffness and strength of sections in the normal direction.

### **3.5.2 Failure modes of under-reinforced and over-reinforced concrete arches**

The failure modes of FRP-reinforced concrete arches can be classified into two categories: under-reinforced and over-reinforced failure. Under-reinforced failure occurs in members with a lower reinforcement ratio, where the compressive strain of the concrete at the critical section does not reach its ultimate strain, while the maximum strain of the FRP reinforcement reaches its rupture limit. Consequently, the load-bearing capacity is governed by the rupture of the FRP reinforcement. Over-reinforced failure, on the other hand, occurs in members with a higher reinforcement ratio, where

the compressive strain of concrete reaches its ultimate limit, while the strain of FRP reinforcement remains within the elastic range. In this case, the load-bearing capacity is controlled by concrete crushing. According to ACI 440.1R-15 (2015), both failure modes are acceptable for flexural failure of FRP-reinforced concrete members, allowing them to be designed as either under-reinforced or over-reinforced.

Due to the significantly lower elastic modulus of GFRP bars compared to steel rebars, the test on an under-reinforced GFRP-reinforced concrete arch revealed that the stress developed in the GFRP longitudinal bars was insufficient to provide the necessary tensile force upon concrete cracking. Under the displacement-controlled loading scheme, the arch achieved equilibrium at a relatively low load during the formation of primary flexural cracks, resulting in sudden drops in the load-deflection curve and degradation of the service performance (e.g., deflection, crack width). As the applied deflection increased, sectional deformation grew, and the strain and stress in the GFRP bars at the cracked sections continued to increase, partially restoring the load-bearing capacity of the arch.

Figure 3.10 presents a parametric analysis investigating the effect of longitudinal reinforcement ratios on the moment-curvature response of sections without stirrups, employing the layer method for analysis. The moment-to-axial force ratio was assumed to be constant during curvature development, consistent with the value obtained for the critical section (the arch crown in this case).

In this study, the reinforcement ratio of the arch was varied by adjusting the diameter of the FRP bars, while keeping section dimensions and concrete cover thickness constant. The upper and lower reinforcements were arranged symmetrically, and the

reinforcement configuration for all groups matched the experimental setup (Figure 3.2). In Figure 3.10, each specimen is identified by a code: the letter “D” followed by the diameter of the FRP bar (e.g., D6 represents the configuration used in the preliminary test). The results indicate that the reinforcement ratio has a minimal impact on the cracking load and initial stiffness before cracking. However, an increase in reinforcement ratio significantly improves both post-cracking stiffness and load-bearing capacity. For higher reinforcement ratios, such as D8, D10, and D12, the moment increased monotonically with increasing curvature. Conversely, specimens with lower reinforcement (D4 and D6) exhibited a peak in the moment-curvature curve near the cracking moment. Greater section deformation is needed in cases with a lower reinforcement ratio to restore the moment-carrying capacity after this peak.

These observations suggest that increasing the reinforcement ratio can effectively prevent reductions in moment/load following cracking. Therefore, a series of over-reinforced GFRP-reinforced concrete arch specimens were prepared and conducted in the next step to verify the assumption and investigate the performance of over-reinforced members, with details presented in Chapter 5.

### **3.5.3 Predictive model**

The simplified theoretical analysis method employed in this chapter is the force method. This method has been widely adopted in analyzing indeterminate elements and structures. This method analyses the unknown support reactions of the indeterminate members based on the un-deformed shape and uniform elastic stiffness along the longitudinal axis. However, the divergence between the initial assumption and the deformed shape of the arch axis during the loading process, as well as the changed and

uneven stiffness response along the arch axis, affects the accuracy of the theoretical method. In the test setup of this chapter, neglecting the effect of geometric nonlinearity on support reactions and the actual location of the critical section leads to an overestimation of the load-bearing capacity of the arch specimen. To achieve more accurate results, solutions should consider the deformed arch axis and the non-uniform distributed stiffness along the arch axis at each loading step.

To improve predictive accuracy, it is essential to develop numerical simulations or theoretical models that account for geometric and material nonlinearity throughout the loading process. Theoretical studies on arch structures generally fall into two categories: the deflection method and FEA. Chapter 6 introduces a theoretical model based on an enhanced deflection method, offering a unified approach for addressing both small and large curvature problems for one-dimensional components. The deflection method is useful for understanding the behavior of FRP-reinforced slender arches, however, it only accounts for uniaxial stress/strain, considering the interaction between axial forces and bending moments while ignoring shear contributions.

While the deflection method is efficient for analyzing simple uniaxial or biaxial loading cases, FEA is more suitable for complex three-dimensional analyses involving intricate load interactions and boundary conditions. In Chapter 7, a three-dimensional finite element model of FRP-reinforced concrete arches was developed using ABAQUS, capable of accurately capturing failure mechanisms under combined actions of axial load, shear load, and bending moment (axial-shear-flexural interaction). This model revealed the structural mechanism and the influence of several key parameters, as detailed in Chapter 7.

### 3.6 CONCLUSIONS

This chapter presents a preliminary investigation through a combined experimental and analytical study, investigating the structural behavior of an FRP-reinforced SSC arch. The experiment confirms that FRP-reinforced concrete arches, characterized by their excellent corrosion resistance, are structurally sound and offer a promising alternative to traditional arch structures. This research offers practical guidance and a theoretical foundation for the design and application of FRP-reinforced concrete arches while identifying challenges and future directions for advancing concrete arch structures utilizing FRP bars as an alternative to traditional steel reinforcement. The key conclusions and recommendations of this chapter are summarized as follows:

1. The quasi-static loading test and theoretical analyses confirm the feasibility of FRP-reinforced concrete arch structures as a novel structural form. Owing to their exceptional corrosion resistance, the structures emerge as a promising alternative to traditional steel-reinforced concrete arches.
2. Experimental observations indicate that due to the anisotropic nature of FRP composites, the inclusion of FRP stirrups, particularly with fibers oriented in the hoop direction, may somewhat weaken the normal section in terms of stiffness response and load-bearing capacity. The results of section analysis validate that both the stiffness response and load-bearing capacity of stirrup-reinforced sections are adversely affected. Thus, it is recommended to innovate the design of FRP transverse reinforcement to enhance their performance in shallow arch structures.
3. Given the lower elastic modulus of GFRP bars compared to steel, significant load drops may occur when major cracking appears in under-reinforced GFRP-

reinforced concrete arches with relatively small reinforcement ratios. This behavior arises as GFRP bars cannot immediately assume the load released by the reduction in tensile stress of concrete. The results of the section analysis suggest that increasing the reinforcement ratio effectively addresses this issue. Therefore, it is advised to consider over-reinforcement in the design of such arches to meet serviceability requirements.

4. While the presented analysis method offers insights into the behavior of the arch and estimates its load capacity, it is semi-empirical in nature, and the absence of comprehensive consideration of structural geometric nonlinearity may lead to an overestimation of the structural capacity. To fully understand and accurately simulate the behavior of FRP-reinforced concrete arches, there is a need to develop more precise numerical simulations or theoretical models for accurately predicting the structural behavior of FRP arch structures, where effects of geometric and material nonlinearity can be taken into account.

### 3.7 REFERENCES

ACI 440.1R-15. (2015) *Guide for the Design and Construction of Structural Concrete Reinforced with Fiber-Reinforced Polymer Bars*. Farmington Hills, Michigan: American Concrete Institute (ACI), USA.

ACI 440.3R-12. (2012) *Guide Test Methods for Fiber-Reinforced Polymers (FRPs) for Reinforcing or Strengthening Concrete Structures*. Farmington Hills, Michigan: American Concrete Institute (ACI), USA.

ACI 440.11R-22. (2022) *Building Code Requirements for Structural Concrete Reinforced with Glass Fiber-Reinforced Polymer (GFRP) Bars*. Farmington Hills, Michigan: American Concrete Institute (ACI), USA.

AS 3600-09. (2009) *Concrete Structures*. Sydney: SAI Global Limited, Australia.

ASTM C192/C192M-19. (2019) *Standard Practice for Making and Curing Concrete Test Specimens in the Laboratory*. West Conshohocken, PA: American Society for Testing and Materials (ASTM), USA.

Collins MP and Mitchell D. (1997) *Prestressed Concrete Structures*, Toronto and Montreal, Canada: Response Publications.

Deitz DH, Harik IE and Gesund H. (2003) Physical properties of glass fiber reinforced polymer rebars in compression. *Journal of Composites for Construction* 7(4): 363-366.

GB 50010. (2015) *Standard for Design of Concrete Structures*. Ministry of Housing and Urban-Rural Development of PRC, Beijing, China.

- Hao ZH. (2024) *Durability of FRP Reinforced Seawater Seasand Concrete Beams and FRP-strengthened Reinforced Concrete Beams*. Hong Kong, China: The Hong Kong Polytechnic University.
- Jiang T and Teng JG. (2012) Theoretical model for slender FRP-confined circular RC columns. *Construction and Building Materials* 32: 66-76.
- Maranan GB, Manalo AC, Benmokrane B, et al. (2016) Behavior of concentrically loaded geopolymer-concrete circular columns reinforced longitudinally and transversely with GFRP bars. *Engineering Structures* 117: 422-436.
- Spagnuolo S, Meda A and Rinaldi Z. (2014) Fiber glass reinforcement in tunneling applications. *Proceedings of the 10th Fib International PhD Symposium in Civil Engineering*. 85-90.
- Tang ZX, Zhou YZ, Feng J, et al. (2021) Concrete protective arches reinforced with BFRP bars: Construction and quasi-static structural performances. *Tunnelling and Underground Space Technology* 108: 103731.
- Teng JG, Yu T, Dai JG, et al. (2011) The current status and opportunities of FRP application in new structures. *Proceedings of 7th National Academic Conference on FRP Applications in Construction Engineering*. Hangzhou, China.
- Vecchio FJ and Collins MP. (1986) The modified compression-field theory for reinforced concrete elements subjected to shear. *ACI Journal* 83(2): 219-231.

Table 3.1 Material properties

Material	Strength		Elastic modulus		Strain corresponds to the strength	
	Average value (MPa)	Coefficient of variation (COV)	Average value (MPa)	Coefficient of variation (COV)	Average value (MPa)	Coefficient of variation (COV)
FRP longitudinal bar	1011.4	0.017	49.83	0.012	2.03%	0.012
concrete	45.2	0.015	29.80	0.043	0.24%	0.088

Table 3.2 Mix proportions

Water/Cement	Water/Binder	Sand ratio	Unit mass(kg/m <sup>3</sup> )						
			Cement	Fly ash	Coarse aggregate	Fine aggregate	Water	Water reducer	Total
0.67	0.48	0.40	290	110	1070	717	193	0.565	2381

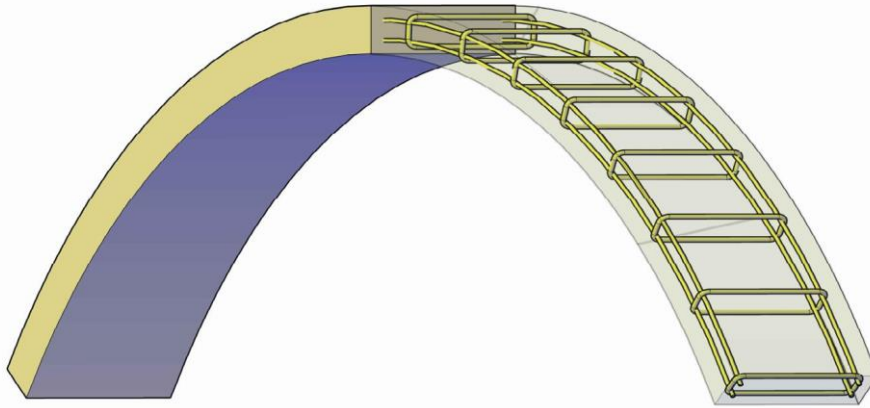
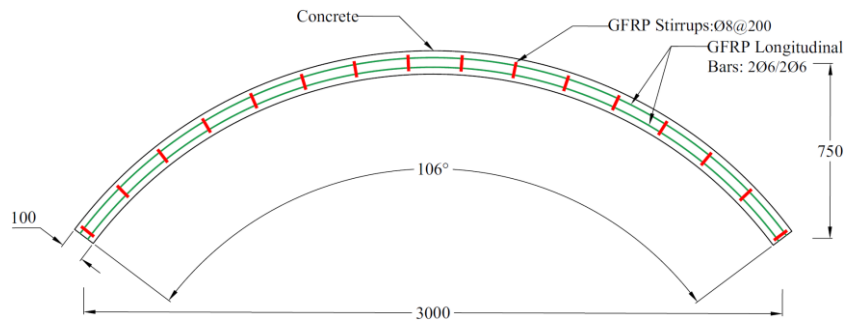


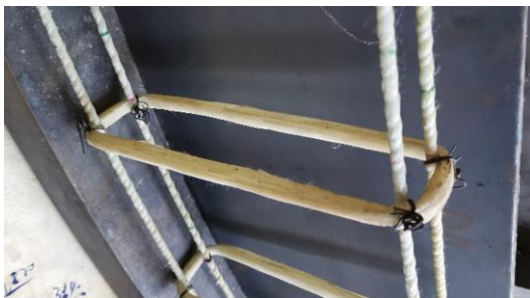
Figure 3.1 Sketch of arch specimen



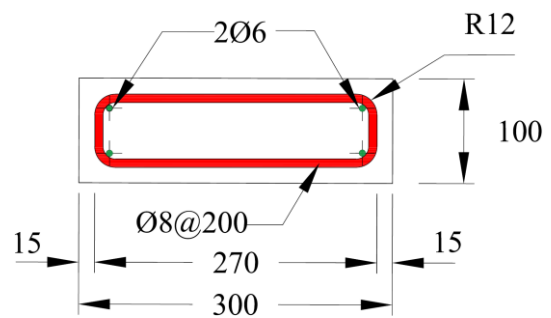
(a) Photo of front view



(b) Sketch of front view

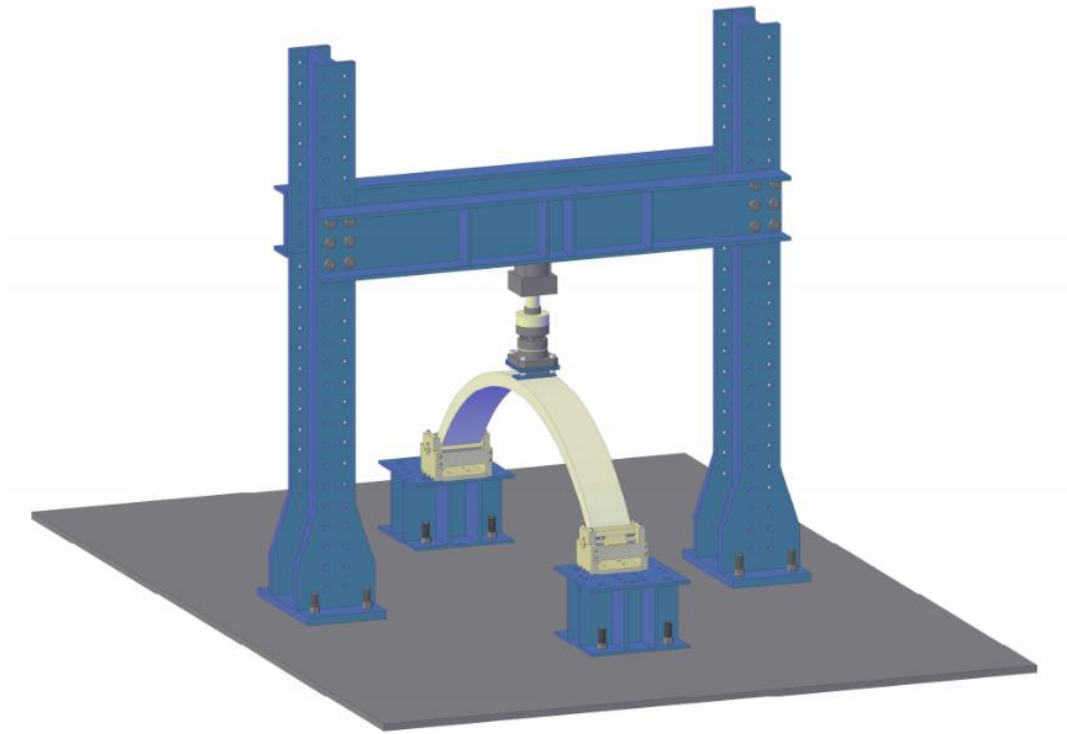


(c) Photo of sectional view



(d) Sketch of sectional view

Figure 3.2 Details of arch specimen (Unit: mm)



(a) Sketch



(b) Photo

Figure 3.3 Test setup of arch test

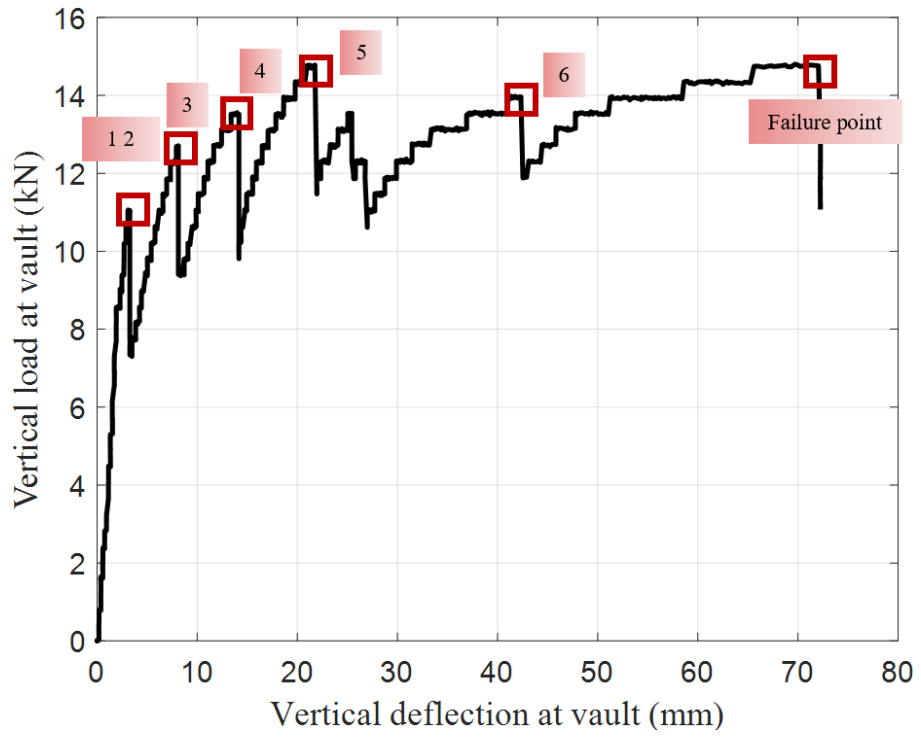
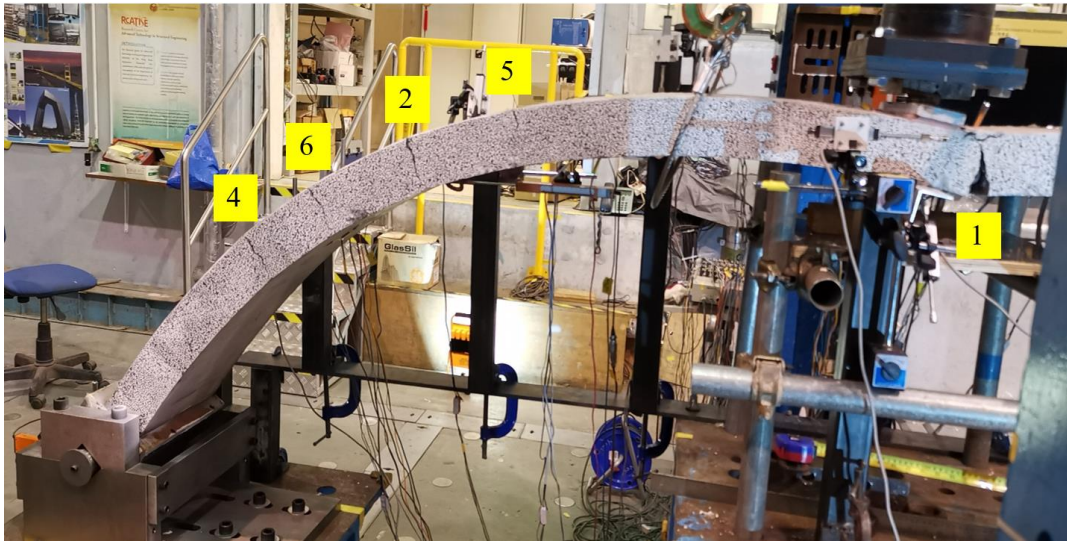


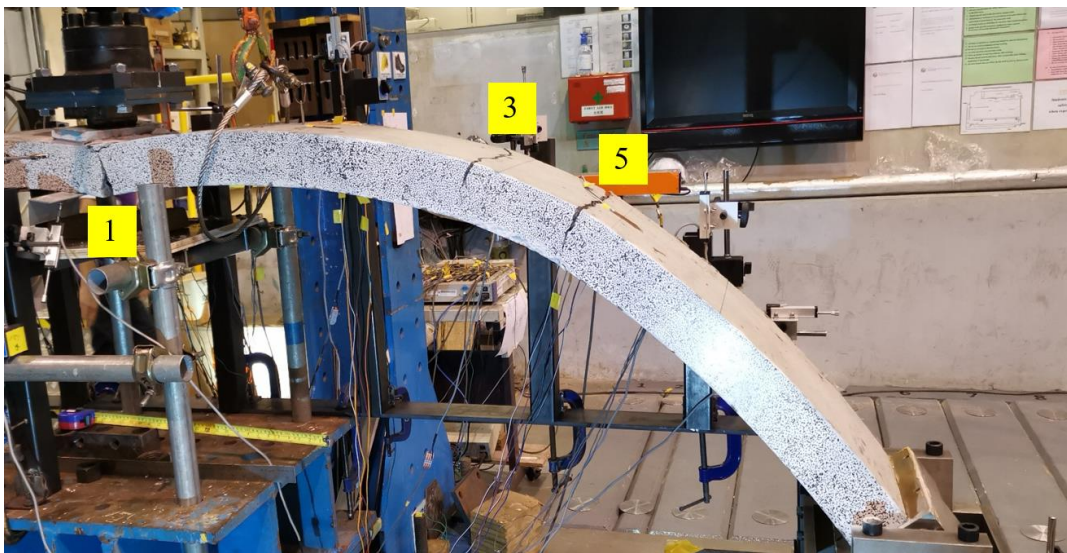
Figure 3.4 Load-deflection curve



Figure 3.5 Fracture of concrete near the arch crown at the failure point



(a) Distribution of cracks of the left-half specimen



(b) Distribution of cracks of the right-half specimen

Figure 3.6 Specimen after test

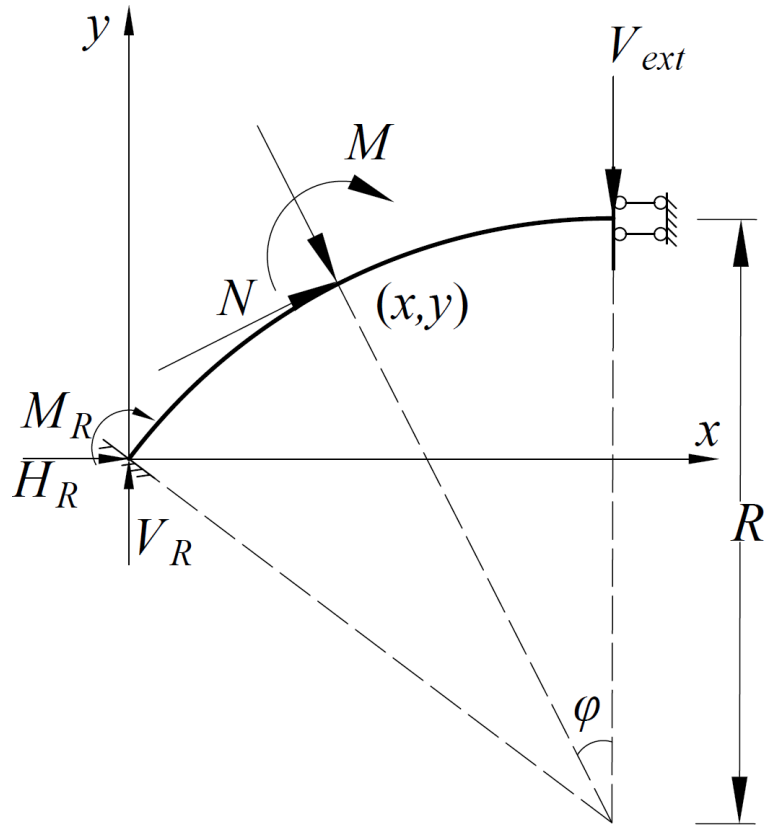


Figure 3.7 Diagram of analysis

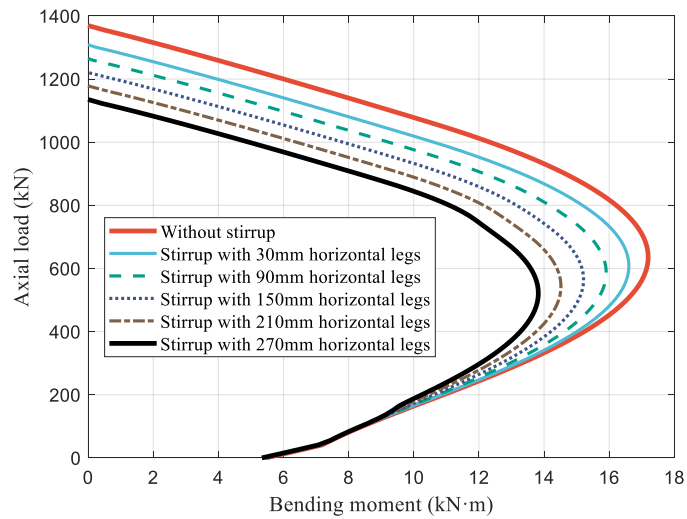


Figure 3.8 The effect of stirrup's horizontal length on axial load-bending moment curve

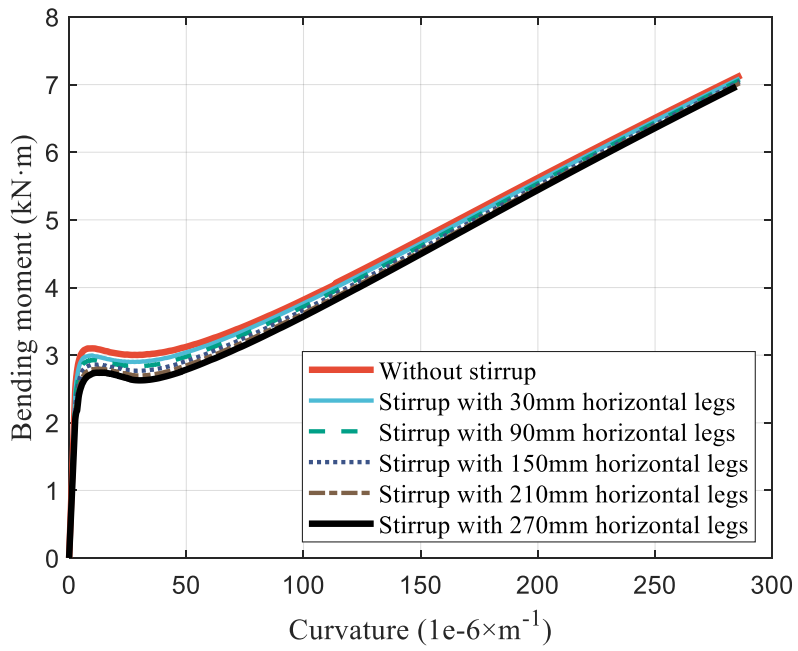


Figure 3.9 The effect of stirrup's horizontal length on bending moment-curvature curve

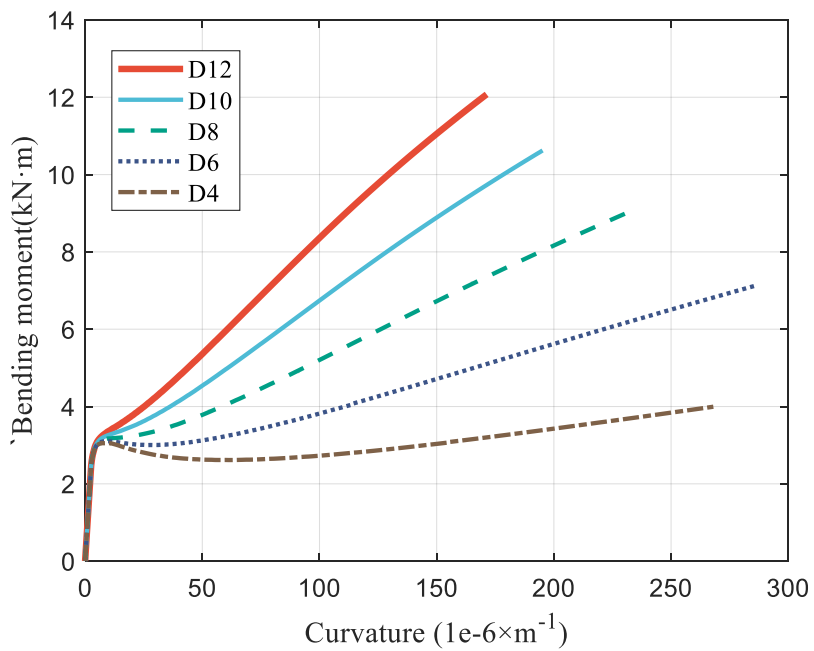


Figure 3.10 The effect of longitudinal reinforcement ratio on bending moment-curvature curve

## **CHAPTER 4**

### **NOVEL NARROW CLOSED FRP STIRRUPS FABRICATED VIA A FILAMENT WINDING PROCESS**

#### **4.1 INTRODUCTION**

Existing products of FRP stirrups suffer from various issues. On the one hand, as the elastic modulus of FRP perpendicular to fiber direction (e.g., 2 to 4 GPa) is notably lower than that of concrete, the transversely oriented FRP stirrups, including particularly their horizontal legs, may pose negative effects on the flexural stiffness/strength of RC members, especially for those with a shallow cross-section. Indeed, Chapter 3 showed that the shallow FRP-reinforced concrete arches often suffered from cracking or even structural failure at the locations of FRP stirrups which weakened the corresponding sections (Xia et al., 2023).

On the other hand, significant strength reduction in the corner regions: unlike ductile steel rebars that can be easily bent into various shapes of stirrups/spirals onsite, FRP stirrups (e.g., U-/C- shaped and rectangular/circular closed stirrups) are typically formed from straight pultruded FRP rebars during manufacturing, before complete curing of the polymeric resin matrix. This forming process generally leads to kinked

and slacked fibers at the corners of FRP stirrups, resulting in the loss of strength and stiffness in the bent regions (Said et al., 2016; Tobbi et al., 2014; El-Sayed et al., 2007; Ehsani et al., 1995; Maruyama et al., 1993; Nakamura and Higai, 1995; Shehata et al., 2000; Ahmed et al., 2010; Lee et al., 2014; Vint and Sheikh, 2015; Guadagnini et al., 2007). The bent regions of FRP stirrups, usually subjected to multi-axial stresses (e.g., longitudinal tension and transverse compression) in concrete structures, are therefore much more vulnerable and fragile than the straight regions of the stirrups. (Ehsani et al., 1995; Maruyama et al., 1993; Nakamura and Higai, 1995; Shehata et al., 2000; Ahmed et al., 2010; Lee et al., 2014; Vint and Sheikh, 2015; Guadagnini et al., 2007). Furthermore, existing closed FRP stirrups (e.g., rectangular stirrups) are generally not actually “closed” but include an overlapping region which might open under forces due to slipping between FRP and concrete (Tobbi et al., 2014; Dong et al., 2018; Maranan et al., 2018).

To address the issues of traditionally pultruded FRP stirrups, recent research (Spadea et al., 2017b; Yuan et al., 2022) has explored the fabrication of FRP stirrups via a filament winding process. Such FRP stirrups, cut from specifically made filament-wound FRP tubes to the intended width, are physically closed and thus would not open before FRP rupture (i.e., not suffering from the FRP-concrete slipping failure). Furthermore, the filament winding process, involving winding resin-saturated, continuous fiber strands over a rotating mandrel layer by layer, effectively mitigates the issues of fiber kinking and slacking (Mantell and Springer, 1994). The relevant existing experimental studies (Spadea et al., 2017a; Yuan et al., 2022) have demonstrated that compared with pultruded FRP stirrups, the filament-wound stirrups effectively alleviate

strength reduction in the corner regions, thereby postponing material failure in these regions due to multiaxial stress concentrations.

The existing studies on filament-wound FRP stirrups (Dong et al., 2018; Yuan et al., 2022), however, are generally limited to stirrups with a width close to the cross-sectional width of the structural members. Unlike traditional FRP stirrups, filament-wound FRP stirrups exhibit distinct geometric properties, characterized by a width that is consistently greater than the thickness. This configuration reduces the cross-sectional area occupied by the stirrups, thereby minimizing their adverse effects on shallow cross-sections.

To further enhance these benefits, this chapter presents the concept of a novel form of narrow closed FRP stirrups fabricated via a filament winding process. The concept and fabrication process of the novel stirrups are first explained, followed by a series of mechanical tests on the stirrups and a series of bending tests on RC beams reinforced by such stirrups which demonstrate the advantages of the novel stirrups.

## **4.2 NOVEL NARROW CLOSED FRP STIRRUPS**

The novel form of FRP stirrups may be considered a variation of existing filament-wound FRP stirrups cut from specifically fabricated FRP tubes. An important novel feature of the new FRP stirrups is their special shape: each stirrup has a narrow cross-section consisting of two vertical legs connected by rounded end portions, devoid of conventional horizontal legs (Figure 4.1). The horizontal legs are purposely removed to minimize the reduction of concrete area and the resulting local weakening of section capacity, noting that the vertical legs are the main components contributing to the shear capacity of an RC member (Nilson and Darwin, 1997). Notably, the stress

concentrations at the corners of conventional stirrups, especially those induced by bending of the horizontal legs, may be significantly reduced in the novel stirrups. Furthermore, the novel FRP stirrups have all the advantages of other filament-wound stirrups, and they do not suffer from fiber kinking and slacking or premature opening due to slipping.

Another important feature of the novel FRP stirrups is that their surfaces are specially treated for improved bonding to concrete. Filament-wound products typically have a smooth surface due to the self-leveling of resin before curing; this is unfavorable to the bond between FRP stirrups and concrete, and may compromise the reinforcing effect of the stirrups (Ali et al., 2019; Fam and Rizkalla, 2002). Two surface treatment methods are proposed herein, including rib-forming and sand-coating. For the former, custom-designed ribs can be formed during the filament winding process in one go through proper program coding of the winding machine, allowing opportunities for optimizing the configuration of ribs for the best performance. Sand-coating of filament-wound tubes is similar to that for pultruded FRP bars, involving applying a mixture of sand and resin on the surfaces of FRP tubes.

The shape of the novel stirrups allows them to each house a pair of longitudinal rebars, one at the top and the other at the bottom, forming a reinforcing unit which may be preassembled in a factory to accelerate onsite construction. Such narrow stirrups may be used alone as shear reinforcement, or used together with conventional wide stirrups at discrete locations especially when the torsional capacity of the RC members is a concern. Alternatively, similar to conventional single-legged stirrups, the novel stirrups may be combined with wide external stirrups to form a nested configuration for large

RC members. Needless to say, the novel stirrups are highly suitable for use in congested reinforcement areas and/or narrow/confined spaces as effective shear reinforcement while minimizing the effect on concrete compaction.

### **4.3 LABORATORY DEMONSTRATION OF FABRICATION**

To demonstrate the fabrication process of the novel stirrups, samples of the stirrups were fabricated at The Hong Kong Polytechnic University. These samples were then used for tensile tests of the stirrups and bending tests of RC beams incorporating the stirrups to demonstrate their mechanical behavior.

In fabricating the samples, the winding process was carried out using a winding machine 4x-23 from X-Winder Co. (Figure 4.1). A specially designed mandrel shaping the inner section of the FRP tube was prepared and was then clamped on two discs which were fixed to the rotation shaft of the winding machine. The samples had a radius of 10 mm at their two rounded end portions and an average thickness of 2.24 mm, leading to a radius-to-thickness ratio comfortably over three, the minimum ratio specified for FRP stirrups in ACI 440.1R-15 (2015).

Continuous glass fibers and epoxy resin were used to fabricate the stirrups. The fabrication process involved impregnating a bundle of glass-fiber filaments with epoxy resin in a resin tank, and then winding the impregnated filaments around the rotating mandrel with the reciprocating spray head. The winding angle of the fibers was around  $89^\circ$  with respect to the central axis of the mandrel, and the volume of fibers used was  $181.7 \text{ mm}^3$  per unit length of the FRP tube. The FRP tubes were cured at room temperature as per the guidelines by the resin supplier. Afterwards, the FRP tubes were removed from the mold and cut into stirrups with a predetermined width of 10 mm.

Three distinct types of stirrups, differentiated by their surface profiles (i.e., smooth, ribbed, and sand-coated surfaces), were fabricated in this study (see Figure 4.1). The stirrups with a smooth surface did not undergo any additional surface treatments Figure 4.1(a). For the ribbed stirrups [Figure 4.1(b)], the ribs were formed by adjusting the shaft speed of the mandrel and the movement speed of the spray head at the end of the winding process, achieving two extra loosely-spaced fiber layers with a winding angle of  $45^\circ$ . For the sand-coated stirrups, river sand with a size ranging from 300 to 600  $\mu\text{m}$ , was mixed with epoxy resin and then applied to the outer surfaces of the stirrups [Figure 4.1(c)].

It should be noted that the internal surfaces of all stirrups fabricated in this study were purposely left smooth and untreated to facilitate the installation of strain gauges for mechanical tests, but the surface treatment methods proposed herein may be applied to both the outer and inner surfaces of the stirrups for further improved bonding when needed.

#### **4.4 TENSILE TESTS**

Tensile tests on five flat coupons cut from a flat side of the filament-wound FRP tubes were conducted as per ASTM D3039/D3039M (2017) to determine the mechanical properties of the straight portions of the novel stirrups. The flat coupons [Figure 4.2(a)], each having a width of 15 mm, were protected by aluminium tabs of the same width at their two ends, and their other dimensions are illustrated in Figure 4.2(a). It should be noted that the overall length of the coupons (120 mm) was shorter than that specified by ASTM D3039/D3039M (2017) (150 mm) due to the limited sectional height of the filament-wound tube, but this is believed to cause little difference in the measured

results according to existing studies (e.g., Saribiyik and Çağlar, 2002). As expected, the tested coupons all experienced sudden and brittle failure by fiber rupture, characterized also by delamination of ruptured fibers from the epoxy resin. The average tensile strength, elastic modulus and ultimate strain obtained from the flat coupon tests are 712.0 MPa, 41.1 GPa and 1.75%, respectively (Table 4.1).

Moreover, tensile tests were conducted as per ACI 440.3R-12 (2012) on five samples of the whole closed stirrup to determine the strength in the rounded ends (i.e., bent regions) [Figure 4.2(b)]. The failure of the test samples was characterized by the fracture of fibers at the junction between the straight and curved portions, where the strip was subjected to multiaxial stresses, as shown in Figure 4.2(b). The average tensile strength obtained from these tests was 449.4 MPa. It should be noted that this strength is significantly higher (by over 30%) than the estimated strength (i.e., 343.4 MPa) of bent regions of FRP stirrups  $f_{frp,b}$  calculated by the following equation provided by ACI 440.1R-15 (2015):

$$\frac{f_{frp,b}}{f_{frp,t}} = 0.092 \frac{R_s}{d_{fe}} + 0.3 \leq 1.0 \quad (4.1)$$

where  $f_{frp,t}$  represents the tensile strength on the straight portion,  $R_s$  denotes the inner bend radius of the bent portion. The nominal diameter  $d_{fe}$  is suggested to be calculated as  $d_{fe} = 2 \sqrt{\frac{w_f \cdot t_f}{\pi}}$ , where  $w_f$  and  $t_f$  are the width and thickness of the FRP strip for rectangular sections (Lee et al., 2016). Noting that Eq. (4.1) was proposed based on the test data of pultruded FRP stirrups, it may be concluded that the filament-wound stirrups,

which do not suffer from fiber kinking and slacking, are superior in terms of strength of bent regions.

## **4.5 BENDING TESTS**

### **4.5.1 Specimen details**

To demonstrate the effectiveness of the novel FRP stirrups as shear reinforcement in RC beams, two RC beam specimens were prepared and tested under bending. Both specimens had a total length of 1500 mm and sectional dimensions of 150 mm × 200 mm with an effective sectional depth of 165 mm. To make full use of the two specimens, they were each segmented along the length into two parts with different types of shear reinforcement, leading to four distinct shear spans: those with smooth stirrups (SM), ribbed stirrups (RB), sand-coated stirrups (SC), and without stirrups (WS), respectively (Figure 4.3). Except for WS, all the other shear spans had the same transverse reinforcement ratio of 0.445%, with the spacing of stirrups being 100 mm. The flexural capacity of the beam specimens was designed to be larger than their shear capacity according to ACI 440.1-15 (2015), by placing three steel bars (two 10-mm bars and one 12-mm bar) close to the bottom and two 10-mm steel bars close to the top of the cross-section, leading to a longitudinal reinforcement ratio of 1.09%. The steel bars had a yield stress of 578.4 MPa and a tensile strength of 641.0 MPa based on tensile tests.

### **4.5.2 Test setup and instrumentation**

Each specimen was designed to undergo two loading tests, on its two distinct shear spans, respectively. In each loading test, half of the specimen was strengthened with metal strips clamped to it by prestressed screws [Figure 4.4(a)], while the other half was used as the test span. The tests were labelled according to the FRP stirrups in the test span (e.g., WS, SM, SC). The test span RB was tested twice, as in the first test (RB-1) the specimen experienced unexpected flexural failure due to the significantly higher shear capacity than that predicted by ACI 440.1-15 (2015); the specimen (for tests WS and RB) was then flexurally strengthened with two additional steel plates at the pure

bending region and retested (i.e., RB-2) to fail in shear. To avoid flexural failure, the other specimen (for tests SM and SB), which was tested afterwards, was also flexurally strengthened with two steel plates before testing [Figure 4.4(b)]. Details of the five loading tests are summarized in Table 4.2. It should be noted that the concrete strength was slightly different for the tests conducted at different time due to the different ages of concrete.

Figure 4.5 shows the test setup. The specimen was simply supported over a span of 1,200 mm and was subjected to two-point loading with a loading rate of 0.8 kN/min. After each load increment of 10 kN, the test was paused for observing and marking the crack path. Two Linear Variable Differential Transducers (LVDTs) were situated at the two loading points with an interval of 340 mm, respectively, while another two LVDTs were placed on the top surface at the two supports, respectively. Furthermore, two strain gauges with a gauge length of 10 mm were symmetrically attached at the middle of the inner surfaces of each critical stirrup to monitor the strain development.

#### **4.5.3 Test results and discussions**

The specimens experienced shear failure in all the tests except RB-1 in which flexural failure characterized by extensive flexural cracking and concrete crushing occurred; the results of RB-1 are thus excluded in the following discussions unless necessary. Among the other four tests, shear-tension failure characterized by a major diagonal crack occurred in WS for the shear span without stirrups, while shear-compression failure occurred in SC and SM due to the existence of stirrups; the crack development of RB-2 was generally similar to SC and SM, but the failure of this test was controlled by the rupture of FRP stirrups associated with an abrupt load drop. Figure 4.6 shows the crack

development with load in WS, SC, SM, RB-1 and RB-2 demonstrating the effects of stirrups in constraining the propagation of cracks.

The key test results are summarized in Table 4.2, while the load-deflection curves are shown in Figure 4.7 where the deflection refers to the average value at the two loading points. It is evident that the novel FRP stirrups contributed significantly to the shear capacity of the specimens, with the shear capacity of SM (i.e., 60.63 kN) being around two times that of WS (i.e., 30.45 kN). It is also evident that the two proposed surface treatment methods are effective in enhancing the shear contribution of FRP stirrups: the shear capacities of SC (i.e., 68.28 kN) and RB-2 (i.e., 65.38 kN) are 12.62% and 7.83% higher than that of SM, respectively, although the three had the same transverse reinforcement ratio. Furthermore, Figure 4.7 shows that the load-deflection curve of WS is characterized by an approximately linear ascending portion followed by a descending portion, while the stirrup-reinforced specimens exhibited a nonlinear curve with a gradually reducing stiffness after the load exceeded around 50 kN.

The effect of the novel stirrups on improving the shear performance at the serviceability limit state is evaluated by comparing the load taken by the specimens at crack widths of 0.5 mm and 0.7 mm, the allowable cracks width specified by ACI 440.1R-15 and CSA S6-14 (ACI 440.1R-15, 2015; CSA S6-14, 2014) for aggressive environments and other scenarios, respectively. At the crack width of 0.5 mm, the load taken by SM, SC and RB-1 are 1.35, 1.87, and 1.71 times greater than that of WS, respectively (Table 4.2), suggesting that: (1) the novel stirrups effectively control shear cracks and enhance the shear capacity at the serviceability limit state; and (2) the two proposed surface treatment methods are both effective in further improving the contributions of the

stirrups by improving the force transfer between the stirrups and the surrounding concrete, thereby controlling the cracks. Similar observations can be made when comparing the load taken by the specimens at a crack width of 0.7 mm (see Table 4.2).

Figure 4.8 shows the development of strains on the FRP stirrups for SM, SC, RB-1 and RB-2. The strains in all stirrups remained minimal in the initial stage of loading before the emergence of shear cracks. Afterwards, the stirrups were activated one by one when one or more shear cracks started to intersect with them; this was then followed by continuous development in the strain of these stirrups with the widening of shear cracks (Figure 4.6). It is not surprising to note that the location of stirrup with the highest strain was generally consistent with the location of the major shear crack (see Figures 4.6 and 4.8). Furthermore, it was found that the maximum recorded strains (e.g., 4680  $\mu\epsilon$ , 5056  $\mu\epsilon$ , 5892  $\mu\epsilon$  and 8534  $\mu\epsilon$  for SM, SC, RB-1 and RB-2, respectively) are significantly higher than 4,000  $\mu\epsilon$ , the strain limit recommended by ACI 440.1R-15 and CSA S806-12 for calculating the shear contribution of FRP stirrups. It was also found that the stirrups with surface treatments generally experienced more uniform stress distributions and thus greater load capacities.

#### **4.5.4 Comparison with design equations**

The test results are compared with the design equations provided in ACI 440.1R-15 (2015), ACI 440.11R-22 (2022), CSA S806-12 (2012) and CSA S6-14 (2014) for the shear capacity of FRP-reinforced concrete beams. When using the design equations, the mean values of the mechanical properties obtained from the material tests were used, and the strength reduction factors for design use were all set to be 1.0. The design equations in all the four design documents are based on the superposition principle,

which posits that the total shear capacity ( $V_{Sta}$ ) of a structural element is equal to the sum of the shear resistance provided by concrete ( $V_c$ ) and that offered by the shear reinforcement ( $V_{fs}$ ), while the contribution of FRP stirrups is calculated by the equation proposed by Razaqpur and Spadea (2015):

$$V_{fs} = \frac{A_{fs} f_{frp,sa} d_v [\cot(\psi) + \cos(\zeta)] \sin(\zeta)}{s} \quad (4.2)$$

where  $A_{fs}$  represents the total cross-sectional area of the transversal FRP stirrups;  $f_{frp,sa}$  is the allowable stress in the stirrups;  $d_v$  is the effective height of the cross-section;  $s$  is the spacing of the stirrups;  $\psi$  is the angle of the critical diagonal crack relative to the longitudinal axis;  $\zeta$  is the orientation of fibers with respect to the longitudinal axis, which is  $90^\circ$  in this study. Specifically, ACI 440.1R-15 and ACI 440.11R-22 specify that  $\psi$  is taken as  $45^\circ$ , while CSA S806-12 and CSA S6-14 recommend two different methods based on the modified compression field theory (MCFT) to obtain this angle (Hoult et al., 2008; Razaqpur and Spadea, 2015), respectively. The allowable stress of FRP stirrups is set to be that corresponding to a strain of 0.004 for ACI 440.1R-15 and CSA S806-12, and 0.005 for ACI 440.11R-22 and CSA S6-14, or the strength of the bent portion of the stirrups, whichever is lower.

Table 4.3 summarizes the comparison between the test results and the predictions of the design equations. It is evident that the test results are higher than the predictions of all the design equations for RC beams reinforced with the novel FRP stirrups, suggesting that these design equations can be used for conservative design of such beams. As these design equations are proposed for conventional pultruded FRP stirrups, the comparison summarized in Table 4.3 also demonstrates that the performance of the

novel stirrups as shear reinforcement are at least as good as, if not better than their conventional counterparts.

## **4.6 CONCLUSIONS**

This chapter has presented the concept of a novel form of narrow closed FRP stirrups fabricated via a filament winding process, and has demonstrated the feasibility and advantages of the novel FRP stirrups through laboratory demonstration of their fabrication process as well as mechanical tests on the stirrups and RC beams reinforced by such stirrups. The main conclusions drawn from this chapter are summarized below:

1. The novel FRP stirrups have many advantages over existing FRP stirrups including their reduced cross-sectional area, minimal adverse effects on the concrete section as well as being impervious to fiber kinking/slacking at the bent regions or premature opening due to slipping.
2. The strength of bent regions of the novel FRP stirrups substantially exceeds that predicted by ACI 440.1R-15 for bent FRP rods, due largely to the filament winding process.
3. The novel FRP stirrups can effectively control the crack development and improve the shear capacity of RC beams. The existing design equations can be used for conservative design of RC beams reinforced with the novel FRP stirrups.
4. The proposed surface treatment methods (i.e., rib-forming and sand-coating) of the novel stirrups significantly improve their bond strength with concrete and thus their performance of shear reinforcement.

## 4.7 REFERENCES

ACI 440.1R-15. (2015) *Guide for the Design and Construction of Structural Concrete Reinforced with Fiber-Reinforced Polymer Bars*. Farmington Hills, Michigan: American Concrete Institute (ACI), USA.

ACI 440.3R-12. (2012) *Guide Test Methods for Fiber-Reinforced Polymers (FRPs) for Reinforcing or Strengthening Concrete Structures*. Farmington Hills, Michigan: American Concrete Institute (ACI), USA.

ACI 440.11R-22. (2022) *Building Code Requirements for Structural Concrete Reinforced with Glass Fiber-Reinforced Polymer (GFRP) Bars*. Farmington Hills, Michigan: American Concrete Institute (ACI), USA.

Ahmed EA, El-Salakawy EF and Benmokrane B. (2010) Shear performance of RC bridge girders reinforced with carbon FRP stirrups. *Journal of Bridge Engineering* 15(1): 44-54.

Ali AM, Robillard D, Masmoudi R, et al. (2019) Experimental investigation of bond and tube thickness effect on the flexural behavior of concrete-filled FPR tube under lateral cyclic loading. *Journal of King Saud University-Engineering Sciences* 31(1): 32-41.

ASTM D3039/D3039M-17. (2017) *Standard Test Method for Tensile Properties of Polymer Matrix Composite Materials*. West Conshohocken, PA: American Society for Testing and Materials (ASTM), USA.

CSA S6-14. (2014) *Canadian Highway Bridge Design Code*. Toronto, Ontario:

Canadian Standards Association (CSA), Canada.

CSA S806-12. (2012) *Design and Construction of Building Components with Fiber Reinforced Polymers*. Toronto, Ontario: Canadian Standards Association (CSA), Canada.

Dong HL, Wang DY, Wang ZY, et al. (2018) Axial compressive behavior of square concrete columns reinforced with innovative closed-type winding GFRP stirrups. *Composite Structures* 192: 115-125.

Ehsani MR, Saadatmanesh H and Tao S. (1995) Bond of hooked glass fiber reinforced plastic (GFRP) reinforcing bars to concrete. *ACI Materials Journal* 92(4): 391-400.

El-Sayed AK, El-Salakawy E and Benmokrane B. (2007) Mechanical and structural characterization of new carbon FRP stirrups for concrete members. *Journal of Composites for Construction* 11(4): 352-362.

Fam AZ and Rizkalla SH. (2002) Flexural behavior of concrete-filled fiber-reinforced polymer circular tubes. *Journal of Composites for Construction* 6(2): 123-132.

Guadagnini M, Imjai T and Pilakoutas K. (2007) The performance of curved FRP reinforcement for concrete structures. *Proceedings of the Non-Metallic (FRP) Reinforcement for Concrete Structures, the 8th International Symposium on Non-Metallic (FRP) Reinforcement for Concrete Structures (FRPRCS-8)*. Patras, Greece, 16-18.

Hoult NA, Sherwood EG, Bentz EC, et al. (2008) Does the use of FRP reinforcement

- change the one-way shear behavior of reinforced concrete slabs? *Journal of Composites for Construction* 12(2): 125-133.
- Lee C, Ko M and Lee Y. (2014) Bend strength of complete closed-type carbon fiber-reinforced polymer stirrups with rectangular section. *Journal of Composites for Construction* 18(1): 04013022.
- Lee C, Lee S and Shin S. (2016) Shear capacity of RC beams with carbon fiber-reinforced polymer stirrups with rectangular section. *Journal of Composites for Construction* 20(4): 04015085.
- Mantell SC and Springer GS. (1994) Filament winding process models. *Composite Structures* 27(1-2): 141-147.
- Maranan GB, Manalo AC, Benmokrane B, et al. (2018) Shear behaviour of geopolymer-concrete beams transversely reinforced with continuous rectangular GFRP composite spirals. *Composite Structures* 187: 454-465.
- Maruyama T, Honma M and Okamura H. (1993) Experimental study on tensile strength of bent portion of FRP rods. *ACI Structural Journal* 138: 163-176.
- Nakamura H and Higai T. (1995) Evaluation of shear strength of concrete beams reinforced with FRP. *Doboku Gakkai Ronbunshu* 1995(508): 89-100.
- Nilson AH and Darwin D. (1997) *Design of Concrete Structures*: McGraw-Hill Education.
- Razaqpur AG and Spadea S. (2015) Shear strength of FRP reinforced concrete members with stirrups. *Journal of Composites for Construction* 19(1): 04014025.

- Said M, Adam MA, Mahmoud AA, et al. (2016) Experimental and analytical shear evaluation of concrete beams reinforced with glass fiber reinforced polymers bars. *Construction and Building Materials* 102: 574-591.
- Saribiyik M and Çağlar N. (2002) Numerical modelling of a short tensile coupon for glass fibre reinforced plastics. *Adadolu Univerisity Journal of Science and Technology* 3: 227-234.
- Shehata E, Morphy R and Rizkalla S. (2000) Fibre reinforced polymer shear reinforcement for concrete members: behaviour and design guidelines. *Canadian Journal of Civil Engineering* 27(5): 859-872.
- Spadea S, Orr J and Ivanova K. (2017a) Bend-strength of novel filament wound shear reinforcement. *Composite Structures* 176: 244-253.
- Spadea S, Orr J, Nanni A, et al. (2017b) Wound FRP Shear Reinforcement for Concrete Structures. *Journal of Composites for Construction* 21(5): 13.
- Tobbi H, Farghaly AS and Benmokrane B. (2014) Behavior of concentrically loaded fiber-reinforced polymer reinforced concrete columns with varying reinforcement types and ratios. *ACI Structural Journal* 111(2): 375-385.
- Vint L and Sheikh S. (2015) Investigation of bond properties of alternate anchorage schemes for glass fiber-reinforced polymer bars. *ACI Structural Journal* 112(1): 59-68.
- Xia ZY, Yu T and Jiang T. (2023) Behaviour of FRP-reinforced concrete arches behavior. *Proceedings of 11th International Conference on Fibre-Reinforced Polymer*

*(FRP) Composites in Civil Engineering*. Rio de Janeiro, Brazil: International Institute for FRP in Construction (IIFC), 1347-1354.

Yuan Y, Wang Z and Wang D. (2022) Shear behavior of concrete beams reinforced with closed-type winding glass fiber-reinforced polymer stirrups. *Advances in Structural Engineering* 25(12): 2577-2589.

Table 4.1 Test results of tensile tests

Material properties	Test method	Set of specimens					Average value
		1	2	3	4	5	
Tensile strength (MPa)		659.4	733.1	795.3	668.7	704.1	712.0
Elastic modulus (MPa)	ASTM D3039/D3039M	39948	41328	42751	39834	39568	41070
Ultimate strain (%)		1.65	1.77	1.86	1.68	1.78	1.75
Reduced tensile strength (MPa)	ACI 440.3R-12	440.4	470.7	452.0	460.0	424.0	449.4

Table 4.2 Test results of bending tests

Test	$f_{cu}$ (MPa)	$V_{Peak}$ (kN)	$\Delta_{Peak}$ (mm)	$V_{0.5}$ (kN)	$\epsilon_{0.5}$ ( $\mu\epsilon$ )	$V_{0.7}$ (kN)	$\epsilon_{0.7}$ ( $\mu\epsilon$ )	Failure mode
WS	40	30.45	3.73	23.37	-	25.22	-	ST
SM	50	60.63	10.41	31.47	995(2)	46.90	1821(2)	SC
SC	50	68.28	15.54	43.78	169(2)	51.89	1088(2)	SC
RB-1	40	56.36	10.95	40.00	305(2)	50.25	1226(4)	FL
RB-2	50	65.38	28.89	-	-	-	-	SC

Note:  $f_{cu}$  = compressive strength of concrete;  $V_{Peak}$  = shear capacity of specimen;  $\Delta_{Peak}$  = deflection at loading point corresponding to peak shear load;  $V_{0.5}$  and  $\epsilon_{0.5}$  = shear load and the maximum stirrup strain corresponding to 0.5 mm crack width;  $V_{0.7}$  and  $\epsilon_{0.7}$  = the same parameters at a 0.7 mm crack width; DT = diagonal tension failure; SC = shear-compression failure; FL = flexural failure.

Table 4.3 Comparison between test results and predictions

Test	ACI 440.1R-15				ACI 440.11R-22				CSA S806-12				CSA S6-14				
	$V_{Peak}$	$V_c$	$V_{fs}$	$V_{Sta}$	$V_{Peak}/V_{Sta}$												
SM	60.6				1.38				1.23				1.13				1.01
SC	68.3	22.4	21.5	43.9	1.56	22.4	26.9	49.3	1.39	40.5	13.1	53.6	1.27	38.4	21.4	59.8	1.14
RB-2	65.4				1.49				1.33				1.22				1.09

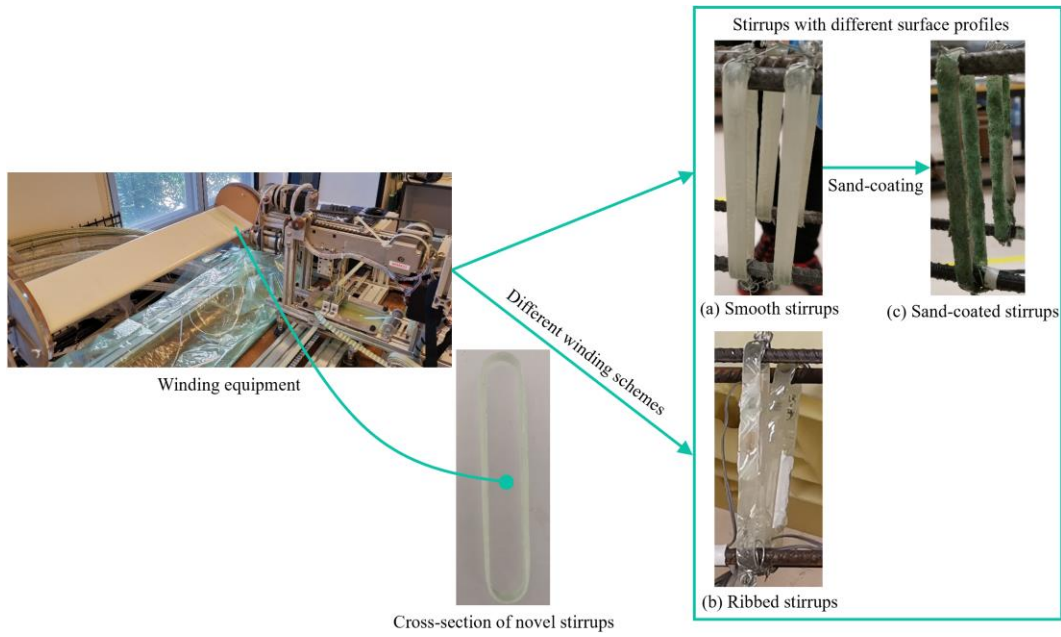
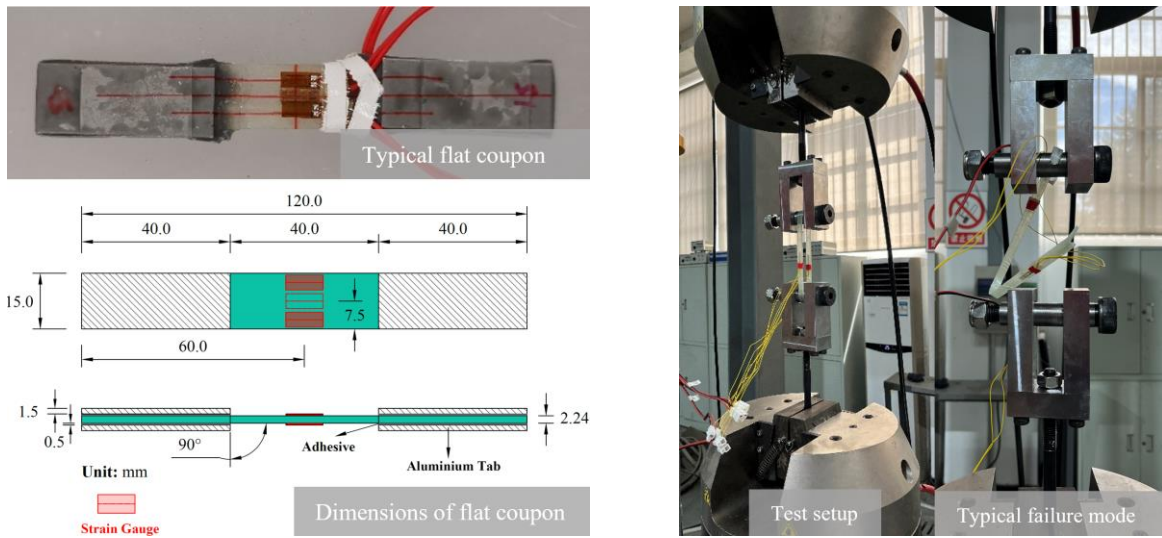


Figure 4.1 Novel filament-wound stirrups



(a) Tensile tests on straight portion

(b) Tensile tests on curved portion

Figure 4.2 Tensile test on novel stirrups

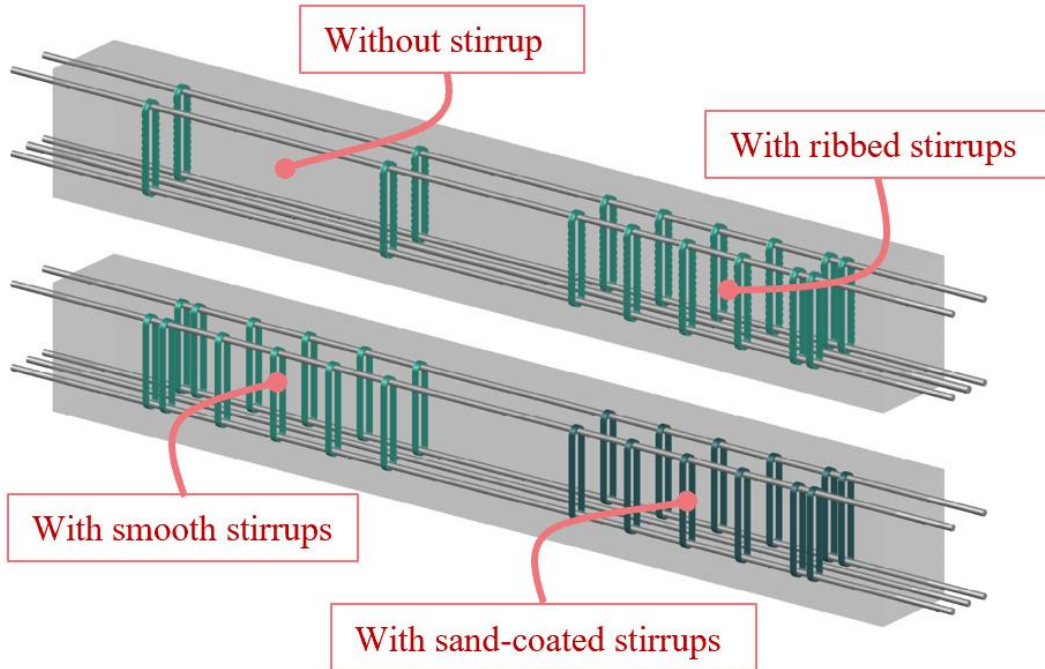
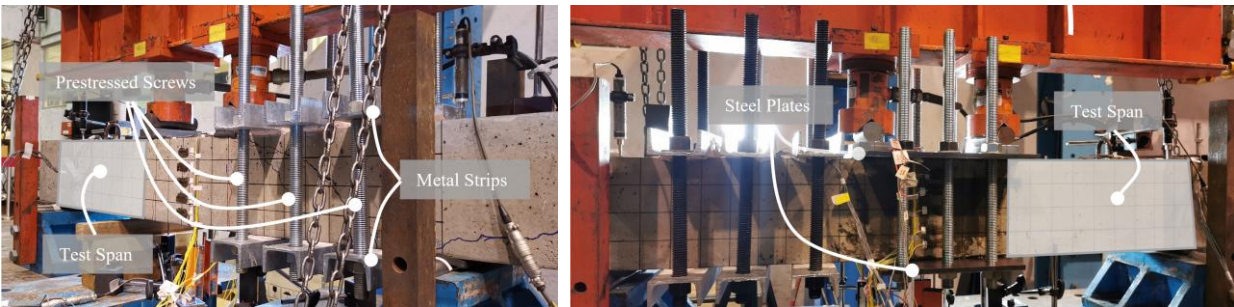


Figure 4.3 Configuration of beams reinforced with novel filament wound GFRP stirrup



(a) Specimens WS and RB-1

(b) Specimens SM, SC and RB-2

Figure 4.4 Strengthened specimens for bending tests

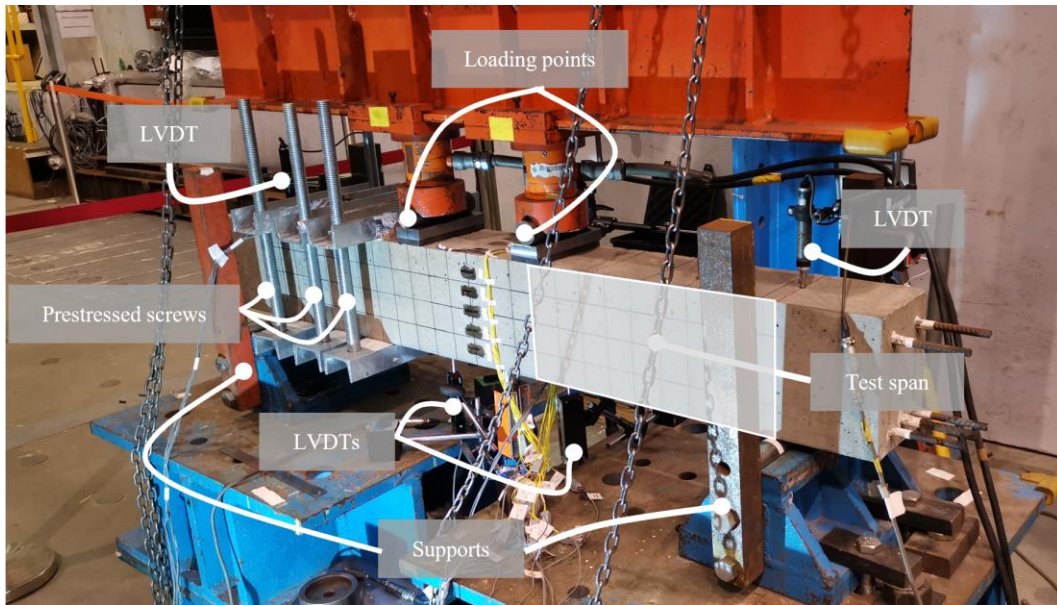
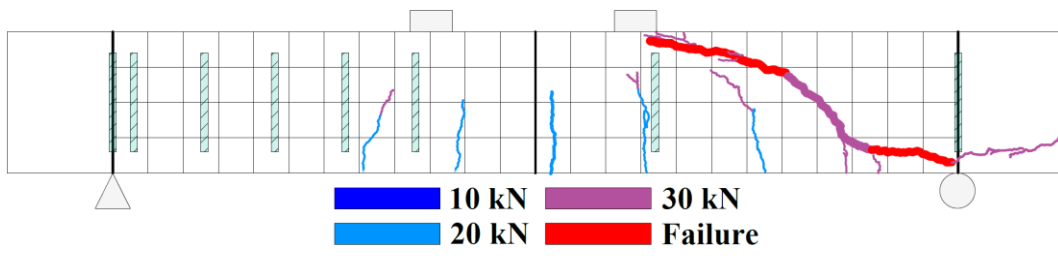
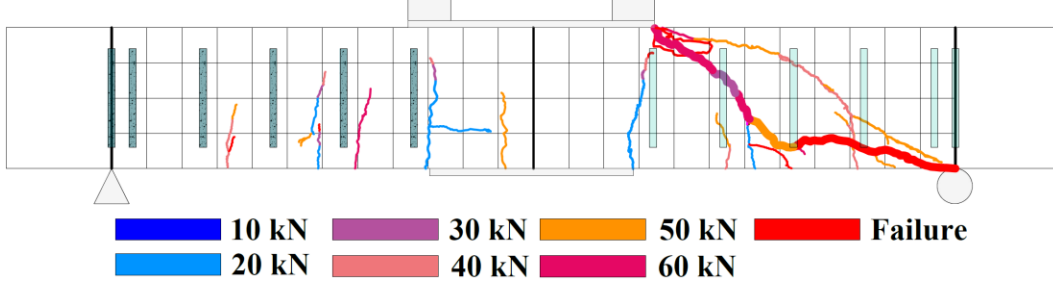


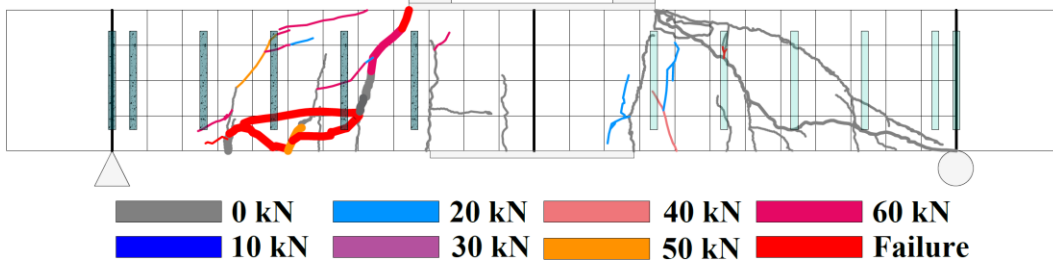
Figure 4.5 Test setup for bending tests



(a) Specimen WS



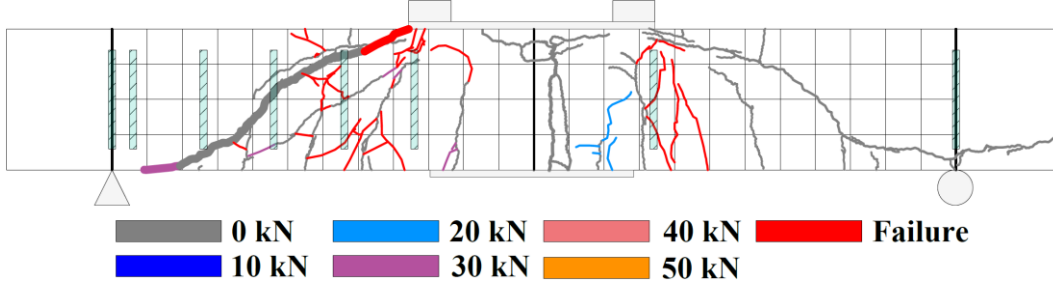
(b) Specimen SM



(c) Specimen SC



(d) Specimen RB-1



(e) Specimen RB-2

Figure 4.6 Cracking pattern and development path in bending test

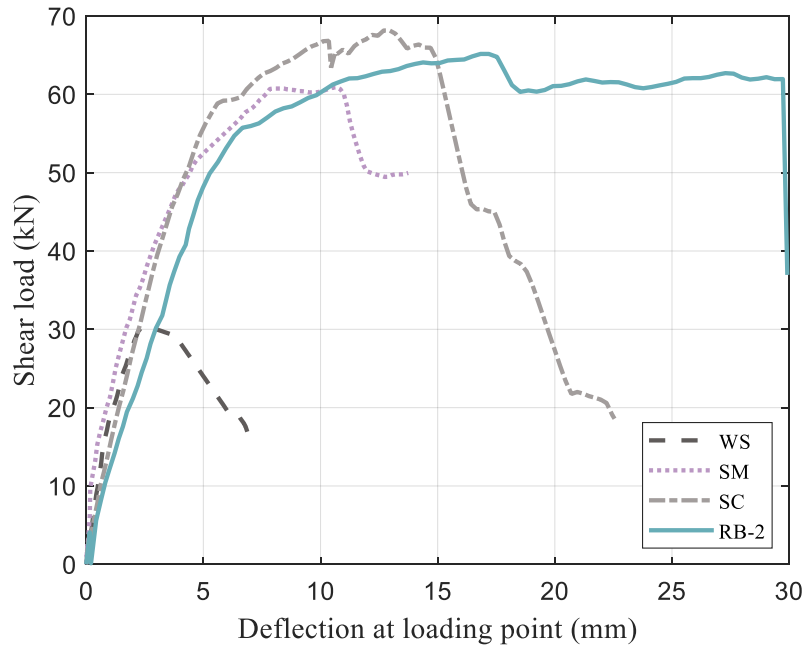
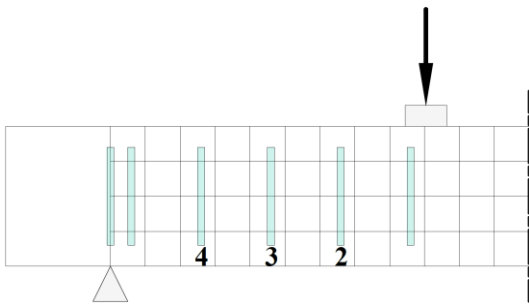
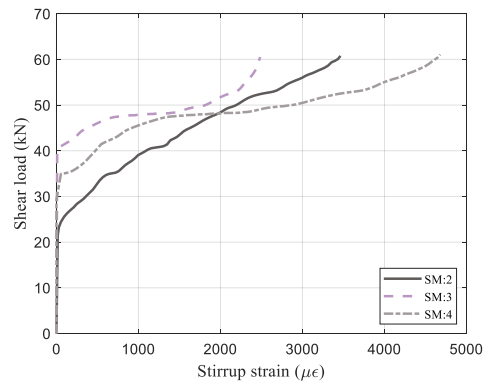


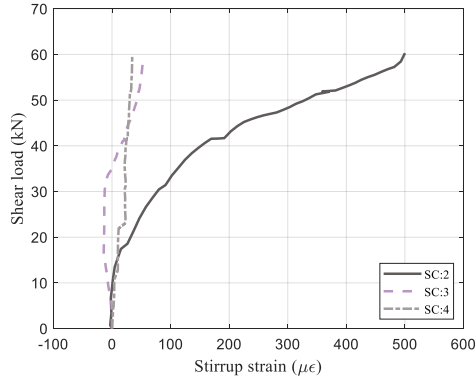
Figure 4.7 Load-deflection curves in bending test



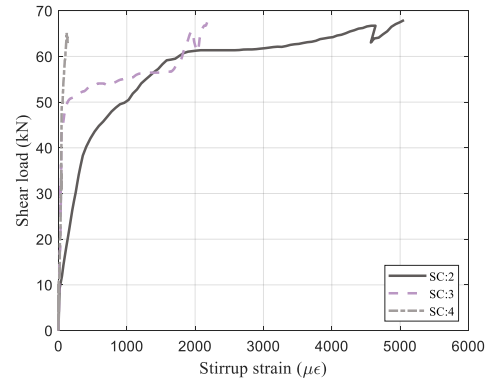
(a) Location of monitored stirrups



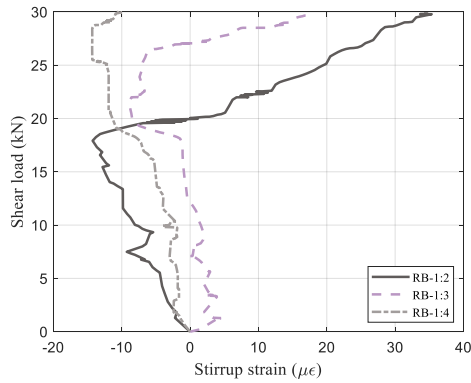
(b) Loading on Specimen SM



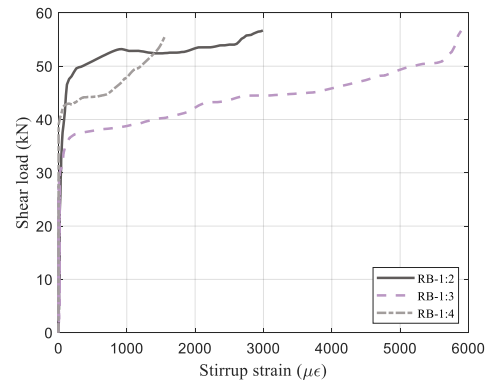
(c) Preloading on Specimen SC



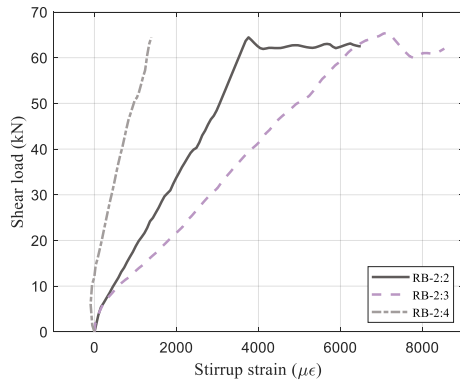
(d) Loading on Specimen SC



(e) Preloading on Specimen RB-1



(f) Loading on Specimen RB-1



(g) Loading on Specimen RB-2

Note: The number “2”, “3” or “4” represents the specific stirrup in the beam as shown in Figure 4.8(a).

Figure 4.8 Strain development on inner surface of stirrups in bending test

# **CHAPTER 5**

## **EXPERIMENTAL STUDY**

### **OF FRP REINFORCED CONCRETE ARCHES**

#### **5.1 INTRODUCTION**

In Chapter 3, the feasibility of under-reinforced GFRP-reinforced concrete arches was demonstrated (Xia et al., 2023b). The tested arch specimen exhibited failure due to the tensile rupture of longitudinal bars, where the long elastic elongation of FRP reinforcement enhanced both ductility and load-bearing capacity. However, FRP-reinforced concrete (FRP-RC) elements showed greater crack widths and deflections compared to steel-RC components, accompanied by notable load drops upon concrete cracking during quasi-static tests (Caratelli et al., 2016; Caratelli et al., 2017; De Rivat et al., 2019; Hosseini et al., 2022; Xia et al., 2023b), particularly in under-reinforced configurations with low reinforcement ratios (Figure 3.4). This behavior is primarily attributed to the lower elastic modulus of FRP compared to steel, which prevents the FRP bars from promptly accommodating the load released by the reduction in tensile stress of concrete upon cracking, thereby failing to meet the serviceability requirements (i.e., deflection and cracking width).

Three mainstream solutions have been developed to address these challenges: (a) FRP-steel

composite bars, where FRP-wrapped core steel provides enhanced stiffness and ductility. Arch structures reinforced with such composite bars exhibit comparable or superior performance to traditional arches under both static and blast loading conditions (Tang et al., 2020; Tang et al., 2021); (b) hybrid solutions combining fiber concrete with FRP reinforcement, where randomly distributed fibers improve the tensile properties and ductility of concrete matrix (De Rivat et al., 2019; Meda et al., 2019; Meda et al., 2020; Hosseini et al., 2023). This approach has been proven effective in FRP-RC slabs, beams, columns, and tunnel segments, where fibers help mitigate crack generation and expansion (Chellapandian et al., 2020; Raza et al., 2022; Hosseini et al., 2023; Zeng et al., 2022); (c) increasing the FRP reinforcement ratio to achieve over-reinforced configuration, requiring approximately quadrupling the reinforcement compared to steel for equivalent tensile stiffness (the ratio is expected to match the elastic modulus ratio of reinforcement).

However, the use of FRP-steel composite bars does not entirely eliminate corrosion concerns due to the involvement of steel, compromising long-term durability under corrosive conditions (Marcos-Meson et al., 2018; Cai et al., 2023; Xiao et al., 2024). Similarly, hybrid solutions incorporating steel fibers also suffer from corrosion damage in extreme environments (Marcos-Meson et al., 2018; Marcos-Meson et al., 2019). While non-metallic synthetic fibers, such as polypropylene (PP) fiber, offer corrosion resistance, their poor bond with concrete and susceptibility to creep limit their tensile performance (Zerbino et al., 2016; Soltanzadeh et al., 2022; Yin et al., 2015; Blazy and Blazy, 2021). On the other hand, increasing the FRP reinforcement ratio, despite potentially raising material costs, offers advantages for arch structures where compression dominates and minimal reinforcement is required, thus balancing initial and lifecycle costs.

Preliminary testing in Chapter 3 has shown that primary flexural cracks typically initiate at sections reinforced with FRP stirrups (Xia et al., 2023b; Barris et al., 2017). The inclusion of FRP stirrups may compromise axial strength and stiffness, thereby exacerbating the severity of load drops, due to the orthotropic nature of FRP results in a relatively low stiffness response along the arch axis. To address these issues, Chapter 4 has proposed a novel narrow closed FRP stirrup design, specifically removing unnecessary horizontal legs to reduce the cross-sectional area of the stirrup reinforcement, thereby minimizing local weakening of the bending capacity. This innovative stirrup, validated in Chapter 4, is manufactured using filament winding technology and features a closed cross-section with two vertical legs connected by rounded end portions (Figure 5.1). This advanced manufacturing technique further enhances the performance of stirrups by effectively preventing fiber slacking and kinking at bent regions (Spadea et al., 2017), as well as avoiding premature failure from slippage in overlapping regions typically associated with open stirrups (Lee et al., 2014; Maranan et al., 2018; Dong et al., 2018).

Given the advantages of over-reinforced FRP-RC configurations and the structural benefits of the novel FRP stirrup design, a hybrid approach emerges as a promising solution for constructing durable arch structures with superior structural performance. In this chapter, the structural behavior of such arches was investigated through a series of tests. The configurations and material properties of the FRP-RC arches were first presented, followed by an overview of the experimental program of quasi-static compression tests. The arches were subjected to a concentrated load at mid-span, providing an ideal scenario for evaluating the contributions of FRP reinforcement in arches (Xia et al., 2023a; Xia et al., 2023b; Dong et al., 2022; Tang et al., 2021; Liu et al., 2021). Subsequently, a comprehensive discussion of the test results, including failure modes, cracking patterns, load-

deflection curves, and strain development of the longitudinal reinforcement, was conducted and compared to a traditional steel-RC arch. The influence of longitudinal reinforcement ratio (0.36% and 0.47%), concrete strength (normal strength and high strength), and transverse reinforcement ratio (0.4% and 2.4%) was examined in terms of ultimate limit state (e.g., failure modes, strength and stiffness), material effectiveness (reinforcement efficiency), and serviceability limit state (e.g., deflection and crack width).

## **5.2 EXPERIMENTAL PROGRAM**

### **5.2.1 Test samples**

The experimental program involved five arch specimens, all with identical dimensions. Each arch had a span of 2000 mm and a rise-to-span ratio of 0.19, as depicted in Figure 5.2(a). The arch profile followed a circular arc with a constant radius of curvature of 1500 mm and a central angle of approximately  $83.62^\circ$ . The cross-section was rectangular, with a width of 300 mm and a depth of 100 mm. All specimens were reinforced with double layers of longitudinal bars, each layer consisting of three equidistant bars of equal diameter. The concrete cover thickness was 20 mm.

The parameters investigated in this study included longitudinal reinforcement ratio, concrete strength, and transverse reinforcement ratio, with the specific details summarized in Table 5.1. Each specimen was identified as follows: the first two letters distinguished the concrete strength: NC for normal strength or HC for high strength. The third character (G or S) denoted the reinforcement material (GFRP or steel, respectively), and the fourth number specified the nominal diameter of the longitudinal reinforcement in mm. The last letter represented the level of transverse reinforcement ratio (H for high level and L for low level). For example, the code “NCG13H”

referred to a GFRP-reinforced arch specimen constructed with normal-strength concrete, 13 mm longitudinal bars, and a high transverse reinforcement ratio.

Stirrups were uniformly spaced at 50-mm intervals along the arch axis. For the steel-RC specimen (NCS12H), conventional rectangular stirrups of 8 mm diameter steel were employed (Zhang et al., 2015; Wang et al., 2018). In the GFRP-reinforced arches, each stirrup-reinforced section contained three novel FRP stirrups, with each stirrup encircling one upper and one lower longitudinal bar to form a reinforcing pair [Sections B-B in Figure 5.2(a)]. Additionally, to maintain the transverse spacing of longitudinal reinforcement during casting and ensure the integrity of the reinforcement cage, two large GFRP fiber-wound stirrups with a width close to the cross-sectional width were fixed at two one-third intervals along the arch axis, as shown in Figure 5.2(b). These large stirrups, expected to experience relatively low internal forces (i.e., near the points of inflection where the bending moment is minimal, as determined by the elastic analysis method in Section 3.4), were strategically placed to minimize the risk of premature cracking or failure in the stirrup-reinforced sections.

### **5.2.2 Preparation of the arch specimens**

The casting molds for constructing the arch specimens were designed as four separate components for ease of assembly and disassembly: the extrados plate, the intrados plate welded to the bottom plate, and two small steel plates at both ends of the arches. The extrados, intrados, and bottom plates were all fabricated from 5 mm-thick steel, which was laser-cut, cold-formed, and welded. To enhance mold rigidity and prevent deformation due to the self-weight of the concrete and heat generated during concrete curing, stiffening ribs were added at 400 mm intervals along the sides of the arch axis [Figure 5.3(a)]. The two small steel plates measured 300 mm in length, 320 mm

in width, and 30 mm in thickness. These components were bolted together to form a complete mold.

To ensure adequate bond stress and minimize slippage between the bars and concrete, both ends of longitudinal bars were welded to steel baseplates at the ends of each arch. For FRP-RC arches, non-metallic GFRP bars were anchored using seamless tubes filled with expansive cement, which were welded to baseplates. Prior to the fabrication of the arch specimens, tests were conducted to evaluate the anchoring performance of the system at different lengths for the GFRP bars in tension. The tests demonstrated that an anchorage length of 100 mm was sufficient to provide the required tensile stress for the GFRP bars near the supports.

The tubes were cold-bent to match the curvature of the longitudinal bars, and their outer surfaces were mechanically grooved (Singhal et al., 2020) to improve the mechanical interlock between the tubes and concrete. Additionally, 8-mm-diameter short steel bars were welded along the tube lengths at 50 mm intervals to provide sufficient shear resistance in the anchorage region (GB 50010, 2015), as shown in Figure 5.3(b). In this configuration, the welded steel longitudinal bars in the steel-RC arch and the steel tubes in the GFRP-reinforced arches also acted as shear studs, ensuring the strength and stiffness of the steel-concrete interfaces, in accordance with the requirements of GB 50017 (2017) for steel-concrete composite structures.

Following the two-point lifting principle for arch ribs, where lifting points are positioned below the center of arch ribs, two steel lifting hooks were symmetrically embedded at 0.24 times the arc length of the arch axis from each end of the arch specimen [Figure 5.3(c)]. These hooks, cast into the concrete, allowed better control and stability of the arch rib during transportation and installation, minimizing the risk of pre-crack damage. Positioned perpendicular to the arch axis,

the lifting hooks have a negligible effect on the flexural-compressive behavior of the placed sections, though they may contribute slightly to shear resistance. Based on the elastic analysis method presented in Section 3.4, the hooks were situated in regions of low shear force, well away from critical sections that could lead to failure. Therefore, their effect on the overall structural behavior of the arch specimens is minimal and can be disregarded in the analysis of the test results.

Cement spacers with 20 mm height were positioned between the steel mold and longitudinal bars to ensure adequate concrete cover. Given that the concrete cover of the arch specimens was only 20 mm, the coarse aggregate was pre-sieved to ensure a maximum size of 10 mm to prevent coarse aggregate from getting trapped between the casting molds and the reinforcement cages, which could reduce the casting quality and affect the bond behavior of the embedded longitudinal bars.

The specimens were constructed with two different concrete strengths and cast in two separate batches. NCS12H, NCG13H, NCG8H, and NCG13L were cast using concrete with a design strength of C45, while HCG13H was cast using high-strength concrete with a design strength of C65. Each batch included arch specimens, as well as pull-out test specimens and material test specimens for compressive strength [Figure 5.4(a)].

Casting was performed at the mixing station of Hangzhou Construction Component Co. Figure 5.4(b) illustrates the process of concrete vibration and compaction to fill the steel arch molds, wooden molds for pull-out test specimens, and plastic molds for compressive test specimens. To prevent deformation during initial curing from affecting dimensional accuracy, the concrete arches were cured in their molds for one week before demolding. Subsequent testing of the specimens was conducted at a concrete age of 43 to 47 days.

### 5.2.3 Material properties

The longitudinal reinforcement was supplied in pre-curved states with a constant radius of curvature along their longitudinal axis. Steel rebars were sourced from Longqing Metal & Machinery Company, while sand-coated GFRP bars with helical wrapping were tailored and provided by Pulwell Composites Company. The manufacturing process of curved GFRP bars is illustrated in Figure 5.5. Specifically, continuous glass fiber filaments (469P, linear density of 2400 Tex) were impregnated with thermosetting resin (Atlac 430) and shaped into a circular cross-section through a pultrusion process. The profiles of ribbed bars were then sand-coated, using quartz sand (10-15 mesh), to enhance their bond strength with concrete. After surface treatment, the partially cured GFRP bars were mechanically bent around a custom-shaped steel mold (typically in a symmetrical shuttle or circular shape) to achieve the desired curvature. This pre-bending was generally conducted when the bars were in tension states to minimize fiber kinking and slacking to ensure strength. Finally, the GFRP products, along with the steel molds, were cured at 180 °C for 1.5 hours.

Uniaxial tensile tests were conducted on steel bars and GFRP rebars according to EN ISO 15630-1:2019 (2019) and ACI 440.3R-12 (2012), respectively. To avoid the challenges associated with testing curved configurations, tests were performed on straight bars from the same batch using the same raw materials as the curved bars (Spagnuolo et al., 2018; Hosseini et al., 2022).

For the steel reinforcement, tensile tests were conducted on five specimens, each 500 mm in length. Two strain gauges were symmetrically attached at 180° intervals in the middle of each specimen to measure strain. Additionally, an extensometer was installed at the midpoint to obtain the stress-strain relationship and ultimate strain of the steel bars [Figure 5.6(a)]. The tensile tests were

performed on an MTS universal testing machine under displacement control. The loading rate was set to 0.22 mm/min until yielding of the steel bars yielded, after which it was increased to 10 mm/min. All tensile specimens fractured near the middle of the specimen, with a typical failure mode shown in Figure 5.6(b). The results are summarized in Table 5.2.

For the GFRP reinforcement, two sets of tensile test specimens, each consisting of five samples of varying diameters, resulted in a total of ten specimens. Each specimen, with a total length of 1000 mm and anchorage lengths of 200 mm at both ends, was anchored using expansive cement-filled steel tubes. Two strain gauges were symmetrically attached at 180° intervals at the middle of each specimen to determine the tensile stress-strain relationship [Figure 5.7(a)]. The tensile tests were conducted using an MTS universal testing machine under displacement control at a rate of 1 mm/min. The mechanical results indicated that all specimens ruptured near the middle of their free length, with a typical failure mode as shown in Figure 5.7(b). The results are summarized in Table 5.2. Prior to the rupture of the FRP bars, the strain gauges reached their measurement capacity, ceasing to function. Consequently, the rupture strain of the GFRP bars was estimated by calculating the measured tensile strength and elastic modulus under the assumption of a linear stress-strain relationship. The results indicated that the tensile strength of the GFRP bars was approximately twice the yield strength of steel, with an elastic elongation of about 2%, which was considerably higher than the elongation of steel within its elastic range. However, the elastic modulus of the GFRP bars was only about a quarter of that of steel.

The novel GFRP stirrups were manufactured by Lian FRP Company using filament winding technology (Figure 5.8). The raw materials used were E-glass fibers (E6DR24-2400) from Jushi Co. and unsaturated polyester resin (PALATAL P65-901) from Li Lian Si Resin Co. To adhere to

the principle of winding fiber strands without overlap or gaps, the winding angle for the novel stirrups was set at  $85.0^\circ$ . This angle was determined based on the known width of the winding filaments and the circumference of the mandrel. After winding, a layer of coarse yarn cloth was applied to the outer surface of the filament-wound tube to enhance the surface roughness of the stirrup, thereby improving bond strength with concrete. After the initial hardening of the resin, the wound GFRP tube, with the mandrel, was removed from the winding machine and cured at room temperature. Upon curing, the GFRP tube was cut to the designed widths using a water jet.

Each stirrup specimen featured an internal diameter of 20 mm at the curved portions, a straight portion length of 40 mm, and a total length of 60 mm. The thick stirrups had a nominal thickness of 4 mm, and the thin stirrups had a nominal thickness of 1 mm. However, the inclusion of the coarse yarn layer and manufacturing variations resulted in actual thicknesses of 1.92 mm and 4.51 mm, respectively.

Tensile tests on the novel FRP stirrups were conducted according to ACI 440.3R-12 (2012) to determine their tensile strength and elastic modulus [Figure 5.9(a)]. Two sets of tensile test specimens, each consisting of five specimens, were prepared for FRP stirrups of varying thicknesses, resulting in a total of ten specimens. To track strain development, two strain gauges were symmetrically attached to the inner surfaces at the middle of each stirrup specimen. The tests indicated that all thin FRP coupons failed at the junction between the straight and bent portions, characterized by FRP fiber rupture, as shown in Figure 5.9(b). The properties of the FRP stirrups are presented in Table 5.2. Due to the load limitations of the testing equipment, the thick stirrup specimens did not undergo rupture; therefore, only the elastic modulus was reported.

On the same day as the loading tests for the arch specimens, uniaxial compression tests were conducted on five standard cylindrical specimens for each batch, following ASTM C469/469M-14 (2014). Two strain gauges were attached at 120° intervals around the mid-height of each specimen to measure longitudinal strain [Figure 5.10(a)], with typical failure modes shown in Figure 5.10(b). The results indicated an average compressive strength of 51.85 MPa for normal-strength concrete and 63.77 MPa for high-strength concrete, as summarized in Table 5.2.

As scale models, the arch specimens featured small casting surfaces, thin concrete covers, and tightly spaced reinforcement. Therefore, concrete with high fluidity was required to ensure dense, void-free casting. Slump, a key indicator of concrete workability, was measured according to ASTM C143/C143M-15 (2015). The slump tests indicated values of 75 mm for C45 concrete and 115 mm for C65 concrete, demonstrating favorable fluidity for both batches (Figure 5.11).

#### **5.2.4 Bond-slip properties of GFRP bars and concrete**

In accordance with ACI 440.3R-12 (2012), the bond properties between GFRP longitudinal bars and concrete were evaluated through pull-out tests. To account for the effects of varying concrete mixes and bar diameters, three sets of pull-out test specimens were prepared, each set consisting of three replicates, for a total of nine specimens. To minimize the effect of concrete variability on bond-slip behavior, the concrete used in the pull-out tests was sourced from the same batch as that used for the RC arch specimens. Additionally, the curing period of the concrete in the pull-out tests was matched with that of the arch specimens to accurately represent the bond-slip behavior observed during loading tests on the arch specimens. The pull-out specimens were 150 mm concrete cubes, with the bonded length of the GFRP bars equal to five times their diameter, as recommended by ACI 440.3R-12 (2012). PVC pipes were used to isolate the free length of the

bars within the concrete cubes. The GFRP bars used in the pull-out tests had a total length of 700 mm, with anchorage lengths of 200 mm at the loading ends, anchored using expansive cement-filled steel tubes.

The pull-out tests were performed on an MTS universal testing machine, employing a displacement-controlled loading mechanism at a rate of 1.3 mm/min. The test setup, shown in Figure 5.12, included an LVDT fixture clamped at the free end of the bar and three LVDTs positioned at 120° intervals on the fixture. Each LVDT had a measurement range of 50 mm with an accuracy of 0.1 mm. The measuring heads of LVDTs rested on the concrete surface to record the slip of the embedded bar, with the average of the three readings representing the slip of the GFRP bar. Representative bond stress-slip curves for the different specimens are presented in Figure 5.13.

Different standards set various benchmarks for the bond performance of FRP bars. ACI 440.6M-08 specifies a minimum bond strength of 9.6 MPa, while ASTM D7957-17 requires a bond strength greater than 7.6 MPa. CSA S807-10 sets a minimum bond strength requirement of 8.0 MPa, whereas the latest version, CSA S807-19, is the strictest, demanding a bond strength greater than 10 MPa when the bar slip does not exceed 0.5 mm. The test results demonstrated that the GFRP bars used in this study met the bond performance requirements of all these standards, as summarized in Table 5.3.

### **5.2.5 Test setup and loading scheme**

Loading tests on the arch specimens were carried out on an MTS universal testing system with a maximum capacity of 1000 kN (Figure 5.14). A concentrated load was applied to the extrados of the arch apex at a rate of 0.2 mm/min. A T-shaped steel component equipped with a roller connected by springs at both ends was bolted beneath the loading head to transfer the load to the

arch. The springs allowed the rollers to self-adjust to accommodate any horizontal movement and rotation within the loading area caused by arch deformation. This mechanism ensured unconstrained relative movement, maintaining a vertically downward load direction throughout the process. To ensure precise alignment, a laser level was used to align the loading point, the arch center of the arch, and the center of the support system vertically. Moreover, high-strength gypsum was applied to create a 40 mm-wide leveled area on the arch specimen (Figure 5.15) to prevent localized stress concentrations and out-of-plane stresses.

To achieve fixed-ended support conditions, the steel baseplates at both ends of each specimen were bolted to the top of custom-made steel supports via 24 high-strength M12 bolts of grade 14.9. According to GB/T 3632-2008 (2008), a pre-tightening torque of about 150 N·m was applied to each bolt using a torque wrench to ensure the strength and stability of interfaces. Each steel support was supported by an underlying steel beam with rigid connections. The bottom of each support and the upper surface of the beam were connected using 24 M14 bolts that were pre-torqued to approximately 250 N·m. Notably, the undersurface of the steel beam was anchored to the ground at mid-span, providing a stable test platform for accommodating long-span specimens.

The arrangement of LVDTs is shown in Figure 5.16, where  $L$  represents the total arc length along the centroidal axis of arch specimens. Deflections were measured at three points along the arch axis: the vertical deflection at the apex and at two symmetrical quarter points (Figure 5.16). At these quarter points, two LVDTs were placed to measure both vertical and horizontal deflections, with aluminum sheets adhered to the side surface serving as deflection measurement points. Furthermore, slips at the bolt connections of the supports were monitored during the loading process. The LVDT at the arch apex had a measurement range of 100 mm, while the others had a

measurement range of 50 mm, all with an accuracy of 0.01 mm. All LVDTs were fixed to magnetic bases. The magnetic bases for the LVDTs measuring the horizontal deflection of the steel supports were attached to the bottom steel beam, while the other magnetic bases were fixed to metal stands independent of the arch specimens.

Strain measurements were symmetrically taken at four points along the arch axis: two points near the arch apex ( $L/2$ ) and two at the quarter points ( $L/4$ ). Each point was instrumented with four strain gauges on the concrete surface and four on embedded longitudinal bars, as shown in Sections A-A (in green) of Figure 5.2(a). In each strain-monitored section, one strain gauge was placed at the midpoint of both the extrados and intrados surfaces. Besides, two strain gauges were positioned at the locations of the upper and lower rows of longitudinal bars on the same side of the arch specimen (indicated by yellow blocks in Figure 5.2(a)). The strain gauges on the concrete were gauges with a 50-mm gauge length, produced by Xing Dongfang Sensor Co. For attachment, the concrete surface was polished with 320  $\mu\text{m}$  sandpaper, and residual dust was removed using alcohol swabs. Once the surface was dry, AB glue was applied as a base layer before attaching the strain gauge.

In each arch specimen, strain gauges were also attached to each diagonal pair of longitudinal bars, as well as to both the upper and lower longitudinal bars at the midpoint. These positions, marked by red blocks in Figure 5.2(a), were instrumented with strain gauges sourced from TML Co., Japan, with a gauge length of 10 mm (FLAB-10-350-11). Due to the rough surface of the ribbed GFRP bars with sand-coating, a leveling surface was created using GEL2 epoxy resin from Composite Easy Buy Co. After the resin hardened, CN adhesive from TML was used to attach the strain

gauges to the resin layer, which was then sealed with SB tape from TML Co. to prevent water infiltration or vibration-induced failure during concrete casting and curing.

For NCG13L, four additional strain gauges were symmetrically installed at the mid-height of the FRP stirrups to monitor strain development at Sections B-B (in blue), located 25 mm and 75 mm from the arch apex, as shown in Figure 5.2(a). Those strain gauges (10 mm gauge length, produced by Xing Dongfang Sensor Co., indicated by the purple blocks in Figure 5.2(a) were symmetrically placed on the inner surface of the novel FRP stirrups. Both displacement and strain data were continuously recorded at a frequency of 1 Hz during the loading process.

On the opposite side of the arch specimens, the surface was sanded using 320  $\mu\text{m}$  sandpaper, cleared of dust, and sprayed in white [Figure 5.14(a)]. During the loading process, a DSLR camera on a tripod was used to record the deformation of the arch specimens and the development of cracks in the concrete using an interval shooting function. Crack development and distribution were marked with different colors at 50 kN intervals until failure occurred.

## **5.3 RESULTS AND DISCUSSION**

### **5.3.1 Failure modes and crack patterns**

Experimental observations indicated that all specimens experienced material failure rather than stability failure. Two distinct failure modes were identified: flexural failure in specimens with higher transverse reinforcement ratios (NCS12H, NCG13H, NCG8H, and HCG13H), and shear failure in the specimen with a lower transverse reinforcement ratio (NCG13L). Figures 5.17(a)-(e) illustrate crack patterns and propagation paths at 50 kN intervals until failure, with failure-inducing

cracks highlighted for clarity. To facilitate crack localization, ring segment-shaped grid blocks of approximately  $25 \times 25$  mm are included in the figures.

During the initial loading stage (up to 50 kN), several flexural cracks formed on the intrados beneath the loading point, where the maximum sagging bending moment occurred. As the load increased, these existing cracks expanded in depth and width, along with new flexural cracks initiating near the intrados of the arch apex. Subsequently, inclined cracks appeared as extensions of the flexural cracks. Meanwhile, hogging bending moments on the extrados of the shoulders led to successive crack development, showcasing a progressive failure mechanism of arch structures.

Overall, the cracks at the shoulders were symmetrically distributed relative to the mid-span, predominantly concentrated near  $L/4$  of the arch axis, with adjacent cracks occurring at about 50 mm intervals. It was found that flexural cracks primarily formed and propagated at stirrup locations for both steel-RC and FRP-RC arches, regardless of stirrup material. This observation is consistent with existing experimental studies on steel/FRP-RC flexural members with a small concrete cover of 25 mm (Barris et al., 2017; Pérez Caldentey et al., 2013).

The concrete cover plays an important role in transferring tension stresses that are generated at the bar-concrete interface to the effective concrete area surrounding the bar (Pérez Caldentey et al., 2013). It is believed that the observed premature cracking behavior arises from partial contact between the longitudinal bars and the stirrups in the stirrup-reinforced sections, rather than full encasement of the bars in concrete, which potentially weakens stress transfer. Additionally, shear lag within the concrete cover (Borosnyoi and Snóbli, 2010; Pérez Caldentey et al., 2013) further exacerbates the inferior performance of stirrup-reinforced sections, where the portion of the stirrup between the longitudinal bars and the concrete cover may degrade stress transfer efficiency. It is

noteworthy that this observation is particularly evident in reinforced concrete (RC) members with small concrete cover (e.g., 20 mm in this study), while larger cover values tend to result in greater variability of results (Pérez Caldentey et al., 2013; Barris et al., 2017).

In comparison to the conventional steel-RC arch (NCS12H), FRP-RC arch specimens exhibited widely spaced crack patterns. Existing formulations suggest that crack spacing is dependent on the concrete cover, the bar spacing, the bond properties of the reinforcement, and the ratio of the diameter of the bar to reinforcement ratio (Borosnyói and Balázs, 2005; EN 1992-1-1:2023, 2023). In this case, the differences in bond performance may be a key factor. Although the bond strength of the steel reinforcement was not experimentally measured in this study, it is generally accepted that the bond strength of steel bars is higher than that of GFRP bars (Achillides and Pilakoutas, 2004; Baena et al., 2009), which typically results in shorter transfer lengths to achieve adequate bond stress and thus leads to narrower crack spacing (Barris et al., 2017; Barris et al., 2013). Among the FRP-RC specimens, a well-distributed crack pattern was observed in HCG13H, particularly at the arch shoulders. This can be attributed to enhanced bond strength, specifically chemical adhesion facilitated by the densification of the concrete matrix, which has been shown to improve with increased concrete strength (Lee et al., 2008).

When the applied load exceeded 250 kN, the specimens underwent moment redistribution, with points of inflection shifting closer to the mid-span, causing a series of cracks on the extrados between  $L/4$  and  $L/2$ . Specimens experiencing flexural failure exhibited wedge-shaped cracks at peak loads of 279.6 kN, 225.6 kN, 194.9 kN, and 257.5 kN for NCS12H, NCG13H, NCG8H, and HCG13H, respectively, likely due to high local bearing stresses beneath the edges of the loading plate. The areas enclosed by the wedge-shaped cracks are highlighted in the corresponding

subfigures. For shear failure in NCG13L, two inclined cracks abruptly appeared at the arch apex under a load of 272.3 kN, accompanied by concrete cover spalling, leading to rapid collapse and significant loss of load-bearing capacity.

### **5.3.2 Load-deflection curves**

Figure 5.18 presents the relationships between applied load and midspan deflection for all specimens. Each specimen exhibited a consistent trend of monotonically increasing load under displacement control, with no significant load drops until reaching peak loads. Initially, all specimens displayed linear behavior, which was disrupted by the formation of cracks at the arch apex. These cracks, along with subsequent cracks at the apex and shoulders, degraded stiffness in the cracked sections, progressively introducing nonlinearity. In these cracked sections, embedded reinforcement assumed the role of the primary tensile element, indicating a significant transition from the pre-cracking phase, during which the structural response was dominated by the concrete properties.

For the conventional steel-RC arch (NCS12H), a plastic hinge formed near the apex upon reaching the yield load (152.7 kN), reducing stiffness and entering a pronounced nonlinear phase characterized by a slightly decreased slope in its load-deflection curve. Material test results indicated that while the tensile strength of GFRP reinforcement was nearly double the yield strength of steel, the elastic modulus of GFRP was only about a quarter of that of steel. Consequently, all GFRP-reinforced specimens exhibited lower structural stiffness compared to the steel-RC arch (NCS12H), albeit to varying degrees.

In general, an increased reinforcement ratio or concrete strength led to improvements in post-cracking stiffness and load-bearing capacity for FRP-RC arches. Specimen NCG8H, with a lower

FRP reinforcement ratio than NCG13H, exhibited a 13.60% decrease in load-bearing capacity (Table 5.4), attributed to reduced stiffness of the longitudinal bars, which led to rapid crack development. Conversely, HCG13H, featuring high-strength concrete and an equivalent reinforcement ratio to NCG13H, demonstrated a 14.12% increase in load-bearing capacity compared to NCG13H. While the initial loading stages showed minimal differentiation due to concrete strength, the divergence between HCG13H and NCG13H became increasingly pronounced during the post-cracking stage (Figure 5.18).

Specimen NCG13L exhibited slightly lower structural stiffness than the steel-RC arch but achieved a comparable load-bearing capacity under similar reinforcement ratios and concrete strengths. This specimen presented an intriguing case, exhibiting superior performance despite a lower transverse reinforcement ratio compared to NCG13H. The enhanced performance of NCG13L may be attributed to the material heterogeneity and variability of concrete, with its mechanical properties exceeding expectations.

### **5.3.3 Strain development of longitudinal reinforcement**

Figures 5.19(a)-(d) present the relationships between applied load and strain development of longitudinal reinforcement, where the final identifier in the legend distinguishes strain gauges on the left (-L) or right (-R) side of the arches. The discussion was based on strain data from both upper and lower longitudinal reinforcements that were successfully measured. Throughout the loading process, the strains in all reinforcement remained below the rupture strain. The sagging bending moments at  $L/2$  sections subjected all lower reinforcement to tension, while the hogging bending moments at  $L/4$  kept all upper bars in tension, consistent with the observed cracking patterns in Figure 5.17.

At the arch crown ( $L/2$ ), the lower reinforcement of NCS12H-L exhibited the highest stiffness response due to its high elastic modulus. The steel bar remained elastic until reaching 152.7 kN, after which it entered the plastic stage. Between loads of 162.4 kN and 237.6 kN, strain readings of all monitored longitudinal steel bars abruptly shifted to negative values, likely due to gauge damage during the yielding phase.

As shown in Figure 5.19(b), the upper reinforcement at  $L/2$  experienced minor compressive strains before the initial flexural cracking for all specimens. After cracking at the applied load of 19.8 kN, the strains of the upper steel bars in NCS12H steadily developed and remained in compression. However, due to the inherently lower elastic modulus of GFRP compared to steel, the depth of compression zone in GFRP-reinforced sections was smaller than that in steel-reinforced sections after cracking, which then quickly shifted over the upper reinforcement (height at about 23.5 mm for sections reinforced with 13-mm-diameter bars and 26 mm for those with 8-mm-diameter bars) as cracks widened (Figure 5.20). The neutral axis remained slightly above the upper reinforcement during the post-cracking stage, which caused the upper FRP reinforcement to behave similarly and remain in a tension state, as shown in Figure 5.19(b). Unlike the sections at  $L/2$ , the strain of upper reinforcement at  $L/4$  exhibited negative values [Figure 5.19(c)]. This behavior can be attributed to the significantly smaller bending moment at  $L/4$  compared to  $L/2$ , which resulted in a deeper compression zone and positioned the upper reinforcement within the compression region for all specimens. As shown in Figure 5.19(c), strain development of the upper reinforcement at  $L/4$  followed a similar trend regardless of reinforcement type, with all strains showing a steady increase until peak load.

Specimen NCG8H, having a lower reinforcement ratio than NCG13H, exhibited accelerated tensile strain development after cracking across all monitored sections (Figure 5.19). This behavior in NCG8H can be attributed to the lower reinforcement ratio, which necessitates greater strain response of FRP bars to distribute tensile forces. Similar strain development trends were observed in NCG13H and NCG13L, as the primary differences between the two specimens were the stirrup dimensions, and the fact that the monitored sections were not reinforced with stirrups [Sections A-A in Figure 5.2(a)].

In the high-strength concrete arch HCG13H, slightly higher stiffness was observed at the arch crown compared to specimen NCG13H with normal-strength concrete [Figure 5.19(a) and 5.19(b)]. This enhanced performance is attributed to the improved elastic modulus of the concrete in HCG13H, enabling lower strain levels in the compression zone under the same load. Consequently, the curvature development in HCG13H was alleviated, exhibiting stiffer strain responses of reinforcement. Notably, however, HCG13H exhibited unexpectedly lower stiffness compared to NCG13H at  $L/4$ , which is further discussed in Section 6.4.1.

#### **5.3.4 Efficiency of longitudinal reinforcement**

Steel-reinforced concrete members are commonly designed with balanced reinforcement, characterized by steel yielding before concrete crushing, thereby providing ductility and an early warning of potential failure. However, FRP reinforcement exhibits linear-elastic stress-strain behavior and lacks ductility, which distinguishes it significantly from steel rebars and necessitates a different design approach. According to ACI 440.1R-15 (2015), FRP-RC members can fail in flexure in two ways: FRP rupture in under-reinforced configurations or concrete crushing in over-reinforced configurations.

This chapter focuses on over-reinforced arches, where failure is governed by concrete crushing. The strain of FRP reinforcement serves as a criterion in assessing structural performance and material efficiency at the ultimate state. The efficiency of FRP reinforcement can be quantified by the utilization efficiency ( $\eta$ ), defined as the ratio of the maximum strain measured in the FRP bars ( $\epsilon_{frp}$ ) to the rupture strain ( $\epsilon_{frp,t}$ ) obtained from material tests (Mofidi and Chaallal, 2011; Bilotta et al., 2011).

As evident from Figures 5.19(a)-(d), the maximum strains recorded in the FRP longitudinal bars of specimens NCG13H, NCG8H, NCG13L, and HCG13H occurred consistently in the lower row of reinforcement near the arch crown under peak loads, registering as 8380  $\mu\epsilon$ , 9992  $\mu\epsilon$ , 9821  $\mu\epsilon$ , and 9210  $\mu\epsilon$ , respectively. It should be noted that these values represent approximations rather than peak values along the arch axis, due to the localized nature of strain gauging, which is based on point measurements.

Table 5.4 presents the utilization efficiency of longitudinal reinforcement in GFRP-reinforced arches. Specimen NCG13H, which used 13-mm-diameter GFRP bars with a rupture strain of 1.79%, achieved an  $\eta$  of 46.82%. Specimen NCG8H, with 8-mm-diameter GFRP bars and a rupture strain of 2.00%, achieved an  $\eta$  of 49.96%. A comparison between NCG13H and NCG8H reveals an increase in FRP efficiency with a reduced reinforcement ratio, despite achieving lower peak loads. This suggests that, in section analysis, while the peak strain is limited by the peak load, the increased curvature resulting from the reduced stiffness at lower reinforcement ratios leads to higher peak strains. Consequently, the efficiency of the reinforcement is enhanced in specimens with lower reinforcement ratios compared to those with higher reinforcement ratios.

Notably, NCG13L exhibited the highest  $\eta$  (54.87%), primarily due to its highest peak load, which demanded higher strain levels for force equilibrium. Moreover, it is believed that the concrete and longitudinal reinforcement in NCG13L were exposed to higher shear stress due to lower transverse reinforcement, which introduced larger transverse deflection and extensive shear cracking that accelerated strain development. In addition, HCG13H showed higher strain in the FRP longitudinal reinforcement compared to NCG13H, registering  $\eta$  values of 51.45%. This enhancement in HCG13H may be attributed to the elevated stress level within the compression zone of high-strength concrete, which improves both load-bearing capacity and reinforcement efficiency.

### **5.3.5 Serviceability**

The structural design of conventional steel-RC members primarily relies on the provisions for the ultimate limit state (ULS), whereas the consideration for FRP-RC elements is generally governed by the serviceability limit state (SLS), mainly due to the lower elastic modulus of FRP bars. At the structural level, key serviceability requirements include limits on deflection and crack width. ACI 440.11 (2022) was used for evaluation because it is the most widely recognized standard for FRP-reinforced construction. According to ACI 440.11 (2022), deflection and crack width limits are typically based on the stress/strain levels of FRP reinforcement to simplify calculations (e.g., deflection limits for compressive members and crack width limits for flexural members). Moreover, the design stress/strain for FRP bars is limited by their susceptibility to creep and the environmental reduction factor (ACI 440.11R-22, 2022; GB 50608-20, 2010; EN 1992-1-1:2023, 2023). For GFRP characteristics, the creep stress limit is set at 30% of its strength, while the environmental reduction factor is 0.85, irrespective of the environment (ACI 440.11R-22, 2022).

Since arches are classified as flexural-compression members, both flexural and compressive design criteria shall be considered. According to ACI 440.11 (2022), the deflection criterion for FRP-RC flexural members was set at 1/240 of the arch span. The tested values were derived from quasi-static tests; hence, an additional time-dependent factor of 1.2 was applied to the deflection limit to account for creep and shrinkage under long-term sustained loads (ACI 440.11R-22, 2022). For FRP-RC compressive members (e.g., columns), the deformation limit is specified by ensuring the tensile strain of longitudinal bars does not exceed 0.01. The crack width is limited by restricting the stress in the longitudinal bars, with the allowable stress ( $f_{fs}$ ) under service load expressed as:

$$f_{fs} \leq \frac{0.09653E_{frp,t}}{d_c\beta_{cr}k_b} \quad (5.1)$$

where  $E_{frp,t}$  represents the elastic modulus of FRP reinforcement,  $d_c$  denotes the concrete cover thickness (taken as 20 mm in this study),  $\beta_{cr}$  signifies the ratio of the distance from the elastic cracked section neutral axis to the extreme tension fiber to the distance from the elastic cracked section neutral axis to the centroid of the longitudinal tensile reinforcement, and  $k_b$  is the bond factor, set at 1.2 for GFRP bars (ACI 440.11R-22, 2022).

The value of  $\beta_{cr}$  depends on the position of the neutral axis, which requires the determination of the strain distribution along the cross-section based on the specified concrete crack width/strain. For cross-sections under pure bending, the strain distribution can be directly derived from force equilibrium equations. However, for cross-sections subjected to combined bending and axial force, force equilibrium requires the consideration of eccentricity (ratio of bending moment to axial force), making the determination of  $\beta_{cr}$  challenging. Within an arch, the eccentricity varies as the bending moment and axial force change along the arch axis. Generally, an increase in axial force

(or a decrease in eccentricity) leads to a deeper compression zone, resulting in a higher  $\beta_{cr}$  value and more stringent stress limits. Therefore, establishing an upper limit for  $\beta_{cr}$  is essential for a conservative stress limit.

For flexural members subjected to pure bending, the SLS (e.g., crack width limits) is typically reached before the ULS (e.g., concrete crushing). However, when a cross-section is subjected to a combined axial compressive load and bending moment, an additional compressive strain, which is non-zero, is induced compared to the pure flexure condition. Therefore, the crack width and tensile strain at the extreme tension fiber can be effectively controlled, whereas the extreme compression fiber becomes more susceptible to reaching its ultimate compressive strain and concrete crushing. The threshold between SLS and ULS occurs when concrete at the extreme compression fiber reaches its crushing strain (i.e., 0.003 as per ACI 440.11) while the crack width limit in the tensile zone is simultaneously met (i.e., 0.71 mm in ACI 440.11). The corresponding eccentricity at this point is known as the critical eccentricity. When the eccentricity is lower than the critical value, concrete crushing occurs before the crack width limit is reached, causing the cross-section to enter the ULS before the SLS. At the critical eccentricity, the depth of the compression zone is 38.33 mm, with corresponding  $\beta_{cr}$  values of 1.75 and 1.64 for cross-sections reinforced with 13 mm and 8 mm longitudinal bars, respectively.

The test results consistently indicated that the maximum deflection occurred at the arch apex, where the highest strain was also recorded in the lower reinforcement [Figure 5.19(a)]. The evaluation was performed using average values of these critical measurements. Based on the test data presented in Figures 5.18 and 5.19, Figure 5.21 shows the load levels for FRP-RC arch specimens under the five specified limits, with the ultimate load included as a reference. Notably,

the serviceability evaluation is derived from experimental data, and the values in Figure 5.21 are restricted so that they do not exceed the peak load at ULS.

Load limits imposed by deflection control in compression members and the environmental reduction factor were constrained by the ultimate strength at ULS, as the maximum reinforcement strains throughout the loading process remained within allowable limits for these two criteria. This suggests that, for over-reinforced members, these two parameters are less critical in the SLS design. The load limit based on deflection control for flexural members and the load derived from reinforcement creep stress were comparable, ranging from 57.77% to 72.24% of the ultimate load. The lowest load limit was governed by crack width, making it the primary factor in determining allowable service load. The ratios of allowable service load to ultimate load ranged from 22.84% to 35.86%, suggesting that FRP-RC arches designed according to the SLS retain significant strength redundancy relative to the ULS.

For specimens NCG13H, NCG13L, and HCG13H, which used 13 mm GFRP bars, the allowable strain for FRP bars corresponding to the crack width limit was 2294  $\mu\epsilon$ . For NCG8H, the smaller diameter of the reinforcement resulted in a lower value of  $\beta_{cr}$ , yielding a higher allowable reinforcement strain of 2457  $\mu\epsilon$ . Nevertheless, increasing the reinforcement ratio from 1.01% to 2.65% resulted in a 60.53% increase in allowable service load. Overall, the variations in allowable service load among the different specimens reflect, to some extent, the differences in stiffness response observed in the strain development of the longitudinal bars (Figure 5.19). The reasons contributing to different stiffness responses also explain the variations in allowable service load, indicating that increasing reinforcement ratio and concrete strength in FRP-RC arches effectively control crack width and enhance allowable service load.

### 5.3.6 Strain development of transverse reinforcement

This section evaluates the contribution of the novel stirrups in specimen NCG13L, which experienced shear failure. Figure 5.22 illustrates the load-strain relationship of the stirrups, with each curve identified by the distance (-25/-75 in mm) and position (“L” for the left side and “R” for the right side) of the corresponding strain gauges relative to the mid-span. Below the concrete cracking load, all stirrups remained inactive with negligible strains, indicating initial shear resistance was primarily provided by the concrete during the pre-cracking stage. As the load reached 39.1 kN for sections near the arch apex (25 mm) and 62.1 kN for sections further away (75 mm), successive cracking triggered strain development in the corresponding stirrups, signifying the onset of shear load-withstanding. The strains in the stirrups increased steadily with further increases in the applied load.

The stirrup strains on the left side developed more rapidly than those on the right (Figure 5.22), consistent with the crack pattern shown in Figure 5.17(c), where the left side exhibited more severe cracking. The difference in strain was particularly pronounced at sections 75 mm from the mid-span. At the load just exceeding 150 kN, the strain in stirrup NCG13L-75L accelerated as it directly intersected a diagonal crack [red crack in Figure 5.17(d)]. Ultimately, the strain in NCG13L-75L became the highest among all stirrups, as significant shear cracks concentrated in this region. This showcases the substantial strain variation across stirrups, driven by their relative positions to diagonal cracks.

As the load reached 272.3 kN, sounds of FRP stirrup rupture were heard, culminating in shear failure near the arch crown. Figure 5.23 shows the rupture locations at the upper corner of stirrup NCG13L-25L, the lower corner of stirrup NCG13L-75L, as well as the shear-tension failure of the

upper longitudinal bars, all of which are consistent with the critical diagonal crack trajectory shown in Figure 5.17(d).

The shear strength of NCG13L was evaluated using three well-established standards for FRP-RC structures: ACI 440.1R-15, CSA S806-12, and CSA S6-14. In the test setup, the maximum shear force occurred at the arch apex and equaled half of the applied load. The shear strength of NCG13L was 136.2 kN, based on the peak load values listed in Table 5.4. All standards calculate the shear strength as the sum of contributions from concrete and stirrups, with the allowable strain in stirrups limited to ensure composite action. Specifically, ACI 440.1R-15 and CSA S806-12 set the stirrup strain limit at 0.004, while CSA S6-14 sets it at 0.005, but none shall exceed the rupture strain of the FRP stirrups. Concrete contributions to shear strength were calculated as 16.23 kN, 22.32 kN, and 28.58 kN, while stirrup contributions were 12.09 kN, 10.07 kN, and 13.42 kN, according to ACI 440.1R-15, CSA S806-12, and CSA S6-14, respectively. Thus, the total design shear strengths were 28.32 kN, 32.38 kN, and 42.0 kN for the respective standards.

The comparison results indicate that all standards provide conservative estimates, with shear strength ratios of 4.81, 4.21, and 3.24 for ACI 440.1R-15, CSA S806-12, and CSA S6-14, respectively (ACI 440.1R-15, 2015; CSA S806-12, 2012; CSA S6-14, 2014). These calculations were based on the tested material properties without considering structural or material reduction factors. The discrepancies stem from two main reasons: inadequate consideration of compressive stress to shear resistance in compression-flexure members and overly conservative service strain limits for FRP shear reinforcement when applied to the proposed stirrups manufactured via filament winding technology. Further research is required to better understand the behavior and

shear strength of FRP-RC members reinforced with these novel stirrups, subjected to combined shear load, bending moment, and axial loads.

## **5.4 CONCLUSIONS**

This chapter presents a research program investigating the feasibility of a novel FRP-reinforced concrete arch design that combines over-reinforced configurations and tailored stirrups to address load drop issues inherent in FRP-RC structures. A series of laboratory tests were conducted to evaluate the effects of longitudinal reinforcement ratio, concrete strength, and transverse reinforcement ratio in this hybrid system. The behavior of the novel arches was analyzed alongside that of a reference steel-RC arch. Based on experimental observations and theoretical insights, the following conclusions are drawn:

1. The combination of an over-reinforced configuration and novel stirrups effectively eliminates the load-drop.
2. Primary failure modes of over-reinforced FRP-RC arches are flexural failure due to concrete crushing and shear failure caused by FRP stirrup rupture. The failure mechanisms are progressive, with initial cracks forming at the crown, followed by successive cracks at the shoulders.
3. An evaluation method for the SLS of FRP-RC arches was developed based on the provisions of ACI 440.11. The evaluation criteria include deflection limit, crack width limit, stress limit due to creep rupture, and environmental reduction factor for strength. Among these, the crack width limit appears to be the primary determinant for establishing the allowable service load.
4. The ultimate limit state and serviceability limit state are key criteria in designing over-reinforced concrete arches. Enhancing both concrete strength and reinforcement ratio increases

allowable service load, ultimate load and stiffness response, whereas reducing the reinforcement ratio while increasing concrete strength can improve the efficiency of longitudinal FRP bars. Although the FRP-RC arch exhibits slightly lower structural stiffness compared to the steel-RC arch, it shows comparable load-bearing capacity under similar reinforcement ratios and concrete strengths.

5. Current standards offer conservative predictions for the shear strength of novel FRP-RC arches, primarily due to insufficient consideration of compressive stress contribution to shear resistance in compression-flexure members and the overly conservative service strain limits imposed on the novel FRP stirrups manufactured via filament winding technology.

## 5.5 REFERENCES

- Achillides Z and Pilakoutas K. (2004) Bond behavior of fiber reinforced polymer bars under direct pullout conditions. *Journal of Composites for Construction* 8(2): 173-181.
- ACI 440.1R-15. (2015) *Guide for the Design and Construction of Structural Concrete Reinforced with Fiber-Reinforced Polymer Bars*. Farmington Hills, Michigan: American Concrete Institute (ACI), USA.
- ACI 440.3R-12. (2012) *Guide Test Methods for Fiber-Reinforced Polymers (FRPs) for Reinforcing or Strengthening Concrete Structures*. Farmington Hills, Michigan: American Concrete Institute (ACI), USA.
- ACI 440.11R-22. (2022) *Building Code Requirements for Structural Concrete Reinforced with Glass Fiber-Reinforced Polymer (GFRP) Bars*. Farmington Hills, Michigan: American Concrete Institute (ACI), USA.
- ASTM C143/C143M-15. (2015) *Standard Test Method for Slump of Hydraulic-cement Concrete*. West Conshohocken, PA: American Society for Testing and Materials (ASTM), USA.
- ASTM C469/469M-14. (2014) *Standard Test Method for Static Modulus of Elasticity and Poisson's Ratio of Concrete in Compression*. West Conshohocken, PA: American Society for Testing and Materials (ASTM), USA.
- Baena M, Torres L, Turon A, et al. (2009) Experimental study of bond behaviour between concrete and FRP bars using a pull-out test. *Composites Part B: Engineering* 40(8): 784-797.

- Barris C, Torres L, Comas J, et al. (2013) Cracking and deflections in GFRP RC beams: an experimental study. *Composites Part B: Engineering* 55: 580-590.
- Barris C, Torres L, Vilanova I, et al. (2017) Experimental study on crack width and crack spacing for Glass-FRP reinforced concrete beams. *Engineering Structures* 131: 231-242.
- Bilotta A, Ceroni F, Di Ludovico M, et al. (2011) Bond efficiency of EBR and NSM FRP systems for strengthening concrete members. *Journal of Composites for Construction* 15(5): 757-772.
- Blazy J and Blazy R. (2021) Polypropylene fiber reinforced concrete and its application in creating architectural forms of public spaces. *Case Studies in Construction Materials* 14: e00549.
- Borosnyói A and Balázs GL. (2005) Models for flexural cracking in concrete: the state of the art. *Structural Concrete* 6(2): 53-62.
- Borosnyoi A and Snóbli I. (2010) Crack width variation within the concrete cover of reinforced concrete members. *Építőanyag* 62(3): 70-74.
- Cai YJ, Xiao SH, Chen YW, et al. (2023) Tensile behavior and durability prediction of GFRP-steel composite bars under chloride environments. *Journal of Materials Research and Technology* 23: 5746-5759.
- Caratelli A, Meda A, Rinaldi Z, et al. (2016) Precast tunnel segments with GFRP reinforcement. *Tunnelling and Underground Space Technology* 60: 10-20.
- Caratelli A, Meda A, Rinaldi Z, et al. (2017) Optimization of GFRP reinforcement in precast

- segments for metro tunnel lining. *Composite Structures* 181: 336-346.
- Chellapandian M, Mani A and Prakash SS. (2020) Effect of macro-synthetic structural fibers on the flexural behavior of concrete beams reinforced with different ratios of GFRP bars. *Composite Structures* 254: 112790.
- CSA S6-14. (2014) *Canadian Highway Bridge Design Code*. Toronto, Ontario: Canadian Standards Association (CSA), Canada.
- CSA S806-12. (2012) *Design and Construction of Building Components with Fiber Reinforced Polymers*. Toronto, Ontario: Canadian Standards Association (CSA), Canada.
- De Rivat B, Giamundo N, Meda A, et al. (2019) Hybrid solution with fiber reinforced concrete and glass fiber reinforced polymer rebars for precast tunnel segments. *Proceedings of Tunnels and Underground Cities: Engineering and Innovation Meet Archaeology, Architecture and Art*. CRC Press, 2018-2025.
- Dong HL, Wang DY, Wang ZY, et al. (2018) Axial compressive behavior of square concrete columns reinforced with innovative closed-type winding GFRP stirrups. *Composite Structures* 192: 115-125.
- Dong ZQ, Liu ZQ, Wu G, et al. (2022) Study on mechanical properties of seawater sea-sand coral aggregate concrete-filled BFRP tubular arches. *Advances in Structural Engineering* 25(9): 1851-1865.
- EN 1992-1-1:2023. (2023) *Eurocode 2: Design of Concrete Structures-Part 1-1: General Rules and Rules for Buildings, Bridges and Civil Engineering Structures*. British Standard

Institution, London, UK.

EN ISO 15630-1. (2019) *Steel for the Reinforcement and Prestressing in Concrete. Part 1: Reinforcing bars, wire rod and wire*. Berlin, Germany.

GB 50608-20. (2010) *Technical Code for Infrastructure Application of FRP Composites*. China Architecture & Building Press, Beijing, China.

GB 50010. (2015) *Standard for Design of Concrete Structures*. Ministry of Housing and Urban-Rural Development of PRC, Beijing, China.

GB 50017. (2017) *Standard for Design of Steel Structures*. Ministry of Housing and Urban-Rural Development of PRC, Beijing, China.

GB/T 3632-2008. (2008) *Sets of Torshear Type High Strength Bolt Hexagon Nut and Plain Washer for Steel Structures*. Standards Press of China, Beijing, China.

Hosseini SM, Mousa S, Mohamed HM, et al. (2022) Experimental and analytical study on precast high-strength concrete tunnel lining segments reinforced with GFRP bars. *Journal of Composites for Construction* 26(5): 04022062.

Hosseini SM, Mousa S, Mohamed HM, et al. (2023) Experimental and analytical investigation of precast fiber-reinforced concrete (FRC) tunnel lining segments reinforced with glass-FRP bars. *Tunnelling and Underground Space Technology* 139: 105230.

Lee C, Ko M and Lee Y. (2014) Bend strength of complete closed-type carbon fiber-reinforced polymer stirrups with rectangular section. *Journal of Composites for Construction* 18(1):

04013022.

Lee JY, Kim TY, Kim TJ, et al. (2008) Interfacial bond strength of glass fiber reinforced polymer bars in high-strength concrete. *Composites Part B: Engineering* 39(2): 258-270.

Liu T, Feng P, Wu Y, et al. (2021) Developing an innovative curved-pultruded large-scale GFRP arch beam. *Composite Structures* 256: 113111.

Maranan GB, Manalo AC, Benmokrane B, et al. (2018) Shear behaviour of geopolymer-concrete beams transversely reinforced with continuous rectangular GFRP composite spirals. *Composite Structures* 187: 454-465.

Marcos-Meson V, Fischer G, Edvardsen C, et al. (2019) Durability of Steel Fibre Reinforced Concrete (SFRC) exposed to acid attack—A literature review. *Construction and Building Materials* 200: 490-501.

Marcos-Meson V, Michel A, Solgaard A, et al. (2018) Corrosion resistance of steel fibre reinforced concrete-A literature review. *Cement and Concrete Research* 103: 1-20.

Meda A, Rinaldi Z, Spagnuolo S, et al. (2019) Hybrid precast tunnel segments in fiber reinforced concrete with glass fiber reinforced bars. *Tunnelling and Underground Space Technology* 86: 100-112.

Meda A, Rinaldi Z, Spagnuolo S, et al. (2020) Experimental behaviour of precast tunnel segments in steel fiber reinforcement with GFRP rebars. *Fib Bulletin*: 153-162.

Mofidi A and Chaallal O. (2011) Shear strengthening of RC beams with externally bonded FRP

- composites: Effect of strip-width-to-strip-spacing ratio. *Journal of Composites for Construction* 15(5): 732-742.
- Pérez Caldentey A, Corres Peiretti H, Peset Iribarren J, et al. (2013) Cracking of RC members revisited: influence of cover,  $\phi/\rho_s$ ,  $e_f$  and stirrup spacing—an experimental and theoretical study. *Structural Concrete* 14(1): 69-78.
- Raza A, El Ouni MH, Ali L, et al. (2022) Structural evaluation of recycled aggregate concrete circular columns having FRP rebars and synthetic fibers. *Engineering Structures* 250: 113392.
- Singhal S, Chourasia A and Parashar J. (2020) Anchorage behaviour of headed bars as connection system for precast reinforced concrete structural components. *Structures* 27: 1405-1418.
- Soltanzadeh F, Behbahani AE, Hosseinmostofi K, et al. (2022) Assessment of the sustainability of fibre-reinforced concrete by considering both environmental and mechanical properties. *Sustainability* 14(10): 6347.
- Spadea S, Orr J and Ivanova K. (2017) Bend-strength of novel filament wound shear reinforcement. *Composite Structures* 176: 244-253.
- Spagnuolo S, Meda A, Rinaldi Z, et al. (2018) Curvilinear GFRP bars for tunnel segments applications. *Composites Part B: Engineering* 141: 137-147.
- Tang ZX, Zhou YZ, Feng J, et al. (2021) Concrete protective arches reinforced with BFRP bars: Construction and quasi-static structural performances. *Tunnelling and Underground Space Technology* 108: 103731.

- Tang ZX, Zhou YZ, Feng J, et al. (2020) Blast responses and damage evaluation of concrete protective arches reinforced with BFRP bars. *Composite Structures* 254: 112864.
- Wang P, Chen HL, Zhou JN, et al. (2018) Failure mechanisms of CFRP-wrapped protective concrete arches under static and blast loadings: Experimental research. *Composite Structures* 198: 1-10.
- Xia ZY, Jiang T and Yu T. (2023a) Innovating arch structures with fiber-reinforced polymer composites: A review. *Advances in Structural Engineering* 26(13): 2341-2358.
- Xia ZY, Yu T and Jiang T. (2023b) Behaviour of FRP-reinforced concrete arches behavior. *Proceedings of 11th International Conference on Fibre-Reinforced Polymer (FRP) Composites in Civil Engineering*. Rio de Janeiro, Brazil: International Institute for FRP in Construction (IIFC), 1347-1354.
- Xiao SH, Cai YJ, Xie ZH, et al. (2024) Bond durability between steel-FRP composite bars and concrete under seawater corrosion environments. *Construction and Building Materials* 419: 135456.
- Yin S, Tuladhar R, Shi F, et al. (2015) Use of macro plastic fibres in concrete: A review. *Construction and Building Materials* 93: 180-188.
- Zeng JJ, Zeng WB, Ye YY, et al. (2022) Flexural behavior of FRP grid reinforced ultra-high-performance concrete composite plates with different types of fibers. *Engineering Structures* 272: 115020.
- Zerbino R, Monetti DH and Giaccio G. (2016) Creep behaviour of cracked steel and macro-

synthetic fibre reinforced concrete. *Materials and Structures* 49: 3397-3410.

Zhang X, Wang P, Jiang M, et al. (2015) CFRP strengthening reinforced concrete arches: Strengthening methods and experimental studies. *Composite Structures* 131: 852-867.

Table 5.1 Experimental program

Specimen ID	Flexural reinforcement		Transverse reinforcement		Concrete strength
	Longitudinal bar	Reinforcement ratio (%)	Stirrup	Reinforcement ratio (%)	
NCS12H	steel bar 3 $\Phi$ 12/3 $\Phi$ 12	2.26	steel stirrup D8@50	0.67	Normal-strength
NCG13H	GFRP bar 3 $\Phi$ 13/3 $\Phi$ 13	2.65	novel FRP stirrup 3D4 $\times$ 15@50	2.40	Normal-strength
NCG8H	GFRP bar 3 $\Phi$ 8/3 $\Phi$ 8	1.01	novel FRP stirrup 3D4 $\times$ 15@50	2.40	Normal-strength
NCG13L	GFRP bar 3 $\Phi$ 13/3 $\Phi$ 13	2.65	novel FRP stirrup 3D1 $\times$ 10@50	0.40	Normal-strength
HCG13H	GFRP bar 3 $\Phi$ 13/3 $\Phi$ 13	2.65	novel FRP stirrup 3D4 $\times$ 15@50	2.40	High-strength

Table 5.2 Mechanical properties of reinforcement and concrete

Components	Material	Nominal dimensions (mm)	Fiber content	(Yield/) Ultimate strength (MPa)	Elastic modulus (GPa)	Elongation
Longitudinal bar	Steel	D12	-	546.77/637.28	182.37	12.72%
Longitudinal bar	GFRP	D8	75%	1100.20	54.92	2.00%
Longitudinal bar	GFRP	D13	75%	919.67	51.32	1.79%
Thin stirrup	GFRP	H60 $\times$ B10 $\times$ T1	70%	477.93	44.26	1.08%
Thick stirrup	GFRP	H60 $\times$ B15 $\times$ T4	70%	-	40.18	-
Normal-strength concrete	Concrete	D150 $\times$ H300	-	51.85	31.37	2.39%
High-strength concrete	Concrete	D150 $\times$ H300	-	63.77	31.80	2.23%

Table 5.3 Results of pullout tests on GFRP bars

Specimens	Concrete strength	Diameter (mm)	Bond strength (MPa)	Slip corresponding to bond strength (mm)	$\alpha_{frp}$	$p$	$S_{frp,2}$
PNCG8	Normal-strength	8	12.41	0.17	0.283	0.07	0.94
PNCG13	Normal-strength	13	17.14	0.47	0.283	0.05	5.54
PHCG13	High-strength	13	17.68	0.29	0.283	0.02	8.31

Table 5.4 Experimental results

Specimen ID	Peak load	Deflection at crown corresponding to peak load	Failure mode	Efficiency factor (%)	Allowable service load
NCS12H	279.6	13.13	Flexural failure	-	-
NCG13H	225.6	11.71	Flexural failure	46.82	80.9
NCG8H	194.9	10.72	Flexural failure	49.96	56.1
NCG13L	272.3	14.38	Shear failure	54.87	72.3
HCG13H	257.5	12.98	Flexural failure	51.45	88.9

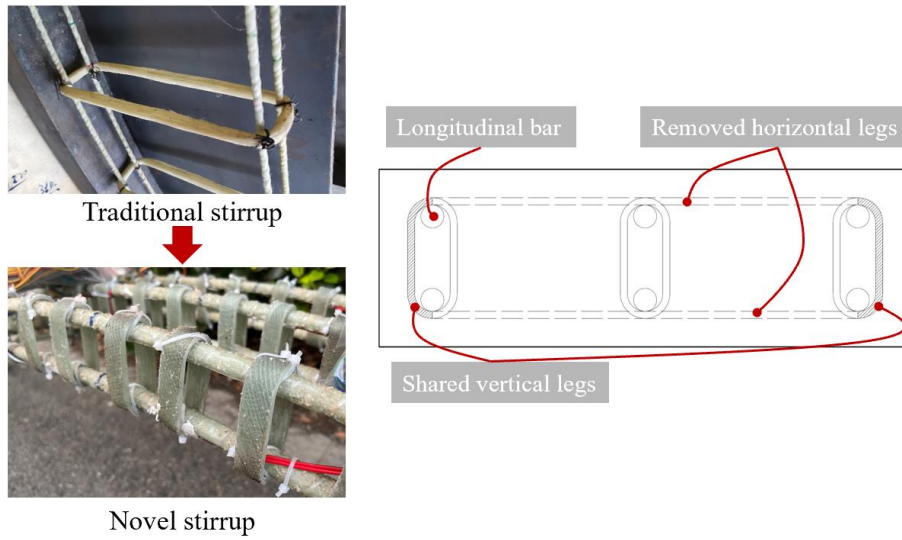
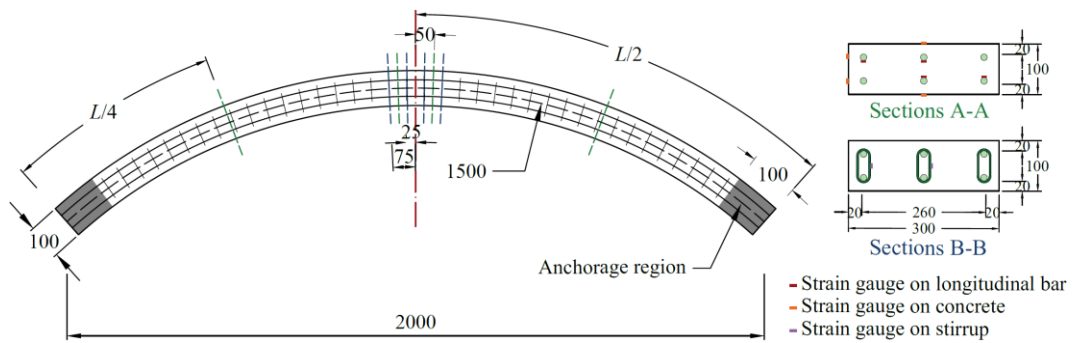
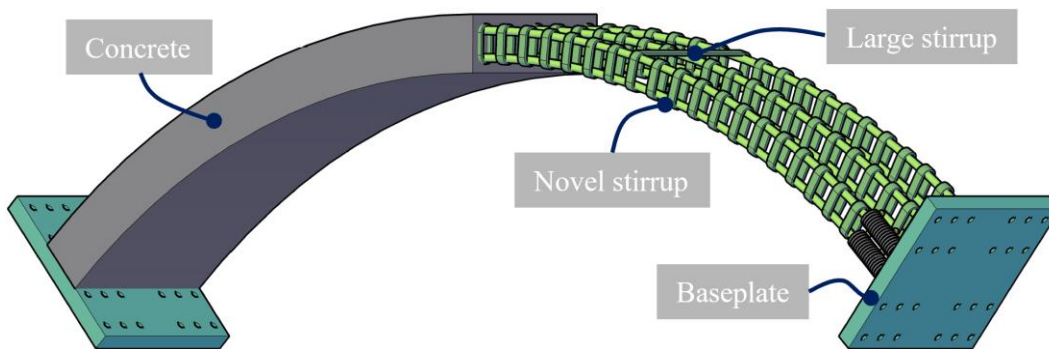


Figure 5.1 Stirrup evolution for novel configuration

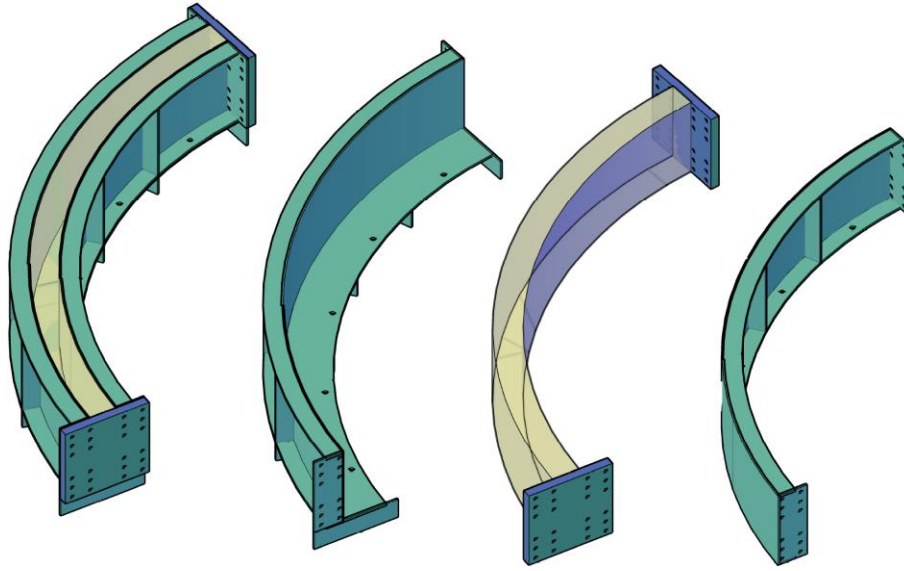


(a) Geometric dimensions and strain-gauge locations (dimensions in mm)

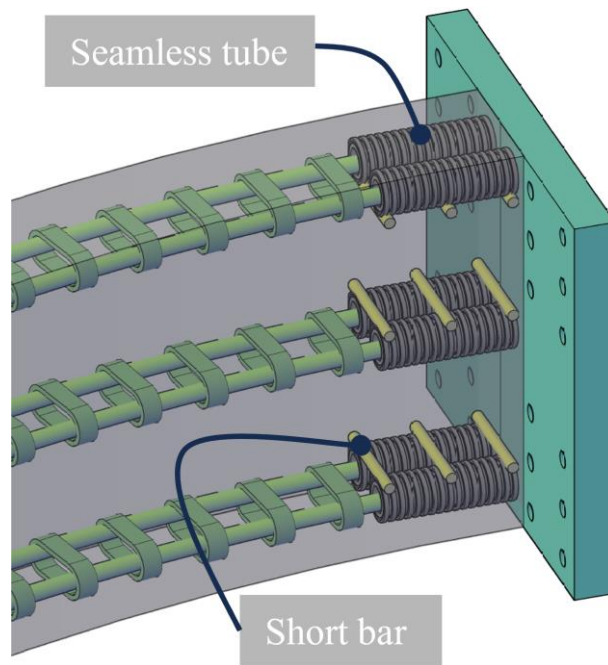


(b) Typical configuration of GFRP-RC arch specimen

Figure 5.2 GFRP-RC arch specimens



(a) Configuration of casting molds for concrete arches



(b) Anchoring system for FRP bars



(c) Layout of reinforcement and lifting hooks

Figure 5.3 Details of arch specimens



(a) Before casting



(b) After casting

Figure 5.4 Concreting casting

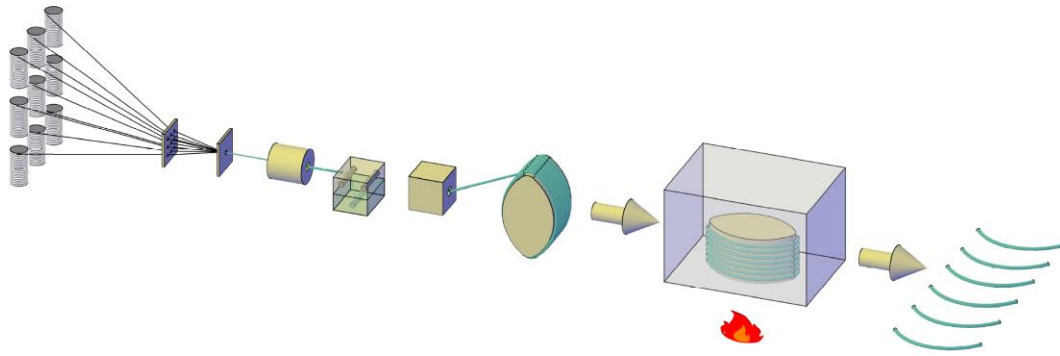
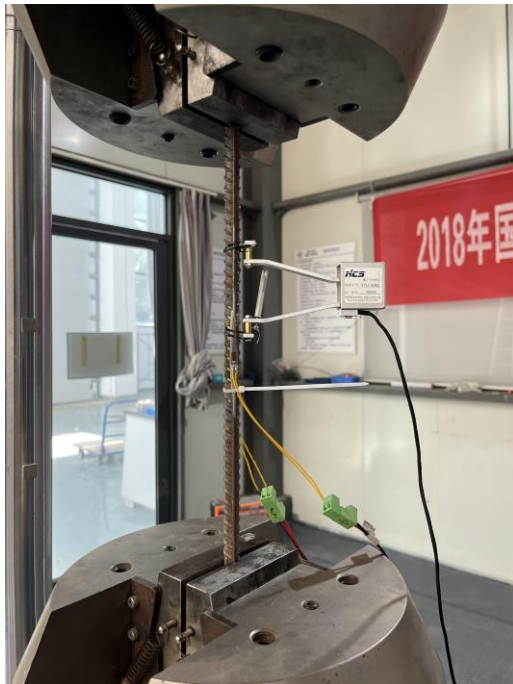


Figure 5.5 Production process of curved FRP bars

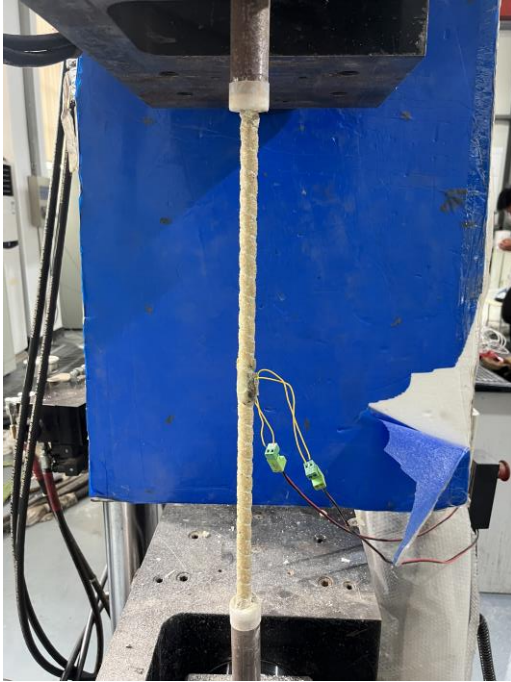


(a) Test setup



(b) Typical failure mode

Figure 5.6 Tensile tests on steel bars



(a) Test setup



(b) Typical failure mode

Figure 5.7 Tensile tests on GFRP bars

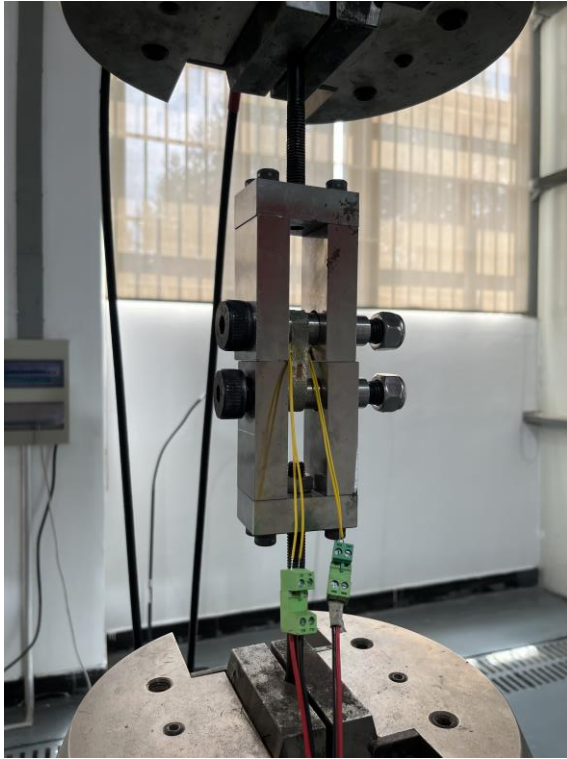


(a) Front view

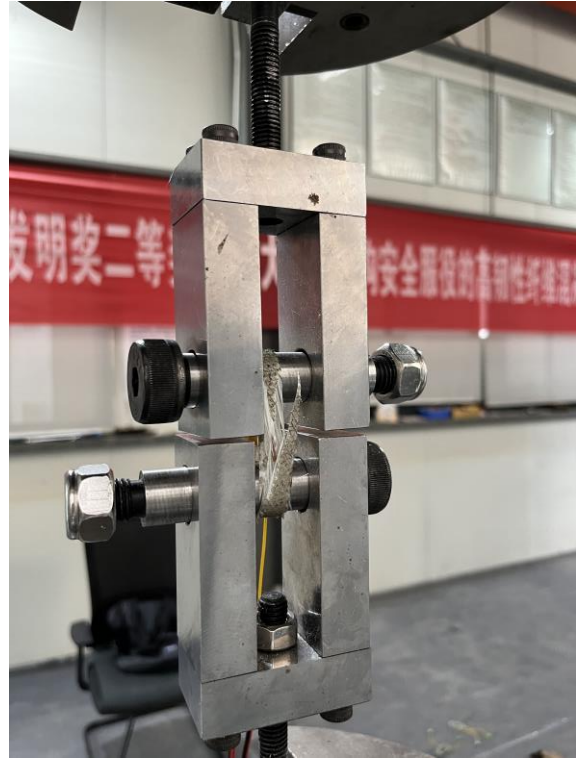


(b) Lateral view

Figure 5.8 Production of novel FRP stirrups



(a) Test setup



(b) Typical failure mode

Figure 5.9 Tensile tests on novel FRP stirrups



(a) Test setup



(b) Typical failure mode

Figure 5.10 Compressive tests on concrete



(a) C45



(b) C65

Figure 5.11 Slump tests on concrete

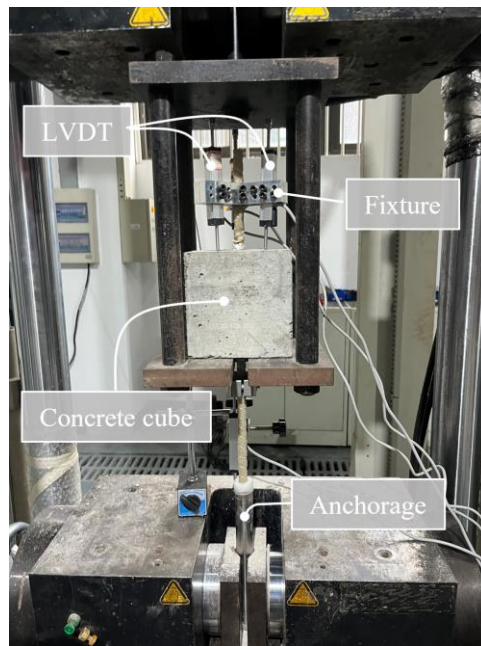
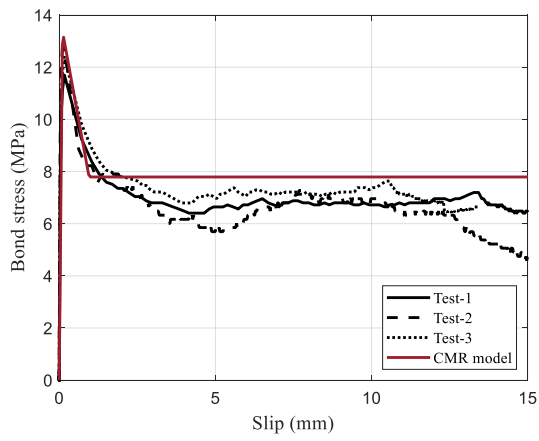
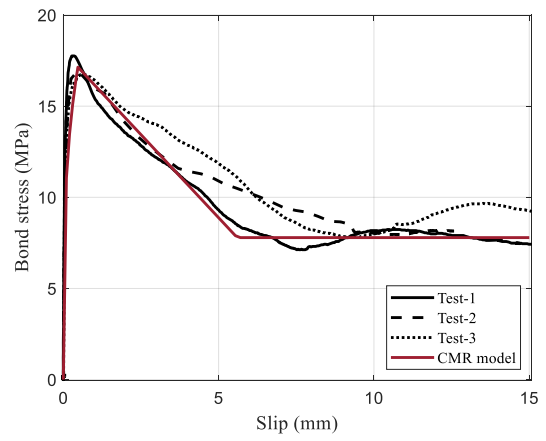


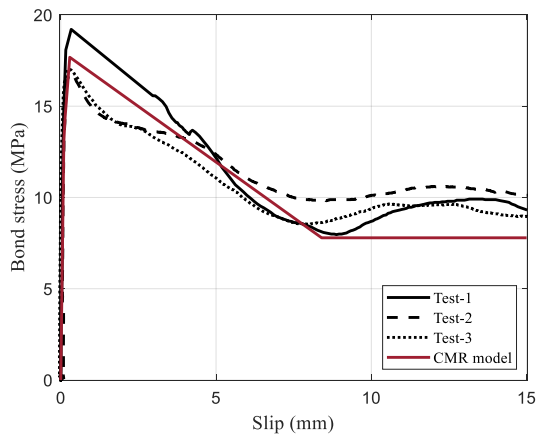
Figure 5.12 Test setup of pullout tests



(a) PNCG8

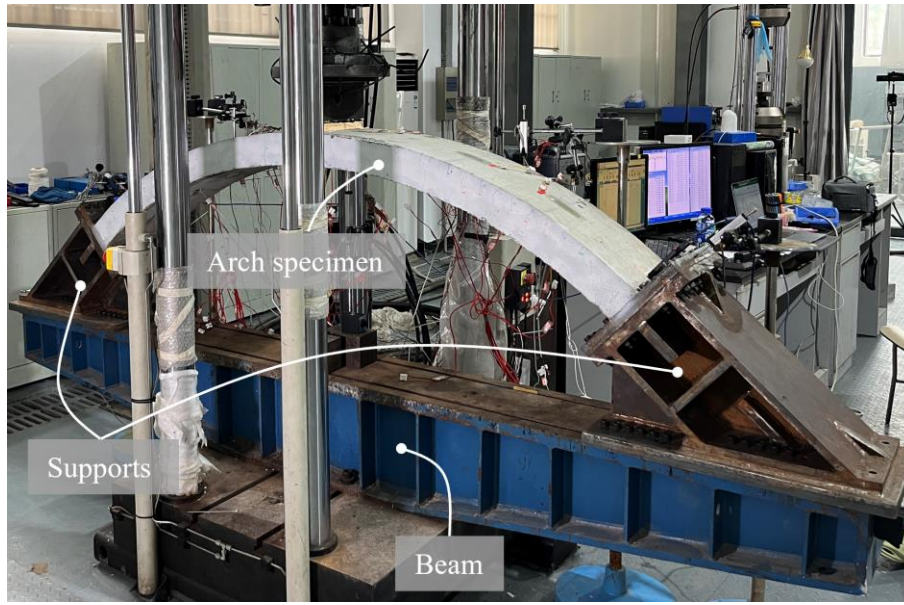


(b) PNCG13

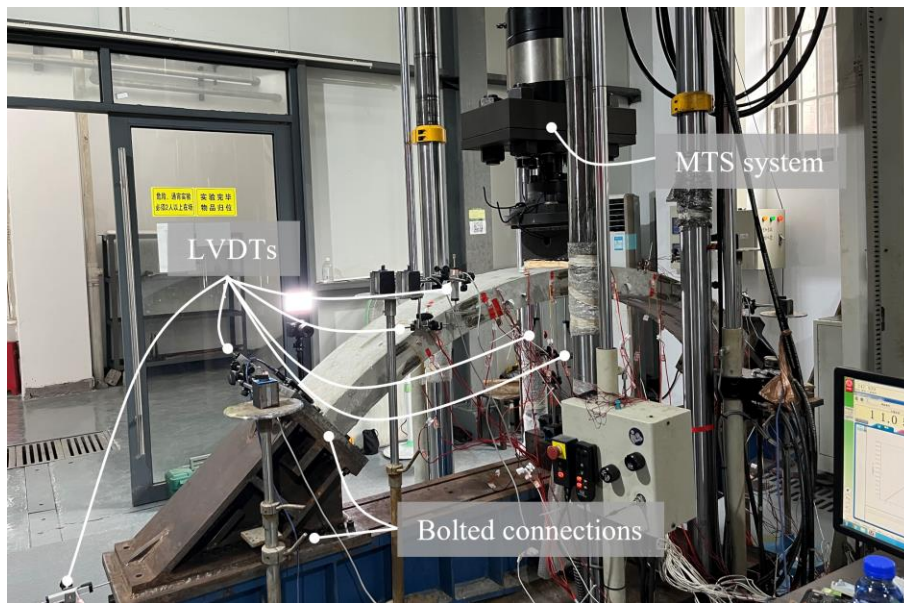


(c) PHCG13

Figure 5.13 Bond stress-slip curves for GFRP bars



(a) Front view



(b) Back view

Figure 5.14 Test setup of arch tests

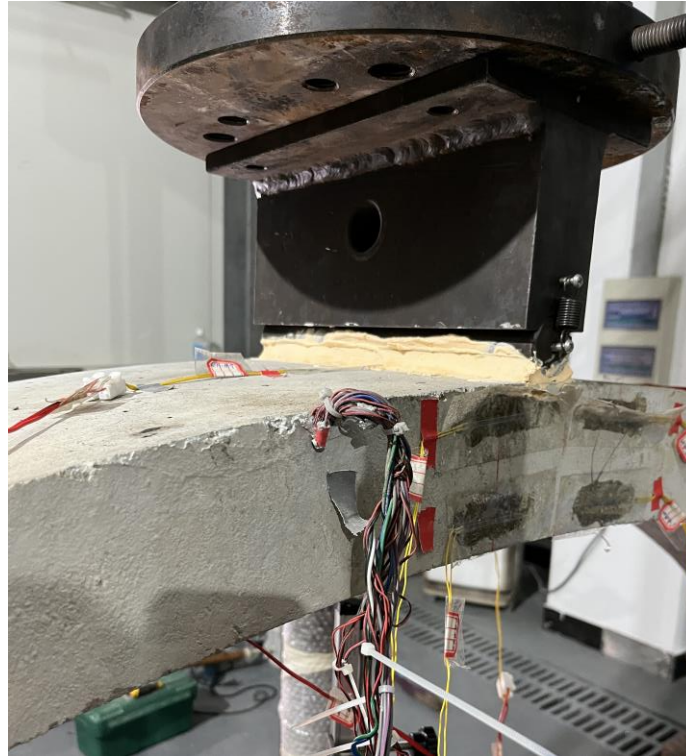


Figure 5.15 Arrangement at loading head

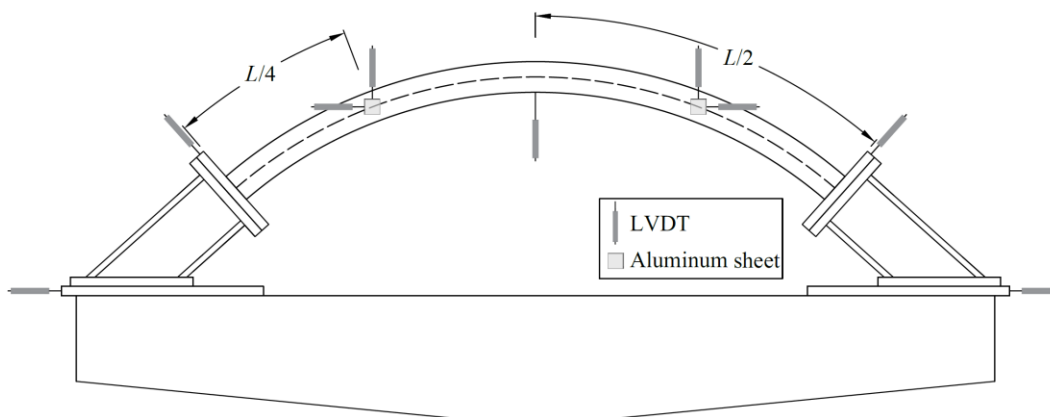
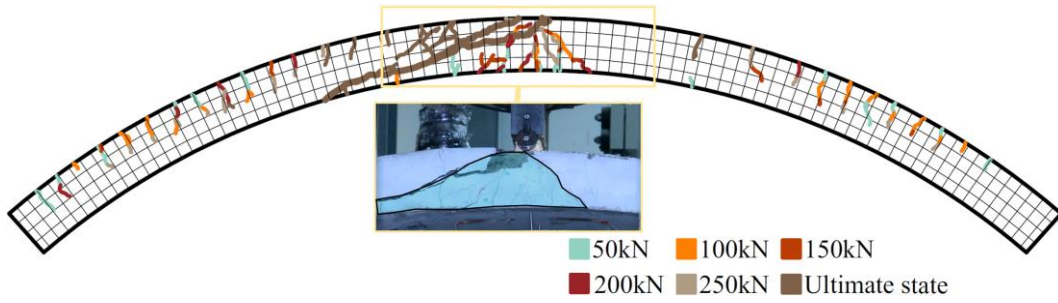
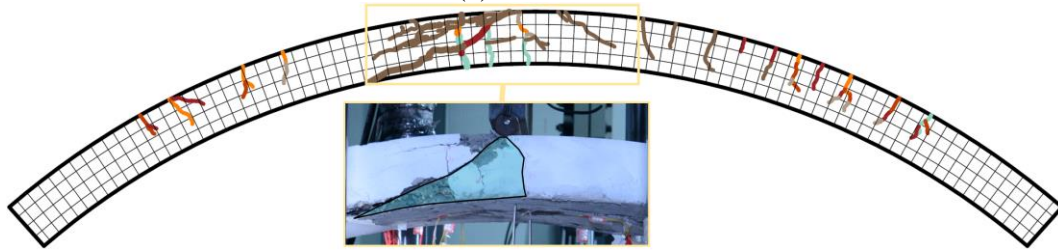


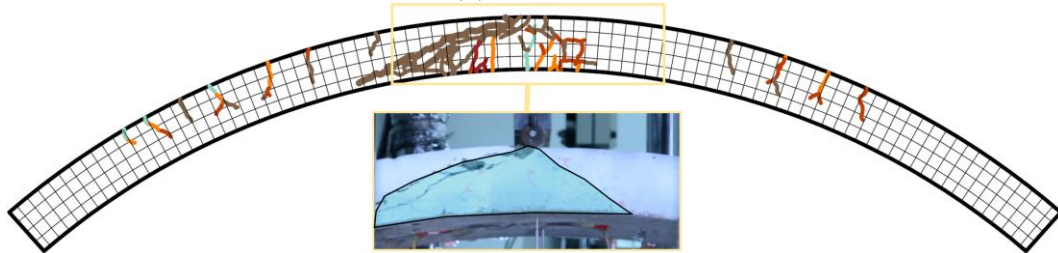
Figure 5.16 Layout of deflection measurement



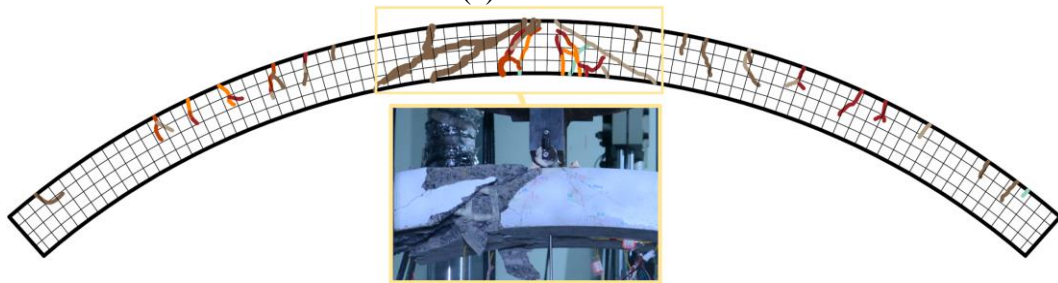
(a) NCS12H



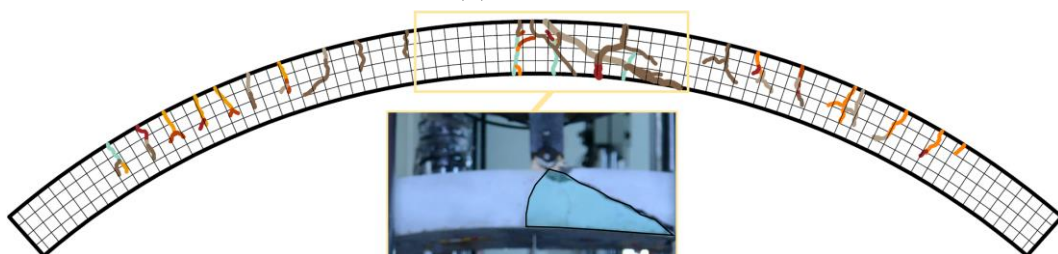
(b) NCG13H



(c) NCG8H



(d) NCG13L



(e) HCG13H

Figure 5.17 Cracking patterns and development paths

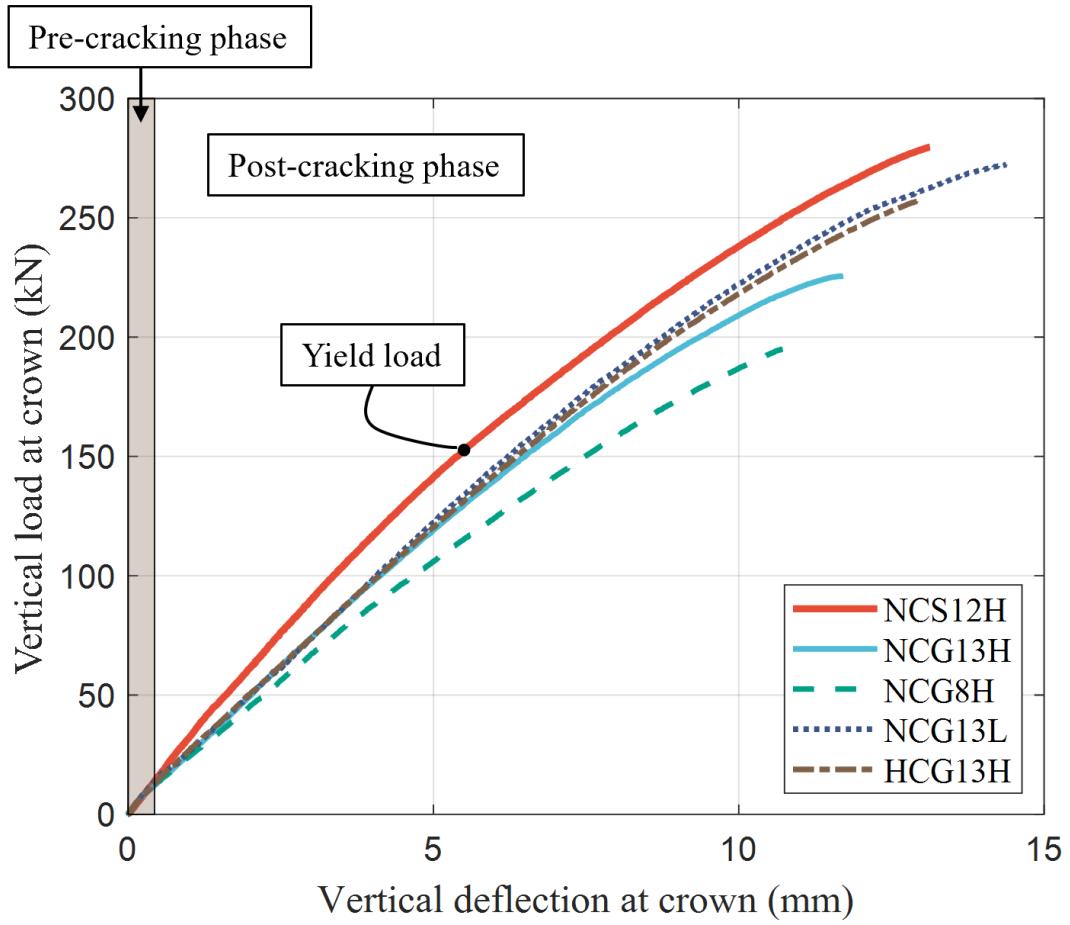
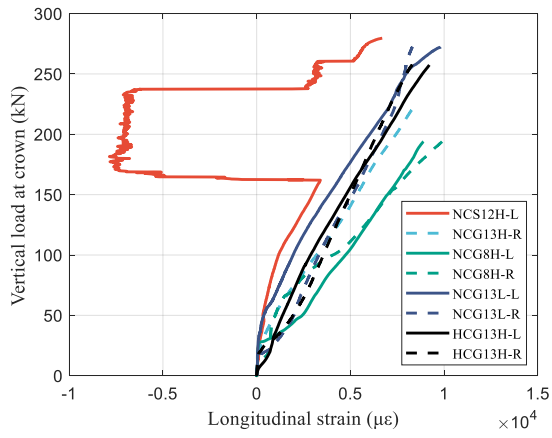
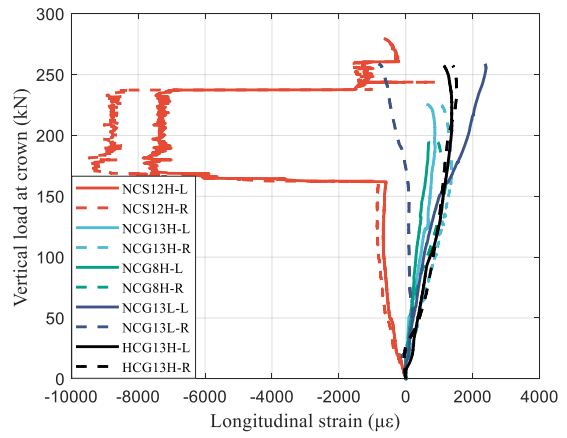


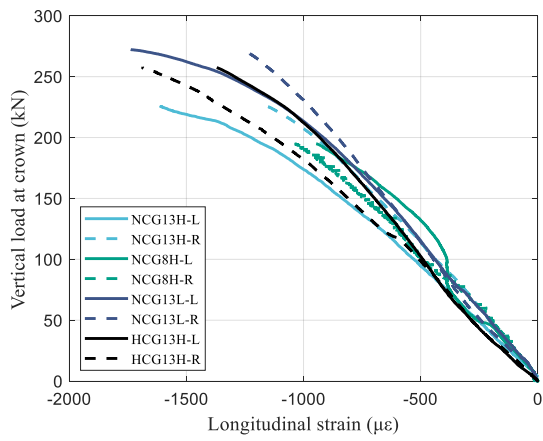
Figure 5.18 Load-deflection curves



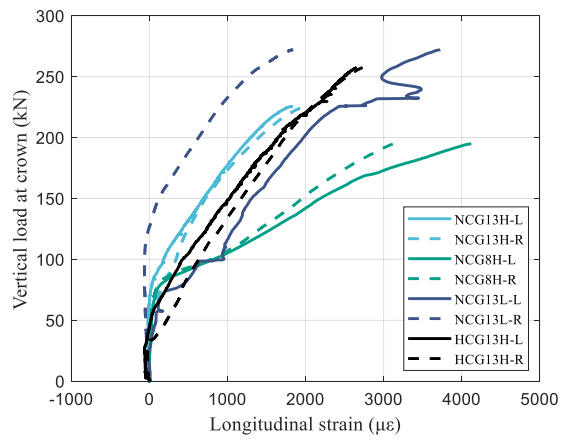
(a)  $L/2$  (Lower)



(b)  $L/2$  (Upper)

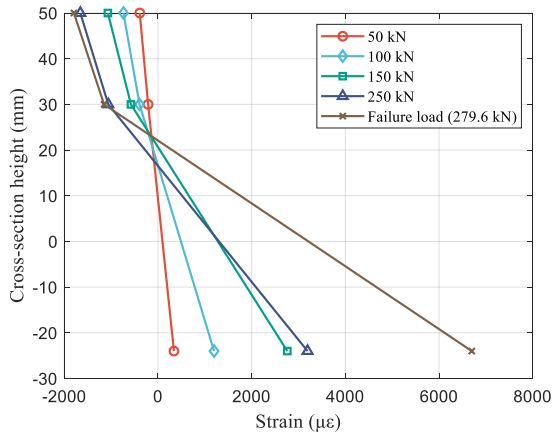


(c)  $L/4$  (Lower)

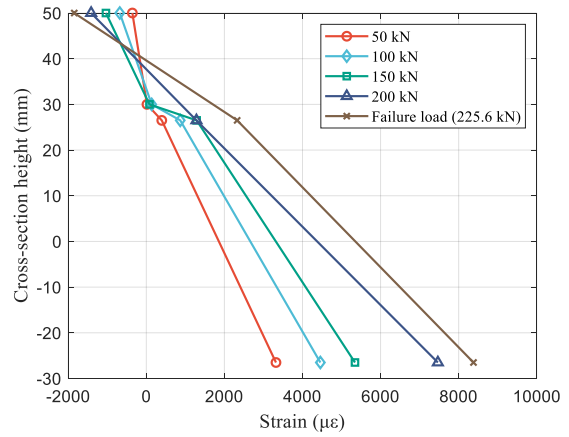


(d)  $L/4$  (Upper)

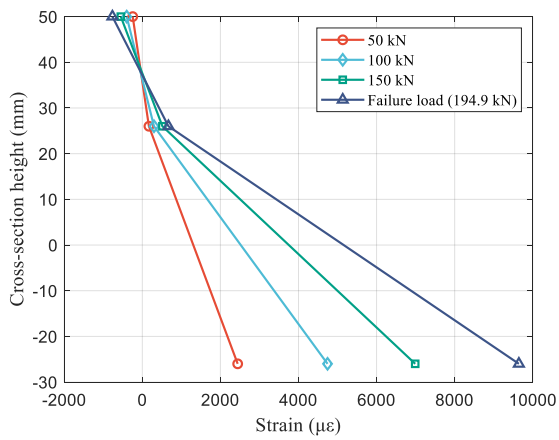
Figure 5.19 Load-strain relationship of longitudinal reinforcement



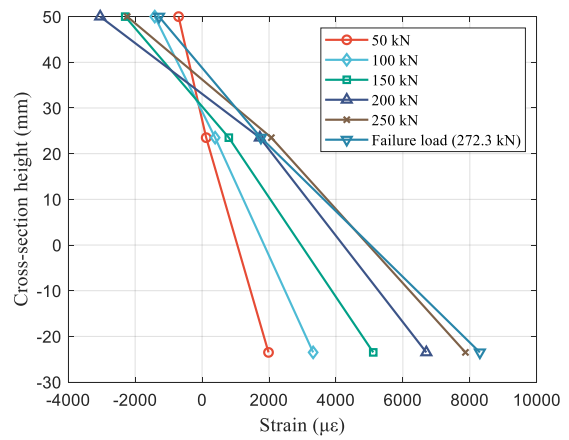
(a) NCS12H



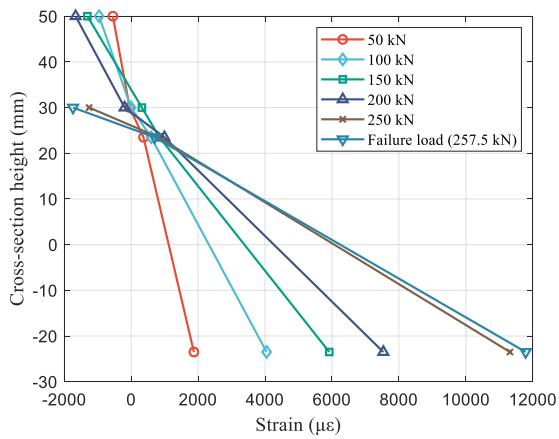
(b) NCG13H



(c) NCG8H



(d) NCG13L



(e) HCG13H

Figure 5.20 Sectional strain distribution at the arch apex

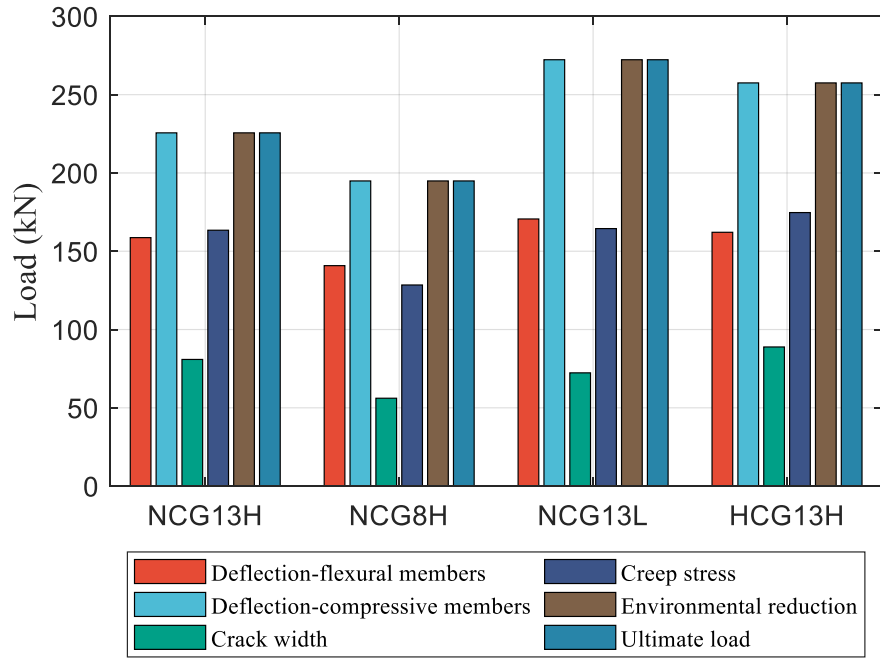


Figure 5.21 Serviceability analysis of FRP-RC arches

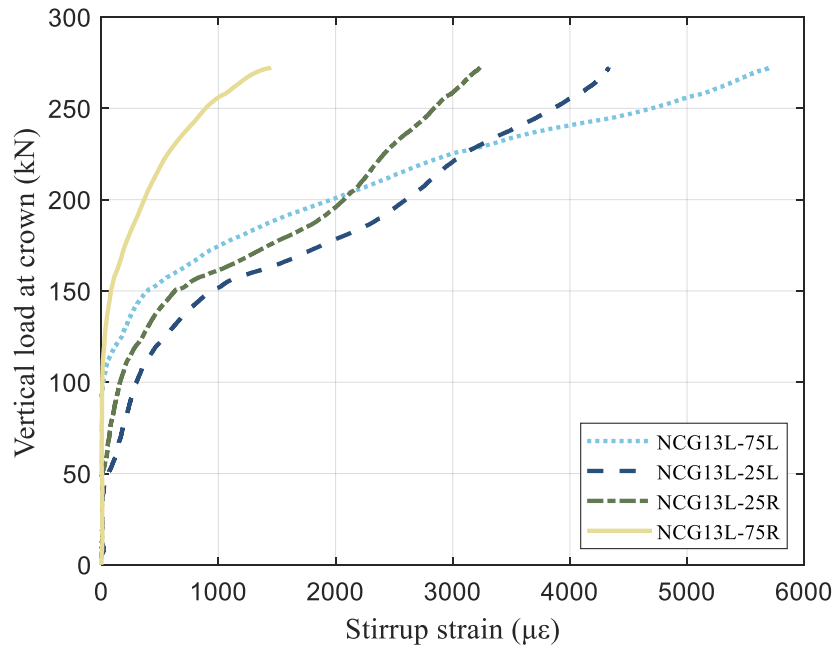


Figure 5.22 Strain development of FRP stirrups in NCG13L

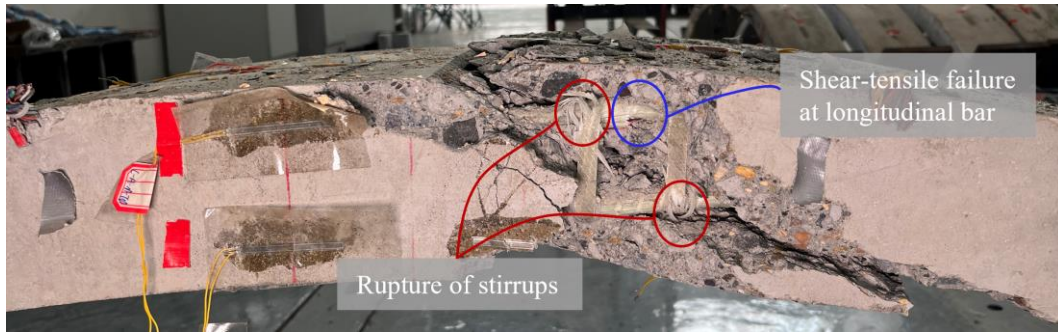


Figure 5.23 Failure at the arch crown of NCG13L (View from the back side)

# **CHAPTER 6**

## **THEORETICAL MODEL**

### **FOR FRP REINFORCED CONCRETE ARCHES**

### **AND OTHER FRP-ENABLED ARCHES**

## **6.1 INTRODUCTION**

### **6.1.1 Numerical simulation**

Chapter 5 of this thesis experimentally investigates the behavior of GFRP bar-reinforced concrete (GFRP-RC) arches, demonstrating that an over-reinforced configuration combined with a novel stirrup design effectively mitigates load drops upon concrete cracking. Furthermore, it was found that increasing concrete strength and reinforcement ratios enhance allowable service load, ultimate load, and stiffness response of GFRP-RC arches.

However, such experimental studies face significant challenges, including the need for large laboratory space, substantial costs, and considerable time requirements. In contrast, numerical simulation offers a cost-effective and time-efficient approach to replicating the experimental responses of FRP-RC members under various loading conditions, enabling comprehensive parametric studies (Salih and Zhou, 2019; Attia et al., 2020; Huang et al., 2021). However, only a few numerical studies specifically focused on the behavior of FRP-RC arches (Wu et al., 2022;

Xia et al., 2024). For dynamic responses, Wu et al. (2022) successfully replicated blast tests on shallow-buried FRP-RC arches using the LS-DYNA numerical method, demonstrating that increasing the diameter of FRP bars reduces the displacement at the arch apex, particularly in scenarios involving large standoff distances and small explosion mass.

To gain a more comprehensive understanding of the structural behavior of FRP-RC arches under static/quasi-static loading, two advanced analytical methods were proposed: an enhanced method for one-dimensional theoretical modeling in Chapter 6 and a three-dimensional FE simulation approach in Chapter 7. The one-dimensional model, based on a simplified approach using the deflection method, provides a relatively straightforward and intuitive tool for understanding the fundamental mechanical behavior of FRP-RC arches. It is particularly useful for preliminary structural design, allowing rapid estimates of deflections and internal forces to verify design assumptions. In contrast, the three-dimensional FE model effectively captures the complex interactions of axial load, shear, and bending moments, as well as the bond-slip behavior between FRP reinforcement and surrounding concrete, enabling detailed analysis of complex geometries.

This chapter focuses on a one-dimensional theoretical model based on an enhanced deflection method. The motivation behind developing the theoretical model largely stems from the author's curiosity in investigating the structural behavior of FRP-RC arches. The test data for GFRP-RC arches were used to verify the proposed model. To further validate the model and expand its application, some representative forms of innovative arch structures enabled by the use of fiber-reinforced polymer (FRP) composites were also included as case studies.

These structural forms, which are referred to as FRP-enabled arches, are made possible or enhanced by the use of FRP. In Chapter 2, the author identified two sub-categories of FRP-enabled

arches: all-FRP arches and FRP-incorporating hybrid arches (Xia et al., 2023). The former takes advantage of FRP's lightweight feature, making them ideal for small- or medium-scale applications where construction speed is a key consideration, such as lightweight footbridges and roofs (Sobrino and Pulido, 2002; Caron et al., 2009; Potyrala, 2011; Pyrzowski and Miśkiewicz, 2017; Bell et al., 2020; Liu et al., 2021; Liu et al., 2022). The latter is mainly intended for large-scale applications, such as long-span arch bridges and tunnel linings, where FRP is used in combination with concrete to address the issue of steel corrosion and to achieve excellent mechanical performance (Caratelli et al., 2016; Tang et al., 2020; Lee and Shin, 2010; Dagher et al., 2012; Jiang, 2020; Dong et al., 2022).

### **6.1.2 Deflection method**

Structural members with a longitudinal dimension much greater than their transverse dimensions are commonly referred to as one-dimensional members. These members can be categorized as straight members (e.g., slabs, beams and columns) or curvilinear members (e.g., curved beams and arches), depending on the shape of their longitudinal axis (i.e., centroidal axis). In structural analysis, one-dimensional members are commonly characterized by their centroidal axis, which serves as an important reference line for analyzing their behavior.

The deflection method is a widely used technique for analyzing one-dimensional members (Chen and Atsuta, 2007). This method effectively determines the deformed shape of the centroidal axis (i.e., deflection curve) of the member under prescribed loading and boundary conditions. Its effectiveness and accuracy have been demonstrated by successful implementations in straight members (e.g., Shen and Lu, 1983; Jiang and Teng, 2012a; Gao et al., 2021). In this method, the centroidal axis is discretized into many short segments with critical points known as grid points,

which are typically located at the ends or midpoint of each segment. This discretization process transforms the continuous deflection curve problem into a discrete initial value problem where numerical procedures are used to solve for the unknown initial values, which are usually the support reactions or displacements at one end of the member.

The deflection method is traditionally based on the small displacement theory, which assumes that the deflection of the member is small compared to its length. This assumption enables simplification of the exact expression for curvature, provided that the centroidal axis of the member is initially straight or nearly so. In these cases, the curvature at any point on the deformed centroidal axis can be approximated as the second-order derivative of the deflection at this point. This simplification allows the deflection and slope at any grid point to be computed from known or assumed information (curvature, slope and deflection) at the previous one or two grid points, depending on the computation scheme employed. As a result, the deflection curve can be generated through a successive process, which involves section analysis at each grid point to determine the corresponding curvature required to proceed to the next grid point. Once the complete deflection curve is generated, boundary conditions are checked and necessary adjustments are repeatedly made to the initial guesses for the unknowns until the updated deflection curve satisfies the prescribed boundary conditions. Detailed descriptions of the conventional deflection method are available in various sources (Shen and Lu, 1983; Jiang and Teng, 2012b).

The use of simplified curvature representation in the conventional deflection method makes it appropriate for small-curvature problems, or more specifically, straight or slightly crooked one-dimensional members experiencing small displacement. However, its application becomes challenging when dealing with large-curvature problems, where the accuracy of the simplified

curvature expression diminishes. Large curvatures in one-dimensional members can arise from geometry-related factors, such as the initial curvatures in arches and curved beams, or from deformation-induced factors, where the large curvatures are developed in initially straight members due to large displacement. In some cases, it can be a combination of both factors.

To address the challenge posed by large-curvature problems, this chapter proposes a theoretical model based on an enhanced formulation of the deflection method. The enhanced formulation enables the model to offer a unified approach for handling both small- and large-curvature problems in one-dimensional members. The central insight of the enhanced formulation is that the deformed shape of each segment of the member can be approximated by a circular arc whose curvature and length are related to the internal axial force and bending moment acting on the segment's midpoint section. This assumption allows the deformed centroidal axis to be represented by a continuous curve consisting of a sequence of circular arcs, rather than only discretely by the transverse displacement of the grid points. Therefore, the requirement of exact curvature representation is intrinsically satisfied in the model formulation.

FRP-enabled arches well exemplify large-curvature problems. In particular, FRP bending-active arches provide a unique case where the large curvatures are deformation-induced, as they utilize FRP's outstanding elastic deformation ability to derive the arch shape through active bending of initially straight FRP profiles (Caron et al., 2009; Bessini et al., 2019; Habibi et al., 2022; Xie et al., 2023a).

The subsequent sections of this chapter are structured as follows. First, the formulation of the theoretical model is presented. This is followed by its verification through comparisons with analytical results of linear elastic arches, serving as an example of large-curvature problems, and

numerical results of slender FRP-confined RC columns, serving as an example of small-curvature problems. Next, the verified model is applied to FRP-RC arches presented in Chapter 5, as well as other representative cases of FRP-enabled arches, including all-FRP arches and FRP-incorporating hybrid arches, to illustrate large-curvature problems involving both initially-born and deformation-induced curvatures. Comparisons with test results from these cases demonstrate the model's ability to accurately predict the behavior of FRP-RC and other FRP-enabled arches. Finally, the limitations of the model are addressed, along with potential improvements aimed at overcoming these limitations.

## 6.2 MODEL FORMULATION

### 6.2.1 Discretization process

Figure 6.1 illustrates an arch with an arbitrary shape defined by its centroidal axis  $y = f(x)$ . To discretize the centroidal axis,  $n + 1$  grid points are used, transforming the original curved axis into  $n$  straight segments  $S_i$ , where  $i \in [1, n]$ . The first grid point represents the left support of the arch and serves as the origin of the coordinate system. The last grid point represents the right support and has coordinates  $(x_{n+1}, y_{n+1})$ . The two supports are usually at the same height, resulting in  $y_{n+1} = 0$ . However, non-zero values are also permitted to account for cases where the supports are at different heights. Intermediate grid points can be placed anywhere along the centroidal axis, following two general rules: (i). set a grid point wherever a concentrated force or bending moment is applied; and (ii). increase the number of grid points in regions with a sharp change in curvature or a sharp gradient of distributed load. The first rule facilitates model formulation and the second enhances model accuracy. Each segment's initial length  $L_{S_i}^0$  and orientation  $\theta_{S_i}^0$  relative to the  $x$ -axis can be easily computed from the grid points' coordinates. Properties of a segment are denoted

by symbols with a subscript  $S_i$ , and those of a grid point by symbols with a subscript  $i$ . Due to the adopted discretization scheme, each intermediate grid point corresponds to two inclination angles  $\theta_{i,l}$  and  $\theta_{i,r}$ , whose initial values are respectively equal to  $\theta_{S_{i-1}}^0$  and  $\theta_{S_i}^0$ . The difference between the two,  $\Delta\theta_i = \theta_{S_i}^0 - \theta_{S_{i-1}}^0$ , is computed for later use. The initial values of  $\theta_1$  and  $\theta_{n+1}$  are respectively equal to  $\theta_{S_1}^0$  and  $\theta_{S_n}^0$ , which are used to replace the corresponding tangential angles of the original curved arch axis in the calculations.

### 6.2.2 Deflection function

The defining feature that sets the model formulation apart from the conventional deflection method is its incorporation of a deflection function. This feature enables the model to provide a unified approach for handling small- and large-curvature problems. The deflection function is derived based on the assumption that, for a small segment, the variations in its internal axial force and bending moment are negligible so that they can be approximated as constants. When the bending moment is constant, the curvature is constant as well, meaning that the deformed segment must take on the shape of a circular arc. Moreover, the axial force being constant means a uniform axial strain along the length of the circular arc, so the change in length of the circular arc is a simple elongation or contraction of the initial segment length. Therefore, the task becomes choosing a representative point on the segment axis and using the axial strain and curvature induced by the internal axial force and bending moment at this point to generate a circular arc that represents the deformed segment shape. To perform this task, the segment midpoint is chosen as the representative point because it well characterizes the average deformation of the segment. An iterative procedure is used to determine the shape of the circular arc, as described below.

Suppose that during a given loading step, the calculation has reached segment  $S_i$  [Figure 6.2(a)],

and the following properties at its left end (i.e., the  $i$  th grid point) have been computed: the coordinates  $(x_i, y_i)$ , the right inclination angle  $\theta_{i,r}$ , and the internal forces  $H_i, V_i$  and  $M_i$ . In a general case, the segment is subjected to a variety of external loads, including both concentrated and distributed loads. As per the first discretization rule, the concentrated loads,  $H_{ext,i+1}, V_{ext,i+1}$  and  $M_{ext,i+1}$ , are applied at the right end of the segment  $i$  (i.e., the  $i + 1$  th grid point). According to the second discretization rule, the four distributed loads,  $q_{x,S_i}, q_{y,S_i}, q_{s,S_i}$  and  $q_{R,S_i}$ , can be simplified as uniform loads with a magnitude equal to their respective value at segment midpoint. These distributed loads are oriented in the horizontal, vertical, arc length and radial directions, respectively, representing different categories of loads, such as pavement load, wind load, gravity, and uniform radial pressure. When acting upon a circular segment, the internal forces caused by  $q_{x,S_i}, q_{y,S_i}, q_{s,S_i}$  and  $q_{R,S_i}$  at any point on the segment can be calculated by integration along the arc defined by the  $i$  th grid point and the point of interest. The expressions for these internal forces are summarized in Table 6.1, where  $\beta$  denotes the central angle at the point of interest (see Table 6.1).

Consider the left half of the circular arc. In the first iterative step, the axial force and bending moment at the segment midpoint,  $N_{i+\frac{1}{2}}$  and  $M_{i+\frac{1}{2}}$ , are assumed to be equal to  $N_i$  and  $M_i$ , respectively, where  $N_i$  is the resultant of  $H_i$  and  $V_i$  in the direction of  $\theta_{i,r}$ . In this study, the subscript  $i + \frac{1}{2}$  is used to denote properties associated with the midpoint of segment  $S_i$ . Section analysis is then performed using the layer method (also known as fiber model) based on the plane section assumption (Jiang and Teng, 2012b). The aim is to find the corresponding strain gradient, defined by the curvature of the neutral axis at the midpoint  $\phi_{i+\frac{1}{2}}$  and the axial strain of the

centroidal axis at the midpoint  $\varepsilon_{i+\frac{1}{2}}$  [Figure 6.2(b)]. To fulfill this aim, Newton's method is used to iteratively adjust the values of  $\phi_{i+\frac{1}{2}}$  and  $\varepsilon_{i+\frac{1}{2}}$  until  $N_{i+\frac{1}{2}}$  and  $M_{i+\frac{1}{2}}$  are balanced (El-Metwally and Chen, 1989). Obviously, the distance between the centroidal axis and the neutral axis  $d_{cn} = \varepsilon_{i+\frac{1}{2}}/\phi_{i+\frac{1}{2}}$ , so the radius of the circular arc can be expressed as:

$$R_{S_i} = \rho_{S_i} + d_{cn} = 1/\phi_{i+\frac{1}{2}} + \varepsilon_{i+\frac{1}{2}}/\phi_{i+\frac{1}{2}} = \left(1 + \varepsilon_{i+\frac{1}{2}}\right)/\phi_{i+\frac{1}{2}} \quad (6.1)$$

where  $\rho_{S_i}$  is the radius of curvature of the neutral axis. Eq. 6.1 is used to determine the radius of the circular arc. The length of the left half of the circular arc is determined by:

$$\frac{L_{S_i}}{2} = \left(1 + \varepsilon_{i+\frac{1}{2}}\right) \frac{L_{S_i}^0}{2} \quad (6.2)$$

With  $R_{S_i}$  and  $L_{S_i}$  known, the left half of the arc can be generated with the additional condition that the tangential angle at its left end is  $\theta_{i,r}$ . The right end of this arc defines a new midpoint whose coordinates are [Figure 6.2(c)]:

$$\begin{cases} x_{i+\frac{1}{2}} = x_i + \Delta x_{i+\frac{1}{2}} = x_i + R_{S_i} \cdot (\sin(\theta_{i,r}) - \sin(\theta_{i,r} - \beta_{S_i}/2)) \\ y_{i+\frac{1}{2}} = y_i + \Delta y_{i+\frac{1}{2}} = y_i + R_{S_i} \cdot (\cos(\theta_{i,r} - \beta_{S_i}/2) - \cos(\theta_{i,r})) \end{cases} \quad (6.3)$$

where  $\beta_{S_i}/2$  is the corresponding central angle and  $= \frac{L_{S_i}}{2}/R_{S_i}$ . The tangential angle at the midpoint is:

$$\theta_{i+\frac{1}{2}} = \theta_{i,r} - \beta_{S_i}/2 \quad (6.4)$$

Now the values of  $N_{i+\frac{1}{2}}$  and  $M_{i+\frac{1}{2}}$  can be updated:

$$N_{i+\frac{1}{2}} = H_{i+\frac{1}{2}} \cdot \cos(\theta_{i+\frac{1}{2}}) + V_{i+\frac{1}{2}} \cdot \sin(\theta_{i+\frac{1}{2}}) \quad (6.5a)$$

$$M_{i+\frac{1}{2}} = M_i + H_i \cdot \Delta y_{i+\frac{1}{2}} + V_i \cdot \Delta x_{i+\frac{1}{2}} + \Delta M_{i+\frac{1}{2},q_x} + \Delta M_{i+\frac{1}{2},q_y} + \Delta M_{i+\frac{1}{2},q_s} + \Delta M_{i+\frac{1}{2},q_R} \quad (6.5b)$$

where

$$H_{i+\frac{1}{2}} = H_i + \Delta H_{i+\frac{1}{2},q_x} + \Delta H_{i+\frac{1}{2},q_s} + \Delta H_{i+\frac{1}{2},q_R} \quad (6.6a)$$

$$V_{i+\frac{1}{2}} = V_i + \Delta V_{i+\frac{1}{2},q_y} + \Delta V_{i+\frac{1}{2},q_s} + \Delta V_{i+\frac{1}{2},q_R} \quad (6.6b)$$

In Eqs 6.5 and 6.6, the contributions from the distributed loads (i.e., the internal force items with  $\Delta$ ) can be calculated using the expressions provided in Table 6.1 by setting  $\beta = \beta_{S_i}/2$ .

The procedure then proceeds to the next iterative step using the updated  $N_{i+\frac{1}{2}}$  and  $M_{i+\frac{1}{2}}$ , and it continues until the distance between the current midpoint and its predecessor obtained in the preceding iterative step is less than  $10^{-6}L_{S_i}^0$ . Once the left half of the arc is determined, the right half can be easily generated by extending the left half around its center by an angle of  $\beta_{S_i}/2$  [Figure 6.2(c)]. The coordinates of the  $i + 1$  th grid point can now be determined:

$$\begin{cases} x_{i+1} = x_i + \Delta x_i = x_i + R_{S_i} \cdot (\sin(\theta_{i,r}) - \sin(\theta_{i,r} - \beta_{S_i})) \\ y_{i+1} = y_i + \Delta y_i = y_i + R_{S_i} \cdot (\cos(\theta_{i,r} - \beta_{S_i}) - \cos(\theta_{i,r})) \end{cases} \quad (6.7)$$

and the left and right inclination angles at the  $i + 1$  th grid point are:

$$\theta_{i+1,l} = \theta_{i,r} - \beta_{S_i} \quad (6.8a)$$

$$\theta_{i+1,r} = \theta_{i+1,l} - \Delta\theta_{i+1} \quad (6.8b)$$

Finally, the internal forces at the  $i + 1$  th grid point are obtained:

$$H_{i+1} = H_i + \Delta H_{i+1,q_x} + \Delta H_{i+1,q_s} + \Delta H_{i+1,q_R} + H_{ext,i+1} \quad (6.9a)$$

$$V_{i+1} = V_i + \Delta V_{i+1,q_y} + \Delta V_{i+1,q_s} + \Delta V_{i+1,q_R} + V_{ext,i+1} \quad (6.9b)$$

$$M_{i+1} = M_i + H_i \cdot \Delta y_i + V_i \cdot \Delta x_i + \Delta M_{i+1,q_x} + \Delta M_{i+1,q_y} + \Delta M_{i+1,q_s} + \Delta M_{i+1,q_R} + M_{ext,i+1} \quad (6.9c)$$

where the contributions from the distributed loads can be determined from the expressions provided in Table 6.1 by setting  $\beta = \beta_{S_i}$ .

### 6.2.3. Solution procedure

The calculations described in the preceding sub-section can be applied sequentially, starting from  $S_1$  and progressing through each intermediate segment until reaching  $S_n$ . To initiate the solution procedure, the unknown initial values at the first grid point must be assumed and used in the calculations for  $S_1$ . These unknowns correspond to the reaction forces or displacements of the left support, such as  $H_1$ ,  $V_1$ ,  $M_1$  and  $\theta_1$ , depending on the type of support. By making appropriate initial guesses for these unknowns, the calculations can proceed from segment to segment, generating the complete deflection curve. Once the deflection curve is obtained, the boundary conditions at the last grid point need to be examined to ensure their satisfaction. These boundary conditions, which also depend on the type of support, involve the reaction forces and displacements of the right support. Table 6.2 provides a summary of the unknown initial values and boundary conditions specific to hinged and fixed supports, which are the two most commonly used support types in practice. Each type corresponds to three initial values and three boundary conditions. The numerical examples of this study also encompassed other support types, including

rotational springs and vertical sliding hinges. Their properties are also summarized in Table 6.2.

It is expedient to present first the solution procedure for the simplest case, where the arch is subjected to a single load. In this scenario, the arch can experience failure either due to material limitations (i.e., material failure) or instability (i.e., stability failure), with the likelihood depending largely on its slenderness. Regardless of the failure type, the arch's final deformation state is associated with material failure. Even when stability failure occurs first in the case of slender arches, post-buckling deformation can continue to develop as the load magnitude decreases until it reaches a point where material failure is triggered.

Therefore, the solution procedure adopts an incremental approach using the displacement-control technique. This technique is chosen over the load-control technique because it provides a unified approach to address both stability failure and material failure possibilities. In each incremental step, an increasing displacement value is applied at a selected grid point. The choice of the grid point may vary between incremental steps to ensure that the displacement at the chosen point continues to increase. The goal is to determine the correct load magnitude that induces the prescribed displacement at each step. In this approach, the load magnitude becomes an additional unknown, while the prescribed displacement serves as an additional boundary condition that must be satisfied by the computed deflection curve at the chosen grid point.

The initial step size, denoted as  $\Delta f$ , can be assigned any reasonable small value (e.g., 1/50 of the ultimate displacement). Initially, the boundary conditions are generally not satisfied by the guessed unknowns. However, the discrepancies between the calculated values and their target values can be used to guide an iterative process that converges toward the correct values of the unknowns. Newton's method is used to implement this iterative process. The process continues until the errors

fall within acceptable tolerances, indicating that the solution for the current incremental step has been found. The procedure then proceeds to the next incremental step and continues until material failure occurs.

Material failure is identified through section analysis performed at the midpoint section of each segment. When the calculated axial strain value at any point on the critical section exceeds the material's strain capacity, it indicates that material failure has occurred. In response, the solution procedure is reverted to the previous incremental step and then resumes with a reduced increment of  $\Delta f/2$ . When material failure is detected again the step size is further halved. This process continues until the step size is eventually reduced to  $\Delta f/2^6$ , marking the conclusion of the solution procedure.

When the arch is subjected to multiple loads, a loading regime needs to be prescribed to specify the ratios between the load magnitudes. One commonly used regime is proportional loading, where the ratios remain consistent throughout the entire loading process. By prescribing these ratios, the number of additional unknowns associated with the applied loads remains at one. Consequently, the load magnitudes can be determined by solving for the equal number of unknowns and boundary conditions. The remaining steps of the solution procedure follow the same approach as described for the single-load case.

#### **6.2.4. Handling of intermediate hinge joints**

Fixed, two-hinged and three-hinged arches are the three basic arch types. So far, the solution procedure has addressed the first two types. However, to apply the procedure to three-hinged arches, a slight modification is required in the model formulation to account for the behavior of the intermediate hinge joint. Consider Figure 6.2(c) and assume a hinge joint is located at the

segment's right end ( $i + 1$  th grid point). In this case, Eq. 6.8 no longer holds, as it is only applicable to rigid connections. Due to the presence of the rotation-free hinge joint, the correlation between the two inclination angles at the  $i + 1$  th grid point is lost. Consequently, the right inclination angle,  $\theta_{i,r}$ , becomes an additional unknown. Simultaneously, a new boundary condition,  $M_{i+1} = 0$ , is imposed. Therefore, the new unknown  $\theta_{i,r}$  can be solved with the other unknowns altogether from the updated boundary conditions using Newton's method.

### 6.2.5. Handling of semi-rigid connections

Hinged and rigid connections represent idealized connection conditions. In practice, the actual connection condition often lies between these two extremes and requires modeling as semi-rigid connections. One common approach is to model them as rotational springs. Rotational springs can be used to represent both supports and intermediate joints. In either case, the bending moment acting on the spring induces an additional rotation  $\omega_i = M_i/k_i$ , where  $k_i$  is the stiffness of the spring. The initial values and boundary conditions associated with rotational spring supports are summarized in Table 6.2, capturing the influence of  $\omega_i$ . Similarly, when an intermediate joint is modeled as a rotational spring, Eq. 6.8 needs to be modified to incorporate an additional term for  $\omega_i$ :

$$\theta_{i+1,r} = \theta_{i,r} - \beta_{S_i} - \Delta\theta_{i+1} + \omega_i \quad (6.10)$$

In fact, hinges and rigid connections can be seen as idealized rotational springs with zero and infinite stiffness magnitudes, respectively. In practice, these idealized spring conditions can be represented by assigning extremely low or extremely high stiffness values. However, hinged and rigid connections are directly represented in the proposed theoretical model instead of modeling

them as rotational springs.

The accuracy of the theoretical model is affected by several factors. These include the number of segments used to divide the member, the number of cross-sectional layers adopted in section analysis, and the tolerances set as convergence criteria. In this chapter, all numerical examples employed 32 segments and  $10^{-6}$  as the convergence tolerance. The number of cross-sectional layers varied around 200, depending on the cross-sectional configuration. A convergence study showed that further refinement of these factors will not yield any significant effect on the numerical results.

## **6.3 VERIFICATION**

### **6.3.1 Comparisons with analytical results of linear elastic arches**

The theoretical model was verified using the analytical solution derived by Pi and Bradford for linear elastic arches (Pi and Bradford, 2009). Their solution represents a significant advancement over classical elastic arch theories (e.g., Timoshenko and Gere, 1963), as it accounts for the effect of pre-buckling deformations on the displacement and geometric stiffness of the arch. This consideration is particularly important for shallow arches, where pre-buckling deformations significantly influence the arch's buckling behavior (Pi and Trahair, 1998).

The solution of Pi and Bradford (2009) is concerned with the specific loading scenario of elastic circular arches subjected to a uniform radial pressure [Figure 6.3(a)]. In classical arch theories, this loading scenario results in a compression line coinciding with the arch's centroidal axis. This implies a pure concentric compression stress state of the arch, neglecting the axial deformation caused by the axial compression force. As a result, the predicted buckling mode according to

classical arch theories is bifurcation buckling (Timoshenko and Gere, 1963). However, when the effect of axial deformation is considered, the compression line deviates from the centroidal axis as the applied radial pressure increases, introducing bending moments to the arch. This deviation can lead to the arch buckling in either a symmetric snap-through mode or an anti-symmetric bifurcation mode (Pi and Bradford, 2009), as illustrated in Figures 6.3(b) and 6.3(c), respectively. The dominant buckling mode depends on factors such as arch slenderness, shallowness, and level of end restraint.

In the study of Pi and Bradford (2009), the supports of the arch were represented by two elastic rotational springs of equal stiffness, providing symmetrical restraint to the arch. The level of end restraint was indicated by the dimensionless flexibility of the rotational springs  $\alpha$ , which was defined as the ratio of the flexural rigidity per arch length to the stiffness of the rotational springs. This parameter can be assigned any value between zero and infinity to represent different levels of end restraint.

Figure 6.4 presents a comparison between the load-deflection curves at the arch crown, as predicted by the theoretical model and the analytical solution of Pi and Bradford (2009). These curves trace the variation of the normalized applied pressure  $q_R R / N_{E2}$  as the normalized vertical displacement of the arch crown  $v_0 / f$  increases, where  $R$  and  $f$  are respectively the radius and rise of the arch,  $v_0$  is the vertical displacement of the arch crown, and  $N_{E2}$  is the second mode flexural buckling load of a pin-ended column with equal rotational end restraints and having the same length as the arch (Pi and Bradford, 2009). Two representative sets of arches were considered, one with  $\alpha = 0.1$  and the other with  $\alpha = 1.5$ , to represent a relatively high and a relatively low level of end restraint, respectively. Each set covered four cases, each corresponding to a specific value of

a geometrical parameter  $\lambda$  introduced by Pi and Bradford (2009). This parameter reflects both the slenderness and shallowness of the arch and has a significant influence on its buckling behavior.

The  $\lambda$  value used for Figure 6.4(a) is a boundary value predicted by the analytical solution. Under this specific  $\lambda$ , the postbuckling descending branch of the load-deflection curve for the arch with  $\alpha = 1.5$  reduces to a single point. That is, it demarcates the boundary between stability and instability for  $\alpha = 1.5$ : any  $\lambda$  greater than this boundary value leads to the occurrence of stability failure, while any lesser  $\lambda$  eliminates the possibility of stability failure and is thus associated with a monotonically increasing load-deflection curve. Similarly, the  $\lambda$  value used for Figure 6.4(b) is the counterpart boundary value for  $\alpha = 0.1$ . Under this  $\lambda$ , due to the lower level of end restraint, the arch with  $\alpha = 1.5$  fails by instability in the symmetrical snap-through mode and exhibits a postbuckling descending branch on its load-deflection curve. The  $\lambda$  value used for Figure 6.4(c) is such that the anti-symmetric bifurcation mode is triggered for the arch with  $\alpha = 1.5$ , although the dominant buckling mode remains the snap-through mode. The portion corresponding to the anti-symmetric deformation phase is defined by the two solid symbols on the load-deflection curve. In Figure 6.4(d),  $\lambda$  is further increased to such a value that bifurcation buckling becomes the dominant buckling mode for the arch with  $\alpha = 1.5$ . It should be noted that a perturbation is needed for the theoretical model to excite the anti-symmetric buckling mode. This perturbation was introduced as a small bending moment with a magnitude of  $10^{-3}N_{E2}f$  applied at the arch crown.

Evidently, the predictions by the theoretical model match those by the analytical solution very well, except for the case shown in Figure 6.4(a) with  $\alpha = 0.1$ . The discrepancy observed for this particular case is believed to arise from an inadvertent mistake made by Pi and Bradford (2009) in using the value of  $N_{E2}$  when normalizing the applied pressure for this case. Pi and Bradford (2009)

claimed that for convenience a fixed value of  $N_{E2}$ , which was determined from the condition  $\alpha = 1.5$ , was consistently used for all cases considered in Figure 6.4, despite the fact that  $N_{E2}$  varies with  $\alpha$ . However, it appears that this rule was not followed by Pi and Bradford (2009) when preparing the plot for this particular case, where it is believed that the value of  $N_{E2}$  was actually determined from the condition  $\alpha = 0.1$ . When this  $N_{E2}$  value is used, the predicted normalized load-deflection curve for this case becomes the additional dashed curve shown in Figure 6.4(a), removing the previously observed discrepancy.

### **6.3.2 Comparisons with numerical result of slender FRP-confined RC columns**

The theoretical model's capability to address small-curvature problems is demonstrated through comparisons with the numerical results of a column model previously developed by Jiang and Teng (2012b). This column model is based on the conventional deflection method and has been verified in Jiang and Teng (2012b), where its accuracy for slender RC columns and FRP-confined RC columns is also shown.

The numerical verification is based on referencing four slender FRP-confined circular RC columns tested by Tao et al. (2004), using the properties of these columns as inputs for both models. These columns, measuring 150 mm in diameter and 1260 mm in height, were reinforced with four 12 mm longitudinal steel bars and enveloped in a circumferential CFRP wrap with a nominal thickness of 0.34 mm. The concrete cover to the longitudinal steel reinforcement was 21 mm. All columns were pin-ended and subjected to equal load eccentricities at the two ends. The four columns were labeled C1-1R, C1-2R, C1-3R, and C1-4R, respectively, distinguished by their nominal load eccentricities (0 mm, 50 mm, 100 mm, and 150 mm). The material properties are as follows. The unconfined concrete strength was 48.2 MPa and the yield strength of the longitudinal

steel reinforcement was 388.7 MPa. The CFRP wrap had an elastic modulus of 255 GPa and a hoop rupture strain of 1.32%. More details of these tests can be found elsewhere (Jiang and Teng, 2012b; Tao et al., 2004).

The load-deflection responses of the four columns were simulated using both the theoretical model and the column model of Jiang and Teng (2012b), with both models incorporating the same stress-strain models. Teng et al.'s (2009) design-oriented model, which is a refined version of Lam and Teng's (2003) model, was employed to characterize the compressive stress-strain behavior of FRP-confined concrete, while the tensile strength of concrete was ignored. The longitudinal steel reinforcement was assumed to possess an elastic-perfectly plastic stress-strain curve.

Figure 6.5 illustrates a comparison between the load-deflection curves at column mid-height, as predicted by the two models. Following the approach of Jiang and Teng (2012b), all cases were modeled with an additional eccentricity of 6.5 mm added to the nominal load eccentricity. The two sets of theoretical curves exhibit excellent agreement, demonstrating the capability of the theoretical model in addressing small-curvature problems.

## **6.4 APPLICATION TO FRP-REINFORCED ARCHES AND OTHER FRP-ENABLED ARCHES**

### **6.4.1 FRP-reinforced concrete arches**

This PhD study mainly investigates the innovative application of FRP hybrid arches in large-scale structures, with a particular focus on FRP-reinforced concrete arch structures. A significant advancement in this field is the substitution of traditional steel rebars with curved GFRP bars, manufactured by pultrusion process (Spagnuolo et al., 2014; Caratelli et al., 2016; Caratelli et al.,

2017; Spagnuolo et al., 2017; Meda et al., 2020; Meda et al., 2018; Spagnuolo et al., 2018; Tengilimoğlu, 2019; Meda et al., 2019). This substitution is advantageous in enhancing the durability of reinforced concrete arch structures, making them ideally suited for harsh environments such as sewage tunnels, aggressive soils, marine and coastal areas, as well as cold regions where de-icing salts are frequently used.

The quasi-static loading tests on over-reinforced GFRP-reinforced concrete arches, as described Chapter 5, served as a case study to validate the applicability of the proposed model (Xia et al., 2024). The experimental setup and material properties for those tests have been detailed in Section 5.2 and do not be reiterated here.

The test setup, illustrated in Figure 5.14, was simplified for modeling purposes, as shown in Figure 6.6, where only half of the arch specimen was modeled due to symmetry. The modeling integrated the arch specimen with its support system (comprising two supports and an underlying beam) to accurately replicate the boundary conditions. Supports and the beam were modeled as I-section components based on measured dimensions, with the beam height varying bilinearly along the span, as shown in Figure 6.6(a). Data from the LVDTs at the supports indicated negligible slip at bolt joints between components, which were therefore treated as rigid connections in the model.

The theoretical model was implemented in a displacement-controlled manner. At each loading step, the deformed shape was generated based on the deformation compatibility between adjacent arc segments and boundary reactions at the mid-span of the beam, including bending moment  $M$ , horizontal force  $H$ , and vertical force  $V$ . These boundary reactions were determined by satisfying the boundary conditions through Newton's iterative method (Xia et al., 2024). The boundary conditions referred to the constraints at the arch apex, specifically: zero horizontal displacement

( $\nu = 0$ ), specified vertical displacement ( $\mu = \text{Given value at each loading step}$ ), and zero rotation ( $\gamma = 0$ ).

The stress-strain relationship of concrete was described using Equation (6.11). The compressive behavior of concrete was characterized by the constitutive model from GB 50010 (2015), while the tensile response was assumed to have a linear ascending branch with an elastic modulus identical to its compressive modulus ( $E_c$ ). The tension-stiffening effect was modeled using the model proposed by Collins and Mitchell (1997):

$$\sigma_c = \begin{cases} f_{cu} & (\varepsilon_{co} < \varepsilon_c) \\ f_{cu} \cdot \left(1 - \left(1 - \frac{\varepsilon_c}{\varepsilon_{co}}\right)^n\right) & (0 < \varepsilon_c \leq \varepsilon_{co}) \\ E_c \cdot \varepsilon_c & (\varepsilon_{to} < \varepsilon_c \leq 0) \\ \frac{0.8f_t}{1 + \sqrt{-1300(\varepsilon_c - \varepsilon_{to})}} & (\varepsilon_c \leq \varepsilon_{to}) \end{cases} \quad (6.11)$$

where  $\sigma_c$  represents the concrete stress at a given strain of  $\varepsilon_c$  and  $f_{cu}$  is the compressive strength of concrete. The shape parameter ( $n$ ) is defined by Equation (6.12), and the strain ( $\varepsilon_{co}$ ) corresponding to  $f_{cu}$  is expressed in Equation (6.13). Both parameters depend on the concrete strength. The tensile strength of concrete ( $f_t$ ) was estimated from its compressive strength as recommended by Collins and Mitchell (1997), using Equation (6.14). The  $\varepsilon_{to}$  denotes the corresponding tensile strain.

$$n = \min \left\{ \left( 2 - \frac{1}{60} (f_{cu} - 50) \right), 2 \right\} \quad (6.12)$$

$$\varepsilon_o = \max\{(0.002 + 0.5(f_{cu} - 50) \times 10^{-5}), 0.002\} \quad (6.13)$$

$$f_t = -0.33\sqrt{f_{cu}} \quad (6.14)$$

FRP and steel reinforcements were characterized as linear-elastic and ideal elasto-plastic materials, respectively, based on the test results listed in Table 5.2. The corresponding stress-strain relationships for FRP bars and steel reinforcement are given in Equations (6.15) and (6.16). The steel supports and the steel beam were assumed to share the same constitutive model as the steel reinforcement, with specified properties for Q235 steel:  $E_s = 200$  GPa and  $f_s = 235$  MPa.

For the FRP bars, the elastic modulus was assumed to be identical for both tensile and compressive behaviors in the model (Si et al., 2022; Maranan et al., 2016). The compressive strength of GFRP bars typically ranges from 30% to 100% of their tensile strength (Hasan et al., 2019). Since the ultimate compressive strain of FRP bars always exceeds that of concrete, FRP bars do not reach their full compressive strength before concrete failure, making the compressive strength of FRP bars unnecessary for the model. A perfect bond between concrete and embedded reinforcement was assumed.

$$\sigma_{frp} = \begin{cases} 0 & (\frac{f_{frp}}{E_{frp,t}} < \varepsilon_{frp}) \\ E_{frp,t} \cdot \varepsilon_{frp} & (\varepsilon_{frp} \leq \frac{f_{frp}}{E_{frp,t}}) \end{cases} \quad (6.15)$$

where  $\sigma_{frp}$  represents the stress of FRP bar at a strain of  $\varepsilon_{frp}$ , and  $f_{frp}$  denotes the tensile strength of the FRP bar.

$$\sigma_s = \begin{cases} f_s + 0.01E_s \cdot \left( \varepsilon_s - \frac{f_s}{E_s} \right) & \left( \frac{f_s}{E_s} < \varepsilon_s \right) \\ E_s \cdot \varepsilon_s & \left( -\frac{f_s}{E_s} < \varepsilon_s \leq \frac{f_s}{E_s} \right) \\ -f_s + 0.01E_s \cdot \left( \varepsilon_s + \frac{f_s}{E_s} \right) & \left( \varepsilon_s \leq -\frac{f_s}{E_s} \right) \end{cases} \quad (6.16)$$

Similarly,  $\sigma_s$  is the steel stress at strain  $\varepsilon_s$ , with  $f_s$  representing the yielding strength of steel and  $E_s$  its elastic modulus.

Existing theoretical studies have shown that the standard-recommended ultimate strains for concrete [3000  $\mu\varepsilon$  in ACI 440.11 (2022) and 3500  $\mu\varepsilon$  in CSA (2012)] often result in inaccurate predictions for FRP-RC members (GangaRao and Vijay, 1997; Kassem et al., 2011; El-Nemr et al., 2018). This discrepancy is primarily due to variability in materials and the potential buckling of compressed FRP bars that may trigger premature concrete crushing (El-Nemr et al., 2018). In this study, pronounced concrete crushing was observed, along with the failure of strain gauges on the compression side at the arch crown, complicating accurate characterization of the ultimate state using either standard-recommended strains or measured concrete strains. Consequently, the criterion for determining failure points was based on the maximum recorded strain values for the reinforcement.

Figures 6.7(a)-(d) present the strain development in tensile reinforcement at various gauge points along the arch axis. The maximum strains were typically observed near the lower reinforcement close to the arch crown for all specimens, serving as the basis for ultimate state determination. Notably, a discrepancy was observed between the tested and predicted strain data at  $L/4$  in specimen NCG13H, which may be attributed to sensitivity of strain distribution to measurement positions. To validate this assumption, Figure 6.7(a) includes strain data over a narrow arc length

of  $\pm 40$  mm centered at the quarter span, capturing the observed variation and highlighting the strain sensitivity in this region. To further validate the accuracy of the model, Figures 6.8(a)-(e) compare experimental and predicted load-deflection curves at the arch crown, demonstrating good agreement between test results and numerical predictions. Table 6.3 summarizes key results, confirming the capacity of the theoretical model in predicting failure states, with errors of peak load within 5% and deflection variations within 10%.

Additionally, Figures 6.9(a)-(e) provide a comparative analysis of deflections at  $L/4$ , where horizontal displacements are defined as positive towards the mid-span and vertical displacements are positive when directed downward. These figures show that the model basically captures deformation trends in both horizontal and vertical directions at  $L/4$  with reliable precision. The quarter-point deformation was measured based on the in-plane motion of aluminum sheets attached at the measurement points. The accuracy of these measurements was limited by the precision of the hand-fabricated aluminum sheets, which may be a primary factor contributing to the discrepancies between measured and predicted deflection values.

In summary, the theoretical model effectively captures both material and geometric nonlinearities, accurately simulating the structural responses of FRP/steel-reinforced arch specimens. This validated model extends the applicability of limited test data and serves as a reliable analytical tool for developing theoretical formulations and establishing standard guidelines.

#### **6.4.2 FRP bending-active arches**

Bending-active arches are a unique category of arch structures. They derive their curved shape from elastic bending of initially straight members (Lienhard et al., 2013; Xie et al., 2023b; Xie et al., 2024). FRP bending-active arches are suitable for use as rapidly assembled crossing bridges

and supporting frames for temporary structures (Xia et al., 2023; Caron et al., 2009; Bessini et al., 2019; Habibi et al., 2022).

The tests conducted by Xie et al. (2023a) were employed as an example of all-FRP arches to validate the theoretical model. In their tests, the arch specimens were bent from straight CFRP strips with a cross section of 48.5 mm by 1.40 mm. During the bending process, the supports of the specimen allowed free rotation in the plane of the arch axis [Figure 6.10(a)]. Once the arch specimen was bent into place, the supports were transitioned to a clamped condition before receiving a concentrated load vertically applied at the arch crown [Figure 6.10(b)]. A total of 16 arch configurations were tested, with the main variables being the strip length and the span ratio (the ratio of arch span to strip length). The strip length was either 1.6 m or 2.0 m, each covering four span ratios (0.6, 0.7, 0.8 and 0.9). The CFRP had a flexural modulus of 127.5 GPa and a density of 1620 kg/m<sup>3</sup>.

Figure 6.11 displays a comparison between the experimental and predicted load-deflection curves at arch crown for all specimens. Each predicted curve was terminated when its predicted load aligned with the load at the final point of the corresponding experimental curve. As only the symmetrical snap-through buckling mode was observed in the tests, the modeling work simplified the arch specimen by considering only half of its original configuration. As a result, the support condition at the arch crown was modeled as a vertical sliding hinge (see Table 6.2). Furthermore, the influence of gravity was considered, as it proved significant due to the large flexibility of the arch specimens. As illustrated in Figure 6.11, the predicted load-deflection curves closely align with their experimental counterparts.

For illustrative purposes, Figure 6.12 provides a further comparison between the experimental and

predicted deformed shapes of Specimen L16SR60. This specimen had a length of 1.6 m and a span ratio of 0.6. The comparisons were made at three representative states (State I, State II and State III), which correspond to the initial point, peak point and valley point of the load-deflection curve, respectively. Evidently, the theoretical model successfully reproduces the deformed shapes, demonstrating its accuracy in capturing the behavior of the arch specimens.

#### **6.4.3 Concrete-filled FRP tubular (CFFT) arches**

CFFT arches are a promising form of FRP-incorporating hybrid arch, offering a combination of strength, ductility and durability. This desirable behavior is attributed to the confinement, reinforcement and protection provided to the concrete core by the FRP tube. The theoretical model is further validated using two series of tests on CFFT arches conducted by the same research group (Dagher et al., 2012; Majeed et al., 2021). Both test series focused on circular arches with a circular cross-section, subjecting them to a concentrated load vertically applied at the arch crown. The geometrical and material properties of the CFFT arches in both test series are summarized in Table 6.4.

The first test series (Dagher et al., 2012) involved four nominally identical CFFT arches (A1, A2, A3 and A4) subjected to monotonic loading. These arch specimens were cast into RC footings at both ends, with the footings being pin-supported on the laboratory floor [Figure 6.13(a)]. For each arch specimen, the FRP tube comprised an inner layer of glass fibers and two outer layers of carbon fibers. By using different fiber orientations for the inner and outer layers, the resulting FRP tube exhibited significant stiffness in both the longitudinal and hoop directions. In the theoretical model, each RC footing was simplified as a rigid link, and the FRP tube's behavior was assumed to be linear elastic in both the longitudinal and hoop directions. The interaction between the tube's

behaviors in these two directions was neglected in the analysis.

In the absence of test data, the elastic modulus and tensile strength of concrete were determined based on its compressive strength in accordance with the ACI standard (ACI 318-19, 2019). For consistency, Teng et al.'s (2009) model was again employed to describe the stress-strain behavior of FRP-confined concrete in compression. It should be noted that Teng et al.'s (2009) model requires the input of the FRP rupture strain. This value was assumed to be 2% as it was not reported in the original literature (Dagher et al., 2012). Varying the rupture strain in the range of 1-3% showed a negligible influence on the model predictions because the failure of the arch specimens was not due to the rupture of the FRP tube in the hoop direction. The stress-strain curve of concrete in tension was assumed to be linear before cracking. The tension-stiffening effect was accounted for using the model proposed by Collins and Mitchell (1997). This model is a modification of Vecchio and Collins's (1986) tension-stiffening model and has demonstrated a good predictive capability concerning moment-curvature relationships for CFFT flexural members in existing studies (Bannon et al., 2009; Fam, 2000). Full composite action was assumed between the FRP tube and the concrete core. Additionally, only half of the arch specimen was considered due to symmetry.

Figure 6.14(a) compares the experimental and predicted load-deflection curves at arch crown. Notably, Specimens A1 and A2 exhibited a less stiff initial response than Specimens A3 and A4. Dagher et al. (2012) attributed this difference to accidental damage prior to testing and initial imperfections. Therefore, the load-deflection curves of Specimens A3 and A4 are considered to better represent the true behavior of the arch specimens. These two curves are closely matched by the predicted curve. Dagher et al. (2012) reported that the failure of all arch specimens was due to

longitudinal rupture of the FRP tube in the tension face, directly below the point of load application [Figure 6.13(b)]. Hence, the predicted curve terminates when the FRP tube reaches its longitudinal rupture strain.

The second test series (Majeed et al., 2021) exclusively focused on a fixed CFFT arch with a more slender configuration [Figure 6.15(a)]. The FRP tube used in this test consisted of two layers of glass fibers, with each layer having a distinct fiber angle. The failure mode observed in this specimen was consistent with the one observed in the first test series [Figure 6.15(b)]. The modeling procedure for this specimen was similar to that used for the first test series, except for a variation in the support condition. As illustrated in Figure 6.14(b), the theoretical model accurately predicts the load-deflection response of this specimen.

## **6.5 LIMITATIONS**

Although the proposed model effectively predicts the structural behavior of FRP-RC arches and other FRP-enabled arches, it has certain limitations that restrict its applicability to preliminary structural design of slender configurations subjected to static or quasi-static loading only.

The main limitation of the present theoretical model is that it does not account for the effect of unloading in non-linear materials (e.g., concrete and steel). In this model, these materials are treated as non-linear elastic, implying that their stress-strain curve is retraced during unloading. As a result, the theoretical model is limited to loading schemes without loading reversals when non-linear materials are used. Bazant et al. (1991) showed that in such cases, the effect of unloading is negligible because unloading typically occurs near the neutral axis as it moves into the previously compressed portion of the cross section. Near the neutral axis, the strain levels are

too low to cause a significant deviation between the unloading stress-strain path and the reversed loading stress-strain path.

To extend the applicability of the theoretical model to situations where unloading plays a significant role (e.g., cyclic loading), the model requires modifications that incorporate appropriate stress-strain models accurately describing the unloading and reloading paths. Consequently, section analysis must be performed based on considering the strain history of each cross-sectional layer, in order to accurately determine the strain gradient over the cross section. The remainder of the model formulation remains unchanged.

Another limitation is that the model does not consider the effect of shear deformation on the behavior of the member. This means that the model's performance may be less satisfactory for thick (short) members, where shear deformation plays a more prominent role than in thin (slender) members. In these members, shear failure may also become the dominant material failure mode. To address this limitation, the model necessitates modifications that introduce an additional rotation due to shear deformation to each deformed segment of the member. This treatment is equivalent to incorporating Timoshenko's beam theory. Additionally, to assess the failure mode properly, a more sophisticated material failure criterion that considers the contribution from shear, such as the modified compression-field theory for RC members (Vecchio and Collins, 1986), needs to be incorporated.

It is also worth noting that the different materials (e.g., FRP and concrete) in composite structures in Sections 6.4.1 and 6.4.3 (e.g., FRP-RC arches and CFFT arches) were assumed to be perfect bonded. This assumption is valid because the bond-slip relationship between FRP reinforcement and concrete in FRP-RC arches meets the most stringent requirements of current standards for FRP

bar-reinforced concrete structures, as detailed in Section 5.2.4, and the perfect-bond assumption for the representative CFFT arches has been verified in Majeed et al. (2021). Comparisons in Sections 6.4.1 and 6.4.3 demonstrate that the predictions based on this assumption accurately replicate the experimental behaviors of both FRP-RC arches (Chapter 5) and CFFT arches (Dagher et al., 2012; Majeed et al., 2021). However, the bond-slip behavior between FRP and concrete may critically affect prediction accuracy, particularly in cases of poor bond performance, where the structural response is highly sensitive to bond-slip behavior. This highlights the need for further refinement of the proposed model to account for the effect (Yan et al., 2016; Gu et al., 2020; Xu et al., 2022; Hussein et al., 2022).

In such cases, the bond-slip relationship can be integrated into the section analysis of the proposed model by assuming relative slip between concrete and FRP reinforcement. The strain difference in the FRP reinforcement, resulting from slip from the perfect bond state, can be derived, enabling the calculation of FRP elongation. The unknown slip can be determined by solving an additional boundary condition, where the stress in the FRP reinforcement, as predicted by the constitutive model, is equal to the stress derived from the bond-slip model (Monti and Spacone, 2000; Spacone and Limkatanyu, 2000; Salari and Spacone, 2001; Lin and Zhang, 2013; Baena et al., 2013). Therefore, the new variable (slip of FRP reinforcement) can be solved alongside the other unknowns from the updated boundary conditions using Newton's method, based on the solution procedure outlined in Section 6.2.3.

## **6.6 CONCLUSIONS**

This chapter has been dedicated to the formulation, verification and application of a theoretical model for one-dimensional members. Originally developed to investigate the structural behavior

of FRP-RC arches and address the challenges associated with large-curvature problems, the model's versatility enables its application to the broader range of general one-dimensional members. The work presented in this chapter allows the following conclusions to be drawn:

1. The theoretical model is built upon an enhanced formulation of the deflection method. Its defining feature is the incorporation of a circular deflection function, which posits that each segment of the deformed centroidal axis can be represented by a circular arc whose curvature and length are related to the internal axial force and bending moment acting on the segment's midpoint section. This feature facilitates the exact representation of curvature, distinguishing the proposed model from the conventional deflection method, where the simplified representation of curvature as the second-order derivative of deflection is valid only for small curvatures. Therefore, the proposed model represents a significant improvement over the conventional deflection method in that it offers a unified approach to address both small- and large-curvature problems.

2. Model verification was carried out through comparisons with both analytical and numerical results from the literature. The analytical verification focused on a large-curvature problem of linear elastic arches, while the numerical verification employed a small-curvature problem of slender FRP-confined RC columns, incorporating material non-linearity. The verification results demonstrated the correct implementation of the theoretical model and its equal capability in handling small- and large-curvature problems.

3. The performance of the theoretical model was evaluated against representative test results from FRP-RC arches and other FRP-enabled arches, comprising two sub-categories: all-FRP arches exemplified by FRP-bending active arches and FRP-incorporating hybrid arches exemplified by CFFT arches and FRP-reinforced concrete arches. In the case of FRP-bending active arches, the

large curvatures were induced by deformation, whereas in CFFT arches and FRP-reinforced concrete arches, the large curvatures were inherent in their initial configuration. The theoretical model demonstrated excellent accuracy in predicting the behavior of arches in both sub-categories, regardless of the source of the large curvatures.

4. Despite its significant advantages, the theoretical model has certain limitations. It does not consider the effect of unloading in non-linear materials and the influence of shear deformation. To address the first limitation, the section analysis procedure requires a modification to take into account the strain history of each cross-sectional layer in determining the strain gradient over the cross section. The second limitation can be addressed by introducing an additional rotation due to shear deformation to each deformed segment of the member, and by incorporating a more sophisticated material failure criterion that accounts for the contribution from shear. By implementing these modifications, the applicability of the theoretical model can be extended to scenarios involving loading reversals, while also enhancing its accuracy for thick (short) members.

## 6.7 REFERENCES

- ACI 318-19. (2019) *Building Code Requirements for Structural Concrete*. Farmington Hills, Michigan: American Concrete Institute (ACI), USA.
- ACI 440.11R-22. (2022) *Building Code Requirements for Structural Concrete Reinforced with Glass Fiber-Reinforced Polymer (GFRP) Bars*. Farmington Hills, Michigan: American Concrete Institute (ACI), USA.
- Attia K, El Refai A and Alnahhal W. (2020) Flexural behavior of basalt fiber-reinforced concrete slab strips with BFRP bars: Experimental testing and numerical simulation. *Journal of Composites for Construction* 24(2): 04020007.
- Baena M, Torres L, Turon A, et al. (2013) Analysis of cracking behaviour and tension stiffening in FRP reinforced concrete tensile elements. *Composites Part B: Engineering* 45(1): 1360-1367.
- Bannon DJ, Dagher HJ and Lopez-Anido RA. (2009) Behavior of inflatable rigidified composite arch bridges. *Composites & Polycon*: 15-17.
- Bazant ZP, Cedolin L and Tabbara MR. (1991) New method of analysis for slender columns. *ACI Structural Journal* 88(4): 391-401.
- Bell M, Fick D, Ament R, et al. (2020) The use of fiber-reinforced polymers in wildlife crossing infrastructure. *Sustainability* 12(4): 1557.
- Bessini J, Lazaro C, Casanova J, et al. (2019) Efficiency-based design of bending-active tied arches.

- Engineering Structures* 200: 109681.
- Caratelli A, Meda A, Rinaldi Z, et al. (2016) Precast tunnel segments with GFRP reinforcement. *Tunnelling and Underground Space Technology* 60: 10-20.
- Caratelli A, Meda A, Rinaldi Z, et al. (2017) Optimization of GFRP reinforcement in precast segments for metro tunnel lining. *Composite Structures* 181: 336-346.
- Caron JF, Julich S and Baverel O. (2009) Selfstressed bowstring footbridge in FRP. *Composite Structures* 89(3): 489-496.
- Chen WF and Atsuta T. (2007) *Theory of Beam-columns*: J. Ross Publishing.
- Collins MP and Mitchell D. (1997) *Prestressed Concrete Structures*, Toronto and Montreal, Canada: Response Publications.
- CSA S806-12. (2012) *Design and Construction of Building Components with Fiber Reinforced Polymers*. Toronto, Ontario: Canadian Standards Association (CSA), Canada.
- Dagher HJ, Bannon DJ, Davids WG, et al. (2012) Bending behavior of concrete-filled tubular FRP arches for bridge structures. *Construction and Building Materials* 37: 432-439.
- Dong ZQ, Liu ZQ, Wu G, et al. (2022) Study on mechanical properties of seawater sea-sand coral aggregate concrete-filled BFRP tubular arches. *Advances in Structural Engineering* 25(9): 1851-1865.
- El-Metwally SE and Chen WF. (1989) Load-deformation relations for reinforced concrete sections. *Structural Journal* 86(2): 163-167.

- El-Nemr A, Ahmed EA, El-Safty A, et al. (2018) Evaluation of the flexural strength and serviceability of concrete beams reinforced with different types of GFRP bars. *Engineering Structures* 173: 606-619.
- Fam AZ. (2000) *Concrete-filled Fibre-reinforced Polymer Tubes for Axial and Flexural Structural Members*. Manitoba, Canada: The University of Manitoba.
- GangaRao H and Vijay P. (1997) Design of concrete members reinforced with GFRP bars. *Proceedings of 3rd Int. Symposium, Fiber Reinforced Polymer Reinforcement for Reinforced Concrete Structures*. Sapporo, Japan, 143-150.
- Gao K, Xie H, Li Z, et al. (2021) Study on eccentric behavior and serviceability performance of slender rectangular concrete columns reinforced with GFRP bars. *Composite Structures* 263: 113680.
- GB 50010. (2015) *Standard for Design of Concrete Structures*. Ministry of Housing and Urban-Rural Development of PRC, Beijing, China.
- Gu XY, Dai YQ and Jiang JW. (2020) Flexural behavior investigation of steel-GFRP hybrid-reinforced concrete beams based on experimental and numerical methods. *Engineering Structures* 206: 110117.
- Habibi T, Rhode Barbarigos L and Keller T. (2022) Fiber-polymer composites for permanent large-scale bending-active elastica beams. *Composite Structures* 294: 115809.
- Hasan HA, Sheikh MN and Hadi MN. (2019) Maximum axial load carrying capacity of Fibre Reinforced-Polymer (FRP) bar reinforced concrete columns under axial compression.

*Structures* 19: 227-233.

Huang ZJ, Chen WS, Tran TT, et al. (2021) Experimental and numerical study on concrete beams reinforced with Basalt FRP bars under static and impact loads. *Composite Structures* 263: 113648.

Hussein A, Huang H, Okuno Y, et al. (2022) Experimental and numerical parametric study on flexural behavior of concrete beams reinforced with hybrid combinations of steel and BFRP bars. *Composite Structures* 302: 116230.

Jiang S. (2020) *Hybrid FRP-concrete-steel Double-skin Tubular Truss Bridge: Design, Construction and Testing*. Queensland, Australia: The University of Queensland.

Jiang T and Teng JG. (2012a) Slenderness limit for short FRP-confined circular RC columns. *Journal of Composites for Construction* 16(6): 650-661.

Jiang T and Teng JG. (2012b) Theoretical model for slender FRP-confined circular RC columns. *Construction and Building Materials* 32: 66-76.

Kassem C, Farghaly AS and Benmokrane B. (2011) Evaluation of flexural behavior and serviceability performance of concrete beams reinforced with FRP bars. *Journal of Composites for Construction* 15(5): 682-695.

Lam L and Teng JG. (2003) Design-oriented stress-strain model for FRP-confined concrete. *Construction and Building Materials* 17(6-7): 471-489.

Lee GP and Shin HS. (2010) A numerical study on feasibility of the circled fiber reinforced

- polymer (FRP) panel for a tunnel lining structure. *Journal of Korean Tunnelling and Underground Space Association* 12(6): 451-461.
- Lienhard J, Alpermann H, Gengnagel C, et al. (2013) Active bending, a review on structures where bending is used as a self-formation process. *International Journal of Space Structures* 28(3-4): 187-196.
- Lin XS and Zhang YX. (2013) Novel composite beam element with bond-slip for nonlinear finite-element analyses of steel/FRP-reinforced concrete beams. *Journal of Structural Engineering* 139(12): 06013003.
- Liu SY, Zhang ZY, Xue X, et al. (2022) Deformation properties of arched glass fiber reinforced plastics structure under static load: Considering the soil cover and rise-span ratio. *Advances in Structural Engineering* 25(6): 1254-1267.
- Liu T, Feng P, Wu Y, et al. (2021) Developing an innovative curved-pultruded large-scale GFRP arch beam. *Composite Structures* 256: 113111.
- Majeed HS, Davids WG and Walton HJ. (2021) Efficient second-order nonlinear finite-element simulation of concrete-filled FRP tubular arches. *Structures* 34: 3738-3749.
- Maranan GB, Manalo AC, Benmokrane B, et al. (2016) Behavior of concentrically loaded geopolymer-concrete circular columns reinforced longitudinally and transversely with GFRP bars. *Engineering Structures* 117: 422-436.
- Meda A, Moja M, Pizzarotti E, et al. (2018) GFRP Reinforcement for Segmental Linings of Mechanized Tunnels. *Proceedings of Conference on Italian Concrete Days*. Springer, 461-

473.

Meda A, Rinaldi Z, Spagnuolo S, et al. (2019) Hybrid precast tunnel segments in fiber reinforced concrete with glass fiber reinforced bars. *Tunnelling and Underground Space Technology* 86: 100-112.

Meda A, Rinaldi Z, Spagnuolo S, et al. (2020) Experimental behaviour of precast tunnel segments in steel fiber reinforcement with GFRP rebars. *Fib Bulletin*: 153-162.

Monti G and Spacone E. (2000) Reinforced concrete fiber beam element with bond-slip. *Journal of Structural Engineering* 126(6): 654-661.

Pi YL and Bradford M. (2009) Non-linear in-plane postbuckling of arches with rotational end restraints under uniform radial loading. *International Journal of Non-Linear Mechanics* 44(9): 975-989.

Pi YL and Trahair NS. (1998) Non-linear buckling and postbuckling of elastic arches. *Engineering Structures* 20(7): 571-579.

Potyrala PB. (2011) *Use of Fibre Reinforced Polymeromposites in Bridge Construction. State of the Art in Hybrid and All-composite Structures*. Catalonia, Spain: Polytechnic University of Catalonia.

Pyrzowski Ł and Miśkiewicz M. (2017) Modern GFRP composite footbridges. *Proceedings of "Environmental Engineering" 10th International Conference*. Vilnius Gediminas Technical University, Ottawa, Canada, 1-8.

- Salari MR and Spacone E. (2001) Finite element formulations of one-dimensional elements with bond-slip. *Engineering Structures* 23(7): 815-826.
- Salih R and Zhou F. (2019) Numerical investigation of the behavior of reinforced concrete beam reinforced with FRP bars. *Civil Engineering Journal* 5(11): 2296-2308.
- Shen ZY and Lu LW. (1983) Analysis of initially crooked, end restrained steel columns. *Journal of Constructional Steel Research* 3(1): 10-18.
- Si JH, Qiu SC, Feng SY, et al. (2022) Experimental study on axial compression buckling of glass fiber reinforced plastics solid pole with circular cross-section. *Advances in Structural Engineering* 25(4): 913-924.
- Sobrino JA and Pulido MDG. (2002) Towards advanced composite material footbridges. *Structural Engineering International* 12(2): 84-86.
- Spacone E and Limkatanyu S. (2000) Responses of reinforced concrete members including bond-slip effects. *Structural Journal* 97(6): 831-839.
- Spagnuolo S, Meda A and Rinaldi Z. (2014) Fiber glass reinforcement in tunneling applications. *Proceedings of the 10th Fib International PhD Symposium in Civil Engineering*. 85-90.
- Spagnuolo S, Meda A, Rinaldi Z, et al. (2017) Precast concrete tunnel segments with GFRP reinforcement. *Journal of Composites for Construction* 21(5): 04017020.
- Spagnuolo S, Meda A, Rinaldi Z, et al. (2018) Curvilinear GFRP bars for tunnel segments applications. *Composites Part B: Engineering* 141: 137-147.

- Tang ZX, Zhou YZ, Feng J, et al. (2020) Blast responses and damage evaluation of concrete protective arches reinforced with BFRP bars. *Composite Structures* 254: 112864.
- Tao Z, Teng JG, Han LH, et al. (2004) Experimental behaviour of FRP-confined slender RC columns under eccentric loading. *Proceedings of Second International Conference on Advanced Polymer Composites for Structural Applications in Construction*. University of Surrey, Guildford, UK, 203-212.
- Teng JG, Jiang T, Lam L, et al. (2009) Refinement of a design-oriented stress–strain model for FRP-confined concrete. *Journal of Composites for Construction* 13(4): 269-278.
- Tengilimoğlu O. (2019) *An Experimental Study to Investigate the Possibility of Using Macro-synthetic Fibers in Precast Tunnel Segments*. Ankara, Turkey: Middle East Technical University.
- Timoshenko SP and Gere JM. (1963) *Theory of Elastic Stability*, New York, USA: McGraw-Hill International Book Company.
- Vecchio FJ and Collins MP. (1986) The modified compression-field theory for reinforced concrete elements subjected to shear. *ACI Journal* 83(2): 219-231.
- Wu J, Zhou J, Xu Y, et al. (2022) Dynamic responses of blast-loaded shallow buried concrete arches strengthened with BFRP bars. *Materials* 15(2): 535.
- Xia ZY, Jiang T and Yu T. (2023) Innovating arch structures with fiber-reinforced polymer composites: A review. *Advances in Structural Engineering* 26(13): 2341-2358.

- Xia ZY, Jiang T and Yu T. (2024) Enhanced deflection method for large-curvature problems: Formulation, verification and application to fiber-reinforced polymer-enabled arches. *Advances in Structural Engineering*: 13694332241263871.
- Xie EL, Jiang T, Xia ZY, et al. (2023a) Postbuckling behavior of FRP bending-active arches subjected to a central point load. *Journal of Composites for Construction* 27(5): 04023039.
- Xie EL, Song YX, Zhang PF, et al. (2024) FRP bending-active gridshells: Numerical simulation and model test. *Structures* 106064.
- Xie P, Lam L and Jiang T. (2023b) Compressive behavior of GFRP tubes filled with self-compacting concrete. *Journal of Composites for Construction* 27(1): 04022103.
- Xu J, Zhu P and Qu W. (2022) Numerical and analytical study of concrete beams reinforced with hybrid fiber-reinforced polymer and steel bars. *Journal of Composites for Construction* 26(5): 04022045.
- Yan F, Lin ZB and Yang MJ. (2016) Bond mechanism and bond strength of GFRP bars to concrete: A review. *Composites Part B: Engineering* 98: 56-69.

Table 6.1 Internal forces caused by distributed loads

Diagram	Load type	Horizontal force	Vertical force	Bending moment
	$q_{x,S_i}$	$q_{x,S_i} R_{S_i} (\cos(\theta_{i,r} - \beta) - \cos(\theta_{i,r}))$	0	$\frac{1}{2} q_{x,S_i} R_{S_i}^2 ((\cos(\theta_{i,r} - \beta) - \cos(\theta_{i,r}))^2$
	$q_{y,S_i}$	0	$q_{y,S_i} R_{S_i} (\sin(\theta_{i,r} - \beta) - \sin(\theta_{i,r}))$	$\frac{1}{2} q_{y,S_i} R_{S_i}^2 (\sin(\theta_{i,r}) - \sin(\theta_{i,r} - \beta))^2$
	$q_{s,S_i}$	0	$-q_{s,S_i} \beta R_{S_i}$	$q_{s,S_i} R_{S_i}^2 (\cos(\theta_{i,r} - \beta) - \cos(\theta_{i,r}) - \beta \sin(\theta_{i,r} - \beta))$
	$q_{R,S_i}$	$q_{R,S_i} R_{S_i} (\cos(\theta_{i,r} - \beta) - \cos(\theta_{i,r}))$	$q_{R,S_i} R_{S_i} (\sin(\theta_{i,r} - \beta) - \sin(\theta_{i,r}))$	$q_{R,S_i} R_{S_i}^2 (1 - \sin(\theta_{i,r}) \sin(\theta_{i,r} - \beta) - \cos(\theta_{i,r}) \cos(\theta_{i,r} - \beta))$

Table 6.2 Unknown initial values and boundary conditions of typical types of supports

Support type	Horizontal load	Vertical load	Bending moment	Horizontal displacement	Vertical displacement	Rotation
Fixed	Unknown	Unknown	Unknown	0	0	0
Hinged	Unknown	Unknown	0	0	0	Unknown
Rotational spring	Unknown	Unknown	Unknown	0	0	moment/spring stiffness
Vertical sliding hinge	Unknown	0	Unknown	0	Unknown	0

Table 6.3 Comparison between predictions and test results of steel/FRP-reinforced concrete arches

Specimen ID	Peak load			Deflection at crown corresponding to peak load		
	Test (kN)	Prediction (kN)	Error (%)	Test (mm)	Prediction (mm)	Error (%)
NCS12H	279.6	271.9	2.74	13.13	13.13	-
NCG13H	225.6	234.3	3.86	11.71	11.63	0.68
NCG8H	194.9	201.6	3.42	10.72	10.84	1.12
NCG13L	272.3	272.3	0.02	14.38	15.35	6.75
HCG13H	257.5	262.2	1.83	12.98	12.34	4.93

Note: The error is defined as the ratio of the absolute difference between two sets relative to the test value.

Table 6.4 Geometrical and material properties of CFFT arches

Test series	Arch span (m)	Arch rise (m)	Arch radius (m)	Boundary condition	Section diameter (mm)	Concrete strength (MPa)	FRP tube wall thickness (mm)	FRP in longitudinal direction		FRP in hoop direction	
								Elastic modulus (GPa)	Rupture Strain (%)	Elastic modulus (GPa)	Rupture Strain (%)
1st	6.71	2.10	3.96	Hinged	300	27	2.5	42.7	1.70	14.3	-
2nd	6.10	1.22	3.28	Fixed	110	25	2.0	13.8	2.27 <sup>a</sup>	19.4	1.93 <sup>a</sup>

Note: <sup>a</sup> These rupture strain values were determined based on the longitudinal and hoop FRP strengths reported in Majeed et al. (2021), assuming the tested coupons were linear elastic.

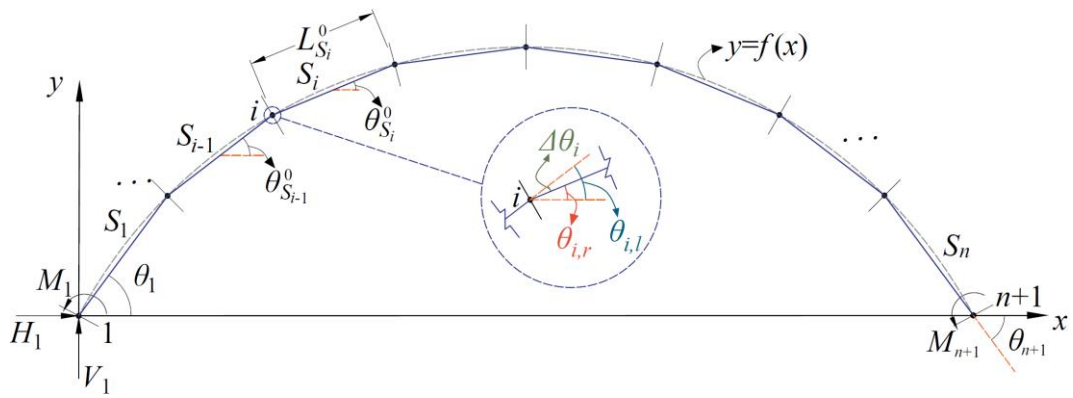
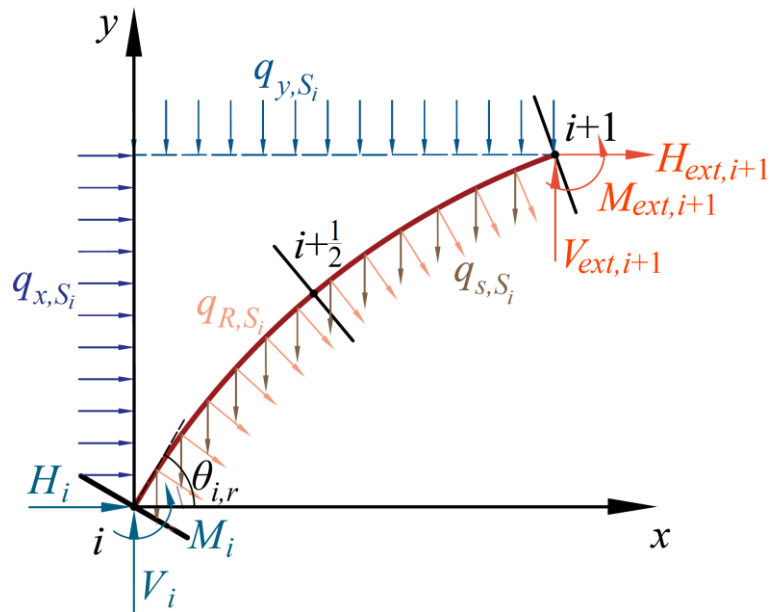
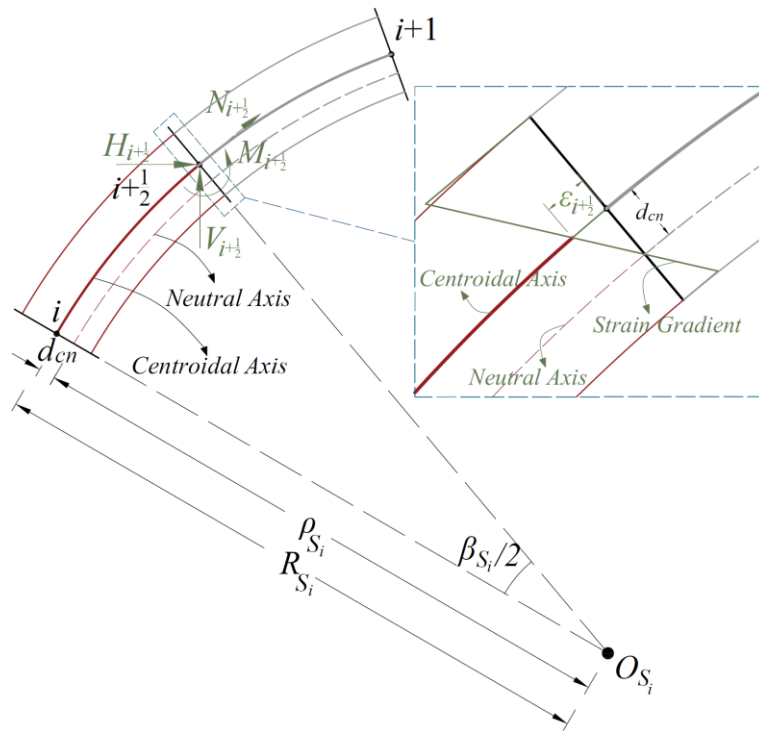


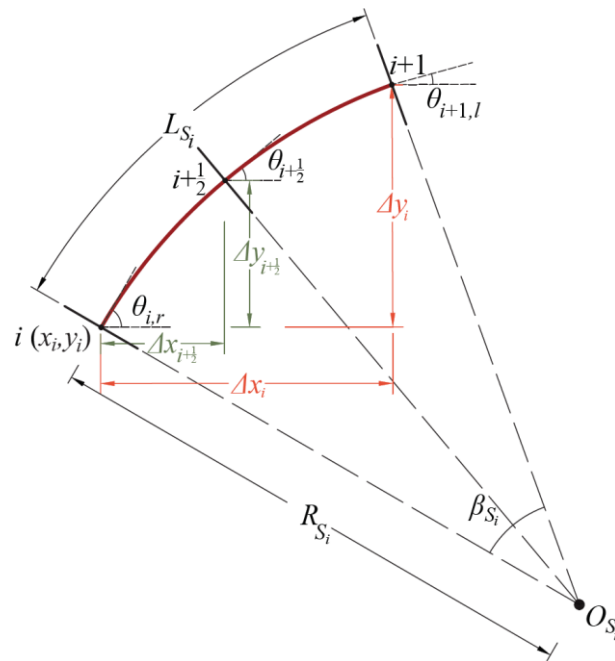
Figure 6.1 Schematic of the theoretical model



(a) Applied loads

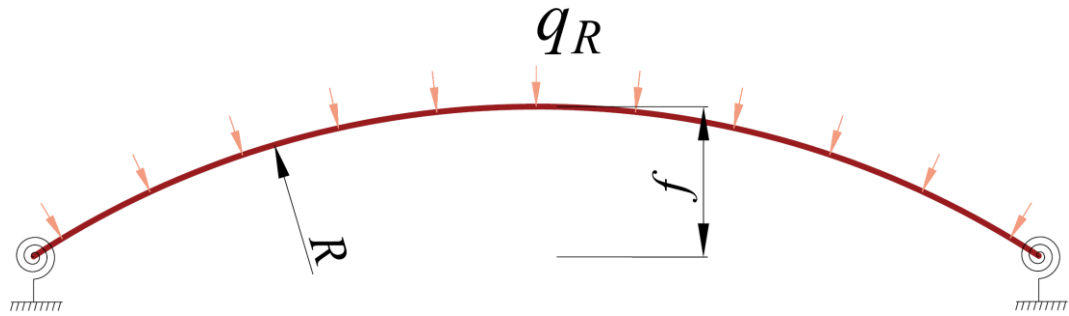


(b) Midpoint determination

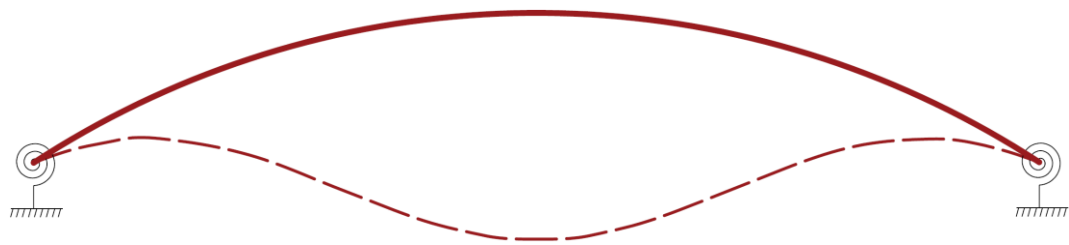


(c) Deformed segment shape

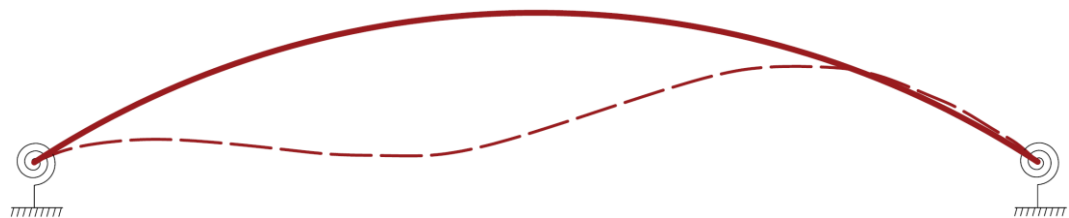
Figure 6.2 Illustration of the deflection function



(a) Arch configuration and loading condition

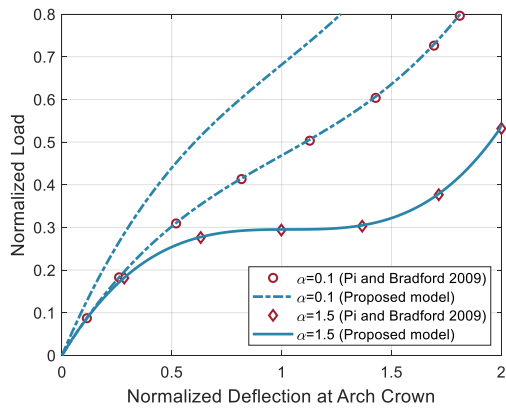


(b) Symmetric snap-through buckling mode

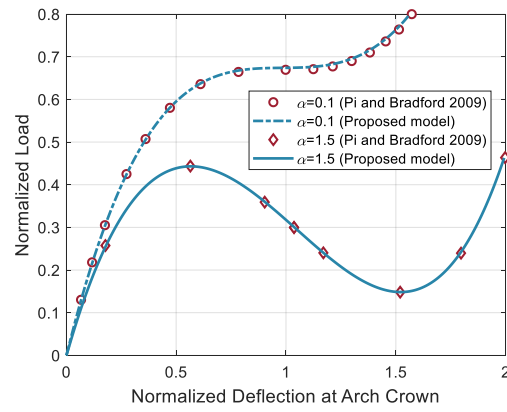


(c) Anti-symmetric bifurcation buckling mode

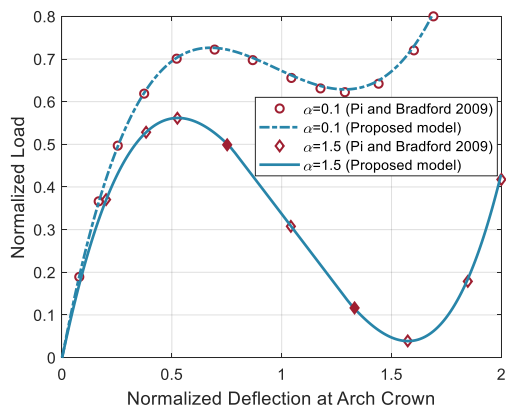
Figure 6.3 Illustration of a circular arch subjected to a uniform radial pressure



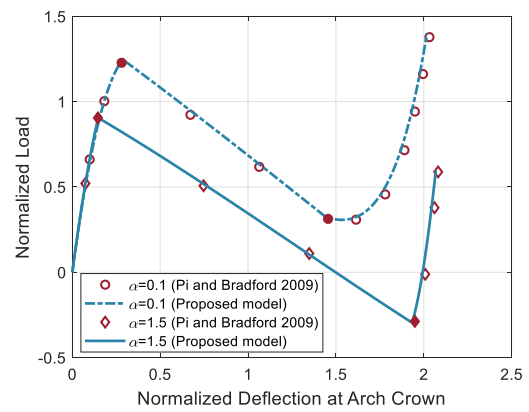
(a)  $\lambda=4.35924$



(b)  $\lambda=7.1431$



(c)  $\lambda=8.5$



(d)  $\lambda=16$

Figure 6.4 Results of analytical verification

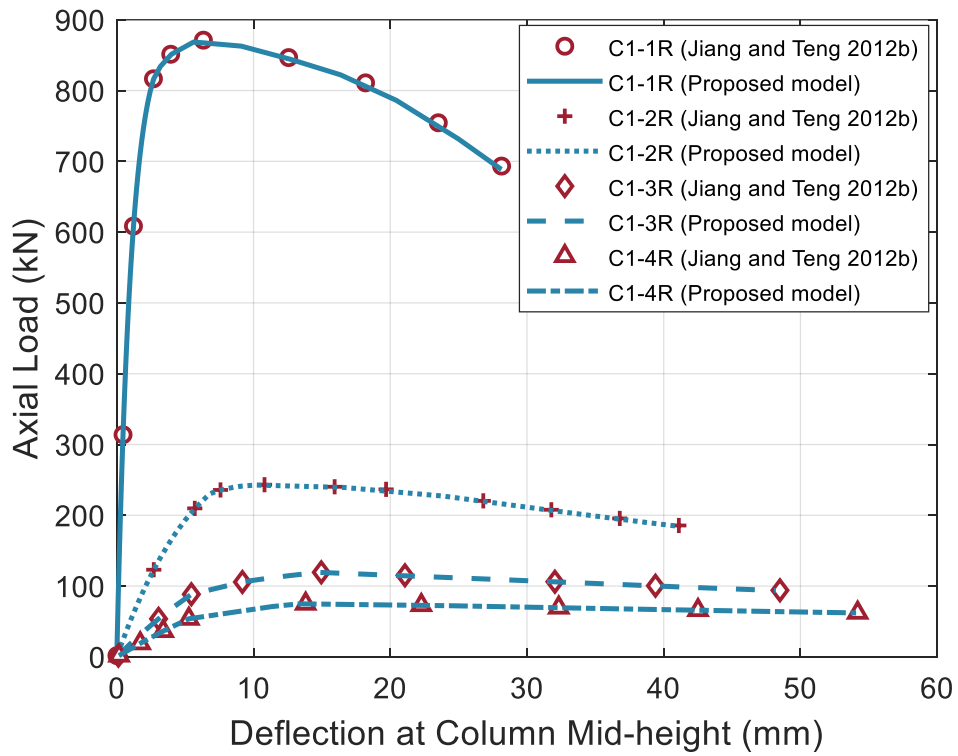
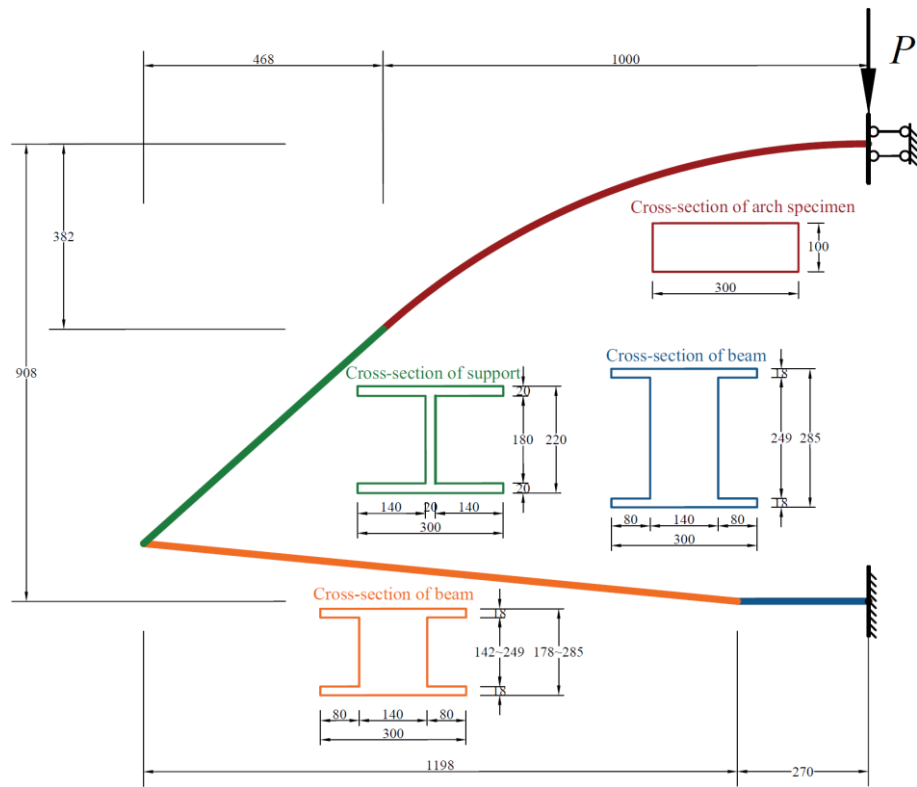
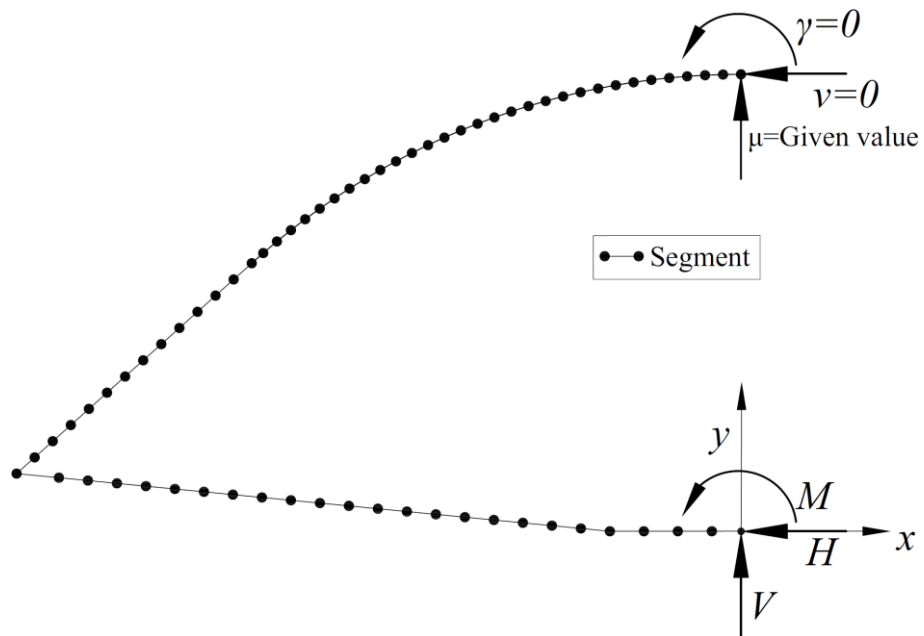


Figure 6.5 Results of numerical verification

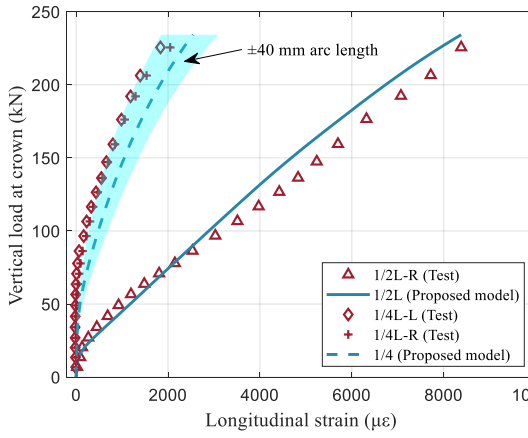


(a) Simplified 1D elements

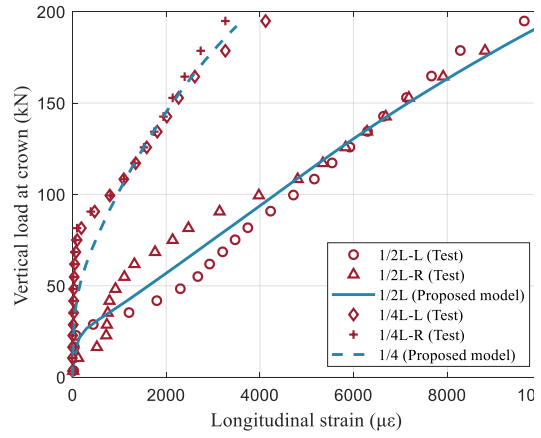


(b) Free-body diagram

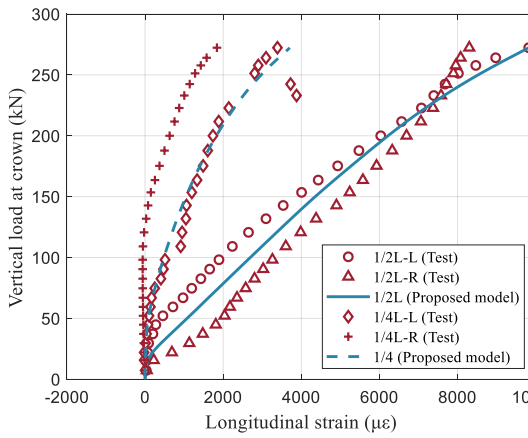
Figure 6.6 Representation of arch specimen with support system in theoretical model (dimensions in mm)



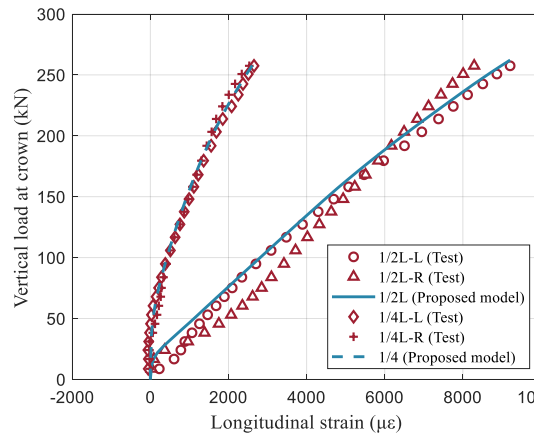
(a) NCG13H



(b) NCG8H

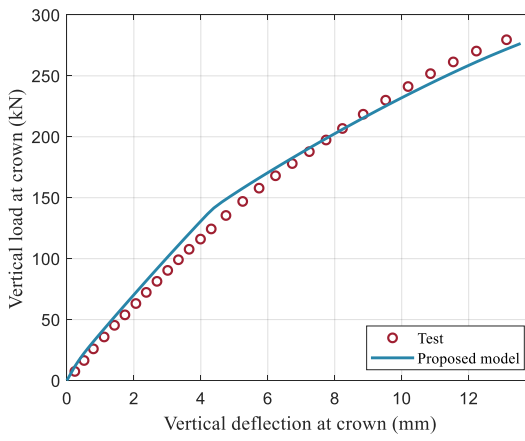


(c) NCG13L

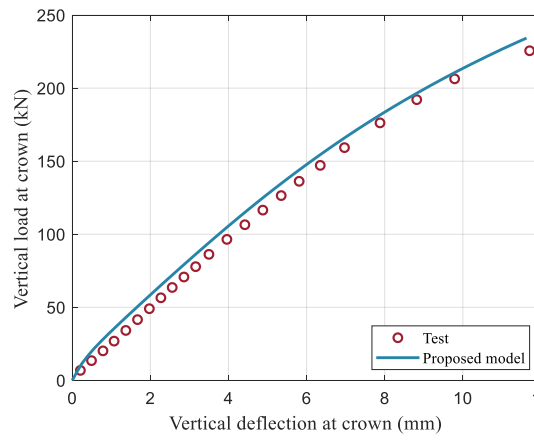


(d) HCG13H

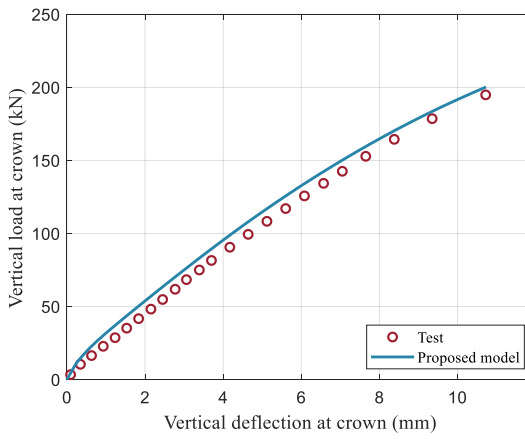
Figure 6.7 Comparisons of load-strain curves of longitudinal reinforcement in tension



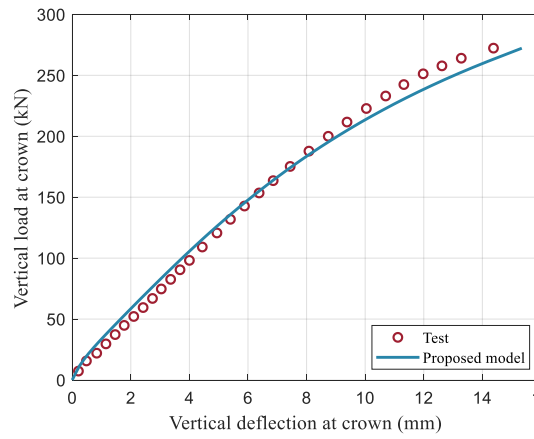
(a) NCS12H



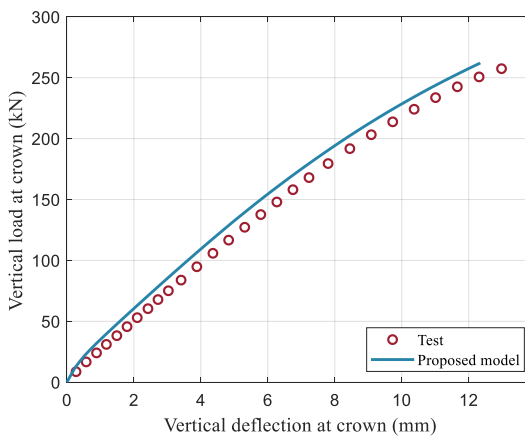
(b) NCG13H



(c) NCG8H

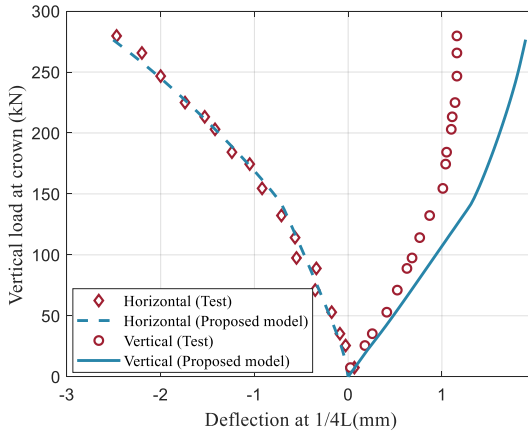


(d) NCG13L

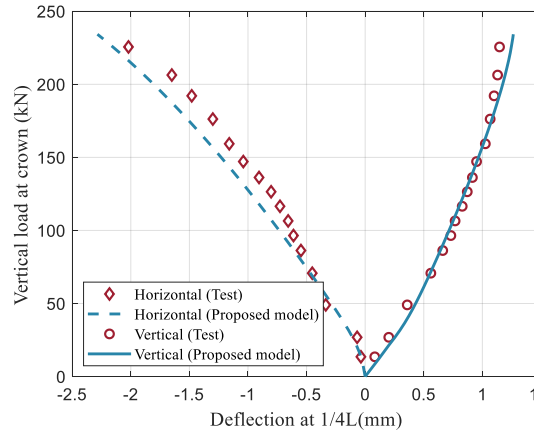


(e) HCG13H

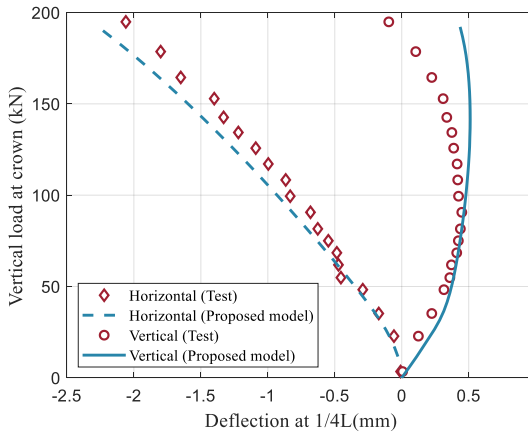
Figure 6.8 Comparisons of load-deflection curves at arch crown



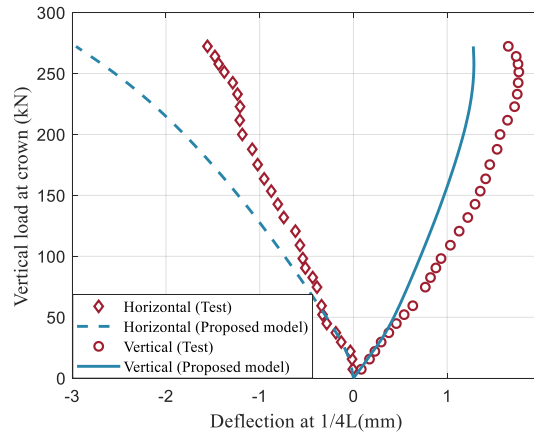
(a) NCS12H



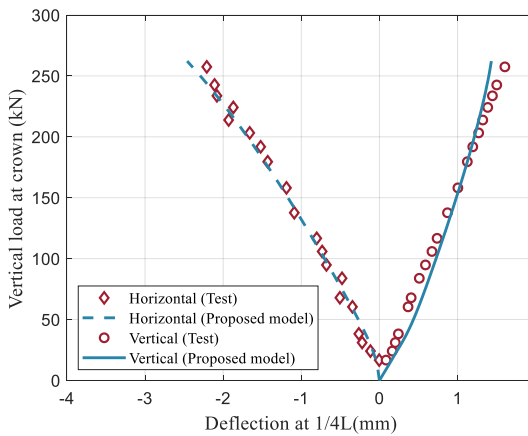
(b) NCG13H



(c) NCG8H

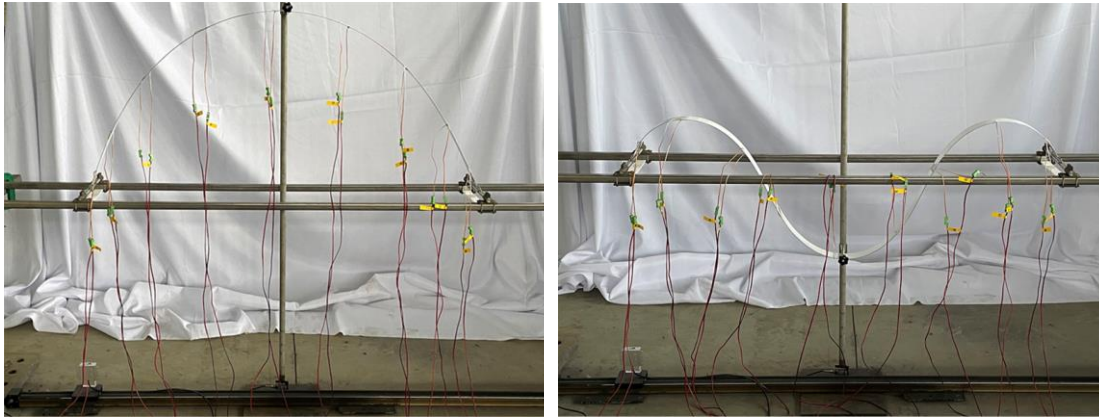


(d) NCG13L



(e) HCG13H

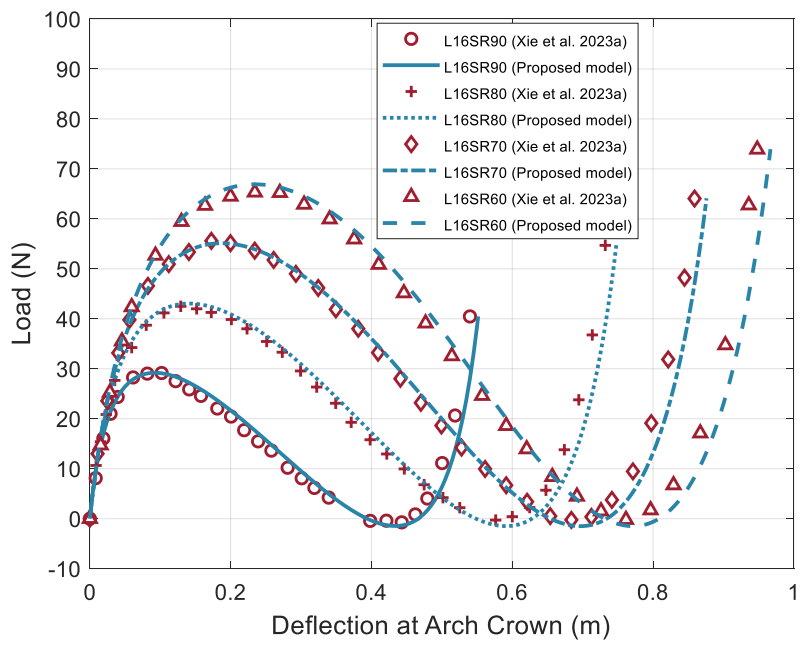
Figure 6.9 Comparisons of load-deflection curves at L/4



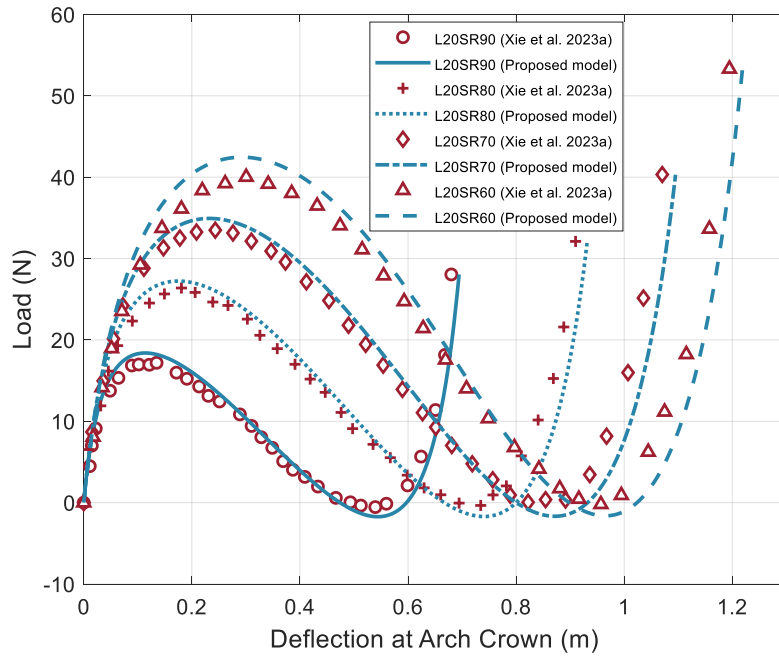
(a) Forming stage

(b) Loading stage

Figure 6.10 Loading tests on active-bending arches (Xie et al., 2023)



(a) L16 specimens



(b) L20 specimens

Figure 6.11 Comparisons with load-deflection curves of FRP bending-active arches

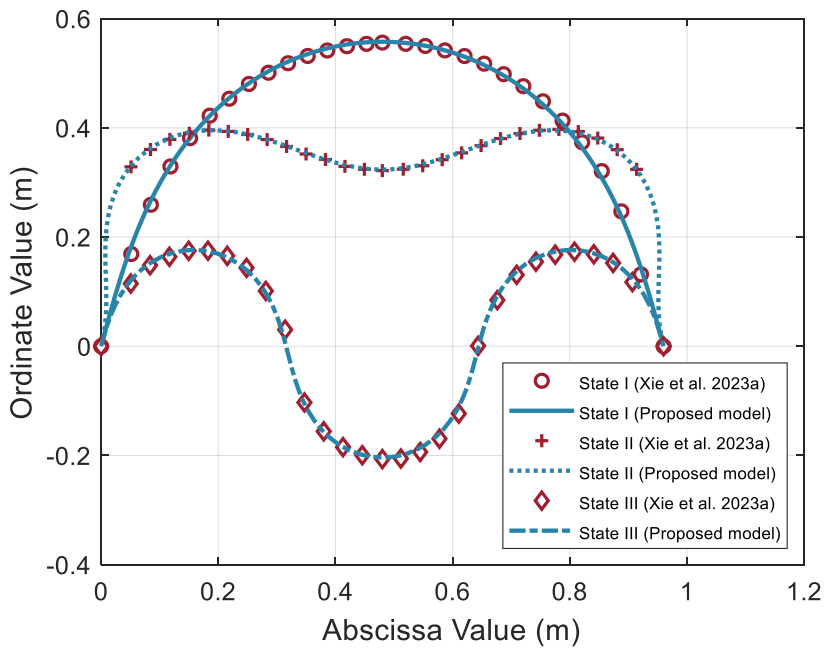


Figure 6.12 Comparisons with deflected shapes of specimen L16SR60

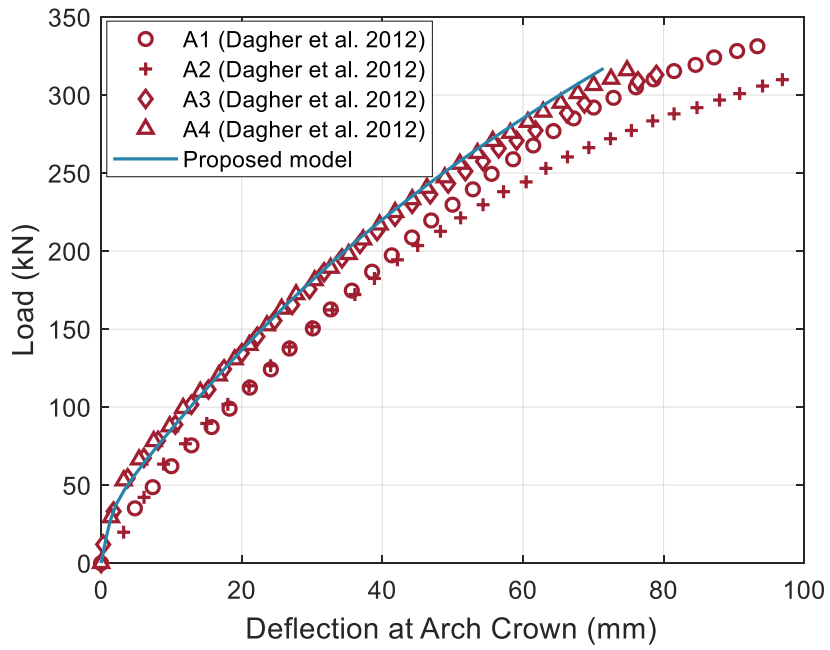


(a) Test setup

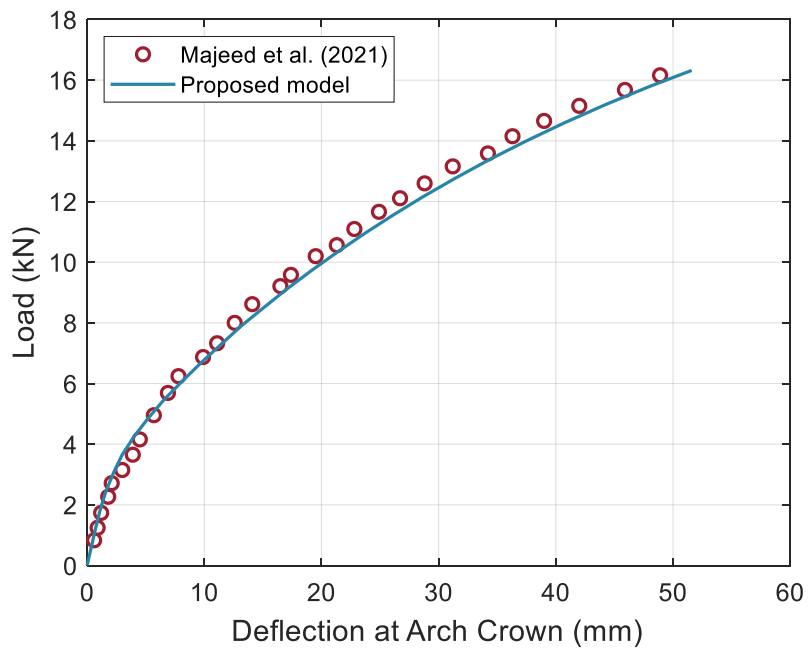


(b) Typical failure mode

Figure 6.13 Hinge-supported CFFT arches (Dagher et al., 2012)



(a) Hinge-supported arches



(b) Fixed arches

Figure 6.14 Comparisons with load-deflection curves of CFFT arches



(a) Test setup



(b) Failure mode

Figure 6.15 A fixed CFFT arch (Majeed et al., 2021)

## **CHAPTER 7**

# **FINITE ELEMENT MODELING OF FRP REINFORCED CONCRETE ARCHES**

### **7.1 INTRODUCTION**

Chapter 6 of this thesis proposed an enhanced deflection method, extending its application from small-curvature to large-curvature problems, which proved effective in predicting the behavior of FRP-enabled slender arches (Xia et al., 2024). Essentially, this method only accounts for uniaxial stress/strain in determining structural deformation and failure states (Chen and Atsuta, 2007). As a result, the method considers only the coupling effects of axial force and bending moment, neglecting shear contributions in structural analysis. While this simplification is generally valid for slender arches, where each cross-section primarily experiences uniaxial stress along the arch axis, in certain cases where shear effects cannot be ignored (e.g., punching shear in localized high-pressure zones) (Yan et al., 2016; Nagheh et al., 2024), the deflection method may overestimate stiffness and load-bearing capacity, requiring a more advanced numerical analysis. This chapter explored the failure mechanisms of FRP-RC arches through the finite element method (FEM), which is capable of accurately analyzing structural members subjected to combined actions of axial load, shear load, and bending moment (axial-shear-flexural interaction) (Kirkland et al., 2015).

Additionally, a key advantage of the FE model presented in this chapter, compared to the theoretical model in Chapter 6, is its enhanced ability to capture the bond-slip behavior between FRP reinforcement and concrete in FRP-RC arches. This refinement addresses one of the main limitations of the theoretical model presented in Chapter 6, allowing the numerical model to more accurately reflect experimental observations (Gu et al., 2020).

To the best knowledge of author, no existing numerical study or parametric analysis has focused specifically on the static/quasi-static performance of FRP-RC arches. Most parametric studies on FRP-RC members have been limited to straight elements, concentrating on the bending moment, shear force, or their combined effects, with studied parameters including concrete strength, reinforcement ratio, concrete cover thickness, and loading conditions (Rasheed et al., 2004; Abushanab and Alnahhal, 2021; Sarhan and Al-Zwainy, 2022; Hussein et al., 2022; Liao et al., 2023; Zinkaah et al., 2022). Several design guidelines and recommended formulas also exist for evaluating the flexural and shear performance of FRP-RC members (ACI 440.11R-22, 2022; ACI 440.1R-15, 2015; GB 50608-20, 2010; Rasheed et al., 2004; Zinkaah et al., 2022; Abushanab and Alnahhal, 2021; Liao et al., 2023). However, these are primarily focused on straight FRP-RC members (e.g., beams and slabs), where axial forces are negligible or nonexistent, in contrast to arch structures where axial forces are critical. Consequently, the accuracy and applicability of using design formulas for straight FRP-RC members in evaluating FRP-RC arches are questionable (Rossi, 2013). Therefore, it is necessary to validate the effects of key parameters and assess whether existing design formulas are applicable to FRP-RC arches, or if modifications are required to extend the design framework to include arch structures.

Furthermore, it is important to note that in FRP-RC arches, some FRP bars inevitably experience compressive stresses. However, existing research on the contribution of compressed FRP bars remains inconclusive. Their compressive strength depends on factors such as fiber type, fiber volume ratio, and manufacturing process (ACI 440.1R-15, 2015), while their compressive elastic modulus is primarily influenced by the length-to-diameter ratio, bar size and type, and boundary conditions. The compressive strength of FRP bars is significantly lower than their tensile strength due to susceptibility to buckling (Hasan et al., 2019; GB 50608-20, 2010). Prior research has reported that the compressive strength and stiffness of GFRP bars range from 30% to 70% and from 77% to 100%, respectively, of their tensile values (Bedard, 1992; Chaallal and Benmokrane, 1993; Deitz et al., 2003). According to existing standards, ACI 440.1-15 (2015) and CSA S806-12 (2012) recommend neglecting the contribution of compressed FRP bars, while ACI 440.11-22 (2022) assumes that compressed GFRP bars have the same strength and stiffness as the surrounding concrete. Therefore, further parametric studies are required to investigate how the contribution of compressed FRP bars may affect the structural behavior of FRP-RC arches.

This chapter numerically investigates the structural behavior of FRP-RC arches under different failure modes. An FE model of FRP-RC arches was first developed and subsequently validated by comparing its predictions with experimental data presented in Chapter 5. Combining experimental and numerical results, the failure modes (i.e., flexural failure and shear failure), load-deflection responses, crack patterns, and strain development were thoroughly examined, offering profound insights into the behavior of FRP-RC arches. Following validation, a parametric analysis was conducted on full-scale arch ribs, considering an expanded range of key parameters influencing structural

behavior, including concrete cover thickness, reinforcement ratio, concrete strength, and compressed bar contributions, under different loading conditions (i.e., single-point loading and multiple-point loading).

## **7.2 FINITE ELEMENT MODELING**

### **7.2.1 General**

The FE models were developed to simulate the tests presented in Chapter 5. Detailed specifications are provided in Figure 7.1(a) and Table 5.1. Figures 7.1(b) and 7.1(c) illustrate the reinforcement cages for the steel-RC and FRP-RC, respectively. Further details of the test setup can be found in Chapter 5.

Based on the experimental program, a three-dimensional (3D) FE model was developed using ABAQUS (2024). The model comprised several components: concrete, longitudinal curved bars, stirrups, two steel supports connected to the arch ends, and the underlying beam foundation. Three-dimensional eight-node reduced integration hexahedral elements (C3D8R) were adopted to simulate the concrete, steel supports, and beam foundation. The longitudinal rebars and stirrups, which were considered only for axial forces and linear displacements, were modeled using three-dimensional two-node truss elements (T3D2).

The characteristic element length for the concrete is typically set to three times the maximum coarse aggregate diameter to ensure continuum smoothing of the randomly inhomogeneous material (Musiket et al., 2017; Bažant and Oh, 1983; Qapo et al., 2016), which in this case was set to 30 mm. For beam specimens with heights of 300 mm or less, a mesh size of around 10% of the beam height is suggested (Jumaa and Yousif, 2019), resulting in a mesh size of 10 mm for this study. A mesh convergence analysis

was conducted with mesh sizes ranging from 5 mm to 30 mm. It was observed that mesh sizes below 10 mm significantly increased computational time with negligible differences in results (e.g., load-deflection curves). Hence, a 10 mm mesh size was chosen (Figure 7.2), providing an optimal balance between computational efficiency and accuracy. The mesh sizes for the longitudinal bars and stirrups were consistent with those of the concrete elements. The steel supports and beam foundation, which experienced minimal stress and remained elastic throughout loading, were meshed with a mesh division of 20 mm to enhance computational efficiency (Figure 7.2). The entire FE model comprised 86,850 solid elements and between 2,754 to 3,735 truss elements, depending on the stirrup configuration and longitudinal bar positioning.

The numerical model utilized the nonlinear quasi-static explicit solver, which is known for its straightforward and intuitive approach. The iterative solution process was carried out using the Newton-Raphson method, with displacements applied incrementally to trace the loading paths and calculate structural responses based on equilibrium equations.

### **7.2.2 Boundary conditions and loading schemes**

In the test setup, each RC arch specimen was cast with steel baseplates at both ends. These baseplates were bolted to custom-made steel supports, which were then secured to the top surface of an underlying steel beam. The bottom surface of the beam was anchored to the ground at its mid-span. The boundary conditions and loading mechanisms of the model were set according to the experimental setup illustrated in Figure 5.14. The top surface of the loading plate was coupled with a reference point, and an external load was applied through displacement control, consistent with the

experimental loading scheme.

The displacement data monitored at the bolted sections (Figure 5.16) indicated that the bolting connections between the arch specimen and steel supports, as well as between the steel supports and the underlying steel beam, provided sufficient strength to prevent relative sliding. Therefore, both arch ends were tied to the steel supports, ensuring the overlapping areas shared identical movement. Additionally, the steel supports and the beam were merged into a unified component, sharing the applied load collectively (Figure 7.2).

During testing, the bottom surface near the mid-span of the beam foundation was bolted to the ground. In the numerical model, the translational and rotational degrees of freedom in this contact area were constrained to a reference point. By setting all degrees of freedom at this reference point to zero, the model ensured that the beam foundation was fixed at mid-span.

### **7.2.3 Material modeling of concrete**

The constitutive behavior of the concrete was represented using the classical Concrete Damaged Plasticity (CDP) model (Lubliner et al., 1989). The compressive strength ( $f_{cu}$ ) and elastic modulus ( $E_c$ ) of the concrete were obtained experimentally using standard 150×300 mm cylinders (ASTM C39/C39M-21, 2021), as summarized in Table 5.2. The tensile strength ( $f_t$ ) was estimated according to GB 50010 (2015). A default Poisson's ratio of 0.2 was used. The uniaxial compressive and tensile stress-strain relationships for the concrete were also adopted from GB 50010 (2015), with specific expressions for these relationships defined in Equations (7.1) and (7.2).

$$\sigma_c = E_c \varepsilon \begin{cases} \frac{f_{cu}/(E_c \varepsilon_{co} - f_{cu})}{E_c \varepsilon_{co}/(E_c \varepsilon_{co} - f_{cu}) - 1 + (\varepsilon/\varepsilon_{co})^{E_c \varepsilon_{co}/(E_c \varepsilon_{co} - f_{cu})}} & \varepsilon \leq \varepsilon_{co} \\ \frac{f_{cu}/(E_c \varepsilon_{co})}{\alpha_c (\varepsilon/\varepsilon_{co} - 1)^2 + \varepsilon/\varepsilon_{co}} & \varepsilon > \varepsilon_{co} \end{cases} \quad (7.1)$$

$$\sigma_t = E_c \varepsilon \begin{cases} f_t/(E_c \varepsilon_{to})(1.2 - 0.2(\varepsilon/\varepsilon_{to})^5) & \varepsilon \leq \varepsilon_{to} \\ \frac{f_t/(E_c \varepsilon_{to})}{\alpha_t (\varepsilon/\varepsilon_{to} - 1)^{1.7} + \varepsilon/\varepsilon_{to}} & \varepsilon > \varepsilon_{to} \end{cases} \quad (7.2)$$

where  $\sigma_c$  and  $\sigma_t$  represent the compressive and tensile stresses of the concrete in MPa, respectively, while  $\varepsilon$  denotes the corresponding strain. The strains corresponding to the uniaxial compressive and tensile strengths are represented by  $\varepsilon_{co}$  and  $\varepsilon_{to}$ . Additionally, the parameters  $\alpha_c$  and  $\alpha_t$ , which are related to the concrete strength, govern the shapes of the descending branches.

In the CDP model, the dilation angle ( $\emptyset$ ) is typically defined within the range of  $0^\circ$  to  $56^\circ$  (Tao et al., 2013) and was set to  $38^\circ$  in this study (Kmieciak and Kamiński, 2011; Ren et al., 2021). The other four plastic damage parameters — flow potential eccentricity ( $\epsilon$ ), the ratio of the initial biaxial compressive yield stress to that of the uniaxial ( $\sigma_{b0}/\sigma_{c0}$ ), the ratio of the second stress invariant on the tensile meridian to that on the compressive meridian ( $K_c$ ), and the viscosity parameter ( $u$ ) — were set to 0.1, 1.16, 0.667, and 0.0005, respectively (Xiong et al., 2017; Simulia, 2013).

#### 7.2.4 Material modeling of steel and FRP reinforcement

For the steel-RC arch, the steel longitudinal bars and stirrups were assumed to behave as elastic-perfectly plastic materials and were modeled using a bilinear isotropic hardening model. The yield strength and elastic modulus of the steel reinforcement were determined from material property tests, as presented in Table 5.2.

Tensile tests demonstrated that FRP bars exhibit a linear elastic response without a yield plateau, failing in a brittle manner. The bilinear isotropic hardening model used for steel reinforcement was also applied to simulate the mechanical properties of FRP bars and stirrups, with the “yield strength” defined as the strength of the FRP reinforcement. To replicate the brittle behavior in the FE analysis, an extremely low value was specified for the ultimate strength, along with a near-zero pseudo-plastic strain. This ensures that the FRP bars maintain linear elastic behavior until failure, with immediate rupture once entering the “plastic stage”. As current standards do not provide adaptable methods for testing the mechanical properties of curved FRP bars, the tensile strength and elastic modulus of the FRP bars were derived from tensile tests on straight FRP bars from the same batch using the same raw materials (Spagnuolo et al., 2014).

The behavior of FRP reinforcement under compression is complex due to its anisotropic and non-homogeneous properties (ACI 440.1R-22, 2022). Deitz et al. (2003) reported that the compressive strength of GFRP bars is approximately half of their tensile strength. The elastic modulus of GFRP bars in compression has been found to be close to their tensile modulus (Si et al., 2022; Maranan et al., 2016; Deitz et al., 2003; Khorramian and Sadeghian, 2021). Therefore, in this model, a 50% reduction in compressive strength compared to tensile strength was applied, while the tensile and compressive elastic modulus for GFRP bars were assumed to be identical ( $E_{frp,t}$ ) (Hadhood et al., 2017). Further discussions on the contributions of compressed FRP bars to the behavior of FRP-RC arches are presented in Section 7.4.5.

The stress-strain relationship for FRP bars was expressed as follows:

$$\sigma_{frp} = \begin{cases} E_{frp,t} \varepsilon_{frp} & -0.5\varepsilon_{frp,t} < \varepsilon_{frp} < \varepsilon_{frp,t} \\ 0 & \varepsilon_{frp} > \varepsilon_{frp,t} \text{ or } \varepsilon_{frp} < -0.5\varepsilon_{frp,t} \end{cases} \quad (7.3)$$

where  $\sigma_{frp}$  and  $\varepsilon_{frp}$  represent the stress and strain of FRP bars in MPa, respectively, while  $\varepsilon_{frp,t}$  is the rupture strain of FRP bars. The elastic modulus and tensile strength of steel and FRP bars in this model were based on experimental values listed in Table 5.2. The default Poisson's ratio was set to 0.3 for both materials.

### 7.2.5 Interface modeling of reinforcement and concrete

To accurately simulate the force transfer mechanism at the interfaces between steel/FRP reinforcement and concrete, a connector was incorporated to represent the longitudinal bond-slip behavior (Mathern and Yang, 2021; Wang et al., 2024). Initially, a “dummy bar” was created for each longitudinal bar, with identical attributes, length, position, and mesh dimensions as the actual longitudinal bars, but with a significantly small cross-sectional area of only 0.001 mm<sup>2</sup>. An embedded constraint was then applied to simulate the contact relationship between the “dummy bar” and the concrete. Finally, spring elements were used to establish the node-to-node connections between the “dummy bar” and the actual reinforcement at the same locations. This arrangement facilitates the uniform stress transmission from reinforcement to concrete. Due to the limitations of the graphical user interface (GUI) of ABAQUS, which does not support zero-length spring elements, these elements were manually incorporated into the FE model via input file scripts (Kadhim et al., 2023).

Utilizing the aforementioned method, a bond-slip law was defined via a force-slip relationship through spring elements based on CEB-FIP guidelines for steel-RC members (Béton, 1993). The behavior was quantified using the following equation:

$$\tau_s = \begin{cases} \tau_{s,max} \left( \frac{s_s}{s_{s,1}} \right)^{\alpha_s} & 0 \leq s_s \leq s_{s,1} \\ \tau_{s,max} & s_{s,1} < s_s \leq s_{s,2} \\ \tau_{s,max} - (\tau_{s,max} - \tau_{s,f}) \left( \frac{s_s - s_{s,2}}{s_{s,3} - s_{s,2}} \right) & s_{s,2} < s_s \leq s_{s,3} \\ \tau_{s,f} & s_{s,3} < s_s \end{cases} \quad (7.4)$$

where  $s_s$  represents the slip in mm, and  $\tau_s$  denotes the corresponding bond stress in MPa. The parameters in Equation (7.4) were determined based on the unconfined state of concrete and the deformed surface profile of steel reinforcement, as specified in CEB-FIP (Béton, 1993). The maximum bond stress,  $\tau_{s,max}$ , is calculated as  $2.0\sqrt{f_{cu}}$  in MPa, and the residual bond stress,  $\tau_{s,f}$ , as  $0.15\tau_{s,max}$  in MPa. The empirical coefficient  $\alpha_s$  was set at 0.4, with  $s_{s,1} = s_{s,2} = 0.6$  mm and  $s_{s,3} = 1.0$  mm (Béton, 1993).

It is noted that the bond strength at the FRP-concrete interface is generally weaker than that at the steel-concrete interface (Wei et al., 2019; Xiong et al., 2022), and plays an important role in the structural behavior of FRP-RC members. An accurate bond-slip constitutive model is essential for properly understanding and simulating the behavior of FRP-RC members. The bond-slip behavior at the interface between longitudinal FRP bars and concrete was characterized using the CMR model (Cosenza et al., 1997), a modified version of the CEB-FIP model [Equation (7.4)] originally developed for traditional steel reinforcement. This modified model has been widely recognized and applied in numerical studies of FRP-RC members (Hawileh, 2012; Gu et al., 2020; Zhang et al., 2023). The constitutive model for this bond-slip relationship was expressed as follows:

$$\tau_{frp} = \begin{cases} \tau_{frp,max} \left( \frac{s_{frp}}{s_{frp,1}} \right)^{\alpha_{frp}} & 0 \leq s_{frp} \leq s_{frp,1} \\ \tau_{frp,max} - p \cdot \tau_{frp,max} \left( \frac{s_{frp}}{s_{frp,1}} - 1 \right) & s_{frp,1} < s_{frp} \leq s_{frp,2} \\ \tau_{frp,f} & s_{frp,2} < s_{frp} \end{cases} \quad (7.5)$$

where  $\tau_{frp,max}$  represents the bond strength in MPa, and  $s_{frp,1}$  denotes the slip in mm at peak stress. These values were derived from the average results of pull-out tests conducted according to ACI 440.3R-12 (2012), as detailed in Table 5.3.  $\tau_{frp,f}$  represents the residual stress and is set to 7.79 MPa based on the specified surface treatment (Cosenza et al., 1997), while  $\alpha_{frp}$ ,  $p$  and  $s_{frp,2}$  are empirical coefficients obtained through statistical regression analysis of bond stress-slip curves (Wei et al., 2019; Xie et al., 2022). A comparison between the experimentally obtained bond-slip relationships and the calculations from the CMR model is presented in Figure 5.13. The comparison shows that the CMR model accurately represents the pull-out test results. Further details of the pull-out tests are provided in Section 5.2.4.

The slip between concrete and embedded longitudinal reinforcement, including both steel and FRP bars, was only considered along the longitudinal axis. To represent this condition in the model, an extremely high stiffness value of 10,000 GPa was assigned to the spring elements in the two directions orthogonal to the longitudinal axis.

Moreover, the slip between stirrups and concrete, whether steel or FRP, was considered insignificant and could be disregarded (Gu et al., 2020; Hussein et al., 2022). Therefore, an embedded constraint was used to simulate the contact behavior between stirrups and concrete (Simulia, 2013), implying a perfect bond between the stirrups and concrete.

### **7.2.6 Material modeling of steel supports and beam foundation**

The steel supports and beam foundation beneath the arch feet were made of low-carbon steel. As these steel components did not experience significant stress or yielding during the loading process, they were characterized as elastic materials in the FE model. The modulus of elasticity was set to a conventional value of 200 GPa.

## **7.3 VALIDATION OF FE MODEL**

### **7.3.1 Load-deflection responses**

Figure 7.3 compares the load-deflection curves obtained from numerical simulations and experimental results for the tested arch specimens. The endpoint of the predicted curves from the FE model was determined based on material failure criteria. In specimen NCG13L, shear failure occurred when the strain in the critical stirrup reached its ultimate limit. Other specimens experienced flexural failure, characterized by concrete crushing (i.e., reaching the ultimate compressive strain) due to over-reinforced configurations. It is noteworthy that FRP-RC flexural members typically fail either by FRP rupture in under-reinforced elements or by concrete crushing in over-reinforced ones, both of which are recognized by ACI 440.1-15 (2015). However, concrete crushing is preferable as it exhibits relatively ductile behavior (GangaRao et al., 2006). The ultimate strain for the extreme concrete compression fiber was set to 0.0035, as recommended by CSA S806-12 (2012), except for specimen NCG13L, where the maximum compressive strain of concrete was adjusted to 0.0055 to account for material heterogeneity and variability and better align the simulation results with the experimental observations (Kassem et al., 2011). The ultimate strain for FRP materials

(e.g., stirrups and longitudinal bars) was determined from material tests. A detailed discussion on strain development in FRP reinforcement and concrete is provided in Section 7.3.3.

The trends observed in Figure 7.3 show a general agreement between the numerical and experimental data. Despite minor variations in accuracy across different specimens, the FE model reliably captured the nonlinear response of the steel/GFRP-reinforced concrete arches throughout the loading process. To further validate the proposed models, Table 7.1 presents a comparison of the peak load and corresponding peak deflection at the arch crown, obtained from both experiments and finite element analysis. For the peak load, the ratio of the experimental result to the numerical result ranged between 0.96 and 1.09, with a mean value of 1.01 and a standard deviation of 0.04.

In terms of the ultimate state, specimens (i.e., NCS12H, NCG13H, NCG8H, HCG13H) exhibiting flexural failure are primarily governed by the ultimate compressive strain of concrete. The observed variation in results (Figure 7.3 and Table 7.1) may be attributed to material variability (e.g., concrete) and the use of an improper ultimate concrete strain assumed in analysis (Kassem et al., 2011). For specimen NCG13L, despite assigning a higher maximum compressive strain of 0.0055, the numerical prediction was still slightly lower than the experimental results. This discrepancy may be attributed to FRP reinforcement being modelled as truss elements based on the centroid axis of longitudinal bars in the FE model. This simplification shortens the effective legs of stirrups in the model compared to the actual test setup, thereby reducing their contribution to shear resistance. This degradation effect is more pronounced in shallow specimens, such as those in Chapter 5, where shear resistance is relatively low and

sensitive to the length of the effective stirrup legs. The peak deflection refers to the deflection at the peak load, as shown in Figure 7.3. The ratio of the experimental result to the numerical result ranged from 0.92 to 1.05, with mean and standard deviation values of 0.98 and 0.05, respectively.

### **7.3.2 Crack patterns and development**

In ABAQUS finite element analysis, there is no dedicated tool for visually displaying the propagation of cracks at integration points or centroids of concrete elements. Instead, indicators such as concrete damage, plastic strain, or logarithmic strain are typically used to represent crack development in concrete (Song et al., 2024).

To highlight the distribution characteristics of cracks in different regions, Figure 7.4 presents the typical tensile damage (DAMAGET) for different failure modes, comparing them with photographs of the tested arch specimens. The crack distributions for both failure modes were concentrated at the intrados near the arch apex and symmetrically at the extrados of the shoulders. The flexural and diagonal cracks were well captured, whereas longitudinal cracks were not. This is because the longitudinal cracks were caused by lateral splitting of the concrete under compression (i.e., Poisson's effect) rather than by principal tensile stress (Ren et al., 2021).

The crack development pattern for the typical specimen, NCG13H, as predicted numerically and observed experimentally, is illustrated in Figure 7.5. The progressive collapse of FRP-RC arches underwent four stages: elastic phase, crack formation at the arch apex, crack formation at both the arch apex and the two shoulders, and overall structural failure. All the numerical results show a good agreement with the experimental observations across the different stages of the loading process. The

specimen was initially uncracked during the elastic stage. Subsequently, several flexural cracks initiated at the intrados of the arch crown [Figure 7.5(a)], indicating that the maximum tensile strain along the arch axis exceeded the cracking strain. These cracks then propagated vertically along the depth of the section. At higher loads, existing flexural cracks widened and several new cracks appeared at the extrados of the two arch shoulders and the intrados of the arch crown successively [Figure 7.5(b)]. Meanwhile, some flexural cracks near the vault inclined toward the mid-span. With further load increased to the peak load, one of the main cracks at the crown nearly propagated to the top of the section, leading to specimen collapse [Figure 7.5(c)].

### **7.3.3 Strain distribution and development**

In addition to the global structural behavior, local strain development in the concrete and reinforcing bars was analyzed to evaluate the accuracy of the proposed FE model. Figure 7.6 shows the relationship between the applied load and strain development, where “Concrete (Test/FE prediction)”, “Top bar (Test/FE prediction)”, and “Bottom bar (Test/FE prediction)” refer to the measured/predicted strains of the extreme compressed concrete and the embedded reinforcement (top and bottom longitudinal bars) at cross-sections located 50 mm from the crown of the GFRP-RC arches. These sections were selected based on the locations of gauge points used in the tests. It should be noted that two symmetrical gauge points relative to the mid-span provided two sets of strain data, however, some gauge data were excluded due to operational errors during the experiments.

As shown in Figure 7.6, both the concrete and embedded GFRP longitudinal bars experienced minimal strain during the initial loading phase. Once cracking occurred,

the strain increased progressively until the arch failed. It can be seen that the predictions from the FE model align closely with the experimental data, demonstrating the overall reliability of the model. However, discrepancies were observed in strain predictions for the top bars across all specimens. This is likely due to the top bars initially experiencing compressive stress before transitioning to tensile stress. The pre-compression effect may have degraded the bond performance between the top bars and the concrete (Kim and Lee, 2019), leading to the actual bond mechanism (bond-slip relationship) in the tests to deviate from the one assumed in the FE model.

Furthermore, numerical simulations were used to estimate control strains indicating the failure state of the GFRP-RC arches, even though the majority were not directly measured in the tests. In Figures 7.6(a), 7.6(b), and 7.6(d), the curve labeled “Concrete (FE prediction-Max)” represents the maximum compressive strain of the concrete in the FE models of the arch specimens, while in Figure 7.6(c), “Stirrup (Test/FE prediction)” denotes the maximum measured/predicted strain of the critical stirrup that induces shear failure. For specimens NCG13H, NCG8H, and HCG13H, the concrete in the compression zone near the edge of the loading plate reached its ultimate compressive strain and subsequently crushed when the ultimate load was applied [“Concrete (FE prediction-Max)” in Figures 7.6(a), 7.6(b), and 7.6(d)], while all GFRP bars remained within the elastic range. Specimen NCG13L, which failed due to shear, exhibited an ultimate state characterized by the stirrup reaching its rupture strain near the most severe shear crack at the arch apex [Figure 7.4(b)], as depicted in the “Stirrup (FE prediction)” curve in Figure 7.6(c). The monitored stirrup strain at the corresponding location (25 mm from the arch apex) [“Stirrup (Test)” in Figure 7.6(c)] was also compared, showing a similar development trend. The simulation results

confirm that the established model in this chapter can predict both flexural failure and shear failure in FRP-RC arches.

## **7.4 PARAMETRIC STUDY**

### **7.4.1 Description of the parametric study**

The validated FE model provides an efficient and cost-effective platform for investigating key parameters not covered in the experiments. A parametric study was conducted on a full-scale steel-RC arch rib in service, where the steel reinforcement was replaced with FRP bars to evaluate the structural responses of FRP-RC arches.

The analyzed arch rib had a span of 19.72 m and a rise of 3.08 m, with fixed boundary conditions at both ends (Tang et al., 2005), as illustrated in Figure 7.7(a). The cross-section was rectangular, with a width of 200 mm and a depth of 280 mm. Reinforcement consisted of six 16 mm diameter steel bars placed as both upper and lower reinforcement, positioned 50 mm from the top and bottom edges of the cross-section [Figure 7.7(b)]. Stirrups with a diameter of 6 mm were spaced at 150 mm intervals. The concrete had a compressive strength of 24.8 MPa, while the embedded steel reinforcement had a yield strength of 360 MPa and an elastic modulus of 210 GPa. Further details on the referred arch rib can be found in Tang et al. (2005). For the FRP reinforcement, the tensile strength and elastic modulus were taken as 1000 MPa and 50 GPa, respectively. Unless specified otherwise, these values were used as default values for the subsequent analysis. The FE modeling and material constitutive relationships were consistent with those outlined in Section 7.2.

To capture the structural responses of FRP-RC arches under different loading conditions, analyses were conducted for both single-point loading and multiple-point loading scenarios. The single-point loading case involved a concentrated load at mid-span under displacement control, while the multiple-point loading case involved three equally distributed loads along the span. Based on requirements for FRP-RC members and commercially available materials, the parametric range was set as follows: concrete cover thickness ( $d_c$ ): 20-50 mm; reinforcement ratio ( $\rho_l$ ): 0.13%-8.62%; concrete strength ( $f_{cu}$ ): 24.8-80 MPa; and two different assumptions regarding the mechanical properties of FRP bars in compression.

The main geometric and material properties of the analyzed arches are summarized in Table 7.2. Each specimen was named using a systematic coding convention: the prefix “S” or “M” represents the loading case (single-point or multiple-point loading), followed by “C” and a number indicating concrete strength in MPa. A third letter, “S” or “G,” indicates the reinforcement material (S for steel, G for GFRP), followed by a number representing the diameter of the reinforcement in mm. The code also includes “CC” and a number to denote the concrete cover thickness in mm. The last letter (“F” or “Z”) distinguishes the two assumptions for the behavior of compressed reinforcement: “F” for Assumption (I) and “Z” for Assumption (II), as detailed in Section 7.4.5. The following sections discuss the studied parameters and their effects.

#### **7.4.2 Effect of concrete cover thickness**

Unlike steel reinforcing bars, where concrete cover is related primarily to durability, the requirements for concrete cover in FRP-RC members only address constructability, bonding, and fire-related concerns. Consequently, standards for FRP-RC members

often permit more lenient concrete cover limits compared to those for steel-RC elements (ACI 440.11R-22, 2022; CSA S806-12, 2012; GB 50608-20, 2010). In ACI 440.11 (2022), the required concrete cover depends on structural exposure conditions, component type, and the diameter of FRP bars. For outdoor members, the recommended cover thickness for FRP bars ranges from 38.1 mm to 50.8 mm (ACI 440.11R-22, 2022). CSA S806 (2012) specifies that the cover thickness should be the greater of 30 mm or twice the FRP bar diameter. GB 50608 has the most lenient requirements: 15 mm for slabs and 20 mm for beams, with no specific recommendations for compression members (GB 50608-20, 2010).

In this study, the effect of concrete cover thickness ( $d_c$ ) on the structural response of FRP-RC arches was evaluated by considering three different values: 50 mm, equivalent to that used for steel reinforcement (Tang et al., 2005); 20 mm, as specified for beam members in GB 50608; and an intermediate value of 35 mm. In the FE model, both longitudinal and transverse reinforcements were modeled as truss elements, disregarding differences induced by their diameters. To maintain consistency, the concrete cover thickness in this section refers to the distance from the center of the longitudinal reinforcement to the edge of the section.

Figures 7.8(a) and 7.8(b) depict the load-deflection responses of the arch ribs under single-point and multiple-point loading, respectively. Under the same concrete cover thickness, the FRP-RC arch exhibits a lower stiffness and load-bearing capacity compared to the steel-RC arch, owing to the lower elastic modulus of FRP. As the concrete cover thickness decreases, the tensile FRP bars are positioned further from the neutral axis, allowing them to better resist tensile forces, thereby enhancing structural

performance. Generally, under single-point loading, which induces greater eccentricity than multiple-point loading, the load-bearing capacity and stiffness of cracked sections depend more on concrete cover thickness. When the concrete cover thickness is reduced from 50 mm to 35 mm, the load-bearing capacity of the FRP-RC arch becomes comparable to that of the steel-RC arch under single-point loading. Further reduction of the concrete cover thickness to 20 mm for the FRP-RC arch results in a 6.8% increase in load-bearing capacity compared to the steel-RC arch, and a 22.0% improvement over the FRP-RC arch with a 50 mm concrete cover.

However, under multiple-point loading, where the arch is closer to the axial compression state, the contribution of tensile FRP bars is limited. Consequently, reducing the concrete cover thickness from 50 mm to 20 mm increases the load-bearing capacity of FRP-RC arches by only 17.6%, which remains significantly lower than that of the steel-RC arch. In terms of stiffness, although the structural stiffness improves with reduced concrete cover, the enhancement effect is not significant and the stiffness of FRP-RC arches remains substantially weaker than that of the steel-RC arch under both loading conditions.

#### **7.4.3 Effect of longitudinal reinforcement ratio**

The reinforcement ratio significantly influences the flexural and compressive performance of FRP-RC members. For flexural members, EN 1992-1-1:2023 (2023) requires that the reinforcement ratio in the tensile zone should not exceed 5%. For compressive members, both ACI 440.11 and GB 50608 specify that the reinforcement ratio should range from a minimum of 1% to a maximum of 8% (GB 50608-20, 2010; ACI 440.11R-22, 2022). The lower limit ensures the sufficient integrity of the section

to achieve the nominal capacity of compressive members  $z$  (Hadhood et al., 2019). The upper limit of 8% is considered a practical maximum for longitudinal reinforcement in terms of economy and placement requirements.

In this study, the reinforcement ratio ( $\rho_l$ ) of arch ribs was varied by adjusting the diameter of FRP bars while maintaining constant section dimensions and concrete cover thickness. The arrangement of reinforcement in the upper and lower layers was kept symmetrical, and the reinforcement ratio was calculated as the ratio of the total longitudinal reinforcement area to the gross area of the cross-section.

Figures 7.9(a) and 7.9(b) show that the initial stiffness during the pre-cracking stage is minimally affected by the reinforcement ratio, resulting in very similar initial stiffness across different ratios. However, as critical sections begin to crack — at approximately 10 kN under single-point loading and 20 kN under multiple-point loading — differences in stiffness responses become more pronounced. Under the same reinforcement ratio, the FRP-RC arches exhibit lower load-bearing capacities and stiffness compared to the steel-RC arches under both single-point and multiple-point loading scenarios. As the reinforcement ratio increases, internal reinforcement enhances post-cracking stiffness and strength, while cracking loads remain almost unchanged. When the  $\rho_l$  of FRP-RC arch increases to 8.62%, the stiffness of the FRP-RC arches (SC25G32CC50F and MC25G32CC50F) approaches that of the steel-RC arches with a reinforcement ratio of 2.16% (SC25S16CC50F and MC25S16CC50F), establishing a correlation between the reinforcement ratio ( $8.62\%/2.16\% = 4$ ) and the ratio of the elastic modulus between steel and FRP ( $210/50 = 4.2$ ). At the ultimate state, due to the high strength and linear elasticity of FRP, the load-bearing capacity of the FRP-RC arch exceeds that of the

steel-RC arch by 48.3% and 4.4% under single-point and multiple-point loading, respectively. To meet the same load-bearing requirements, the reinforcement ratio for the FRP-RC arch needs to be increased to 1.89 and 3.06 times that of the steel-RC arch under the respective loading conditions.

The ultimate load shows a nonlinear increase with increasing reinforcement ratio under both loading conditions, as shown in Figure 7.9(c). For single-point loading, a dramatic increase in load-bearing capacity occurs between 0.13% (SC25G4CC50F) and 0.84% (SC25G13CC50F), where the failure mode shifts from FRP rupture to concrete crushing. In terms of failure modes, only the specimen with an extremely low reinforcement ratio ( $\rho_l = 0.13\%$ , SC25G4CC50F) experiences FRP rupture failure (Table 7.2). The majority of arch ribs fail by concrete crushing, which can be attributed to the low rise-to-span ratio of the arch rib (0.16), leading to significant axial forces that reduce eccentricity and favor small eccentric compression failures. Typically, the rise-to-span ratio for arches ranges from 1/5 to 1/8 (Chen and Duan, 2014), with the eccentricity decreasing as the span-to-rise ratio increases (Han et al., 2020), suggesting that brittle FRP rupture failure is generally avoidable in such shallow arch structures with a rise-to-span ratio of 0.16 or less if the minimum reinforcement ratio is satisfied. An accurate critical rise-to-span ratio still requires further studies on the effect of different arch shapes under different loading cases. It is worth noting that when the reinforcement ratio increases to 8.62% (SC25G32CC50F), the increased load-bearing capacity ultimately results in shear failure rather than flexural failure.

The maximum strain of FRP reinforcement exhibits an inverse trend compared to the load-bearing capacity, as the increase in reinforcement ratio enhances the cross-

sectional stiffness, thereby limiting deformation and strain development. In reality, the mechanical properties of FRP bars tend to decrease with increasing diameter (Faza and GangaRao, 1993; ACI 440.1R-15, 2015). However, since specific values were not provided, the strength and modulus of elasticity were assumed to be constant across different diameters in the FE model. Therefore, in practice, increasing the diameter of FRP bars may have a lesser effect on enhancing arch performance than indicated by the numerical results.

#### **7.4.4 Effect of concrete compressive strength**

To evaluate the effects of concrete compressive strength ( $f_{cu}$ ), FRP-RC arches with concrete strengths of 24.8 MPa (original), 40 MPa, 60 MPa, and 80 MPa were modeled. It is noteworthy that related concrete properties (e.g., tensile strength, elastic modulus, stress-strain behavior and damage parameters) were also adjusted to match the varying compressive strengths.

Generally, FRP-RC arches under single-point loading experience flexural failure due to concrete crushing. Under multiple-point loading, specimen M25G16CC50F also experiences flexural failure; however, shear failure is induced in specimens with concrete strength of 40 MPa, 60 MPa, and 80 MPa, as presented in Table 7.2. This indicates that shear failure is more likely for FRP-RC arches with high concrete strength under multiple-point loading. The distributed load reduced the bending moment along the arch axis, restricting flexural failure. Moreover, the increased load-bearing capacity due to higher concrete strength further challenged the shear resistance of arches.

Figures 7.10(a) and 7.10(b) illustrate that the increased concrete strength leads to elevated load-carrying capacity and higher stiffness responses in both loading scenarios.

Under multiple-point loading, where the ratio of bending moment to axial load of sections is small, the impact of concrete strength on structural stiffness and load-bearing capacity is more pronounced compared to single-point loading. For instance, increasing concrete strength from 24.8 MPa to 40 MPa results in a 29.8% increase in load resistance under multiple-point loading, whereas the improvement is only 21.1% under single-point loading, as shown in Figure 7.10(c). The relationship between concrete strength and load capacity/maximum reinforcement strain is nearly linear for single-point loading. In contrast, the increase in load capacity with higher concrete strength diminishes dramatically under multiple-point loading when concrete strength exceeds 40 MPa, as shear failure is induced, limiting the full utilization of both concrete strength and FRP reinforcement. As shown in Figure 7.10(c), under multiple-point loading, the maximum strain in FRP reinforcement decreases steadily with increasing concrete strength, indicating reduced material efficiency.

As concrete compressive strength increases, the effect on enhancing structural stiffness becomes progressively limited. For instance, when  $f_{cu}$  increases from 60 MPa to 80 MPa, the stiffness response shows minimal variation. This can be attributed to two main factors: (1) the elastic modulus of concrete is generally proportional to the square root of its compressive strength, which increases at a diminishing rate at higher strengths; (2) as concrete strength increases, structural stiffness becomes increasingly dependent on the tensile stiffness provided by the FRP reinforcement.

#### **7.4.5 Effect of longitudinal reinforcement in compression**

As discussed in Section 7.1, the mechanical properties of FRP bars under compression remain inconclusive. In this section, two different assumptions regarding their

contribution to the structural performance of FRP-RC arches are compared and discussed: (I) assuming FRP bars behave identically in tension and compression; and (II) ignoring the contribution of FRP bars in compression. Assumption (I) was adopted in Section 7.2.4, while Assumption (II) was implemented by defining different elastic modulus under tension and compression for FRP bars in the user-subroutine UMAT of ABAQUS. Since FRP bars in compression always remain within their elastic range (about 20%-30% of ultimate strength) without damage (Paramanatham, 1993), the effect of longitudinal reinforcement in this section is confined to stiffness response.

Figures 7.11(a) and 7.11(b) demonstrate that the initial difference between the load-deflection curves based on the two distinct assumptions is negligible; however, as the strain in the compressed bars develops with the increased applied load, the difference gradually becomes pronounced until the failure. As illustrated in Figure 7.11, the structural performance based on Assumption (II) is consistently weaker than that based on Assumption (I) under all loading conditions, with multiple-point loading causing a significantly greater reduction in strength, stiffness, and ductility compared to single-point loading. This is because the compressed bars in the multiple-point condition experience higher compression strain and thus play a more critical role in the structural behavior.

Although both assumptions show a similar uptrend for the ultimate load as the reinforcement ratio increases [Figures 7.11(c) and 7.11(d)], Assumption (II) results in a significantly reduced increase. The discrepancy becomes more pronounced as the reinforcement ratio increases. At lower reinforcement ratios [e.g., cases inducing FRP rupture failure ( $\rho_l = 0.13\%$ ) and those just above the minimum reinforcement ratio

requirement ( $\rho_l = 1.42\% > 1\%$ ), the limited reinforcement area leads in minimal differences. For reinforcement ratios within the limits specified by GB 50608 and ACI 440.11R ( $\rho_l = 4.07\%$ ), the strength reductions for single-point and multiple-point loading are 6.0% and 14.8%, respectively. When the reinforcement ratio exceeds the maximum allowable ( $\rho_l = 8.62\% > 8\%$ ), the reduction increases dramatically to 20.4% and 21.5%, respectively. The gap in maximum reinforcement strain widens as the reinforcement ratio increases, which is directly related to the improved load-bearing capacity. For arches under multiple-point loading, however, the variation of maximum reinforcement strain with reinforcement ratio shows an opposite trend, with the two curves converging as the reinforcement ratio increases [Figure 11(d)]. The reduced stiffness observed in Assumption (II), compared to Assumption (I), reflects weaker structural stiffness at the section level, potentially resulting in higher strain values under the same load and thus partially reducing the difference in strain.

## 7.5 CONCLUSIONS

This chapter presents the development, evaluation, and analysis of a three-dimensional finite element model of FRP-RC arch implemented with ABAQUS/Standard. The model is capable of accurately simulating the axial-shear-flexural interaction in FRP-RC arches and predicting their failure modes, including both flexural and shear failures — a feature that distinguishes it from the theoretical model presented in Chapter 6. The model was then employed in an extensive parametric analysis on full-scale arch ribs to evaluate the contributions of key parameters on the structural performance of FRP-RC arches. Based on the analysis and discussion, the following conclusions are drawn:

1. The FE model predictions exhibited good agreement with experimental observations concerning failure modes, load-deflection responses, crack patterns, and strain development in FRP-RC arches.
2. Reducing concrete cover thickness, increasing reinforcement ratio, and increasing concrete strength, enhance the ultimate load and post-cracking stiffness of FRP-RC arches. The effects of concrete cover and reinforcement ratio are significant under single-point loading, whereas the influence of concrete strength is more pronounced under multiple-point loading.
3. Although the elastic modulus of FRP is lower than that of steel, its superior corrosion resistance allows for reduced concrete cover requirements. This reduction increases the load-bearing capacity and post-cracking stiffness to varying degrees, particularly under loading conditions with greater eccentricity.
4. At equivalent reinforcement ratios, FRP-RC arches exhibit lower strength and stiffness compared to steel-RC arches. When the reinforcement ratio of the GFRP-RC arch is increased to approximately four times that of the steel-RC arch, the axial stiffness provided by the two materials is similar, resulting in nearly identical structural stiffness responses. Due to the high strength and linear elasticity of FRP, the load-bearing capacity of FRP-RC arches exceeds that of steel-RC arches.
5. Brittle FRP rupture failure is generally avoidable in FRP-RC shallow arches if the minimum reinforcement ratio (1%) is satisfied.
6. Increasing concrete strength leads in higher cracking loads, ultimate loads, and stiffness throughout the loading process. However, special attention should be

given to shear resistance in FRP-RC arches with high concrete strength, particularly under uniform loading conditions.

7. Different assumptions regarding compressed FRP bars do not significantly affect arch behavior (e.g., load-deflection response and reinforcement stress levels) when the reinforcement ratio is near the minimum requirement. However, as the reinforcement ratio increases, discrepancies in strength, stiffness, and ductility become more pronounced, especially under multiple-point loading conditions that induce high compressive strains in the FRP bars.

## 7.6 REFERENCES

ABAQUS. (2024) *ABAQUS Analysis User's Manual*. Dassault Systemes Simulia Corporation, Providence, Rhode Island, USA.

Abushanab A and Alnahhal W. (2021) Numerical parametric investigation on the moment redistribution of basalt FRC continuous beams with basalt FRP bars. *Composite Structures* 277: 114618.

ACI 440.1R-15. (2015) *Guide for the Design and Construction of Structural Concrete Reinforced with Fiber-Reinforced Polymer Bars*. Farmington Hills, Michigan: American Concrete Institute (ACI), USA.

ACI 440.3R-12. (2012) *Guide Test Methods for Fiber-Reinforced Polymers (FRPs) for Reinforcing or Strengthening Concrete Structures*. Farmington Hills, Michigan: American Concrete Institute (ACI), USA.

ACI 440.11R-22. (2022) *Building Code Requirements for Structural Concrete Reinforced with Glass Fiber-Reinforced Polymer (GFRP) Bars*. Farmington Hills, Michigan: American Concrete Institute (ACI), USA.

ASTM C39/C39M-21. (2021) *Standard Test Method for Compressive Strength of Cylindrical Concrete Specimens*. West Conshohocken, PA: American Society for Testing and Materials (ASTM), USA.

Bažant ZP and Oh BH. (1983) Crack band theory for fracture of concrete. *Materials and Structures* 16(3): 155-177.

Bedard C. (1992) Composite reinforcing bars: assessing their use in construction.

*Concrete International* 14(1): 55-59.

Béton CE-Id. (1993) *CEB-FIP Model Code 1990: Design Code*. Thomas Telford Publishing.

Chaallal O and Benmokrane B. (1993) Physical and mechanical performance of an innovative glass-fiber-reinforced plastic rod for concrete and grouted anchorages. *Canadian Journal of Civil Engineering* 20(2): 254-268.

Chen WF and Atsuta T. (2007) *Theory of Beam-columns*: J. Ross Publishing.

Chen WF and Duan L. (2014) *Bridge Engineering Handbook: Construction and Maintenance*. CRC press.

Cosenza E, Manfredi G and Realfonzo R. (1997) Behavior and modeling of bond of FRP rebars to concrete. *Journal of Composites for Construction*: 40-51.

CSA S806-12. (2012) *Design and Construction of Building Components with Fiber Reinforced Polymers*. Toronto, Ontario: Canadian Standards Association (CSA), Canada.

Dagher HJ, Bannon DJ, Davids WG, et al. (2012) Bending behavior of concrete-filled tubular FRP arches for bridge structures. *Construction and Building Materials* 37(4): 432-439.

Deitz DH, Harik IE and Gesund H. (2003) Physical properties of glass fiber reinforced polymer rebars in compression. *Journal of Composites for Construction* 7(4): 363-366.

- EN 1992-1-1:2023. (2023) *Eurocode 2: Design of Concrete Structures-Part 1-1: General Rules and Rules for Buildings, Bridges and Civil Engineering Structures*. British Standard Institution, London, UK.
- Faza S and GangaRao H. (1993) Glass FRP reinforcing bars for concrete. *Developments in Civil Engineering* 42: 167-188.
- GangaRao HV, Taly N and Vijay P. (2006) *Reinforced Concrete Design with FRP Composites*. CRC press.
- GB 50608-20. (2010) *Technical Code for Infrastructure Application of FRP Composites*. China Architecture & Building Press, Beijing, China.
- GB 50010. (2015) *Standard for Design of Concrete Structures*. Ministry of Housing and Urban-Rural Development of PRC, Beijing, China.
- Gu XY, Dai YQ and Jiang JW. (2020) Flexural behavior investigation of steel-GFRP hybrid-reinforced concrete beams based on experimental and numerical methods. *Engineering Structures* 206: 110117.
- Hadhood A, Mohamed HM, Benmokrane B, et al. (2019) Assessment of design guidelines of concrete columns reinforced with glass fiber-reinforced polymer bars. *ACI Structural Journal* 116(4): 193-207.
- Hadhood A, Mohamed HM, Ghrib F, et al. (2017) Efficiency of glass-fiber reinforced-polymer (GFRP) discrete hoops and bars in concrete columns under combined axial and flexural loads. *Composites Part B: Engineering* 114: 223-236.
- Han X, Fernando D and Han B. (2020) Numerical modelling of the in-plane behaviour

- of concrete-filled circular steel tubular arches. *Construction and Building Materials* 264: 120693.
- Hasan HA, Sheikh MN and Hadi MN. (2019) Maximum axial load carrying capacity of Fibre Reinforced-Polymer (FRP) bar reinforced concrete columns under axial compression. *Structures* 19: 227-233.
- Hawileh RA. (2012) Nonlinear finite element modeling of RC beams strengthened with NSM FRP rods. *Construction and Building Materials* 27(1): 461-471.
- Hussein A, Huang H, Okuno Y, et al. (2022) Experimental and numerical parametric study on flexural behavior of concrete beams reinforced with hybrid combinations of steel and BFRP bars. *Composite Structures* 302: 116230.
- Jumaa GB and Yousif AR. (2019) Numerical modeling of size effect in shear strength of FRP-reinforced concrete beams. *Structures* 20: 237-254.
- Kadhim MMA, Jawdhari A, Altaee MM, et al. (2023) Parametric investigation of continuous beams strengthened with near surface mounted FRP bars. *Engineering Structures* 293: 116619.
- Kassem C, Farghaly AS and Benmokrane B. (2011) Evaluation of flexural behavior and serviceability performance of concrete beams reinforced with FRP bars. *Journal of Composites for Construction* 15(5): 682-695.
- Khorramian K and Sadeghian P. (2021) Material characterization of GFRP bars in compression using a new test method. *Journal of Testing and Evaluation* 49(2): 1037-1052.

- Kim B and Lee JY. (2019) Resistance of interfacial debonding failure of GFRP bars embedded in concrete reinforced with structural fibers under cycling loads. *Composites Part B: Engineering* 156: 201-211.
- Kirkland B, Kim P, Uy B, et al. (2015) Moment–shear–axial force interaction in composite beams. *Journal of Constructional Steel Research* 114: 66-76.
- Kmiecik P and Kamiński M. (2011) Modelling of reinforced concrete structures and composite structures with concrete strength degradation taken into consideration. *Archives of Civil Mechanical Engineering* 11(3): 623-636.
- Liao Q, Yu JT, Su YR, et al. (2023) Shear failure mechanism and parametric study for seawater sea-sand engineered cementitious composites beams reinforced by FRP bars: Finite element analysis. *Construction and Building Materials* 407: 133497.
- Lubliner J, Oliver J, Oller S, et al. (1989) A plastic-damage model for concrete. *International Journal of Solids Structures* 25(3): 299-326.
- Majeed HS, Davids WG and Walton HJ. (2021) Efficient second-order nonlinear finite-element simulation of concrete-filled FRP tubular arches. *Structures* 34: 3738-3749.
- Maranan GB, Manalo AC, Benmokrane B, et al. (2016) Behavior of concentrically loaded geopolymer-concrete circular columns reinforced longitudinally and transversely with GFRP bars. *Engineering Structures* 117: 422-436.
- Mathern A and Yang JC. (2021) A practical finite element modeling strategy to capture

- cracking and crushing behavior of reinforced concrete structures. *Materials* 14(3): 506.
- Musiket K, Vernerey F and Xi Y. (2017) Numerical modeling of fracture failure of recycled aggregate concrete beams under high loading rates. *International Journal of Fracture* 203(1-2): 263-276.
- Nagheh E, Mostofinejad D and Saljoughian A. (2024) Shear strengthening of RC arches with FRP composites using EBR and EBROG methods: Experimental and theoretical study. *Construction and Building Materials* 427: 136212.
- Paramanantham NS. (1993) *Investigation of the Behavior of Concrete Columns Reinforced with Fiber Reinforced Plastic Rebars*. Texas, America: Lamar University-Beaumont.
- Qapo M, Dirar S and Jemaa Y. (2016) Finite element parametric study of reinforced concrete beams shear-strengthened with embedded FRP bars. *Composite Structures* 149: 93-105.
- Rasheed HA, Nayal R and Melhem H. (2004) Response prediction of concrete beams reinforced with FRP bars. *Composite Structures* 65(2): 193-204.
- Ren F, Liu T, Chen G, et al. (2021) Flexural behavior and modelling of FRP-bar reinforced seawater sea sand concrete beams exposed to subtropical coastal environment. *Construction and Building Materials* 309: 125071.
- Rossi PP. (2013) Evaluation of the ultimate strength of RC rectangular columns subjected to axial force, bending moment and shear force. *Engineering*

*Structures* 57: 339-355.

Sarhan MM and Al-Zwainy FMS. (2022) Analytical investigations of concrete beams reinforced with FRP bars under static loads. *Structures* 44: 152-158.

Si JH, Qiu SC, Feng SY, et al. (2022) Experimental study on axial compression buckling of glass fiber reinforced plastics solid pole with circular cross-section. *Advances in Structural Engineering* 25(4): 913-924.

Simulia DS. (2013) *ABAQUS 6.13 User's manual*. Dassault Systems, Providence, RI 305: 306.

Song XY, Yue ZY, Zheng EH, et al. (2024) Numerical simulation on the load-bearing capacity of CFRP-strengthened concrete arches. *Case Studies in Construction Materials* 20: e03137.

Spagnuolo S, Meda A and Rinaldi Z. (2014) Fiber glass reinforcement in tunneling applications. *Proceedings of the 10th Fib International PhD Symposium in Civil Engineering*. 85-90.

Tang XS, Zhang JR, Li CX, et al. (2005) Damage analysis and numerical simulation for failure process of a reinforced concrete arch structure. *Computers & Structures* 83(31-32): 2609-2631.

Tao Z, Wang ZB and Yu Q. (2013) Finite element modelling of concrete-filled steel stub columns under axial compression. *Journal of Constructional Steel Research* 89: 121-131.

Wang X, Liu Z, Tong T, et al. (2024) Bond-slip behavior of deformed rebar in grouted

- duct connection: Experiment, theoretical analysis and cohesive-zone element model. *Construction and Building Materials* 421: 135694.
- Wei W, Liu F, Xiong Z, et al. (2019) Bond performance between fibre-reinforced polymer bars and concrete under pull-out tests. *Construction and Building Materials* 227: 116803.
- Xia ZY, Jiang T and Yu T. (2024) Enhanced deflection method for large-curvature problems: Formulation, verification and application to fiber-reinforced polymer-enabled arches. *Advances in Structural Engineering*: 13694332241263871.
- Xie EL, Jiang T, Xia ZY, et al. (2023) Postbuckling behavior of FRP bending-active arches subjected to a central point load. *Journal of Composites for Construction* 27(5): 04023039.
- Xie J, Liu Y, Qiao Y, et al. (2022) Bond behaviors of ribbed CFRP bars in concrete exposed to low temperatures. *Construction and Building Materials* 341: 127910.
- Xiong MX, Xiong DX and Liew JR. (2017) Behaviour of steel tubular members infilled with ultra high strength concrete. *Journal of Constructional Steel Research* 138: 168-183.
- Xiong Z, Zhou KT, Ye ZW, et al. (2022) Bond behavior of basalt fiber reinforced polymer bars in seawater sea-sand concrete exposed to daily temperature variations. *Advances in Structural Engineering* 25(9): 2021-2039.
- Yan JB, Liew JYR, Zhang MH, et al. (2016) Punching shear resistance of steel-

concrete–steel sandwich composite shell structure. *Engineering Structures* 117: 470-485.

Zhang ZY, Wu XH, Zhang JH, et al. (2023) Numerical investigation on the flexural behavior of GFRP reinforced concrete beams with CFRP grid-reinforced engineered cementitious composites. *Engineering Structures* 288: 116163.

Zinkaah OH, Alridha Z and Alhawat M. (2022) Numerical and theoretical analysis of FRP reinforced geopolymer concrete beams. *Case Studies in Construction Materials* 16: e01052.

Table 7.1 Comparisons of key results from experiment and FE analysis

Specimen ID	Peak load (kN)		Peak deflection (mm)		Failure mode
	Experimental result	Numerical result	Experimental result	Numerical result	
NCS12H	279.6	257.2	13.13	12.50	Flexural failure
NCG13H	225.6	230.2	11.71	12.75	Flexural failure
NCG8H	194.9	203.2	10.72	11.02	Flexural failure
NCG13L	272.3	268.8	14.38	15.49	Shear failure
HCG13H	257.4	248.7	12.98	12.55	Flexural failure

Table 7.2 Details of investigated arch ribs and key results from parametric study

Specimen ID	Loading condition	$f_{cu}$ (MPa)	Longitudinal reinforcement	$\rho_l$ (%)	$d_c$ (mm)	Stiffness of compressed FRP	Peak load (kN)	Peak deflection at vault (mm)	Maximum strain of reinforcement ( $\mu\epsilon$ )	Failure mode <sup>1</sup>
SC25S16CC50 F			steel 3 $\Phi$ 16/3 $\Phi$ 16		50	-	55.5	34.36	3330	Flexural failure-CC
SC25G16CC50 F			FRP 3 $\Phi$ 16/3 $\Phi$ 16		50		48.6	80.65	6338	Flexural failure-CC
SC25G16CC35 F	Single-point	24.8	FRP 3 $\Phi$ 16/3 $\Phi$ 16	2.1 5	35		52.9	83.40	6535	Flexural failure-CC
SC25G16CC20 F			FRP 3 $\Phi$ 16/3 $\Phi$ 16		20	FRP	59.3	83.83	5764	Flexural failure-CC
SC25G4CC50F			FRP 3 $\Phi$ 4/3 $\Phi$ 4	0.1 3	50		13.0	144.29	20000	Flexural failure-FR
SC25G13CC50 F			FRP 3 $\Phi$ 13/3 $\Phi$ 13	1.4 2			41.1	98.83	8033	Flexural

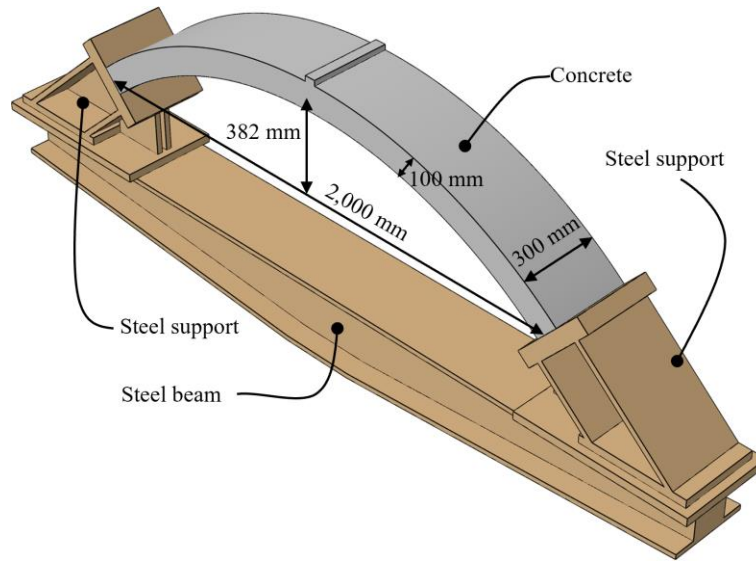
SC25G22CC50 F		FRP 3Φ22/3Φ22	4.0 7			60.5	71.57	4451	failure- CC Flexur al failure- CC	
SC25G28CC50 F		FRP 3Φ28/3Φ28	6.6 0			71.4	63.53	3383	Flexur al failure- CC	
SC25G32CC50 F		FRP 3Φ32/3Φ32	8.6 2			82.3	64.48	3103	Flexur al failure- CC	
SC40G16CC50 F	40	FRP 3Φ16/3Φ16				58.9	89.23	7421	Flexur al failure- CC	
SC60G16CC50 F	60	FRP 3Φ16/3Φ16	2.1 5			71.4	99.90	8870	Flexur al failure- CC	
SC80G16CC50 F	80	FRP 3Φ16/3Φ16				79.2	113.54	9885	Flexur al failure- CC	
SC25G4CC50Z		FRP 3Φ4/3Φ4	0.1 3			12.9	141.58	20000	Flexur al failure- FR	
SC25G13CC50 Z		FRP 3Φ13/3Φ13	1.4 2			40.6	97.07	7863	Flexur al failure- CC	
	24.8				Zero				Flexur al failure- CC	
SC25G22CC50 Z		FRP 3Φ22/3Φ22	4.0 7			56.9	70.60	4222	Flexur al failure- CC	
SC25G32CC50 Z		FRP 3Φ32/3Φ32	8.6 2			65.5	58.03	2539	Flexur al failure- CC	
MC25S16CC50 F	Multipl e-point	24.8	steel 3Φ16/3Φ16	2.1 5	50	-	111. 2	22.74	1135	Shear failure

MC25G16CC5 0F		FRP 3Φ16/3Φ16	50		81.8	24.01	2799	Flexural failure- CC
MC25G16CC3 5F		FRP 3Φ16/3Φ16	35		91.2	26.65	2830	Flexural failure- CC
MC25G16CC2 0F		FRP 3Φ16/3Φ16	20		96.2	26.78	2263	Flexural failure- CC
MC25G4CC50 F		FRP 3Φ4/3Φ4	0.1 3		56.0	21.00	11104	Flexural failure- CC
MC25G13CC5 0F		FRP 3Φ13/3Φ13	1.4 2	FRP	76.2	23.81	3134	Flexural failure- CC
MC25G22CC5 0F		FRP 3Φ22/3Φ22	4.0 7		101. 2	28.35	2131	Flexural failure- CC
MC25G28CC5 0F		FRP 3Φ28/3Φ28	6.6 0		111. 2	29.98	1679	Flexural failure- CC
MC25G32CC5 0F		FRP 3Φ32/3Φ32	8.6 2	50	116. 2	27.06	1333	Shear failure
MC40G16CC5 0F	40	FRP 3Φ16/3Φ16			106. 2	19.76	2628	Shear failure
MC60G16CC5 0F	60	FRP 3Φ16/3Φ16	2.1 5		121. 2	16.05	2449	Shear failure
MC80G16CC5 0F	80	FRP 3Φ16/3Φ16			131. 2	15.99	2478	Shear failure
MC25G4CC50 Z		FRP 3Φ4/3Φ4	0.1 3		49.2	16.25	8107	Flexural failure- CC
	24.8			Zero				
MC25G13CC5 0Z		FRP 3Φ13/3Φ13	1.4 2		73.2	23.38	2979	Flexural failure- CC

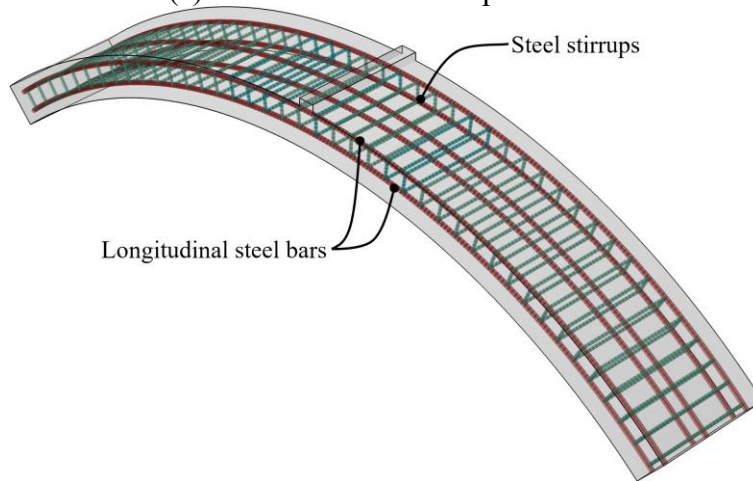
MC25G22CC5 0Z	FRP 3Φ22/3Φ22	4.0 7	86.2	25.79	2017	Flexural failure- CC
MC25G32CC5 0Z	FRP 3Φ32/3Φ32	8.6 2	91.2	26.38	1139	Flexural failure- CC

---

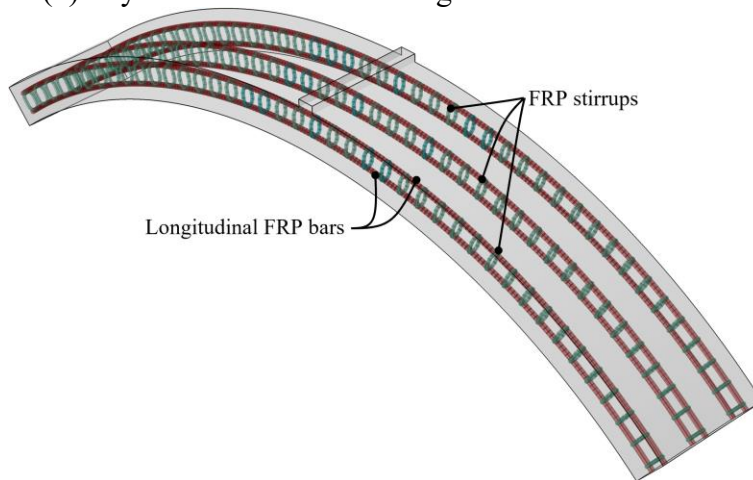
<sup>1</sup> – “Flexural failure-CC” refers the flexural failure caused by concrete crushing, while “Flexural failure-FR” specifically denotes flexural failure due to FRP rupture.



(a) Dimensions of arch specimens



(b) Layout of reinforcement cage in the steel-RC arch



(c) Layout of reinforcement cage in FRP-RC arches

Figure 7.1 Configurations of RC arches

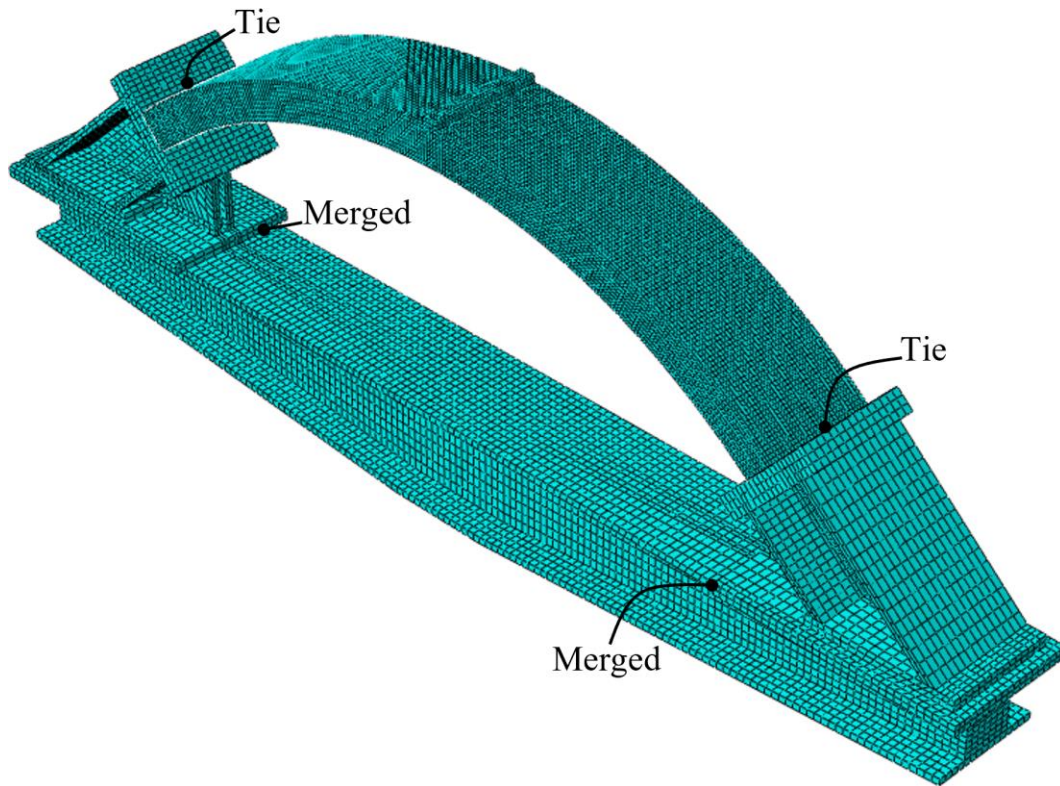
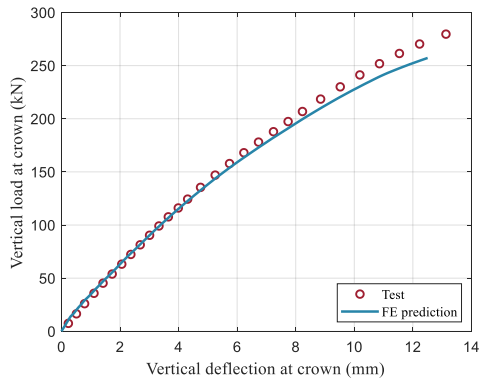
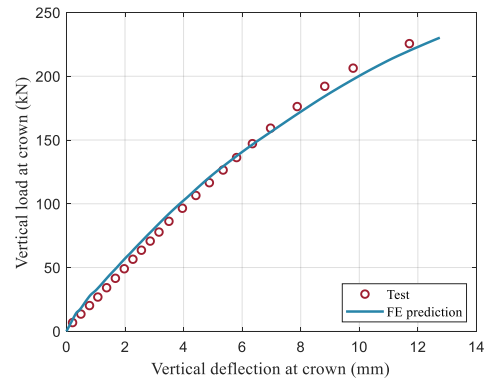


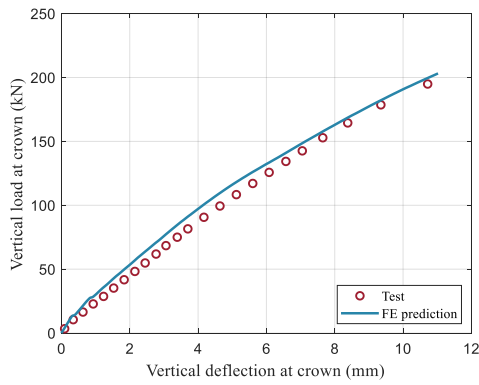
Figure 7.2 FE model of arch specimen with supports and beam foundation



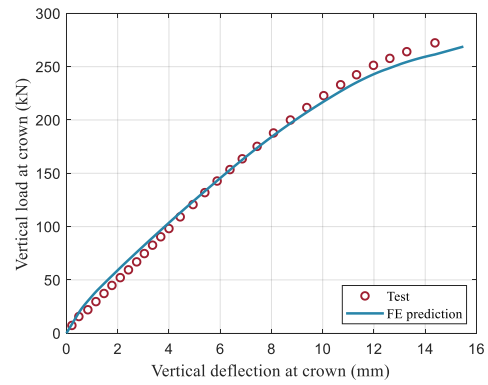
(a) NCS12H



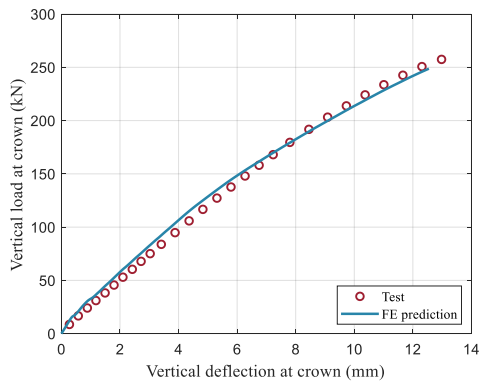
(b) NCG13H



(c) NCG8H

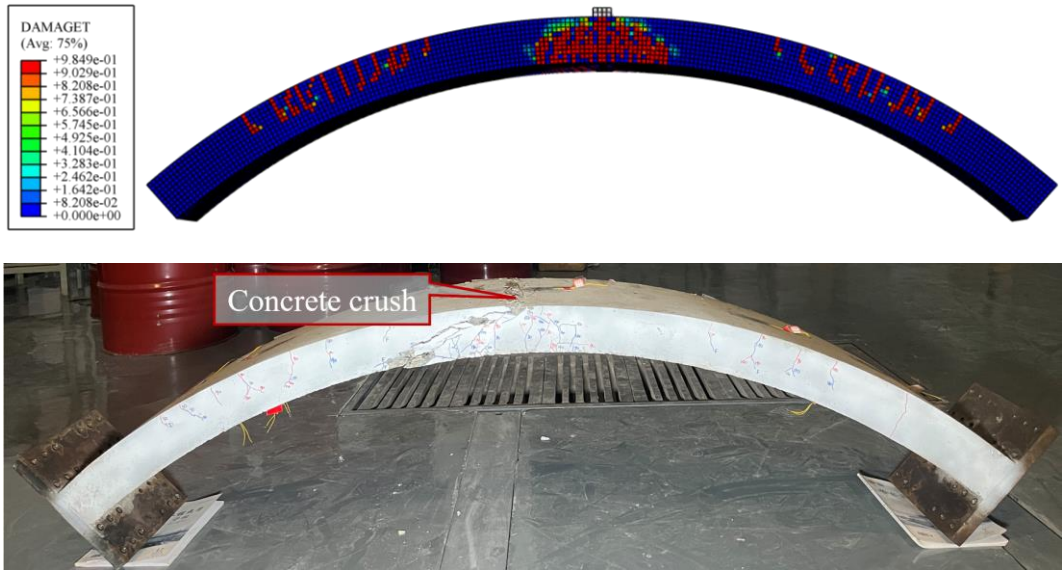


(d) NCG13L

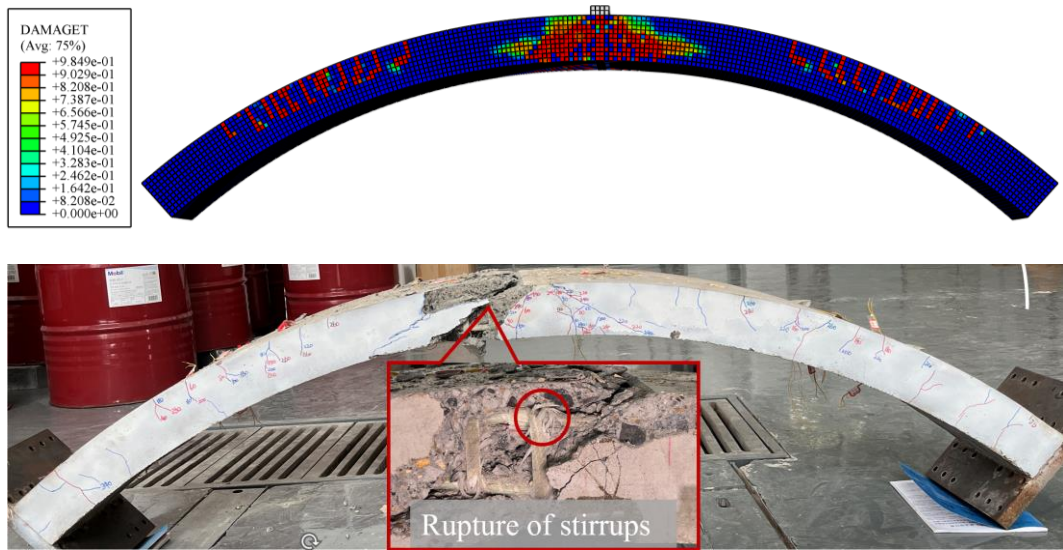


(e) HCG13H

Figure 7.3 Comparisons of load-deflection curves

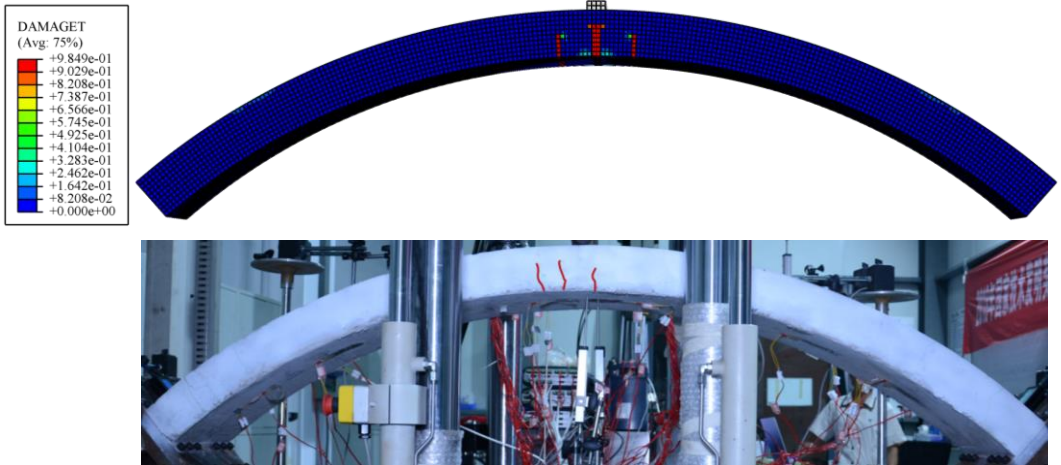


(a) Flexural failure (NCG8H)

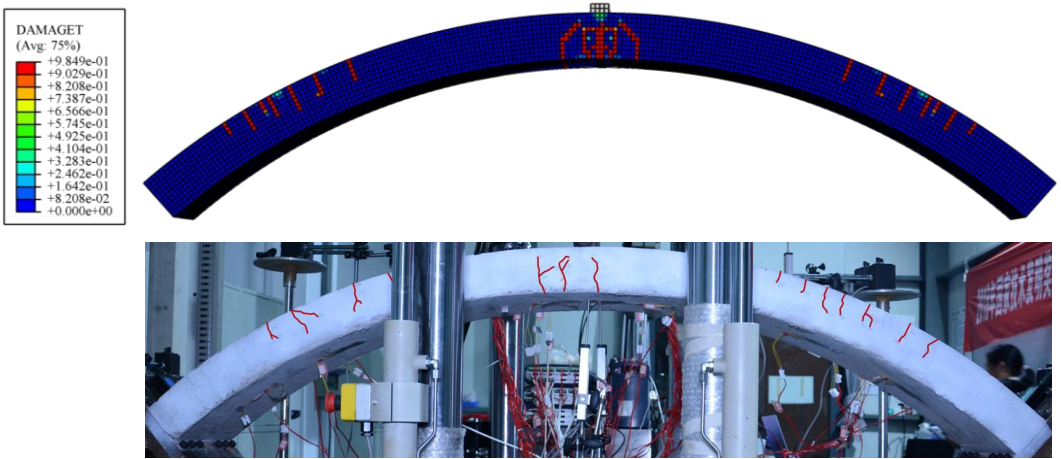


(b) Shear failure (NCG13L)

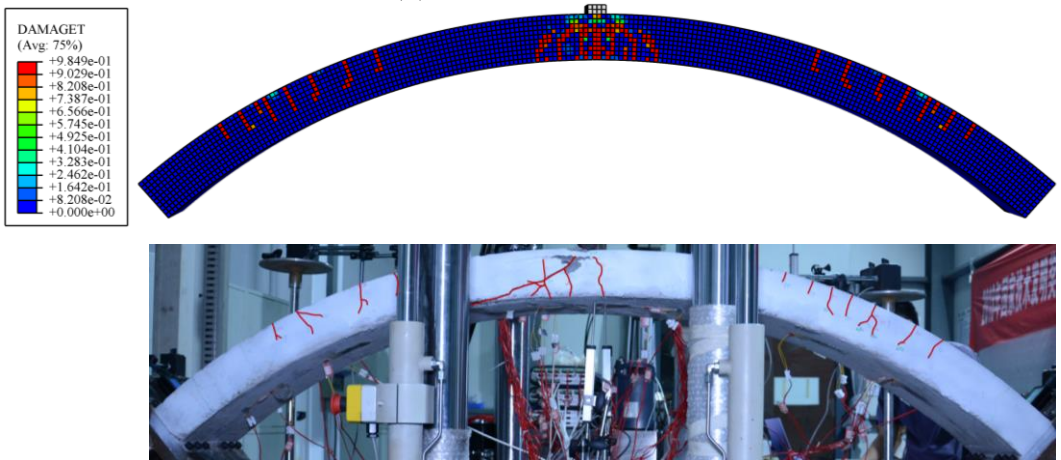
Figure 7.4 The comparisons and distributions of tensile damage of concrete



(a) At load = 51.2 kN

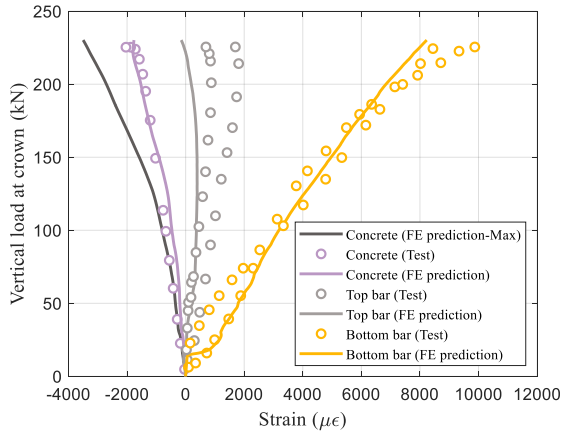


(b) At load = 97.0 kN

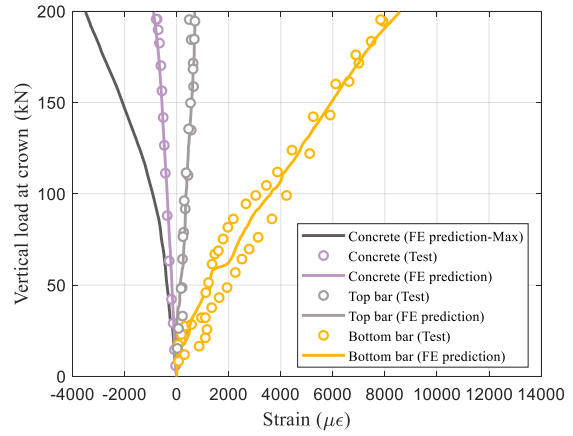


(c) At load = 225.6 kN

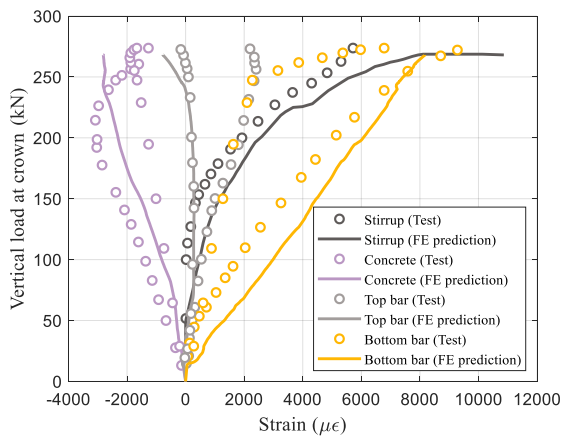
Figure 7.5 Crack development of NCG13H



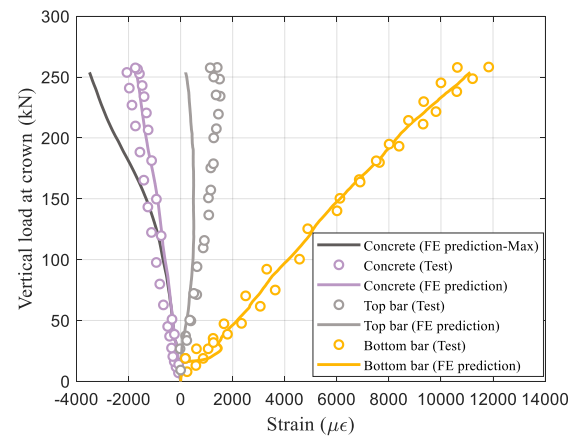
(a) NCG13H



(b) NCG8H

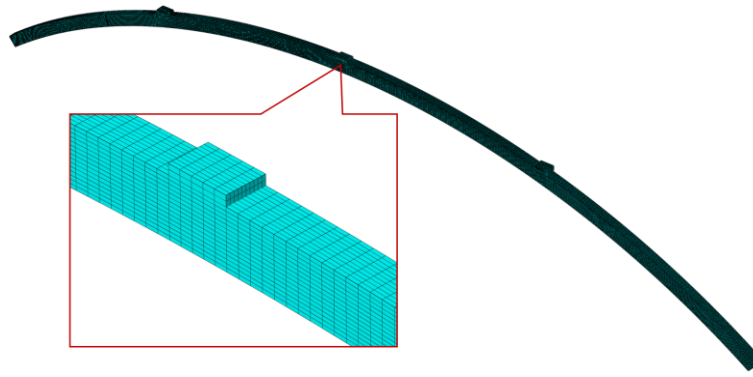


(c) NCG13L

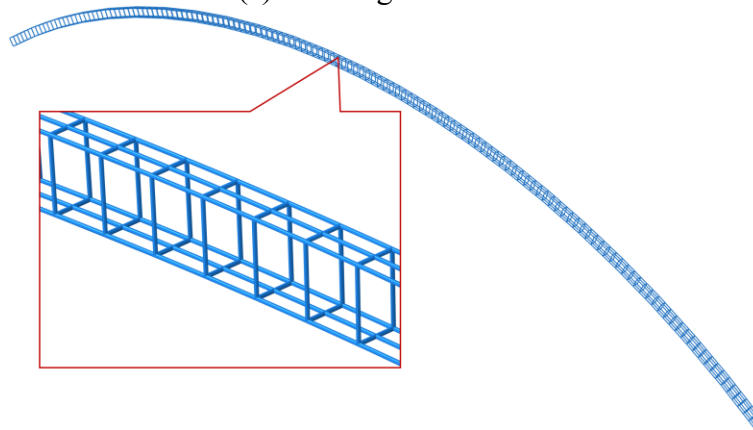


(d) HCG13H

Figure 7.6 Load-strain development near arch apex

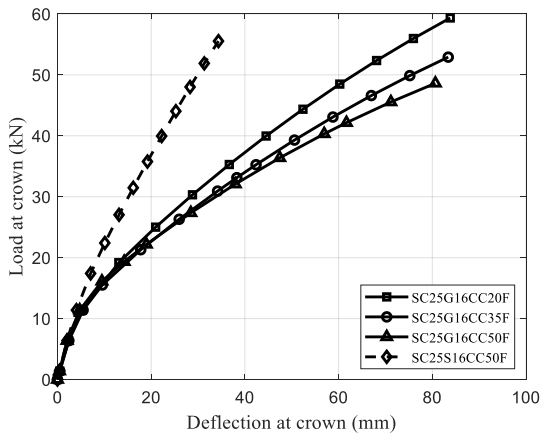


(a) Meshing of arch rib

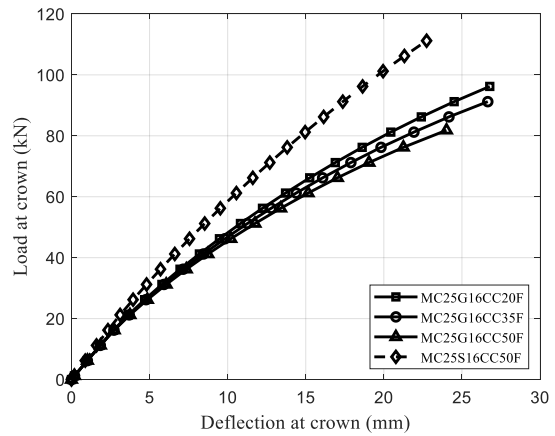


(b) Layout of reinforcement cage

Figure 7.7 FE model of full-scale arch rib

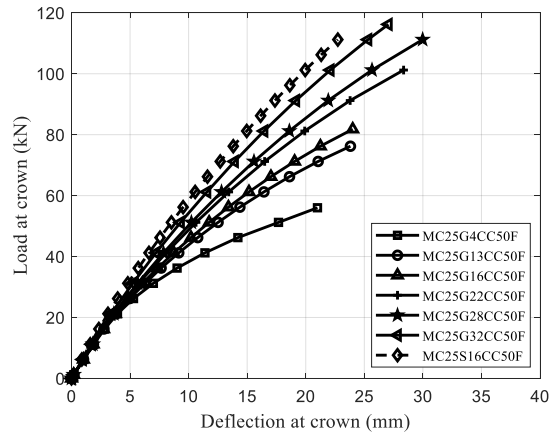
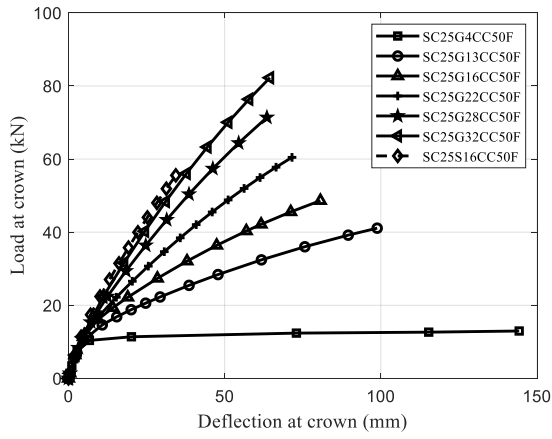


(a) Load-deflection relationships under single point loading



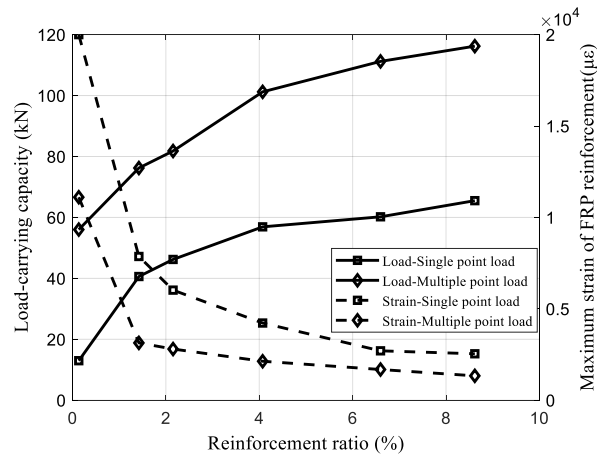
(b) Load-deflection relationships under multiple point loading

Figure 7.8 Effect of concrete cover to the structural responses



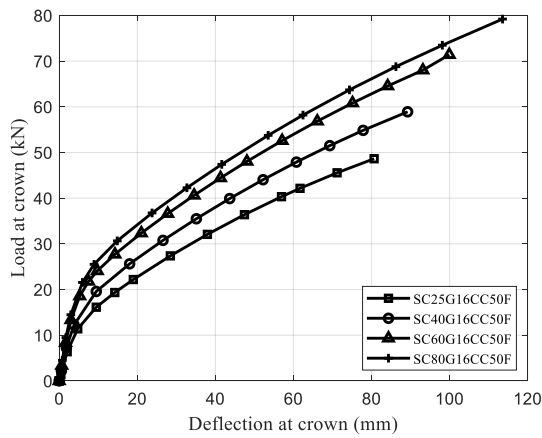
(a) Load-deflection relationships under single point loading

(b) Load-deflection relationships under multiple point loading

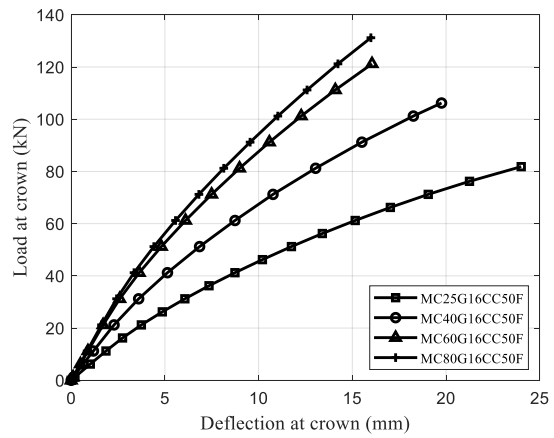


(c) Effect to load-bearing capacity and FRP strain level

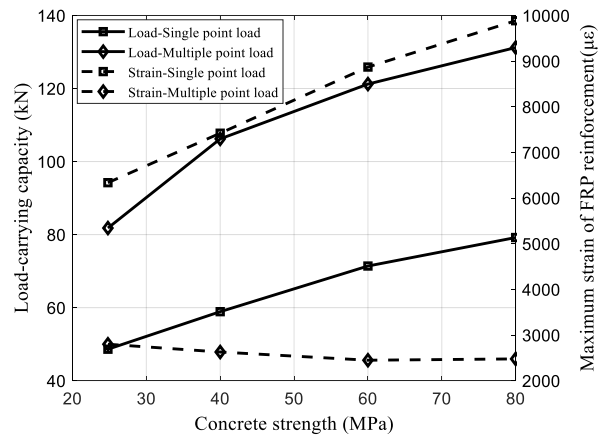
Figure 7.9 Effect of longitudinal reinforcement ratio to the structural responses



(a) Load-deflection relationships under single point loading

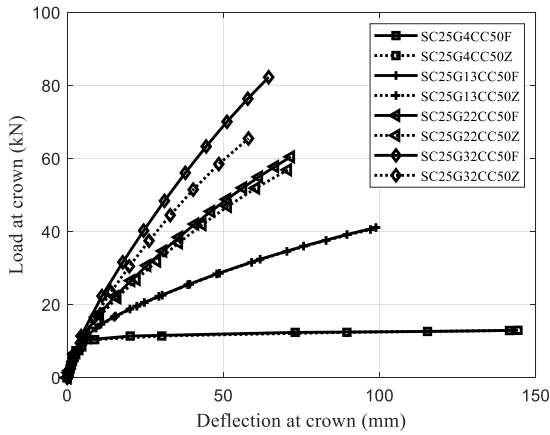


(b) Load-deflection relationships under multiple point loading

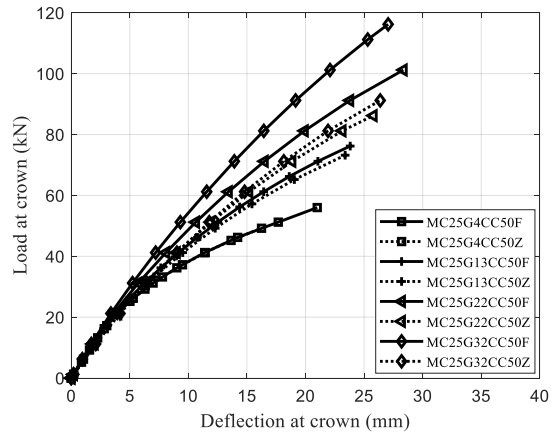


(c) Effect to load-bearing capacity and FRP strain level

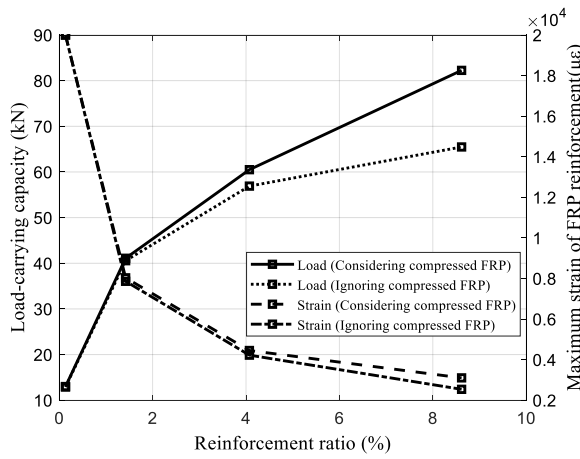
Figure 7.10 Effect of concrete strength to the structural responses



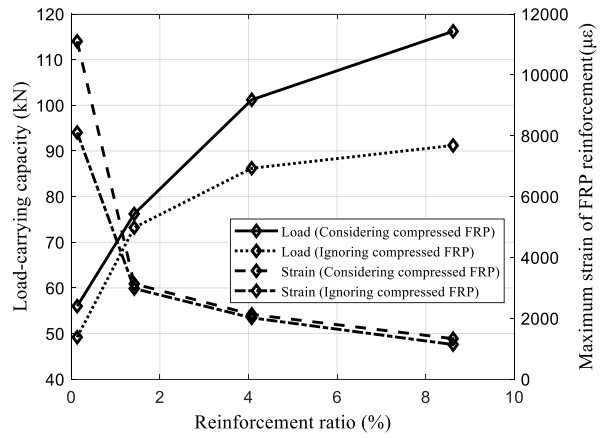
(a) Load-deflection relationships under single point loading



(b) Load-deflection relationships under multiple point loading



(c) Effect to load-bearing capacity and FRP strain level under single point loading



(d) Effect to load-bearing capacity and FRP strain level under multiple point loading

Figure 7.11 Effect of compressed FRP bar to the structural responses

## **CHAPTER 8**

### **CONCLUSIONS**

#### **8.1 INTRODUCTION**

Arch structures, renowned for their exceptional spanning and load-bearing capabilities, are widely utilized across various domains of civil engineering. Traditional arch structures, such as tunnel linings and arch bridges, are typically designed for a long service life (e.g., more than 100 years). The adoption of FRP rebars as a substitution for conventional steel reinforcement allows a series of advantages and is a promising solution for enhancing the durability of arch structures.

The main objective of this PhD study is to achieve a full understanding of, and reliable theoretical models for, the structural behavior of FRP-RC arch structures. Drawing upon a thorough review of existing FRP-enabled arch projects and relevant novel concepts, this study investigates the structural performance of FRP-RC arch structures through a series of experimental studies, numerical simulations, and theoretical analyses. This chapter summarizes the key findings of the current research and presents recommendations for future work in this field.

## 8.2 CHALLENGES IN FRP-REINFORCED CONCRETE ARCHES

The preliminary investigation, through a combined experimental and theoretical study, confirmed the feasibility of the novel FRP-RC arch. Several issues were identified and addressed in the experiment on an under-reinforced FRP-RC arch specimen. By analyzing the fundamental mechanisms contributing to these problems, corresponding solutions and design recommendations were addressed:

- (i). Due to the anisotropic nature of FRP materials, transversely oriented FRP stirrups may somewhat weaken its flexural stiffness and strength of reinforced structures, particularly those with shallow cross-sections. This suggests a need for geometric optimization of FRP stirrups to enhance their applicability.
- (ii). The lower elastic modulus of GFRP compared to steel may lead to significant load drops when major cracks appear in under-reinforced GFRP-reinforced concrete arches, as GFRP bars are unable to immediately take over the load previously resisted by the tensile concrete. Over-reinforcement is therefore recommended to facilitate these arch structures in meeting SLS requirements (e.g., acceptable deformation, cracking width).
- (iii). While the fundamental theoretical analysis can be used to provide insights into the general behavior of FRP-RC arches and estimate their load capacity, it overlooks the effect of geometric nonlinearity, thus potentially leading to an overestimation of load-bearing capacity. To overcome this limitation, advanced theoretical models or numerical simulations that account for the effects of geometric nonlinearity and material nonlinearity are required.

### **8.3 NOVEL FRP STIRRUPS**

A novel form of narrow closed FRP stirrups fabricated via a filament winding process was proposed. These stirrups have many advantages over existing FRP stirrups including their reduced cross-sectional area, minimal adverse effects on the concrete section, as well as being impervious to fiber kinking/slacking at the bent regions or premature opening due to slipping.

The strength of bent regions of the novel FRP stirrups substantially exceeds that predicted by ACI 440.1R-15 for bent FRP rods, due largely to the filament winding process. The novel FRP stirrups can effectively control crack development and improve the shear capacity of RC members. The existing design equations can be used for the conservative design of RC members reinforced with the novel FRP stirrups. Moreover, the experiment results based on three different surface treatments of stirrups show that the surface treatment methods (i.e., rib-forming and sand-coating) of the novel stirrups significantly improve their bond strength with concrete and thus their performance of shear reinforcement.

### **8.4 EXPERIMENTAL STUDY**

A series of laboratory tests were conducted to evaluate the effects of longitudinal reinforcement ratio, concrete strength, and transverse reinforcement ratio in a novel FRP-RC arch form combining over-reinforced configurations and tailored stirrups. The combination of an over-reinforced configuration with novel stirrups effectively eliminated the load drop phenomenon, resulting in arches that exhibited a monotonically increasing load profile until peak load.

The primary failure modes for over-reinforced FRP-RC arches were flexural failure, characterized by concrete crushing and shear failure due to FRP stirrup rupture. The failure mechanisms were

progressive, starting with initial cracking at the crown, followed by successive cracks at the shoulders. Due to the relatively poor bond performance between FRP and concrete, FRP-RC arches exhibited widely spaced crack patterns compared to steel-RC arches. However, improved concrete strength contributed to a more well-distributed crack pattern. The flexural cracks primarily develop at stirrup locations in both steel-RC and FRP-RC arches with small concrete cover, which may be attributed to the adverse effect of the stirrups on stress transfer between longitudinal bars and concrete.

An evaluation method for the SLS of FRP-RC arches was developed based on the provisions in ACI 440.11. The evaluation criteria include deflection limit, crack width limit, stress limit due to creep rupture, and environmental reduction factor for strength. Among these, the crack width limit appears to be the primary determinant for establishing the allowable service load. Enhancing concrete strength and reinforcement ratio increased allowable service load, ultimate load, and stiffness response, while a reduced reinforcement ratio combined with increased concrete strength improved the efficiency of longitudinal FRP bars.

Although the FRP-RC arch exhibited slightly lower structural stiffness compared to the steel-RC arch, it demonstrated comparable load-bearing capacities under similar reinforcement ratios and concrete strengths. Current standards offer conservative predictions for the shear strength of novel FRP-RC arches, primarily due to insufficient consideration of compressive stress contribution to shear resistance in compression-flexure members and the overly conservative service strain limits imposed on the novel FRP stirrups manufactured via filament winding technology.

## 8.5 THEORETICAL MODEL

To provide a straightforward and intuitive tool for understanding the fundamental mechanical behavior of FRP-RC arches and to offer guidance for preliminary structural design, a simplified theoretical model was proposed. This model is based on an enhanced deflection method, offering a unified approach for handling both small- and large-curvature problems in one-dimensional members. Its defining feature is the incorporation of a circular deflection function, which assumes that each segment of the deformed centroidal axis can be represented by a circular arc. This feature intrinsically allows for an exact curvature representation, distinguishing the proposed model from the conventional deflection method, where the simplified representation of curvature as the second-order derivative of deflection is only valid for small curvatures.

Model verification was carried out through comparisons with both analytical and numerical results. The analytical verification focused on a large-curvature problem of linear elastic arches, while the numerical verification employed a small-curvature problem of slender FRP-confined RC columns, incorporating material non-linearity. The performance of the verified model was evaluated against representative test results from FRP-RC arches and other FRP-enabled arches, comprising two sub-categories: all-FRP arches exemplified by FRP-bending active arches and FRP-incorporating hybrid arches exemplified by FRP-RC arches and CFFT arches. In the case of FRP-bending active arches, the large curvatures were induced by deformation, whereas in FRP-RC arches CFFT arches, the large curvatures were inherent in their initial configuration. The theoretical model demonstrated excellent accuracy in predicting the behavior of arches in both sub-categories, regardless of the source of large curvatures.

## 8.6 FINITE ELEMENT ANALYSIS

To capture the complex interactions of axial load, shear, and bending moments, along with the bond-slip behavior between FRP reinforcement and surrounding concrete, the structural performance of FRP-RC arches was investigated numerically using ABAQUS. A three-dimensional finite element model was developed and validated against experimental observations. This model incorporated key characteristics of FRP bars, including their distinct behaviors under tension and compression, brittle rupture properties, and the bond-slip relationship between FRP reinforcement and concrete. The model successfully captured load-bearing capacities with an average deviation of 5%, as well as failure modes (i.e., flexural and shear failures), load-deflection behaviors, crack patterns, and strain development.

The validated model was then employed for a parametric study to evaluate the influence of factors such as concrete cover thickness, reinforcement ratio, concrete strength, and contributions from compressed bars on the structural performance of FRP-RC arches. Results demonstrated that reducing concrete cover, as well as increasing reinforcement ratio and concrete strength, enhances the ultimate load and post-cracking stiffness of FRP-RC arches. The effects of concrete cover and reinforcement ratio are significant under single-point loading, whereas the influence of concrete strength is more evident under multiple-point loading. Brittle FRP rupture failure is generally avoidable in FRP-RC shallow arches if the minimum reinforcement ratio (1%) is satisfied. However, special attention should be given to shear resistance in FRP-RC arches with high concrete strength, particularly under uniform loading conditions. The discrepancies caused by different considerations for compressed FRP bars become more evident as the reinforcement ratio rises, especially under multiple-point loading conditions.

## 8.7 RECOMMENDATIONS

FRP-RC arches, characterized by their excellent corrosion resistance, represent a promising alternative to traditional steel-reinforced concrete arch structures. Future development in this field should consider the following points:

- (i). Although both concrete crushing and FRP rupture are acceptable failure modes for flexural members, concrete crushing is preferred for FRP-RC arches, as it exhibits higher stiffness, smaller deflections, reduced crack widths, and a more progressive, less catastrophic failure.
- (ii). Given the orthotropic nature of FRP composites, the stiffness and strength perpendicular to the fiber direction are significantly lower compared to those parallel to it, presenting opportunities for topological optimization. Unlike isotropic materials like steel, the design of FRP-reinforced structures should consider the fiber orientation, aligning the fiber direction with the sustained stresses (e.g., principal stresses) to optimize structural performance. In joints subjected to multiple stresses, the laminate stacking sequence of FRP can be optimized to enhance load-bearing efficiency by adjusting the orientation and thickness of individual layers. Additionally, attention should be given to potential weakening effects, such as the adverse impact of FRP stirrups on the flexural stiffness and strength of shallow arch members.
- (iii). Filament winding technology enables optimization of the geometric shape, surface texture, and fiber orientation of FRP reinforcement, thereby enhancing material efficiency. This method allows for precise control of fiber orientation and can be tailored to produce components for specific applications. Moreover, filament winding, as a machine-driven, automated, and intelligent construction technique, reduces reliance on manual labor, making

it a cost-effective approach with potential for expanding the application of FRP in innovative structural forms.

## **8.8 FUTURE RESEARCH**

Based upon the findings of this study, future research can be organized around the following key areas:

### **8.8.1 Experimental research on FRP anchorage systems**

In Chapter 5, the anchorage system for FRP bars in the tested concrete arches still relied on steel welding at the arch feet. For enhanced durability, it is recommended to replace all steel components with corrosion-resistant FRP materials, achieving a fully steel-free construction. Future research should therefore focus on developing FRP anchorage systems suitable for curved FRP bars.

A promising concept involves a novel anchorage system using filament winding technology, wherein pre-impregnated FRP filaments are wound around curved FRP bars to create mechanical anchorage that enhances bond strength. Preliminary testing has indicated the potential effectiveness of this new system and future studies should investigate key variables (e.g., anchorage length, diameter, winding angle, and spacing) to determine their effects on anchoring efficiency and failure modes. Based on these parameter studies, optimized geometric configuration for improved anchoring performance, while minimizing costs and simplifying construction.

### **8.8.2 Further experimental research on FRP-reinforced concrete arches**

The experimental studies presented in this thesis provides a solid foundation for understanding the structural mechanism of FRP-RC arches and sufficiently demonstrates the accuracy of the proposed models. However, existing experimental research is primarily limited to in-plane

responses of FRP-RC arches under single-point loading at the arch crown, which does not accurately reflect practical application scenarios. For a more comprehensive demonstration, further experimental studies should focus on full-scale testing under more realistic conditions. Additionally, future research should also include multi-point loading tests, investigations of soil-arch interaction, and studies of out-of-plane behavior to enhance the understanding of FRP-RC arches under diverse conditions.

### **8.8.3 Development of simplified design formulas for load-bearing capacity**

Building upon the fundamental principles of the equivalent beam-column simplification method used for steel-reinforced concrete arches, as well as insights from existing research on FRP-RC members under flexure and axial loads, a specialized calculation method for estimating the load-bearing capacity of FRP-RC arches should be developed for design purposes. This approach will involve a detailed analysis of parameter selection (e.g., effective length and equivalent loads) and the derivation of the load-bearing capacity for the equivalent compression-flexure member. A comprehensive parameter analysis will be conducted to evaluate the effects of reinforcement ratio, slenderness ratio, rise-to-span ratio, and loading conditions. The resulting formula will be refined through regression analysis based on comparisons with theoretical predictions and experimental data to develop a more accurate and reliable design tool.